γ-spectroscopic determination of mean lifetimes and magnetic moments of excited nuclear states

γ-spektroskopische Bestimmung von Lebensdauern und magnetischen Momenten angeregter Kernzustände

Zur Erlangung des Grades eines Doktors der Naturwissenschaften (Dr. rer. nat.) genehmigte Dissertation von Johannes Christoph Wiederhold aus Frankfurt am Main

Tag der Einreichung: 17. Dezember 2019, Tag der Prüfung: 05. Februar 2020

1. Gutachten: Prof. Dr. Dr. h.c. mult. Norbert Pietralla
2. Gutachten: Prof. Dr. Alexandre Obertelli
Darmstadt – D 17

TECHNISCHE
UNIVERSITÄT
DARMSTADT

Fachbereich Physik
Institut für Kernphysik
AG Pietralla

γ-spectroscopic determination of mean lifetimes and magnetic moments of excited nuclear states
γ-spektroskopische Bestimmung von Lebensdauern und magnetischen Momenten angeregter Kernzustände

genehmigte Dissertation von Johannes Christoph Wiederhold

1. Gutachten: Prof. Dr. Dr. h.c. mult. Norbert Pietralla
2. Gutachten: Prof. Dr. Alexandre Obertelli

Tag der Einreichung: 17. Dezember 2019
Tag der Prüfung: 05. Februar 2020

Darmstadt – D 17

Zusammenfassung

Die mittlere Lebensdauer eines angeregten Kernzustands ist eine wichtige Beobachtungsgröße, die in direktem Zusammenhang mit der Übergangswahrscheinlichkeit steht. Informationen über die mittlere Lebensdauer von angeregten Kernzuständen können Aufschluss über die Entwicklung der Kernform als Funktion der Nukleonenzahl geben. Für diese Arbeit wurden die mittleren Lebensdauern der Selten Erden Isotope ^{174,176,178,180}Hf und ^{152}Gd gemessen. Die mittleren Lebensdauern wurden mittels der bereits in den 1950er Jahren eingeführten Fast-Timing Methode bestimmt. Auf Grund der rasanten Fortschritte bei der Entwicklung neuer Szintillationsdetektoren in den letzten zwei Jahrzehnten kann diese Messmethode auf einen größeren Bereich angeregter Kernzustände angewendet werden. Die Experimente wurden am FN-Tandembeschleuniger des IFIN-HH mit dem ROSPHERE-Detektorarray durchgeführt.

Eine mögliche neue Signatur für den bekannten Quantenphasenübergang bei $N = 90$ wurde mit Hilfe der Ergebnisse des ^{152}Gd-Experiments bestätigt, und deren Korrelation mit anderen bekannten Signaturen wie der $E0$-Übergangsstärke wurde getestet. Die Entwicklung der Kollektivität und der Rotationsstruktur der Hafniumisotope wurde untersucht und ein Maxiumum der Kollektivität bei $N = 100$ identifiziert. Insgesamt wurden 13 mittlere Lebensdauern für die ^{174,176,178,180}Hf-Isotope bestimmt.

Das kernmagnetische Dipolmoment ist ein wichtiger Indikator für die Zusammensetzung der Protonen-Neutronen Wellenfunktion und damit für die Einteilcheneigenschaften des Kernzustands. Der zweite Teil dieser Arbeit präsentiert die Ergebnisse einer g-Faktormessung des 2_1^+-Zustands von ^{18}O mit der kürzlich entwickelten ECR-TDRIV-Technik. Das Verfahren ist insbesondere für die Anwendung auf radioaktive Ionenstrahlen vorgesehen, muss jedoch zuvor mit stabilen Strahlen getestet werden. Das Analyseverfahren des ^{18}O-Experiments wird beschrieben und die Ergebnisse für den g-Faktor werden mit früheren Messungen und Schalenmodellberechnungen verglichen.

Abstract

The mean lifetime of an excited nuclear state is an important observable directly related to the transition probability. Information on the mean lifetimes of nuclear excited states can give insight into the evolution of the nuclear shape as a function of nucleon number. For this work, mean lifetimes of the rare-earth isotopes ^{174,176,178,180}Hf and ^{152}Gd have been measured. The mean lifetimes have been determined with the fast-timing technique, already introduced in the 1950s, but applicable to a wider range of excited nuclear states, due to rapid progress in the development of new scintillation detectors in the last two decades. Both experiments have been performed at the FN Tandem accelerator of the IFIN-HH with the ROSPHERE detector array.

A possible new signature for the known quantum phase transition at $N = 90$ has been established with the results from the ^{152}Gd experiment and the correlation to other observables, such as the $E0$ transition strength, has been investigated. The evolution of collectivity and the rotational structure of the hafnium isotopes have been investigated and a maximum of the collectivity at $N = 100$ has been identified. In total 13 mean lifetimes have been determined for the ^{174,176,178,180}Hf isotopes.

The nuclear magnetic dipole moment is an important indicator of the composition of the proton neutron wave function, and therefore the single particle properties of the nuclear state. The second part of this thesis presents the results from a g-factor measurement of the 2^+_1 state of ^{18}O with the recently developed ECR-TDRIV technique. The method is in particular foreseen for the application to radioactive ion beams, but has to be tested with stable beams. The analysis procedure of the ^{18}O experiment is outlined and the results for the g factor are compared to previous measurements and shell model calculations.

Acknowledgments

This work would not have been possible without the help and the support of many people. In particular, I would like to thank:

- my parents along with my sisters and their families for their strong support during my student and PhD time.

- my doctoral supervisor **Norbert Pietralla** for giving me the opportunity to work on this project, his support and encouragement during the whole time, and his constant helpful remarks and new ideas.

- **Volker Werner** for his guidance, fruitful discussions, and the many things he taught me on the topics of γ-ray spectroscopy during my time at the IKP.

- **Rostislav Jolos** for his help with the interpretation of the ^{152}Gd data. **Andrew Stuchbery** for introducing me to the finer details of the measurements of magnetic moments.

- **Alexandre Obertelli** for agreeing to be the second reviewer of this thesis and his helpful comments.

- for the local support during the experiments at the IKP Cologne and at IFIN-HH in Bucharest, in particular from **Claus Müller-Gatermann** and **Christoph Fransen**, and **Nicu Marginean** and his group, respectively.

- the administrative staff of our institute, in particular **Marco Brunken**, **Catja Noll**, **Carina Seeger**, **Giovanna Umberti Caroli**, and **Ursula von Dungen** for all their administrative help.

- for proofreading the drafts of this manuscript: **Tobias Beck**, **Katharina Ide**, **Philipp John**, **Ralph Kern**, **Pavlos Koseoglou**, **Philipp Napiralla** and **Volker Werner**.

- my many roommates during my time at the IKP and the rest of our working group for the comfortable working environment, interesting conversations about nuclear physics and beyond: **Usama Ahmed**, **Christopher Bauer**, **Tobias Beck**, **Marcel Berger** (né Schilling), **Liliana Cortes**, **Udo Friman-Gayer**, **Katharina Ide**, **Philipp John**, **Ralph Kern**, **Jörn Kleemann**, **Pavlos Koseoglou**, **Marc Lettmann**, **Cesar Lizarazo**, **Oliver Möller**, **Thomas Möller**, **Philipp Napiralla**, **Oliver Papst**, **Philipp Ries**, **Pär-Anders Söderström**, **Robert Stegmann**, **Volker Werner**, **Waldemar Witt**, **Radostina Zidarova**, and **Markus Zweidinger** and many others.

Contents

"There are these two young fish swimming along and they happen to meet an older fish swimming the other way, who nods at them and says "Morning, boys. How's the water?" And the two young fish swim on for a bit, and then eventually one of them looks over at the other and goes "What the hell is water?".....

— David Foster Wallace, *This Is Water: Some Thoughts, Delivered on a Significant Occasion, about Living a Compassionate Life*

1. Introduction & motivation

The atomic nucleus is an interesting research object. It is a complex, many particle quantum object, composed of protons and neutrons. Even though more than 100 years passed since the discovery of radioactivity by H. Becquerel [1] and the atomic nucleus by E. Rutherford [2], the binding force holding the nucleons together still has to be fully understood. The ultimate goal of nuclear structure physics would be a description of the nuclear force from basic principles, based on the fundamental interactions: gravitation, the electromagnetic interaction, the weak and the strong interaction. The electromagnetic repulsion of the positively charged protons has to be counteracted by some other force, captivating the nucleons in the atomic nucleus. Gravitation and the weak force are not strong enough, leaving the strong interaction, which is responsible for the formation of hadrons, binding quarks and gluons together. The residual color force of the quarks and gluons, the constituents of protons and neutrons, has to be responsible for the formation of atomic nuclei [3]. The best theoretical description of the strong force is given by quantum chromodynamics (QCD) [4]. Unfortunately a perturbative treatment of QCD is not possible at the energy scale of the nucleons. Furthermore, the finite amount of nucleons in the atomic nucleus prevents to a large degree the application of statistical methods. Therefore, alternative ways have to be taken to describe nuclear matter and to treat QCD.

Several aspects of the nuclear force are empirically known. The binding energy per nucleon is nearly constant for all known stable isotopes, around 8 MeV/A. Indicating, that the nuclear force has a short range of a few fm and only acts on direct neighbours. It has to be predominantly attractive to form nuclei and is repulsive at very short distances, ~ 0.7 fm, which can be deduced from the saturation of the nuclear density in the core and the Pauli principle. The nuclear force is charge independent (apart from the Coulomb repulsion), i.e. proton-proton, neutron-neutron and proton-neutron interactions are equal, leading to the concept of isospin. Moreover, the great number of non-spherical shaped nu-
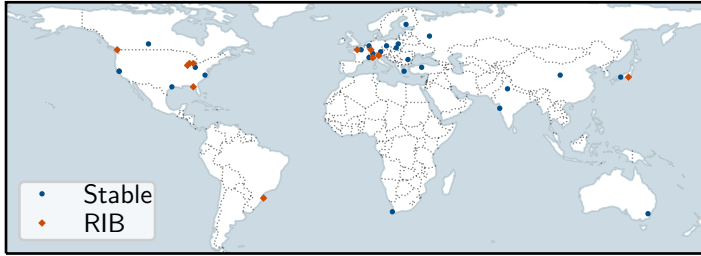
Figure 1.1.: List of nuclear structure research facilities worldwide for stable beams (●) and radioactive ion beams (RIBs) (◆).

clei imply the existence of spin-dependent tensor forces.

The empirical information about the atomic nucleus and the nuclear force have to be incorporated in a comprehensive theoretical description. Over the years, a multitude of different theoretical models have been introduced, describing certain aspects of nuclear structure. Three main groups of models are the shell models (SMs), collective models, and algebraic models, such as the interacting boson model (IBM). Through the advent of new radioactive ion beam (RIB) facilities in the last 20 years many new insights on nuclei far away from the valley of β stability have been gained. Figure 1.1 shows some of today's important heavy ion beam facilities worldwide. Marked with ● are stable beam facilities and ◆ mark current and future RIB facilities. More information on the production of RIB are given in Refs. [5, 6]. The new available data lead to a further improvement of our understanding of nuclear matter and serve as a test ground for the different available theoretical descriptions. The playground of nuclear physics, the nuclear chart is depicted in Figure 1.2, where all isotopes are represented in a N-Z chart. Here, only isotopes with an even number of protons and neutrons, whose excited 2_1^+ and 4_1^+ states are known, are depicted. The color code represents the energy ratio of the first excited 4^+ state and the first excited 2^+ state $R_{4/2}$. Nuclei, whose lifetimes are greater than 10^{15} years, are considered stable (□) and form the valley of stability. The $R_{4/2}$ is an easily accessible observable, connected to the shape of the nucleus. The ratios of all isotopes fall into three categories. A value of less than 2 for isotopes at certain proton and neu-
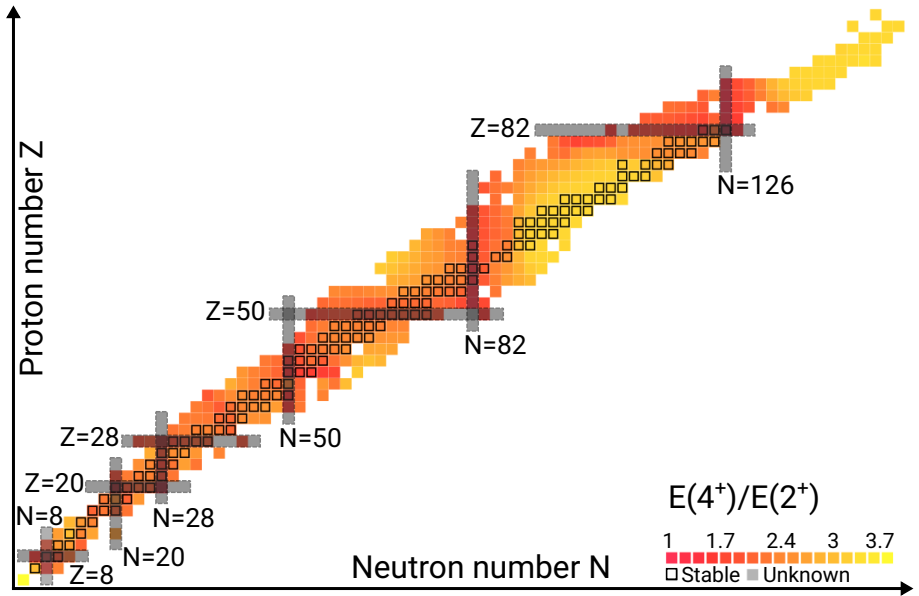
Figure 1.2.: Nuclear chart (adapted from [7]). Data from [8]. The color code represents the $R_{4/2}$ energy ratio of the shown isotopes. Stable isotopes are marked by □.

tron numbers, the so-called "magic numbers" ($Z, N = 2, 8, 20, 28, 50, 82, 126$), corresponding to a spherical configuration of the nucleus. A value between 2 and 2.4 for isotopes in the vicinity of the magic numbers (vibrational nuclei) and values of ~ 3.33 for isotopes in between the magic shell closures (rigid rotor).

Low-lying excited states of most accessible atomic nuclei decay mainly via the emission of γ radiation, high-energetic photons. The measurement of the de-excitation γ rays allows to infer properties of excited nuclear states and therefore the structure of the nucleus, for instance its mean lifetime or its decay behavior. New instrumentation, like the cerium doped lanthanum bromide ($LaBr_3(Ce)$) detectors [9] with their excellent timing properties in combination with a comparatively good energy resolution for a scintillation detector or γ-ray tracking

arrays composed of high-purity germanium (HPGe) detectors, such as the advanced gamma-tracking array (AGATA) [10] or the gamma-ray energy tracking in-beam nuclear array (GRETINA) [11, 12] gave rise to new wave of high precision experiments and new insights into nuclear matter, e.g. the emergence and disappearance of magic numbers far from stability (see Refs. [13–19]).

This work addresses two different techniques of γ-ray spectroscopy, foreseen for the application to RIB: the investigation of mean lifetimes of excited nuclear states in the rare-earth region of the nuclear chart via fast electronic scintillation timing (FEST) and the investigation of magnetic dipole moments of excited nuclear states of low-Z nuclei with the electron-configuration-reset time-differential recoil-in-vacuum (ECR-TDRIV) technique.

1.1. Lifetime measurements of excited states of rare earth isotopes

1.1.1. Evolution of $E2$ transitions strengths of Hf isotopes

Another important observable, besides the $R_{4/2}$ ratio, regarding the nuclear shape of even-even nuclei, is the $B(E2; 2_1^+ \to 0_{GS}^+)$ transition strength, connecting the ground state (GS) and the 2_1^+ state. Since most nuclei far from shell closures are quadrupole deformed [20] the $B(E2)$ strength is an appropriate measure of collectivity. Nuclei close to magic shell closures show small $E2$ transition strengths (~ 1 to 10 W.u.), whereas the $B(E2)$ values of well-deformed nuclei can reach a few hundred W.u. (see Refs. [21–34]). Examples are the rare-earth isotopes around the mass number $A \approx 170$ with quadrupole deformation values $\beta \sim 0.2 - 0.4$. In a naive valence-shell picture, solely allowing for an excitation of valence nucleons, collectivity should be directly proportional to the number of valence nucleons (holes) and thus maximize at mid-shell. A similar evolution has also been predicted within the SU(3) dynamical symmetry of the IBM [35, 36]. Zhang et al. [37] pointed out, that the available experimental data indicate a saturation of the $B(E2)$ values and g factors [38, 39] of the first excited states of even-even nuclei around $A \approx 170$, near mid-shell (between $N = 82$ and $N = 126$), instead of a maximum. Figure 1.3 presents the pre-year 2006[1]

---

[1]Only the data available before the experimental campaign described in this work is shown in Figure 1.3. In the meantime, the results obtained by M. Rudigier et al. for the Hf isotopes have
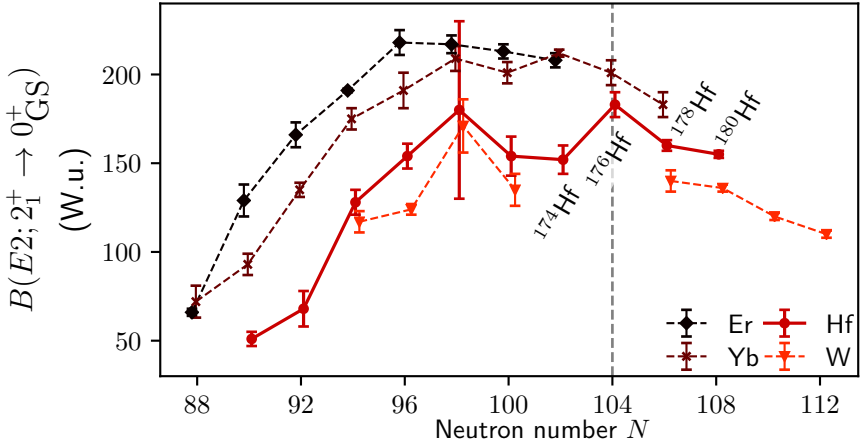
Figure 1.3.: Evolution of $B(E2; 2_1^+ \to 0_{GS}^+)$ values of even-even Er ($\blacklozenge$), Yb ($\boldsymbol{\times}$), Hf ($\bullet$) and W ($\blacktriangledown$) isotopes around neutron number $N = 104$ (marked by a vertical grey dashed line) . Data are taken from Refs. [21–34, 41].

$B(E2)$ data of the Er ($\blacklozenge$), Yb ($\boldsymbol{\times}$), Hf ($\bullet$) and W ($\blacktriangledown$) isotopes in that area of the nuclear chart. A near constant behaviour for the $B(E2)$ transition strength is visible for the Er, Yb and the Hf isotopes at or below mid-shell ($N = 104$), which is in agreement with the statement of Zhang. An overlap of the proton and neutron wave functions alongside a reduction of the proton-neutron interaction near mid-shell was given as a qualitative explanation for the saturation.

In addition, it was revealed in Refs. [36, 42] that the tungsten and hafnium isotopes display an irregularity in the differential of the $B(E2)$ strengths, which is defined as $\delta B(E2) = B(E2)_N - B(E2)_{N-2}$. The trend of the differential should be smooth, but sharp drops and oscillations can be identified for the data of the Hf and W isotopic chains. These oscillations and drops may hint at changes in the underlying microscopic nuclear structure or simply point out incorrect experimental data [the same $B(E2)_N$ value occurs in $\delta B(E2)_N$ and $\delta B(E2)_{N+2}$

---

been published [40] and are in agreement with the results from this work. The new values of the Hf isotopes show a similar trend to the Yb and Er isotopes. See also Section 6.1.
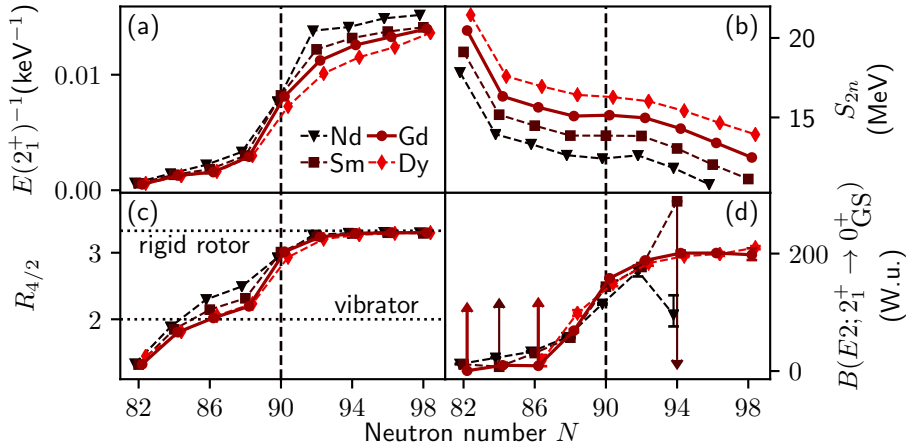
Figure 1.4.: (a) Inverse excitation energy of the 2_1^+ state in keV^{-1}, (b) two neutron separation energy in keV, (c) $R_{4/2}$ values, and (d) reduced transition probability $B(E2; 2_1^+ \rightarrow 0_{GS}^+)$ in W.u. of the even-even Nd (▼), Sm (■), Gd (●) and Dy (♦) isotopes around $N = 90$ as a function of neutron number. Data taken from Refs. [21–25, 41, 46–53].

[36] amplifying the effect]. New experiments in this region of the nuclear chart [36, 40, 43–45], indeed, revealed large discrepancies on the order of up to 20% from the literature values for the mean lifetime $\tau(2_1^+)$ of the Hf and W isotopes. For that reason, a measurement campaign to determine the $E2$ transition strengths of low-lying yrast states of ^{174,176,178,180}Hf was performed at the Institutul National de Cercetare-Dezvoltare pentru Fizica si Inginerie Nucleara (Horia Hulubei) (IFIN-HH) and will be presented in this thesis.

1.1.2. New signatures for a QPT in atomic nuclei

By going along the isotopic chains of the rare-earth isotopes from the magic shell closure at $N = 82$ towards mid-shell, the $B(E2)$ transition strength suddenly jumps from values of just a few W.u. below $N = 90$ to a few 100 W.u. [54–57]. A similar behaviour is found for the $R_{4/2}$ ratios. These trends hint at a sudden change in the nuclear shape as a function of nucleon number, known as a quan-

tum phase transition (QPT) [58]. Further examples of such a sudden change can be found, e.g. in the Zr, Sr region [59–62]. Figure 1.4 shows the evolution of the inverse excitation energy of the first 2^+ state (a), the two-neutron separation energy S_{2n} (b), the $R_{4/2}$ energy ratio (c), and the $E2$ transition strength $B(E2; 2_1^+ \rightarrow 0_{GS}^+)$ for the even-even rare-earth Nd ($\blacktriangledown$), Sm ($\blacksquare$), Gd ($\bullet$) and Dy ($\blacklozenge$) isotopic chains. A clear change of these observables is visible at $N = 90$, more rapid in Sm and Gd, indicating a QPT. Investigating these and further observables and their correlations can help to further improve our understanding of QPTs [58, 63, 64].

A possible new signature of QPT is the product of transition probabilities, connecting the first excited 2^+ state to the ground state and the first excited 0^+ state, $B(E2)_{prod} = B(E2; 0_1^+ \rightarrow 2_1^+) \times B(E2; 0_2^+ \rightarrow 2_1^+)$. The product can be related to the $E0$ transition strength ρ^2, an established signature for a QPT (see Refs. [65–67]). The Gd isotopes happen to be the perfect test case, since all the experimental data, $B(E2)$ strengths and ρ^2, are available for the isotopic chain over the QPT from $N = 88$ (^{152}Gd) to $N = 92$ (^{156}Gd). Due to the fact, that the mean lifetime of the 0_2^+ state [the $B(E2; 2_1^+ \rightarrow 0_2^+)$ value is derived from this lifetime] was previously only determined in one experiment [68] with an uncertainty of 22 %, a fast-timing lifetime measurement was performed with the goal to verify or falsify this single measurement and further investigate the correlations between different observables around the QPT.

1.2. Measurement of the g factor of ^{18}O with the ECR-TDRIV technique

The second part of this work focuses on the measurement of magnetic dipole moments. These are an important indicator of the proton neutron wave function composition and therefore the single-particle properties of the unpaired nucleons of the investigated excited states [69, 70]. The determination of magnetic moments of exotic nuclei can help to expand our knowledge of the underlying microscopic structure of these nuclei. Customized experimental techniques are required for the measurement of magnetic moments of exotic nuclei, because additional experimental obstacles have to be overcome, compared to the application to stable beams. For example the potential need to identify the reaction

products with particle detectors[2].

The region of the sd shell has been extensively studied in recent years, due to a multitude of phenomena, e.g. as mentioned previously the emergence of the magic number $N = 16$ [71] and the disappearance of $N = 20$ or the so-called island of inversion at the edge of the sd shell [72]. Figure 1.5 (c) shows the literature values of the g factors of the $N = Z + 2$ nuclei (▼) in the sd shell along with predictions from the large scale shell model calculation code (NUSHELLX) [73] employing the universal sd interaction B (USDB) [74, 75] (●). There is an overall good agreement between the experimental values and the SM predictions, but at the edges of the sd shell the theoretical predictions deviate and the experimental values are further from one (minus) in comparison to the theory. The SM calculations with the USDB interaction are capable to reproduce various properties of the $N = Z + 2$ isotopes. Figure 1.5 (a,b,d) presents, in addition to the g factors, the excitation energies $E(2_1^+)$, the reduced transition strengths $B(E2; 2_1^+ \rightarrow 0_{GS}^+)$, and the quadrupole moments $Q(2_1^+)$ of the 2_1^+ states. Discrepancies between theory and experimental data can be identified solely for ^{18}O and ^{38}Ar. Hence, an experiment was performed at the Institut für Kernphysik (IKP) of the Universität zu Köln, in order to determine the g factor of the first 2^+ state of ^{18}O, testing the new experimental method ECR-TDRIV. It is an extension of the traditional time-differential recoil-in-vacuum (TDRIV) technique [76] for the application to RIB to relatively low Z nuclei ($Z \leq 20$), introduced by Stuchbery et al. in Ref. [77]. The technique has already been successfully applied in the case of ^{24}Mg [78, 79].

---

[2]Since a sizable amount of material is necessary to construct targets, nuclear reactions with radioactive isotopes are often performed in inverse kinematics.

1. Introduction & motivation
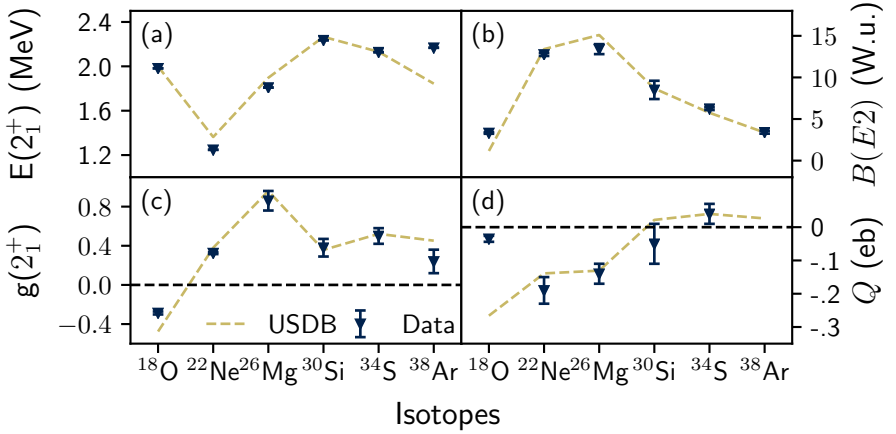
Figure 1.5.: Comparison between experimental data of the $N = Z + 2$ isotopes in the sd-shell (▼) with SM calculations from NUSHELLX [73] with the USDB interaction [74, 75] (●). Depicted are (a) the excitation energy $E(2_1^+)$, (b) the $B(E2; 2_1^+ \to 0_{GS}^+)$ transition strength, (c) the g factors $g(2_1^+)$, and (d) the quadrupole moment $Q(2_1^+)$. Data taken from Refs. [80–86].

Outline

The thesis is structured in the following way:

- Chapter 2 introduces the main theoretical concepts used for the interpretation of the experimental results.

- Chapter 3 presents the utilized nuclear reactions to populate excited states of the isotopes of interest, γ-ray spectroscopy, and the experimental techniques employed in this work, i.e. the FEST method and the ECR-TDRIV technique.

- Chapter 4 describes the two experimental setups used in this work at the IFIN-HH in Bucharest and the IKP der Universität zu Köln. The properties of the used detector systems and the beam properties.

- The analysis procedure for the two types of experiments, e.g. data preparation and calibration procedures, and the extraction of the results are expounded in Chapter 5.

- The discussion and interpretation of the results are presented in Chapter 6.

2. Nuclear structure models

The following Chapter introduces the main theoretical concepts employed to interpret the data of this work. It starts by introducing the reader to the different approaches of the collective model by A. Bohr and B.R. Mottelson and the IBM, as well as the concept of the QPT of atomic nuclei and the description of its critical point. The introduced models are already treated extensively in standard textbooks and, if not stated otherwise in this Chapter, the text follows Refs. [20, 35, 87–89] and references therein.

2.1. Collective model

Historically, the SM was the first successful model to describe the magic shell closures at the nucleon numbers 2,8,20,28,50,82,126 and make predictions for the properties of the ground-state and excited states in the vicinity of these magic numbers. However, the SM calculations or the interpretation of their results becomes increasingly difficult with growing valence space of the nucleons, e.g. for ^{154}Sm, the valence protons and neutrons can couple to 3×10^{14} possible $J^{\pi} = 2^+$ SM states [89]. Furthermore, the lowest excited state of even-even nuclei is often a 2^+ state, whose energy is quite below the energy needed to break a pair of valence nucleons. Hence, there have to be other properties that are common in even-even nuclei across the nuclear chart, i.e. collective properties. The liquid drop model, introduced by A. Bohr, B.R. Mottelson [88], and many others, treats the atomic nucleus as a drop of nuclear liquid, which may vibrate or deform and rotate. The nuclear surface of such a liquid drop can be described by the distance of the surface to the origin $R(\theta, \phi)$ in the collective coordinates
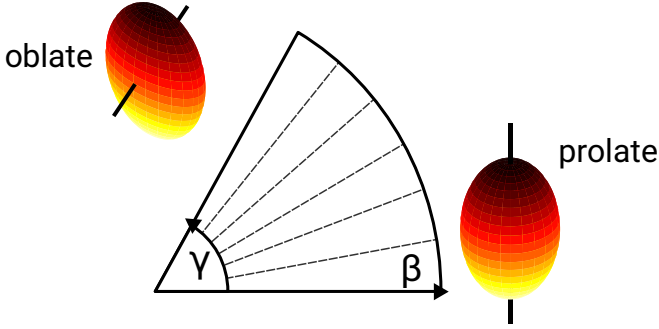
Figure 2.1.: Nuclear shapes from spherical to prolate and oblate deformation in
the $\{\beta, \gamma\}$ plane.

$a_{\lambda\mu}$ by an expansion in terms of the spherical harmonics Y:

$$R(\theta, \phi) = R_0 \left[1 + \sum_{\lambda\mu} a_{\lambda\mu} Y_{\lambda\mu}^*(\theta, \phi) \right], \tag{2.1}$$

with the equilibrium nuclear radius $R_0 \approx 1.25 \sqrt[3]{A}$ fm. Terms with the multipole
order $\lambda = 0$ represent a compression of the nucleus without changing its shape,
$\lambda = 1$ is equivalent to a displacement of the whole nucleus, which cannot result
from internal forces. Therefore, the $\lambda = 2$ (quadrupole) multipole mode is the
lowest order of interest at low energies, invoking a change in the nuclear shape.
Quadrupole deformation plays an important role for low-lying collective struc-
tures of atomic nuclei. Transforming the collective coordinate system of Eq. (2.1)
to the body-fixed system reduces the parameters $a_{\lambda\mu}$ to two real parameters β
and γ in the case of quadrupole deformation. These are defined as

$$a_{20} = \beta \cos\gamma, \ a_{2\pm2} = \frac{1}{\sqrt{2}}\beta \sin\gamma \text{ and } a_{2\pm1} = 0. \tag{2.2}$$

The deformation strength (degree of axial deformation) is given by the quadrupole
deformation parameter $\beta \geq 0$ and the asymmetry by the parameter γ, i.e. the

degree of triaxiality, ranging from $\gamma = 0°$ (prolate) to $\gamma = 60°$ (oblate). In these variables, the Bohr Hamiltonian can be written as [88]:

$$H = T + V = T_{\text{vib}} + T_{\text{rot}} + V, \tag{2.3}$$

with

$$T_{\text{vib}} = -\frac{\hbar^2}{2D}\left[\frac{1}{\beta^4}\frac{\partial}{\partial\beta}\beta^4\frac{\partial}{\partial\beta} + \frac{1}{\beta^2}\frac{1}{\sin 3\gamma}\frac{\partial}{\partial\gamma}\sin 3\gamma\frac{\partial}{\partial\gamma}\right], \tag{2.4}$$

$$T_{\text{rot}} = \frac{\hbar^2}{8D\beta^2}\sum_\kappa\frac{J_\kappa^2}{\sin^2\gamma - 2/3\kappa\pi}, \tag{2.5}$$

$$V = V(\beta, \gamma). \tag{2.6}$$

Here, D denotes the mass parameter and J_κ are the angular momentum operators in the Euler angles. For certain values of β and γ, the Hamiltonian is analytically solvable and the solution leads to, e.g. the harmonic oscillator (HO) vibrator energy spectrum [$\beta = 0, \gamma = 0$, U(5)] [88, 90] or to the rigid-rotor energy spectrum [$\beta > 0, \gamma = 0$ or $\gamma = 60$, SU(3)] [88, 91], with their typical energy ratios $R_{4/2} = E(4_1^+)/E(2_1^+)$, for even-even nuclei, of $R_{4/2} = 2$ (vibrator) and $R_{4/2} = 3.33$ (rotor).

In addition, analytical solutions of the Bohr Hamiltonian have been found for the QPT between spherical [U(5)] and γ-soft nuclei [O(6)], i.e. the E(5) symmetry [92] and for the QPT between spherical and symmetrical axially deformed nuclei [SU(3)], i.e. the X(5) solution [93], and the entire range between X(5) and the rigid-rotor limit in terms of the confined-β-soft rotor (CBS) model [94]. The evolution of the potential energy surface for the QPT U(5)→S(U3) is depicted in Figure 2.2.

2.1.1. X(5) model

The X(5) solution of the Bohr Hamiltonian was established by F. Iachello in Ref. [93]. It describes the critical point of a QPT between spherical and axially deformed nuclei. The ansatz is to describe the potential in β with an infinite square well with the barrier width β_w and the potential in γ as a HO with the
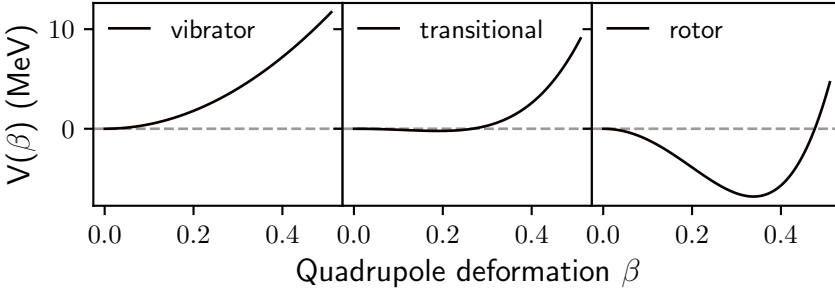
Figure 2.2.: Schematic evolution of the potential energy surface in the $\gamma = 0°$ plane from the geometric collective model [95], i.e. U(5)→SU(3). Parameters taken from Ref. [20].

minimum at $\gamma = 0°$, if the potential $V(\beta, \gamma)$ can be separated into $v(\beta)$ and $u(\gamma)$:

$$v(\beta) = \begin{cases} 0, & \text{for } \beta \le \beta_w, \\ \infty, & \text{for } \beta > \beta_w. \end{cases} \tag{2.7}$$

Figure 2.3 (a) shows the comparison between a potential derived from the collective model and the approximation of the square well potential employed in the X(5) ansatz. Empirical signatures for X(5) are, e.g. the ratios $R_{4/2} = 2.9$ and $B_{4/2} = B(E2; 4_1^+ \rightarrow 2_1^+)/B(E2; 2_1^+ \rightarrow 0_{GS}^+) = 1.58$ and the placement of the first excited band. Several empirical realizations of X(5) were found in the rare-earth region of the nuclear chart along $N = 90$, e.g. ^{152}Sm, ^{150}Nd, ^{154}Gd, and ^{156}Dy [54–57].

2.1.2. Confined β-soft rotor model

The CBS model [94] extends the X(5) approach towards the rigid-rotor limit. It introduces an inner boundary for the infinite square potential $v(\beta)$ and assumes a HO potential for $u(\gamma)$ with the minimum at $\gamma = 0°$. The stiffness of the potential in β is given by

$$r_\beta = \frac{\beta_{min}}{\beta_{max}}, \tag{2.8}$$

2. Nuclear structure models
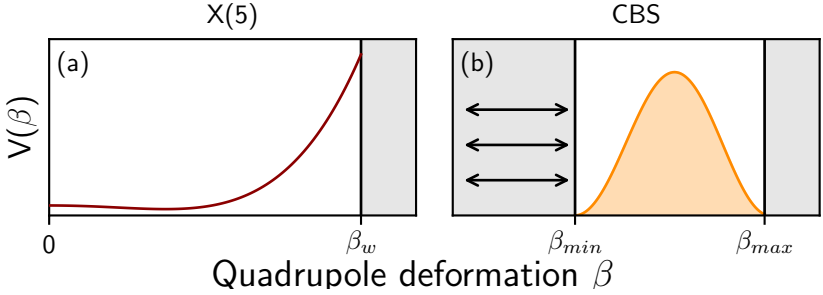
Figure 2.3.: Approximation of the nuclear potential as a function of the deformation parameter β for (a) the X(5) and (b) the CBS model. (a) The dark red line indicates a potential from the collective model. (b) The black arrows indicate the moving inner boundary of the infinite square well potential of the CBS model. The wave function of a 0^+_1 state is shown.

with the inner and outer boundaries β_{min} and β_{max}, respectively. Figure 2.3 (b) shows the CBS potential for $r_\beta = 0.4$. The potential is equivalent to the X(5) model for $r_\beta = 0$ and corresponds to the rigid-rotor limit for $r_\beta \to 1$.

The CBS model successfully describes the evolution of low-energy 0^+ bands [94], the ground-state bands of strongly deformed nuclei [96] and for studying the evolution of the $E0$ transition strength from X(5) nuclei to the rigid-rotor limit [66]. In addition, it can be shown that

$$\rho^2(E0) \propto B(E2)_1 B(E2)_2, \tag{2.9}$$

where $B(E2)_i = B(E2; 2^+_1 \to 0^+_i)$. Thus, the product of $B(E2)$ values might be a new signature for a QPT in atomic nuclei. The full derivation can be found in Appendix A.2. The limits of the Bohr Hamiltonian directly connect the collective model to the IBM, which will be discussed in the next Section.
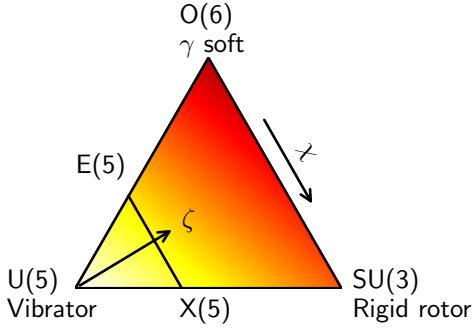
Figure 2.4.: IBM symmetry triangle and the corresponding limits of the collective model. X(5) and E(5) are analytical solutions of the Bohr-Hamiltonian, see Section 2.1.1.

2.2. Interacting boson model

The IBM [35] offers another approach to describe atomic nuclei. It is derived from a truncation of the SM space, but is also able to interpret collective phenomena. It is an algebraic model describing low energy collective excitations of atomic nuclei over the whole nuclear chart. The building blocks of the model are valence nucleons (protons or neutrons) paired to bosons, in analogy to Cooper pairs in the electron gas [97]. In the *sd-IBM-1* version, protons and neutrons are treated as indistinguishable nucleons and the bosons can carry the angular momentum $L = 0$ (*s* bosons) or $L = 2$ (*d* bosons). Naturally, the number of bosons is given by

$$N = (N_\pi + N_\nu)/2, \qquad (2.10)$$

with the number of valence protons and neutrons N_π, and N_ν, respectively. The boson creation and annihilation operators of the *sd-IBM-1* are

$$s^\dagger, s, \text{ and } d^\dagger_\mu, \tilde{d}_\mu \qquad (2.11)$$

with $\mu \in \{\pm 2, \pm 1, 0\}$. Operators are written in terms of these boson operators. For instance, a simplified Hamiltonian in the consistent-Q formalism[1] [98, 99] is given by [100]

$$H = \epsilon n_d - \kappa Q^\chi \cdot Q^\chi = c \left[(1 - \zeta) n_d - \frac{\zeta}{4N} Q^\chi \cdot Q^\chi \right], \qquad (2.12)$$

where n_d is the d boson number operator $(d^\dagger \tilde{d})$, $Q^\chi = (s^\dagger \tilde{d} + d^\dagger s) + \chi (d^\dagger \tilde{d})^{(2)}$ the quadrupole structure operator and $\zeta = 4N/(4N + \epsilon/\kappa)$.

The *sd-IBM-1* structure can be expressed in terms of the algebraic group U(6) (see Refs. [35, 101]). Three analytical solutions of the *sd-IBM-1* exist for the three subgroups U(5), SU(3), and O(6) of U(6). They describe the three edges of the IBM symmetry triangle, which can be mapped with the parameters $\chi \in [-\sqrt{7}/2, 0]$ and $\zeta \in [0, 1]$ as depicted in Figure 2.4. U(5) corresponds to $\zeta = 0$, SU(3) to $\zeta = 1$ and $\chi = -\sqrt{7}/2$ and O(6) to $\zeta = 1$ and $\chi = 0$.

2.2.1. *Q*-phonon scheme

The Q-phonon scheme was developed to describe low-lying excited states of even-even nuclei [102–107]. Low-lying positive parity states can be approximated in terms of multiple quadrupole (Q) phonon excitations of the ground state $|0^+_{GS}\rangle$ of a nucleus

$$|L^+, n\rangle = \underbrace{[Q...Q]}_{n}^{(L)} |0^+_{GS}\rangle. \qquad (2.13)$$

By an evaluation of the ratio

$$R^{(2)} = \frac{\Sigma_{i>1} B(E2; 0^+_{GS} \to 2^+_i)}{\Sigma_{i \geq 1} B(E2; 0^+_{GS} \to 2^+_i)}, \qquad (2.14)$$

it was empirically proven in Ref. [104] that the first 2^+ state of all collective nuclei between $Z = 30$ and $Z = 82$ exhausts ($\geq 90\%$) of the known $E2$ transition strength from the GS. Moreover, a similar approach has come to the same results for odd-spin states of collective nuclei [105].

---

[1]In the consistent Q formalism the same parameter χ is used for Q^χ in the Hamiltonian and the $E2$ transition operator $T(E2) = e_B Q$, with the boson charge e_B.

3. Experimental techniques

In this Chapter several aspects of nuclear structure physics, that are particularly important for this work, will be introduced. The first Section will acquaint the reader with the exploited nuclear reactions, which populate excited states of the isotopes of interest. It follows a short introduction to excited nuclear states and the subsequent γ decay. Afterwards, the measurement of lifetimes of excited nuclear levels will be discussed. The last part of this Chapter outlines the measurement of magnetic moments, in particular with the TDRIV technique.
The following Sections are based on standard textbooks of nuclear structure physics, i.e. Refs. [20, 87, 108–110], and further details on specific topics can be found there or in references therein.

3.1. Nuclear reactions

There is only a limited number of stable isotopes ($\sim$ 300 [111]) available to study in nature. Therefore, studying properties of the atomic nucleus almost always requires the production of these nuclei by nuclear reactions. Nuclear reactions were investigated for the first time about 100 years ago by Rutherford et al. [2], by scattering α particles from a radioactive source on gold foils. With the advent of many new technological advancements, reactor or accelerator facilities worldwide allow to study a large variety of nuclear reactions and their products.

A nuclear reaction is typically written in two equivalent ways:

$$a + X \rightarrow Y + b,$$
$$X(a, b)Y,$$
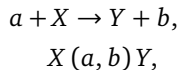
with the projectile a, the target X, and the reaction products Y and b. All reaction partners can be nuclei, single nucleons or γ rays. Nuclear reactions can be categorized in different ways. The process is called *elastic scattering*, if the
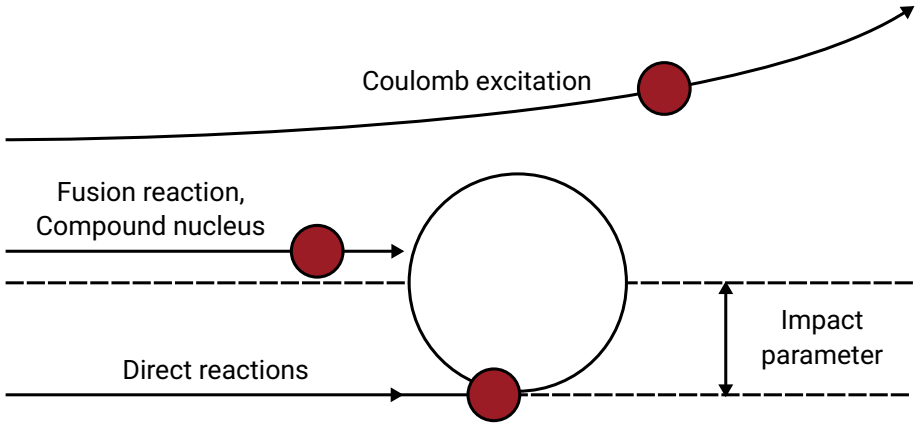
Figure 3.1.: Different trajectories for different reaction processes between heavy ions.

incoming and outgoing particles are the same, i.e. $a = b$ and $X = Y$, and the outgoing particles are not in an excited state. If the impact parameter, i.e. the perpendicular distance between the path of the projectile a and the target X (as illustrated in Figure 3.1), is small, *compound reactions* can take place. These will be further discussed in detail in Section 3.1.2. *Direct reactions* can occur in the peripheral collision between the incoming particles and the target. The reaction is called *inelastic*, if any of the outgoing particles emerges in an excited state.

This work will focus on two types of nuclear reactions (see Ref. [87] and references therein for information on further nuclear reactions);Coulomb excitation (CoulEx) and fusion evaporation (FE). They will be introduced in the following Sections.

3.1.1. Coulomb excitation

The excitation of an atomic nucleus via the electromagnetic (EM) field of another nucleus by the exchange of virtual photons is CoulEx. The method is well understood, because it is based on the EM interaction, and has already been used to study atomic nuclei for decades. The theoretical description was
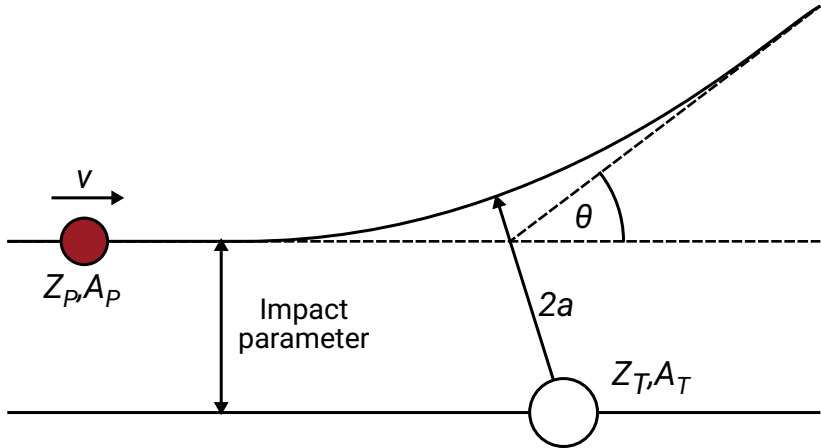
Figure 3.2.: Classical orbit of the projectile in the Coulomb field of the target nucleus, shown in the rest frame of reference of the target nucleus.

developed by K. Alder and A. Winther [112, 113]. If it is guaranteed that the interaction between the nuclei is purely EM, CoulEx can be adequately described in a semi-classical way. The following brief introduction of CoulEx is based on the classical work of Refs. [112–114].

One requirement for the semi-classical treatment is, that the effective strength of the interaction, i.e. the Sommerfeld parameter η, which can be written as the ratio between the half-distance of closest approach in a head-on collision a and the de Broglie wavelength λ of the relative motion of the two particles, is large compared to unity:

$$\eta = \frac{a}{\lambda} = \frac{Z_P Z_T e^2}{\hbar v} \gg 1, \tag{3.1}$$

where v is the relative velocity and Z_P and Z_T are the proton numbers of the projectile and the target, respectively. Furthermore, the energy loss of the projectile ΔE should be small in comparison to its kinetic energy, i.e. $\Delta E / E \ll 1$. Thereby, it is guaranteed, that the radii of the projectile and the target nucleus do not overlap during the scattering process and the orbits of the particles are only negligibly modified during the excitation process.

The cross section of elastic scattering in a heavy-ion collision can be described by

$$\left(\frac{d\sigma}{d\Omega}\right)_{\text{Rutherford}} = \frac{1}{4}\frac{a^2}{\sin^4(\theta/2)}, \tag{3.2}$$

with the scattering angle θ. In a semi-classical description, the CoulEx cross section is equal to the Rutherford cross section modified by the probability that a nucleus is excited from the initial state i to the final state f $P_{i\to f}$:

$$\left(\frac{d\sigma}{d\Omega}\right)_{\text{CoulEx}} = P_{i\to f}\left(\frac{d\sigma}{d\Omega}\right)_{\text{Rutherford}}, \tag{3.3}$$

The probability $P_{i\to f}$ can be expressed in terms of the excitation amplitudes b_{if}, summed over all magnetic substates m_i and m_f of the initial and final states:

$$P_{i\to f} = \frac{1}{(2I_i + 1)}\sum_{m_i,m_f}|b_{if}|^2, \tag{3.4}$$

with the spin of the initial state I_i. The excitation amplitudes of one-step excitation processes can be calculated in first order perturbation theory. The CoulEx cross-section can be related to the reduced transition probability $B(\sigma\lambda; I_i \to I_f)$ with radiation character σ and multipolarity λ:

$$d\sigma_{E\lambda} = \left(\frac{Z_P e}{\hbar c}\right)^2 a^{-2\lambda+2}B(E\lambda)f_{E\lambda}(\xi), \tag{3.5a}$$

$$d\sigma_{M\lambda} = \left(\frac{Z_P e}{\hbar c}\right)^2 a^{-2\lambda+2}B(M\lambda)f_{M\lambda}(\xi). \tag{3.5b}$$

Here, a is the earlier referred to half-distance of closest approach, the $f_{\sigma\lambda}(\xi)$ are tabulated in Ref. [112], and ξ is the dimensionless adiabaticity parameter, defined by

$$\xi = \frac{a}{\hbar v}\Delta E = \frac{Z_P Z_T e^2}{\hbar v}\frac{\Delta E}{2E}, \tag{3.6}$$

with the classical kinetic energy $E = 1/2m_0 v^2$. The reduced transition probability is related to the reduced transition matrix elements through the Wigner-

Eckart theorem [115]

$$B(\sigma\lambda)_{fi} = \sum_{\mu,m_f} \left| \langle I_f m_f | \mathfrak{M}(\sigma\lambda,\mu) | I_i m_i \rangle \right|^2$$

$$= \frac{1}{2I_i + 1} \left| \langle I_f \| \mathfrak{M}(\sigma\lambda) \| I_i \rangle \right|^2. \tag{3.7}$$

Here, $\mathfrak{M}(\sigma\lambda,\mu)$ denotes the multipole transition operator associated with the multipole radiation field $\sigma\lambda\mu$. Eqs. (3.5a) and (3.5b) show that the CoulEx cross-section for one-step excitation processes decreases by two orders of magnitude with increasing multipolarity. Magnetic excitations are further reduced by a factor $\beta^2 = (v/c)^2$ in comparison to electric excitations, due to the relative motion of projectile and target and the thereby reduced magnetic field of the projectile. Consequently, electric dipole ($\lambda = 1$) and quadrupole ($\lambda = 2$) transitions play a paramount role in CoulEx experiments, compared to transitions with $\lambda > 2$. Quadrupole, i.e. $E2$, transitions are even more enhanced in comparison to other multipolarities in CoulEx experiments, because the excitation transition probability of energetically low-lying excited states via $E2$ transitions, $B(E2)$, is usually many orders of magnitude larger than the transition probabilities via $E1$ or $M1$ transitions, $B(E1)$ or $B(M1)$, given $v \ll c$.

The CoulEx cross sections can be calculated with many different computer codes, e.g. the multiple Coulomb excitation program (CLX) by H. Ower [116], which include the correct treatment of higher order effects that can play an important role in real experiments, e.g. multi step excitation processes.

3.1.2. Fusion evaporation

If the impact parameter of the incident particle p of a reaction is small in comparison to the radius of the target nucleus T (see Figure 3.1) and the energy of p is high enough to overcome the Coulomb barrier and the collision time is greater than 10^{-22} s, then there is a high probability that a compound nucleus $X^\star$ is formed, due to random collisions of the nucleons of the projectile and target nucleus. The compound nucleus is highly excited and decays via evaporation of particles z and γ rays to the ground state of residual nuclei Y.

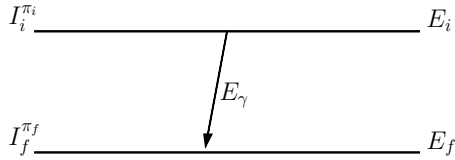$$p + T \rightarrow X^\star \rightarrow Y + z + \gamma. \tag{3.8}$$

Figure 3.3.: Simple level scheme of two states and the γ-ray transition connecting these two states $I_i^{\pi_i} \rightarrow I_f^{\pi_f}$.

There are many possible exit channels, potential decay paths, for the compound nucleus, but the relative decay probabilities of these channels are independent of the creation process of the compound nucleus [87] and do only depend on the total energy and the total angular momentum of the compound nucleus. The decay of the compound nucleus is heavily dependent on the total energy, with higher energy increases the probability for the evaporation of more nucleons. Estimations of reaction yields can be calculated with specific FE computer codes, such as the program to calculate fusion-evaporation cross sections (CASCADE) [117] and the projection angular-momentum coupled evaporation code (PACE) [118, 119].

3.2. Excited nuclear states

The EM transition between two states is characterized by the radiation character σ and the multipolarity λ, where σ is either of electrical (E) or magnetic (M) nature. Figure 3.3 illustrates a simple level scheme comprised of two states. Conservation of energy, spin and momentum results in selection rules for energy E, angular momentum λ and parity π of EM transitions

$$E_\gamma = E_i - E_f, \tag{3.9a}$$

$$|I_i - I_f| \leq \lambda \leq I_i + I_f, \tag{3.9b}$$

$$\pi_f = \pi_i \cdot \pi_\gamma. \tag{3.9c}$$

An EM transition of order λ involves a change of the parity quantum number by $(-1)^\lambda$ for electrical or $(-1)^{\lambda+1}$ for magnetic transitions. The transition prob-

ability per unit time T_{fi} of the γ decay from an initial nuclear state $I_i^{\pi_i}$ to a final nuclear state $I_f^{\pi_f}$ is anti-proportional to the lifetime τ of the transition [108]:

$$T_{fi} = \frac{1}{\tau} = \sum_f \frac{1}{\tau_f}. \tag{3.10}$$

In general, for several final states or mixing multipolarities, the total transition probability is given by the sum over the partial probabilities. The total decay rate, summed over the magnetic substates of the photon and of the final nuclear state, can be expressed as [120]:

$$T(\sigma\lambda)_{fi} = \frac{8\pi(\lambda+1)}{\lambda[(2\lambda+1)!!]^2} \frac{1}{\hbar} \left(\frac{E_\gamma}{\hbar c}\right)^{2\lambda+1} B(\sigma\lambda; i \to f), \tag{3.11}$$

with the reduced transition strength $B(\sigma\lambda)$ from Eq. (3.7). Typical units for the transition strengths $B(\sigma\lambda)$ are

$$[B(E\lambda)] = e^2 \text{fm}^{2\lambda}, \qquad\qquad [B(M\lambda)] = \mu_N^2 \text{fm}^{2\lambda-2}. \tag{3.12}$$

Typically the reduced transition strength is often found in the literature in units of barn (b) instead of femtometer (fm^2), with $1\,\text{b} = 100\,\text{fm}^2$. Numerical forms for the transition probabilities [108] can be stated,

$$T_{fi}^{E\lambda} = 5.498 \times 10^{22} f(\lambda) \left(\frac{E_\gamma[\text{MeV}]}{197.33}\right)^{2\lambda+1} B(E\lambda)\left[e^2\text{fm}^{2\lambda}\right] 1/\text{s}, \tag{3.13a}$$

$$T_{fi}^{M\lambda} = 6.080 \times 10^{20} f(\lambda) \left(\frac{E_\gamma[\text{MeV}]}{197.33}\right)^{2\lambda+1} B(M\lambda)\left[\mu_N^2\text{fm}^{2\lambda-2}\right] 1/\text{s}, \tag{3.13b}$$

$$\text{with } f(\lambda) = \frac{\lambda+1}{\lambda[(2\lambda+1)!!]^2},$$

with the convention $c = 1$ and the relations

$$e^2 = 1.44\,\text{MeV}\,\text{fm}, \qquad\qquad \hbar c = 197.33\,\text{MeV}\,\text{fm}. \tag{3.14}$$

Single-particle estimations, so called Weisskopf estimates [121], are often used to compare different experimental results. They are a rough evaluation of the

collectivity of a transition, i.e. the number of nucleons contributing to a transition. For a transition from the excited nuclear state $I_i^{\pi_i}$ to the state $I_f^{\pi_f}$ they can be calculated by

$$B(E\lambda, i \rightarrow f) = \frac{(1.2)^{2\lambda}}{4\pi}\left(\frac{3}{\lambda+3}\right)^2 A^{\frac{2\lambda}{3}}, \tag{3.15a}$$

$$B(M\lambda, i \rightarrow f) = \frac{10 \times (1.2)^{2\lambda-2}}{\pi}\left(\frac{3}{\lambda+3}\right)^2 A^{\frac{2\lambda-2}{3}}. \tag{3.15b}$$

A measurement of the lifetime, as performed in this work, can therefore give insight into the collectivity of an atomic nucleus. The next Section will introduce the reader to the measurement of mean lifetimes of excited nuclear states and in particular to the experimental technique of FEST.

3.3. Lifetime measurements

A wide variety of experimental techniques for the measurement of nuclear level lifetimes or transition strengths is available, each technique with a particular range of applicability depending on the order of magnitude of the lifetime. It is therefore important to select the correct experimental method, since the transition energies and level lifetimes range over multiple orders of magnitude, i.e. from few keV up to several MeV in the case of transition energies and from femtoseconds lifetimes or even less for short-lived levels to some milliseconds for long-lived isomeric states in the case of level lifetimes up to years and gigayears.

The experimental methods can mainly be categorized into two types: direct and indirect lifetime measurements. Figure 3.4 gives an overview of some of these methods and their range of applicability in terms of the feasibility to investigate lifetimes.

The following Section 3.3.1 will present the method of electronic timing in more detail. The method of CoulEx has already been introduced in Section 3.1.1. Eqs. (3.5a) and (3.5b) show that the CoulEx cross section is directly proportional to the reduced transition strength $B(\sigma\lambda)$, which in turn is connected to the mean lifetime via Eqs. (3.10) and (3.11). The measurement of the CoulEx cross sections therefore determines the mean lifetime of the excited state. The other methods mentioned will not be further discussed here, but information on nuclear resonance fluorescence (NRF) can be found in Refs. [122–124], on the
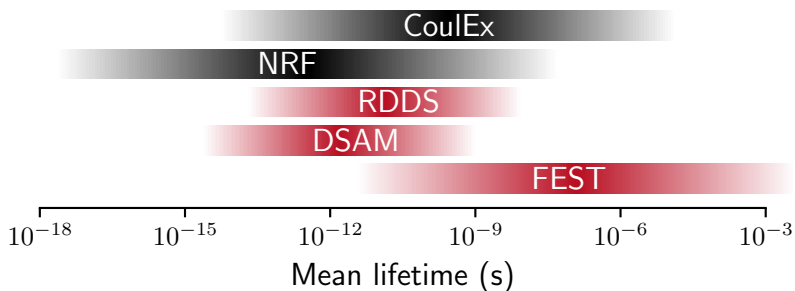
Figure 3.4.: Experimental methods and their range of applicability in terms of lifetimes. Red boxes represent indirect methods determining lifetimes and black boxes direct methods.

Doppler-shift attenuation method (DSAM) in Refs. [125, 126], and on the recoil distance Doppler-shift (RDDS) technique in Ref. [127] and references therein.

3.3.1. Fast electronic scintillation timing

Lifetimes of excited nuclear states in the range of ns down to a few tens of ps can be measured with the FEST technique by measuring the time difference between a start and a stop signal, e.g. the detection of a transition populating and the detection of a second transition depopulating the nuclear state of interest. The measurable lifetimes are limited by the time resolution of the utilized detectors and the electronics setup. Table 3.1 summarizes the properties of a few commonly used detectors for γ-ray spectroscopy. It shows, that semiconductor detectors, i.e. here HPGe detectors, have in general a better energy resolution in comparison to inorganic scintillators, but their time resolution is one or two orders of magnitude larger and therefore limiting their usage for lifetime measurements with fast-timing methods to the ns regime. Traditionally the FEST method was introduced for $\beta\gamma\gamma$ coincidences [132, 133], where BaF_2 scintillator detectors were used in combination with HPGe detectors and plastic scintillators for the detection of the electrons. But for FE reactions the energy resolution of the BaF_2 is usually too low to resolve the close lying transitions. The energy resolution of most scintillators, $\Delta E/E \approx 10\%$, narrows their applica-

Table 3.1.: Overview and comparison of often used detectors in nuclear structure experiments.

Detector	Type	Light Output $(\gamma(e^-)/MeV)$	Decay Time (ns)	$\Delta E/E$ @ 662 keV (%)
HPGe	semicond.	3×10^6[♦]		0.2[♦]
LaBr$_3$(Ce)	inorg.scint.	61000[♥]	15-26[♣]	2.8[♣]
NaI	inorg.scint.	38000[♦]	230[♦]	5.6[♣]
BaF$_2$(slow)	inorg.scint.	9500[♦]	630[♦]	12.0[★]
BaF$_2$(fast)	inorg.scint.	1400[♦]	0.6[♦]	12.0[★]
BGO	inorg.scint.	8200[♦]	300[♦]	10.0[⁑]

[♦] Data taken from Ref. [109] [♥] Data taken from Ref. [9] [♣] Data taken from Ref. [128] [♣] Data taken from Ref. [129] [⁑] Data taken from Ref. [130] [★] Data taken from Ref. [131]

tion to study only a few cases of excited nuclear states, where the level density is very low. The development of a new type of scintillator, i.e. the LaBr$_3$(Ce) detector [9], was the driving force behind a new wave of FEST measurements in the last decade and the construction of a number of new detector arrays incorporating these detectors in combination with HPGe detectors to combine the high energy resolution of the HPGe detectors and the good time resolution of the LaBr$_3$(Ce) detectors. Examples are the high efficiency observatory for γ-ray unique spectroscopy (HORUS) setup in Cologne [134, 135], in Bucharest the romanian array for spectroscopy in heavy ion reactions (ROSPHERE) array [136–139] the fast timing array (FATIMA) for the facility for anti-proton and ion research (FAIR) [140, 141], which was used in different combinations with HPGe detectors such as the EXOGAM at ILL (EXILL) spectrometer [142–144], Gammasphere at the Argonne national laboratory (ANL) [145] or the ν-ball spectrometer [146] at the l'institut de physique nucléaire (IPN), Orsay.

The FEST method is shown schematically for a radioactive source and a pair of scintillation detectors in Figure 3.5. A more detailed description of the method and the setup in Bucharest, that was used in this work, can be found in Refs. [136, 137]. The two γ-ray transitions populating and depopulating the state of interest are detected with, e.g. two LaBr$_3$(Ce) detectors. The signals go through a constant fraction discriminator (CFD) to extract the timing information of the
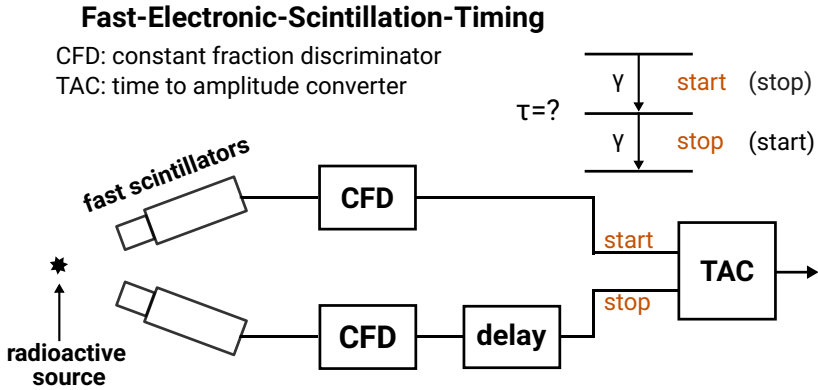
Figure 3.5.: Pair of scintillation detectors, two signal paths, one path delayed with analogue electronics.

signals. One signal is delayed and both signals are fed into a time-to-amplitude converter (TAC), whose output signal amplitude is proportional to the time difference between the start and the stop signal. The resulting delayed time distribution $D_\lambda(t)$, assuming no background contributions, is a convoluted function of the exponential decay of the investigated nuclear state and the time response of the experimental setup $P(t)$, i.e. electronics and signal processing [147]:

$$D_\lambda(t) = n\lambda \int_{-\infty}^{t} P(t')\mathrm{e}^{-\lambda(t-t')}\mathrm{d}t', \qquad (3.16)$$

with the transition rate $\lambda = 1/\tau$ and the normalization n. If the start and the stop signals are swapped, i.e. the start is on the depopulating transition (Decay) and the stop on the populating transition (Feeder), the time distribution will be mirrored and the exponential flank is towards negative time differences (anti-delayed case).
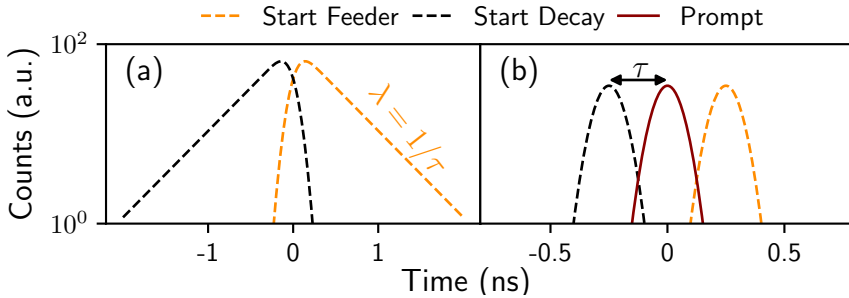
Figure 3.6.: Logarithmic plot of counts over time for (a) the slope method and (b) the centroid-shift method.

Slope method

If the lifetime of the nuclear state of interest is large in comparison to the full width at half maximum (FWHM) of the system's response, a simple fit of the exponential tail of the time distribution gives directly the lifetime of the nuclear state [see Eq. (3.16)]. Figure 3.6 (a) shows the time distributions for a lifetime larger than the FWHM of the system once with the start signal from the populating transition (orange line, Feeder) and with a start signal stemming from the depopulating transition (black line, Decay). The slope of the decay tail of the time distributions gives directly the exponential decay constant and therefore the lifetime ($\lambda = 1/\tau$).

It is important to ensure during the fitting procedure not to include contributions from the background and the prompt response of the setup.

Centroid shift

For shorter lifetimes, other methods, e.g. the centroid-shift method [132, 133] or the generalized centroid difference method [135], have to be used to determine the lifetime of the nuclear state, since a fit to the decay tail of the time distribution becomes unreliable, because the decay tail becomes very short. The

center of gravity or centroid of a time distribution is defined as [148]:

$$C(D_\lambda) = <t> = \frac{\int t D_\lambda(t) \mathrm{d}t}{\int D_\lambda(t) \mathrm{d}t}, \tag{3.17}$$

resulting in the case of a start condition on the feeding transition (delayed case) in

$$\tau = C_d(D_\lambda) - C_d(P), \tag{3.18}$$

with the centroid of the delayed time distribution $C_d(D_\lambda)$ and of the system's prompt response $C_d(P)$. If the start condition is set to a depopulating transition $C(D)$ and $C(P)$ switch places in the equation. After the time walk correction $C_d(P)$ is equal to $C_a(P)$ of the anti-delayed time distribution (more details on the time-walk calibration can be found in Section 5.2.4). It follows for the centroid difference [134]:

$$\begin{aligned} \Delta C &= C_d(D) - C_a(D) \\ &= C_d(P) + \tau - (C_a(P) - \tau) \\ &= 2\tau. \end{aligned} \tag{3.19}$$

Figure 3.6 (b) shows the expected prompt time response of the experimental setup and the influence of the mean lifetime on the centroid of the delayed (Start Feeder) and anti-delayed (Start Decay) time distributions. The difference between the centroid of the delayed and the anti-delayed time distribution is equivalent to twice the mean lifetime τ.

3.4. Magnetic dipole moments

This section is mainly based on Refs. [76–79, 87, 149].
As was already mentioned in the CoulEx section 3.1.1, the EM interaction offers a great way to probe nuclear structure without disturbing the underlying structure of the atomic nucleus. The EM interaction is well understood, making it possible to perform model-independent measurements. The leading non-vanishing term of a multipole expansion of a current distribution is the magnetic

dipole moment. The magnetic dipole moment μ can be defined as

$$\mu = \frac{e\hbar}{2m}l, \tag{3.20}$$

with the electron charge e, the mass m and the angular momentum l. The quantity $\mu_N = e\hbar/2m_p$ with the proton mass is called the nuclear magneton. The nuclear magneton $\mu_N = 5.05084 \times 10^{-27}$ J/T is three orders of magnitude smaller than the Bohr magneton $\mu_B = 9.27405 \times 10^{-24}$ J/T, using the electron mass instead of the proton mass. Hence, nuclear magnetism has a much smaller effect in comparison to the magnetism of the electron shell.

The nuclear magnetic dipole moment is proportional to the nuclear spin [150]

$$\mu \propto I\mu_N, \tag{3.21}$$
$$\Rightarrow \mu = gI\mu_N. \tag{3.22}$$

Its proportionality constant is given by the dimensionless g factor or Landé factor [151]. Nuclear magnetic moments are created from the orbital angular momentum l and the intrinsic spin s of the individual nucleons. Therefore, the nuclear magnetic dipole operator is expressed as

$$\mu = \sum_{i=1}^{A}(g_l^i l_i + g_s^i s_i)\mu_N, \tag{3.23}$$

where l_i, s_i are the orbital and intrinsic spin angular momentum operators and g_l^i, g_s^i are the orbital and spin g factors, which account for the orbital and intrinsic spin contributions, of the i-th nucleon. The orbital g factor of protons is $g_l = +1$ and zero for the neutron, because it carries no electric charge. Quantum mechanics predicts a spin g factor of two for fermions (particles with $s = 1/2$), like the proton, neutron and electron. The electron spin g factor is indeed close to that value, i.e. $g_s = -2.00231930436256(35)$ [152] and the small deviation can be explained by quantum electrodynamics [153]. But the g factors of the free nucleons differ substantially. They were experimentally determined to be $g_{\pi,s} = 5.5856946893(16)$ and $g_{v,s} = -3.82608545(90)$ [152], giving a hint to their internal structure.

Since the pairing force favors the coupling of pairs of nucleons to a total angular momentum of zero, valence nucleons have the biggest influence on the nuclear

magnetic moment.

The magnetic dipole moment of an excited nuclear state can be measured by the interaction between μ and an external (internal) magnetic field or by the precession of an aligned nuclear spin I in a magnetic field. Strong magnetic fields (on the order of kT), which are to date nearly impossible to reach in the laboratory, are required to measure the Larmor frequency

$$\omega_L = g(2I + 1)\frac{\mu_N}{\hbar}B, \tag{3.24}$$

where B is the magnetic field, if the lifetime of the investigated excited state is on the order of picoseconds. Two such strong magnetic fields are the transient field (TF) [154, 155], acting on swiftly moving nuclei of ions within a magnetized ferromagnetic medium [156], and the free-ion hyperfine fields of ions recoiling into vacuum (recoil-in-vacuum (RIV)) [76]. Precise knowledge of the charge distribution of the electron shell of the projectile or the target are necessary to calculate these magnetic fields to sufficient precision. Accordingly, calibration measurements with known magnetic moments are often required.

RIV and TF have to be modified for their application to RIB. Since the focus of this work is on the RIV technique the reader is referred to Refs. [157, 158] for more information on the application of TF methods to RIB. The following section will introduce the ECR-TDRIV technique based on Refs. [76–79, 159].

3.4.1. Time-differential recoil-in-vacuum

In the traditional RIV technique (time-integral attenuation) an ion beam impinges on a target and excited ions emerge from the target into vacuum. If the excited ions carry one or more electrons, the nuclear spin I and the atomic spin J of the electrons couple to $F = I + J$ and precess around F. The angular distribution of the de-excitation γ-radiation of the emerging ions is measured. By comparing the perturbed angular distribution to the unperturbed angular distribution, the attenuation coefficients can be extracted. Using a plunger device the technique can be extended (time-differential attenuation). By changing the distance between the target foil and an adjustable stopper foil behind the target, the frequency of precession ω_L can be measured, since the orientation of the nuclear spin freezes, when the ions are stopped in the stopper foil (see Ref, [77]). In the case of hydrogen-like ions, where the sole electron sits in the
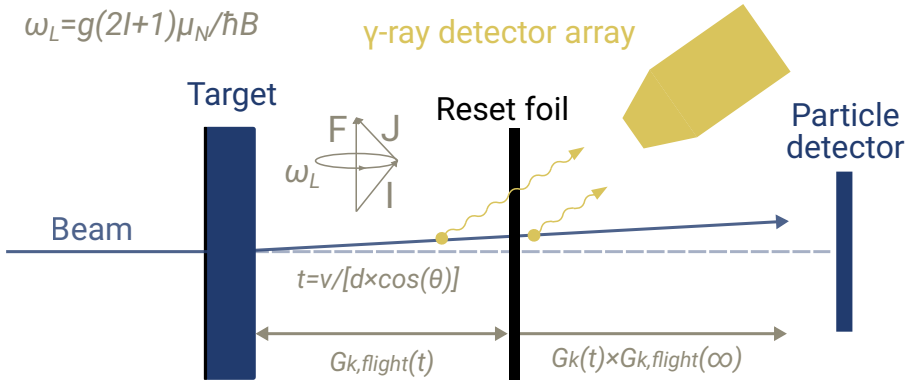
Figure 3.7.: ECR-TDRIV scheme. A particle detector is placed in forward direction and HPGe detectors around the target chamber.

$1s$ orbital, the hyperfine field at the location of the nucleus can be calculated by

$$B_{1s} = 16.7 Z^3 R(Z)\,\text{T}, \qquad (3.25)$$

with the proton number Z and the Z-dependent relativistic correction factor $R(Z) \approx 1 + (Z/84)^{2.5}$, which is near unity for small Z. Other electron configurations decay to the ground state within 10^{-13}s [160] and therefore only play a minor role.

Accordingly, the Larmor frequency ω_L is given by

$$\omega_L \approx g(2I + 1)800 Z^3\,\text{MHz}. \qquad (3.26)$$

The precession of the nuclear spin can be measured by investigating the perturbed angular correlation of γ-rays depopulating the excited state. RIV has to be adjusted in the case of RIB. There, it is necessary to also detect the outgoing particles with particle detectors. Hence, it was proposed by Stuchbery et al. [77] to replace the stopper foil by a thin electron configuration reset foil, allowing to place particle detectors in forward direction. The ECR-TDRIV technique is illustrated in Figure 3.7. The perturbed particle-γ angular correlation has the

following form, taken from Ref. [78]

$$W(\theta_p, \theta_\gamma, \Delta\phi, t) = \sum_{kq} a_{kq}(\theta_p) G_k(t) D^{k*}_{q0}(\Delta\phi, \theta_\gamma, 0), \qquad (3.27)$$

where θ_γ and θ_p denote the polar detection angles of the coincident γ rays and particles, $\Delta\phi = \phi_\gamma - \phi_p$ is the difference between the azimuthal angles of the coincident γ rays and particles. The parameters $a_{kq}(\theta_p)$ are equal to the product of the orientation parameters B_{kq}, the attenuation factors Q_k, due to the finite solid angle of the HPGe detectors, and the angular distribution coefficients F_k. $D^{k*}_{q0}(\Delta\phi, \theta_\gamma, 0)$ is the Wigner-D matrix and responsible for the transformation into the reference system of the scattered ions. The time-dependent attenuation coefficients $G_k(t)$ depend on the nuclear g factor. The terms will be explained in the following subsections.

Statistical tensor

The statistical tensor ρ_{kq} contains the information about the degree of orientation of the initial state. It is connected to the density matrix ρ [114]

$$\rho_{kq} = \sqrt{2I_i + 1} \sum_{m,m'} (-1)^{I_i + m'} \begin{pmatrix} I_i & k & I_i \\ -m' & q & m \end{pmatrix} \langle m | \rho | m' \rangle, \qquad (3.28)$$

$k = 0, 1, 2, \ldots, 2I_i$, if I_i is an integer and q goes from $-k$ to k. For aligned states, where substates with m and $-m$ are equally populated, only statistical tensors with even k values are non-zero [149]. The orientation parameter B_{kq} of Eq. (3.27) is related to the statistical tensor ρ_{kq} via

$$\rho_{kq} = \frac{B_{kq}}{\sqrt{2k+1}}. \qquad (3.29)$$

Solid angle correction factor

Because of the finite solid angle of the HPGe detectors, the observed anisotropies of the angular correlation are reduced. Therefore, the attenuation factors Q_k are
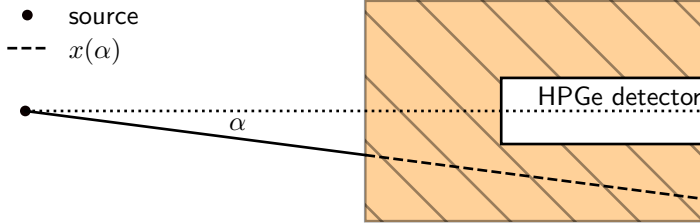
Figure 3.8.: Detector geometry for the calculation of the solid-angle attenuation coefficient. Adapted from Ref. [163].

introduced (see also Refs. [161–163])

$$Q_k = \frac{J_k}{J_0},$$ (3.30)

where

$$J_k = \int P_k(\cos\alpha)\left(1 - e^{\tau x(\alpha)}\right)\sin\alpha \, d\alpha,$$ (3.31)

with the γ-ray absorption coefficient τ and the ordinary Legendre polynomials P_k. The integration is carried out over the path length $x(\alpha)$ of the γ ray in the detector material, as shown in Figure 3.8, α is the angle between the propagation of the γ ray and the symmetry axis of the detector.

Geometrical factors

The F_k coefficients only depend on the spin of the initial state I_i and final state I_f and on the transition's multipolarity connecting these states. They are defined as [113]

$$F_k = (-1)^{I_i + I_f - 1}\sqrt{(2k+1)(2\lambda_1 + 1)(2\lambda_2 + 1)(2I_i + 1)}$$
$$\times \begin{pmatrix} \lambda_1 & \lambda_2 & k \\ 1 & -1 & 0 \end{pmatrix} \begin{Bmatrix} \lambda_1 & \lambda_2 & k \\ I_i & I_i & I_f \end{Bmatrix},$$ (3.32)

3. Experimental techniques

where λ_i are the multipole order of the transition connecting i and f, $(\cdots)$ is the Wigner 3-j symbol and $\{\cdots\}$ the Wigner 6-j symbol, introduced in Ref. [164]. For a pure $E2$ transition, e.g. $2_1^+ \rightarrow 0_{GS}^+$, λ_1 is equal to λ_2.

Wigner-D matrix

By rotating the statistical tensor ρ_{kq} with the Wigner-D matrix by the Euler angles (α, β, γ), it is possible to transform the frame of reference, in which the beam axis is the quantization axis, to a frame of reference, where the outgoing reaction products define the quantization axis.

$$\rho_{kq}^{\text{z-axis}} = \sum_{q'} \rho_{kq'}^{\text{reaction}} D_{qq'}^k(\alpha, \beta, \gamma). \tag{3.33}$$

The Wigner-D matrix can be expressed in terms of the spherical harmonics [114]

$$D_{q0}^{k*}(\Delta\phi, \theta_\gamma, 0) = (-1)^q \sqrt{\frac{4\pi}{2k+1}} Y_{-q}^k(\theta_\gamma, \Delta\phi). \tag{3.34}$$

The sole ϕ dependence of the angular correlation is on $\Delta\phi = \phi_\gamma - \phi_p$. Only the orientation parameters B_{kq} depends on ϕ_p and can be rewritten as

$$B_{kq}(\theta_p, \phi_p) = B_{kq}(\theta_p, 0)e^{-iq\phi_p} = B_{kq}(\theta_p)e^{-iq\phi_p}, \tag{3.35}$$

which can be incorporated into the spherical harmonics, with the Condon-Shortley phase convention, and leads to

$$Y_l^m(\theta_\gamma, \phi_\gamma)e^{-iq\phi_p} = (-1)^m \sqrt{\frac{(2l+1)}{4\pi}\frac{(l-m)!}{(l+m)!}} P_l^m(\cos\theta_\gamma)e^{im\phi_\gamma}e^{-iq\phi_p}$$
$$\equiv Y_q^k(\theta_\gamma, \Delta\phi = \phi_\gamma - \phi_p). \tag{3.36}$$

Time-dependent attenuation coefficients

The time-dependent de-orientation effect can be described by the attenuation coefficients $G_k(t)$. These attenuation, or perturbation, coefficients have a cosine dependence on the time in the case of hydrogen-like ions with $J = 1/2$ [76]

$$G_k(t) = 1 - b_k(1 - \cos\omega_L t), \tag{3.37}$$

with $b_k = k(k+1)/(2I+1)^2$. The attenuation coefficient for stopped ions is (for the traditional RIV method, with a stopper foil)

$$G_k^{\text{stopped}}(t) = G_k(t). \tag{3.38}$$

Ions that decay in flight have an average attenuation coefficient

$$G_k^{\text{flight}}(t) = \int_o^t G_k(t')e^{-\lambda t'}\lambda dt' \Big/ \int_o^t e^{-\lambda t'}\lambda dt'$$
$$= 1 - b_k[1 - F(t)], \tag{3.39}$$

and

$$F(t) = \frac{1 - e^{-\lambda t}(\cos \omega_L t - \omega_L t \sin \omega_L t)}{(1 + \omega_L^2 \tau^2)(1 - e^{-\lambda t})}, \tag{3.40}$$

with the lifetime τ of the excited state. In the limit $t \to \infty$, the attenuation coefficient can be written as

$$G_k^{\text{flight}}(\infty) = 1 - b_k \left(\frac{\omega_L^2 \tau^2}{1 + \omega_L^2 \tau^2} \right). \tag{3.41}$$

The observed attenuation coefficient contains both the flight and the stopped terms, if the flight and the stopped components cannot be resolved in the γ-ray energy spectrum

$$G_k^{\text{sum}} = \left(1 - e^{-t/\tau}\right) G_k^{\text{flight}} + e^{-t/\tau} G_k^{\text{stopped}}. \tag{3.42}$$

The second term has to be adjusted, if the stopper foil is replaced by a electron configuration reset foil. The average attenuation factor for γ decays that happen after the reset foil is the product of $G_k(t)$ and $G_k^{\text{flight}}(\infty)$, i.e. the electron configuration is randomly reset when the ion passes the reset foil and the nucleus experiences further perturbations [77]. The attenuation factors G_k^{flight}, $G_k^{\text{reset}} \equiv G_k^{\text{flight}}(\infty) \times G_k$ and G_k^{sum} are plotted in Figure 3.9 for the case of ^{18}O with data taken from Ref. [80].
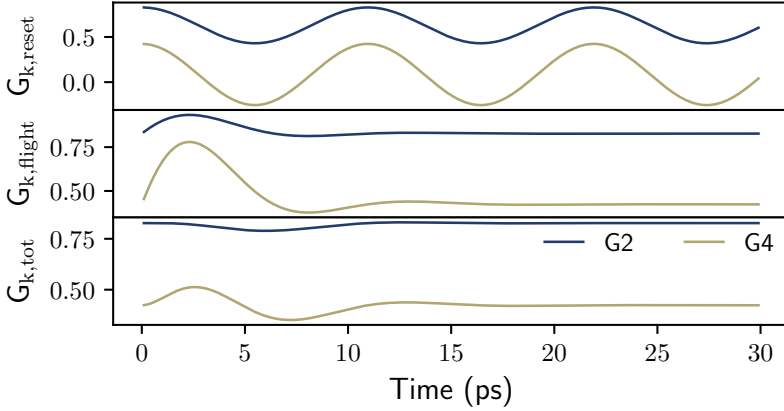
3. Experimental techniques

Figure 3.9.: Expected attenuation factors G_k as a function of time with a g factor of 0.28 for ^{18}O. $G_k^{\text{reset}}(t) = G_k(t) \times G_k^{\text{flight}}(\infty)$.

Relativistic corrections

The following relations have been taken from Refs. [149, 165, 166] and references therein. If the investigated nucleus is in motion, rather than at rest, the emitted γ radiation will be detected by a detector, resting in the laboratory (LAB) frame of reference, here denoted as $^{\text{L}}$, with a shifted energy

$$E_{\text{shifted}} = E_0 \frac{\sqrt{1 - \beta^2}}{1 - \beta \cos \alpha^{\text{L}}}, \tag{3.43}$$

with the energy emitted in the rest frame of the nucleus E_0, the velocity $\beta = v/c$ and the emission angle α^{L} between the direction of the moving particle and the detection angle. The emission angle α^{L} can be calculated by

$$\cos \alpha^{\text{L}} = \cos \theta_\gamma^{\text{L}} \cos \theta_p^{\text{L}} + \sin \theta_\gamma^{\text{L}} \sin \theta_p^{\text{L}} \cos \Delta\phi^{\text{L}}. \tag{3.44}$$

The relation between the angles in the rest frame of the moving nucleus (NUC), denoted as ^{N}, and laboratory frame, denoted as ^{L}, are given by

$$\cos \theta_\gamma^N = \frac{\cos \theta_\gamma^L - \cos \theta_p^L \left[\beta \gamma_L - (\gamma_L - 1) \cos \alpha^L \right]}{\gamma_L (1 - \beta \cos \alpha^L)}, \tag{3.45a}$$

$$\tan \phi_\gamma^N = \frac{\sin \theta_\gamma^L \sin \phi_\gamma^L - \sin \theta_p^L \sin \phi_p^L \left[\beta \gamma_L - (\gamma_L - 1) \cos \alpha^L \right]}{\sin \theta_\gamma^L \cos \phi_\gamma^L - \sin \theta_p^L \cos \phi_p^L \left[\beta \gamma_L - (\gamma_L - 1) \cos \alpha^L \right]}, \tag{3.45b}$$

where $\gamma_L = 1/\sqrt{(1 - \beta^2)}$ is the Lorentz factor. If the z-axis is chosen as the direction of the moving nucleus Eqs. (3.45a) and (3.45b) have the simpler form:

$$\cos \theta_\gamma^L = \frac{\cos \theta_\gamma^N + \beta}{1 + \beta \cos \theta_\gamma^N}, \tag{3.46a}$$

$$\phi_\gamma^L = \phi_\gamma^N. \tag{3.46b}$$

The solid angle transformation, due to the Lorentz boost, is given by

$$d\Omega^L = \frac{1 - \beta^2}{(1 + \beta \cos \theta^N)^2} d\Omega^N, \tag{3.47}$$

$$W^L(\theta^L) = W^N(\theta^N) \frac{d\Omega^N}{d\Omega^L}. \tag{3.48}$$

4. Experimental setups

It is important to carefully select the facility and experimental method depending on the desired nuclei and its properties to investigate. In the field of nuclear physics, there are several different facilities available worldwide[1], each with advantages and disadvantages. In the last decade, many new RIB facilities started operation. As a result, many so-called exotic nuclei, unstable nuclei far off the valley of stability, are now available for investigation. An overview of the different RIB facilities in operation (and under construction) can be found in Ref. [168]. Moreover, alongside the development of new accelerator facilities, the instrumentation has seen many new developments and advancements. In the field of γ-ray spectroscopy, these include improvements in the spatial resolution of HPGe detectors by using pulse shape analysis (PSA) for the determination of the interaction points of the γ rays in the detector and γ-ray tracking algorithms for the reconstruction of the detected photons, e.g. for AGATA [10] or the use of new detector materials like $LaBr_3(Ce)$ detectors [9].

The presented experiments with stable beams have been performed at the 9 MV FN Tandem accelerator of the IFIN-HH in Bucharest-Magurele, Romania [169] using the ROSPHERE detector array [137] and at the 10 MV FN Tandem accelerator of the IKP, Universität zu Köln, Germany using the HORUS detector array [170, 171] together with the Darmstadt Cologne Yale (DARCY) plunger device.

The two setups will be presented in detail in the following sections.

4.1. FEST @ IFIN-HH, Bucharest-Magurele

At IFIN-HH, a variety of ions can be produced by the two available ion sources, a source of negative ions by caesium sputtering (SNICS) and a duoplasmatron.

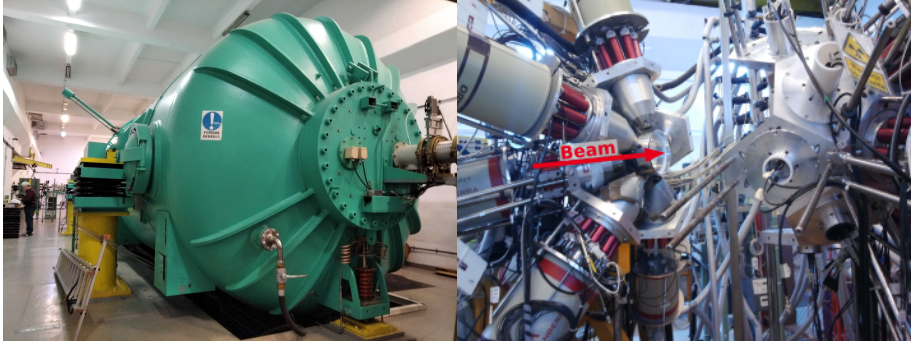[1]An overview of the available facilities in Europe is given in the NuPECC long-range plan [167].

Figure 4.1.: (*left*) SF$_6$ gas tank of the 9 MV FN Tandem accelerator at IFIN-HH (taken October 2019, courtesy of P.R. John).(*right*) Open RO-SPHERE detector array (taken June 2014).

Details on the working principle of those and further ion sources can be found in Ref. [172]. The emitted ions can be accelerated up to $9(Q+1)/A$ MeV/A, where Q is the positive charge state of the accelerated ions after passing the stripper foil, by the 9 MV FN Tandem accelerator. The Tandem accelerator, as introduced in Ref. [173], allows to use an applied terminal voltage a second time for the acceleration of heavy ions, by removing the electron of ions with a stripper foil at the center of the accelerator. The accelerated ions can be sent to different experimental sites, e.g. the ROSPHERE detector array for γ-ray spectroscopy experiments. Figure 4.1 shows the gas tank of the Tandem accelerator and the open ROSPHERE array.

4.1.1. ROSPHERE detector array

The main device for the analysis of this work was the γ-ray spectroscopy detector array ROSPHERE. It consists of 25 available detector positions that are typically filled by LaBr$_3$(Ce) scintillator detectors and/or HPGe detectors with anti-Compton bismuth germanium oxide (BGO) shields. There are two types of coaxial p-type HPGe detectors available at the IFIN-HH, either from ORTEC or CANBERRA with relative efficiencies of 50-60%. The array is designed in a spherical geometry and is divided into five rings, which are placed at 37°, 70°,

Table 4.1.: Overview of the mixed ROSPHERE configuration used in the experiments for this work. The target to detector distances are given for both types of HPGe detectors (ORTEC/Canberra). The polar angle θ for each of the five rings and the azimuthal angle ϕ of each of the five positions is given.

Ring	Number of detectors & Type	θ (deg)	ϕ (deg)	Distance (mm)
1	5 HPGe	37	0, 72, 144, 216, 288	179/210
2	5 LaBr$_3$(Ce)	70	36, 108, 180, 252, 324	186/217
3	4 HPGe/1 LaBr$_3$(Ce)	90	0, 72, 144, 216, 288	176/208
4	5 LaBr$_3$(Ce)	110	36, 108, 180, 252, 324	186/217
5	5HPGe	143	0, 72, 144, 216, 288	179/210

90°, 110°, and 143° with respect to the beam axis, respectively. Each ring can accommodate up to five detectors. The most commonly used configuration is a mixture of HPGe and LaBr$_3$(Ce) detectors to determine lifetimes using the FEST method (see Ref. [136]). For this work the array was used in such a mixed configuration with eleven LaBr$_3$(Ce) and 14 HPGe detectors. Thereby, employing the excellent timing properties of the LaBr$_3$(Ce) detectors for the determination of the investigated lifetimes, e.g. an individual time resolution of 200-300 ps and the high energy resolution of the HPGe detectors of about 1.9 keV at 1.33 MeV [137] in order to select the γ-decay cascade of interest. The achievable total γ-ray detection efficiency in this mixed configuration is 1.10(3)% at 1332 keV for the HPGe detectors and 1.75(5)% for the LaBr$_3$(Ce) detectors [137]. The distance of the detectors to the target position depends on the detector type and the position within the array. Furthermore, it is possible to utilize ROSPHERE together with a plunger device for lifetime measurements with the RDDS technique [127, 174, 175] in the femtosecond to picosecond range or other auxiliary detectors such as the solar cells for reaction experiments at ROSPHERE (SORCERER) array, to distinguish transfer reactions from FE reactions [176]. The position information of the detector setup for the present work is summarized in Table 4.1.

The electronics and data aquisition system (DAQ) system of ROSPHERE has two main branches: a slow branch for HPGe coincidences (usually two or three
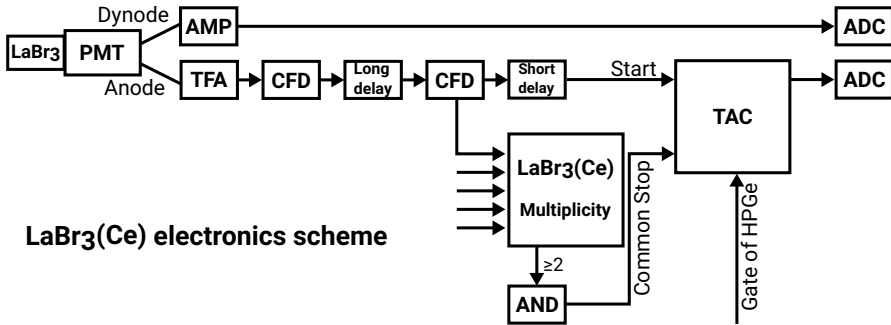
Figure 4.2.: Block diagram of the LaBr$_3$(Ce) electronics. Complete scheme, including HPGe electronics is shown in Ref. [137].

detectors registering events during a set coincidence time window) and a delayed coincidence branch for fast timing measurements. The block diagram of the LaBr$_3$(Ce) electronics is shown in Figure 4.2. The energy information is taken from the last dynode of the photo-multiplier tube (PMT). The signal of the anode is used to extract the timing information of the detected events. Further details about this experimental setup can be found in Refs. [136, 137].

4.1.2. Conducted experiments @ IFIN-HH

An overview of the conducted experiments at IFIN-HH that were performed and analyzed during this work is given in Table 4.2. Stated are the employed reactions, the target and beam information, and the aim of each experiment. This text will restrict itself to a description of the ^{152}Gd and Hf experiments. The main part of the analysis of the ^{152}Gd experiment was already reported in Ref. [177], but was rechecked in preparation to publish the results in Ref. [138]. The results of the Hf experiments and their discussion are published in Ref. [139] and the publication of the results of the ^{150}Gd experiment is in preparation.

Excited states of ^{152}Gd were populated via the ^{149}Sm(α,n)^{152}Gd FE reaction. Calculations using the computer codes CASCADE [117] and PACE [118, 119] have been performed before the experiment, estimating contributions from other reaction channels, e.g. the evaporation of more neutrons. The results of the CASCADE calculation can be found in Appendix C.1. Hence, it was possible to

Table 4.2.: List of conducted experiments at the IFIN-HH that are referred to in this work. Excited states of the Hf isotopes were populated by β decay of the Ta reaction products.

Isotope of interest	Target		Reaction	Beam Energy (MeV)	Aim
	Isotope	Thickness (mg/cm^2)			
^{174}Hf	^{171}Yb	3.0	(^{6}Li,3n)^{174}Ta	30	$\tau(2_1^+)$
^{176}Hf	^{172}Yb	2.3	(^{7}Li,3n)^{176}Ta	30	$\tau(2_1^+)$
^{178}Hf	^{174}Yb	2.5	(^{7}Li,3n)^{178}Ta	30	$\tau(2_1^+)$
^{180}Hf	^{180}Hf	12.0	(^{16}O,^{16}O)	55	$\tau(2_1^+)$
^{152}Gd	^{149}Sm + Au	1.3 + 4.3	(α,n)	17.5	$\tau(0_2^+)$
^{150}Gd	^{147}Sm + Au	2 + 5	(α,n)	17.5	$\tau(3_1^-)$

optimize the beam energy for the desired 1-n reaction channel. The beam energy was set to 17.5 MeV, slightly above the Coulomb barrier ($V_C = 17.18$ MeV), after measuring the excitation function around the calculated optimum of the beam energy, and thereby reducing other evaporation channels to a minimum. The α particles impinged on a two layered target of 1.3 mg/cm^2 enriched ^{149}Sm evaporated on a 4.3 mg/cm^2 gold backing. The Sm target material was composed of 93.2% of ^{149}Sm with small contaminants from ^{150}Sm (3.3%), ^{148}Sm (1.5%), ^{152}Sm (1.2%) and 0.8% of other elements. The aim of the experiment was the determination of the mean lifetime of the first excited 0^+ state of ^{152}Gd and the search for new signatures for a QPT from $E2$ observables.

For the population of excited states of the even-even ^{174,176,178,180}Hf isotopes two different nuclear reactions were employed. Excited states of ^{180}Hf were populated via CoulEx. An oxygen beam with a primary beam energy of 55 MeV, just at the Cline-criterion for safe Coulomb excitation [178] and well below the Coulomb barrier at 88 MeV, impinged on a 12 mg/cm^2 thick ^{180}Hf target. The target consisted of 93.9% of ^{180}Hf with small contaminants from other stable Hf isotopes, i.e. ^{179}Hf (1.6%), ^{178}Hf (2.8%), ^{177}Hf (1.3%), and 0.4% of other elements. Excited states of the other investigated hafnium isotopes, i.e. ^{174,176,178}Hf, were populated via β-decay following FE reactions with a Li beam, ^{171}Yb(^{6}Li,3n)^{174}Ta, ^{172}Yb(^{7}Li,3n)^{176}Ta and ^{174}Yb(^{7}Li,3n)^{178}Ta, with target thick-

nesses of ^{172}Yb: 2.3 mg/cm^2, ^{171}Yb: 3 mg/cm^2 and ^{174}Yb: 2.5 mg/cm^2. The primary beam energy has been set to 30 MeV. The beam was cycled between *on* (one hour) and *off* (one hour) to take in- and off-beam data and to stay in the activation maximum of the β decay. Here, the aim was the determination of more precise values of the mean lifetimes of the 2_1^+ states of the even-even ^{174,176,178,180}Hf isotopes, investigating the evolution of the $E2$ transition strengths around mid-shell, between $N = 82$ and $N = 128$.

4.2. ECR-TDRIV @ IKP, Universität zu Köln

The 10 MeV FN Tandem accelerator at the IKP of the Universität zu Köln, similar to the tandem accelerator of IFIN-HH, provides a wide variety of ion beams up to an energy of $10(Q+1)/A$ MeV/A to the different experimental sites, such as the HORUS setup [171] (for nuclear structure and astrophysics experiments and FEST lifetime measurements), the plunger setup (for DSAM and RDDS lifetime measurements) [127] or the atomic mass spectroscopy (AMS) setup [179, 180]. There are three different ion sources available: a duoplasmatron for He beams and two sputter sources for negative ion beams.

For this work the HORUS setup was used in combination with the DARCY plunger device and a double-sided silicon strip detector (DSSD) for particle identification.

4.2.1. HORUS detector array & DARCY plunger device

Up to 14 HPGe detectors can be placed in the HORUS array at five different polar angles θ with respect to the beam axis. An overview of the available detector positions and the used configuration is given in Table 4.3. For this work only HPGe detectors were mounted in the holding structure of HORUS. The BGO shields of the individual HPGe detectors were removed, in order to place the HPGe crystals as close as possible to the DARCY target chamber and thereby increasing the detection efficiency of γ rays. Absorbers, consisting of lead and copper foils with a thickness of one millimeter each, were placed in front of the detectors to suppress low-energy γ-ray radiation. Figure 4.3 shows the HORUS array and the target chamber of the DARCY plunger device. The pre-amplified signals from the HPGe detectors were fed into XIA digitizers and then read
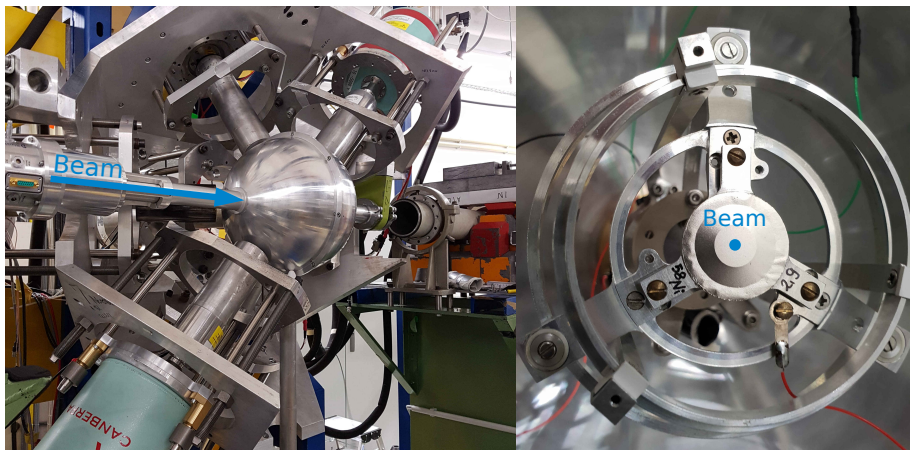
Figure 4.3.: (*left*) Open HORUS array with the installed DARCY plunger device. (*right*) Open DARCY target chamber with the mounted ^{58}Ni target (images taken February 2019).

out. Target and degrader foils were mounted in the DARCY device [see Figure 4.4 (*left*)]. DARCY was constructed in collaboration with the Universität zu Köln and Yale University and commissioned during this work for the ^{18}O ECR-TDRIV measurement. A computer-aided design (CAD) drawing of the device is shown in Figure 4.4 (*left*), where the beam direction is depicted by a blue arrow and the target and degrader (stopper) holding structures are colored green and red, respectively. The adjusted target-to-stopper (degrader) distances have to be maintained during the experiment by a feedback loop. Figure 4.5 shows the utilized electronics of the feedback loop for DARCY. A BNC P8-5 pulse generator sends a voltage pulse V to the degrader foil. The amplified output signal from the target foil, which is proportional to the product of the capacitance C and V, assuming the foils to act as a parallel-plate capacitor, is measured. Here, the experimental capacitance (C_{exp}) is a combination of the capacitance of the foils (C_{foils}), which is anti-proportional to the distance at short distances, and the capacitance of the holding structures (C_{frame}), assumed to be constant (see also Ref. [182]). The voltage on a piezo-electric crystal is adjusted, by comparing the measured voltage to a distance calibration curve, taken right before the ex-

Table 4.3.: The HORUS detector configuration used in this work. The efficiencies are given relative to a 3" × 3" NaI(Tl) scintillation crystal at a γ-ray energy of 1.33 MeV [109, 181].

Name	Detector type / Rel. efficiency	θ (deg)	ϕ (deg)	Distance to degrader (mm)
Ge 0	HPGe; 60%	90	0	175(2)
Ge 1	HPGe; 85%	90	55	175(2)
Ge 2	HPGe; 60%	90	125	175(2)
Ge 3	HPGe; 60%	90	180	175(2)
Ge 4	HPGe; 60%	90	235	175(2)
Ge 5	HPGe; 60%	90	305	175(2)
Ge 6	HPGe; 60%	135	270	168(2)
Ge 7	HPGe; 80%	45	270	168(2)
Ge 8	HPGe; 60%	45	90	168(2)
Ge 9	HPGe; 85%	135	90	168(2)
Ge 10	HPGe; 80%	145	180	168(2)
Ge 11	HPGe; 100%	145	180	168(2)
Ge 12	HPGe; 60%	35	180	168(2)
Ge 13	HPGe; 100%	35	0	168(2)

periment. The piezo-element control is turned off and the plunger motor moves to certain distances from the contact point of the two foils to a set maximum distance (typically a few 100 µm, depending on the estimated lifetime to be measured). For each distance the motor position and the voltage are saved (●, see Figure 4.6). The data points are fitted by a series of second order polynomials. The uncertainty in the distance depends on the distance itself. Close to the electrical contact, the uncertainty is $\Delta d = 0.1$ µm and for distances larger than 100 µm it is $\Delta d = 1$ µm. Figure 4.6 shows the data of the calibration run. Due to surface imperfections of the two foils, the electrical contact does not necessarily correspond to a distance of 0 µm, but a certain offset. The offset of the experiment was determined to be 15(2) µm by extrapolating the calibration points to the point, where $C_{exp} - C_{frame}$ goes to infinity, i.e. the limit of the inverse $C_{exp} - C_{frame}$ goes to zero [see Figure 4.6 (b)]. Only small distances are taken
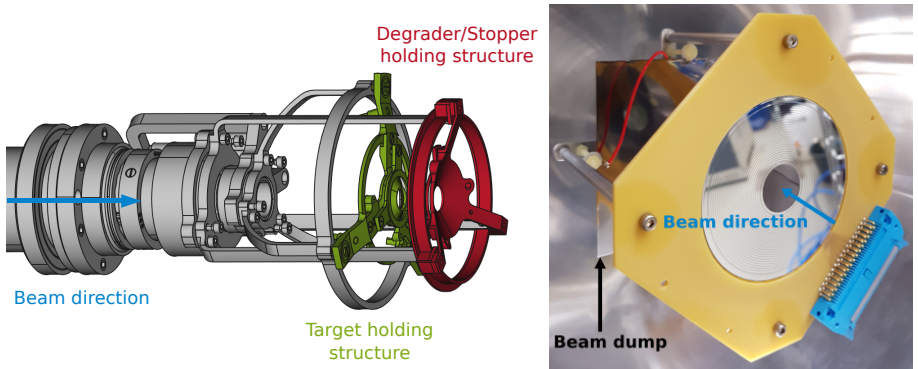
Figure 4.4.: (*left*) CAD drawing of the DARCY plunger. The blue arrow indicates the beam direction and the target and degrader position are colored green and red, respectively. (*right*) The 24 rings of the mounted DSSD in the DARCY target chamber are visible. In the back the Ta beam catcher can be seen (taken February 2019). The blue arrow indicates the beam direction.

into account, because the assumption of a parallel-plate capacitor becomes less accurate for larger distances. The systematic uncertainty of the offset has been obtained by varying the number of calibration points taken into account for the extrapolation.

For the detection of scattered beam-like particles and FE reaction products a S3-500 DSSD from Micron Semiconductor Ltd in the shape of a compact disc (CD) [183] was mounted in the DARCY target chamber at forward angles with respect to the incoming beam. The DSSD has an inner radius of 10(1) mm and an outer radius of 35(1) mm. It is segmented into 32 strips (wedges) on the back and 24 rings on the front (see Figure 4.4). Due to a limited amount of available channels of the XIA modules, two neighboring rings (strips) were readout together, condensing the number of individual rings to twelve and the strips to 16, resulting in a total amount of $12 \times 16 = 192$ pixels and therefore an angular segmentation of $\Delta\theta = 2.5(2)°$, $\Delta\phi = 22.5°$. The DSSD was placed as close as possible to the mounted degrader foil of DARCY at 27(1) mm, ensuring a larger angular coverage, ranging from $\theta = 22(2)°$ to $\theta = 52(2)°$. The front side (rings)
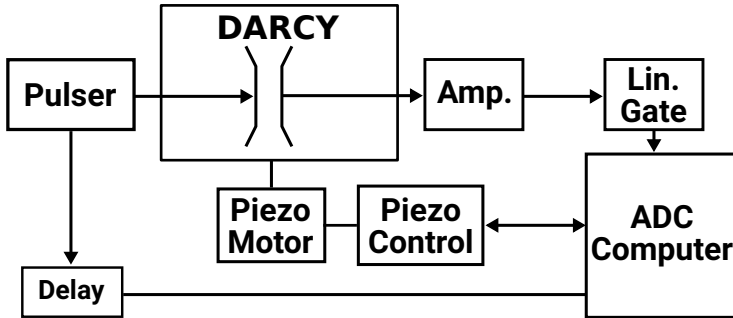
Figure 4.5.: Schematics of the electronics setup used to control the DARCY plunger device. The output signal of DARCY is amplified by an amplifier (Amp.) and shaped with a linear gate and stretcher module (Lin. Gate).

of the mounted DSSD is shown in Figure 4.4 (*right*). In addition, hits on the CD detector stemming from Rutherford scattering of the beam with the target foil or the degrader foil can be reduced by the increased inner polar angle of the DSSD. Rutherford scattering is one limiting factor of the experiment, because of the increased count rate of the inner CD rings. Behind the DSSD a thick Ta foil was placed as the beam dump.

For the further analysis, the segments of the DSSD were combined into three rings and 16 strips. Table 4.4 gives an overview of the segments and their properties.

The goal of the conducted experiment at the IKP was the determination of the *g* factor of the first excited 2^+ state of ^{18}O with the ECR-TDRIV method. Excited states of ^{18}O were populated via the $^{58}Ni(^{18}O,^{18}O^{\star})^{58}Ni$ CoulEx reaction. The ^{18}O projectiles impinged on a $2.9\,mg/cm^2$ ^{58}Ni target. Subsequently, the excited ions exit the target, pass through a $1.8\,mg/cm^2$ Ta degrader foil, and are detected by the DSSD at forward angles. The beam energy was set to $56\,MeV$, i.e. above the Coulomb barrier, allowing the oxygen ions to emerge from the target foil in a mostly hydrogen-like or fully stripped charge state. Only certain polar angles of the DSSD were used for the analysis to ensure that only safe CoulEx events are evaluated (see Section 5.3.2). Data was taken for
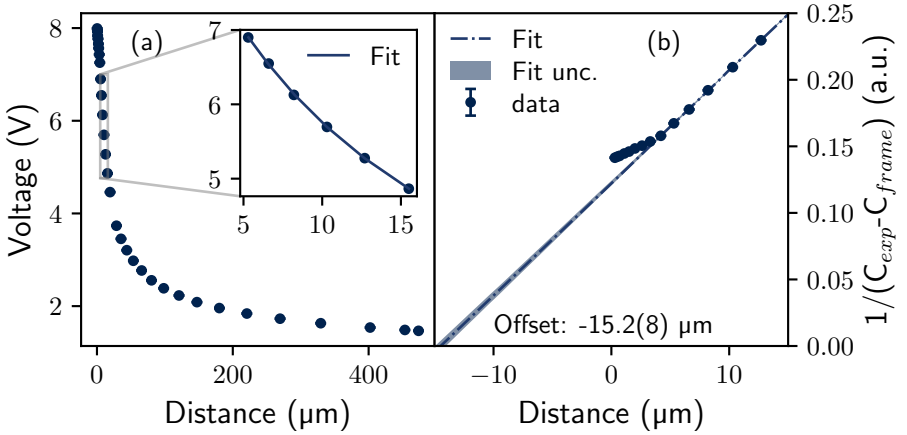
Figure 4.6.: Distance calibration of DARCY. The inset of (a) shows the fit to the data with $d = a/(C_{exp} - C_{frame}) + \text{Offset}$. (b) Determination of the offset of the distance to the electrical contact by extrapolation. Here, only the statistical uncertainty of the offset is given.

eleven different target-degrader distances between 1.0(1) and 145(1) µm (i.e. 1, 10, 20, 30, 40, 50, 60, 70, 85, 100, and 145 µm), not including the offset of the DARCY distance calibration of 15(2) µm.

Table 4.4.: Angles of the DSSD segments. The left side shows the polar angle θ of the DSSD front. The right side the azimuthal angle ϕ of the DSSD back. Every two rings and two strips were read-out together, because of the limited available digitizer channels.

Ring	Name	θ (deg)	Strip	Name	ϕ (deg)
R1-R8	*inner*	$29.1^{+6.0}_{-6.9}$	S1-S2	*S1*	179.6(113)
R9-R16	*middle*	$40.4^{+4.6}_{-5.3}$	S3-S4	*S2*	157.1(113)
R17-R24	*outer*	$48.9^{+3.5}_{-3.9}$	S5-S6	*S3*	134.6(113)
			S7-S8	*S4*	112.1(113)
			S9-S10	*S5*	89.6(113)
			S11-S12	*S6*	67.1(113)
			S13-S14	*S7*	44.6(113)
			S15-S16	*S8*	22.1(113)
			S17-S18	*S9*	-0.4(113)
			S19-S20	*S10*	-22.9(113)
			S21-S22	*S11*	-45.4(113)
			S23-S24	*S12*	-67.9(113)
			S25-S26	*S13*	-90.4(113)
			S27-S28	*S14*	-112.9(113)
			S29-S30	*S15*	-135.4(113)
			S31-S32	*S16*	-157.9(113)

5. Data analysis & results

The first part of this Chapter outlines the necessary steps of the data preparation and analysis procedure of the FEST experiments at IFIN-HH, Bucharest - Magurele and presents the obtained results. The second part outlines the data analysis procedure and the results of the ECR-TDRIV measurement at IKP, Cologne.

5.1. General remarks

Numerical evaluations of this work have been performed using the interactive shell IPython [184] and the Python libraries NumPy [185, 186], pandas [187], and SciPy [188, 189]. For symbolic calculations (e.g. spherical harmonics) the Python library SymPy [190] has been used. The results are visualized with the help of the Python libraries Matplotlib [191] and Cartopy [192] and the vector-graphics program Inkscape [193]. Energy and time spectra, matrices, and cubes have been additionally investigated with the nuclear spectrum analysis tool (hdtv) [194] with the version of [195], based on tv [196] for the oxygen data and with the gamma-ray spectrometer software (GASPWARE) package [197] in the case of the FEST experiments.

5.1.1. Propagation of uncertainties

For the published results in Ref. [138, 139], the stated uncertainties of the measured mean lifetimes and all derived quantities have been calculated in the following way. If the output quantity Y has a functional relation with the input quantities X_i, $Y_i = f(X_i)$, and if each input quantity X_i is subject to its own uncertainty σ_{X_i} and f can be approximated by a Taylor expansion, σ_f^2 can be

given as (see Ref. [198]):

$$\sigma_f^2 = \sum_i \left| \frac{\partial f}{\partial X_i} \right|^2 \sigma_{X_i}^2 + \sum_{i,j \neq i} \frac{\partial f}{\partial X_i} \frac{\partial f}{\partial X_j} \text{cov}_{X_i, X_j}, \qquad (5.1)$$

where cov_{X_i, X_j} is the covariance between X_i and X_j.

For this work, the propagation of uncertainty follows the recommended method of the Guide to the Expression of Uncertainty in Measurement (GUM) [198] adopted from Refs. [199, 200]. The input and output quantities X_i and Y_i follow a probability-distribution function (PDF). The PDF can be approximated by sampling a random number N_R of X_R from the PDF. Evaluating f for each X_R results in a set of values Y_R. The results of Y are then given as:

$$\text{mode}(Y)_{-[\text{mode}(Y)-\text{sci}_l(Y)]}^{+[\text{sci}_u(Y)-\text{mode}(Y)]}, \qquad (5.2)$$

where $\text{mode}(Y)$ gives the most probable value of Y and $\text{sci}_i(Y)$ the upper (u) and lower (l) boundary of the shortest coverage interval ("sci") of the approximated distribution, including 68% of the distribution analogous to the one-σ environment of a Gaussian distribution. The most probable value is obtained by approximating the PDF of Y by a Gaussian kernel-density estimator and determining the maximum of the PDF. The estimator, using a bandwidth following Scott's rule [201], smoothes the distribution of Y_R.

5.1.2. Weighted mean

Based on the methodology of the particle data group (PDG) review article [202], a standard weighted least-squares procedure has been used in this work for averaging data

$$\overline{Y} \pm \delta Y = \frac{\sum_i w_i \cdot Y_i}{\sum_i w_i} \pm \left(\sum_i w_i \right)^{-1/2}, \qquad (5.3)$$

with $w_i = 1/(\delta Y_i)^2$. $1/(N-1)\chi^2 = 1/(N-1)\sum_i w_i \cdot (\overline{Y} - Y_i)^2$ was calculated to compare the measurement data, assuming that they follow a Gaussian Distribution, with the weighted average. For data values with asymmetric uncertainties the weights were set to $w_i = [(\delta Y_{u,i} + \delta Y_{l,i})/2]^{-2}$. If $\chi^2/(N-1)$ is less or equal

5. Data analysis & results

to one, the result is quoted as in Eq. (5.3). In the case that $\chi^2/(N-1) > 1$ a scaling factor S was used to increase the quoted uncertainty under the assumption that the uncertainties of the data points were underestimated or that systematic uncertainties cannot be excluded,

$$S = \left[\chi^2/(N-1)\right]^{1/2}. \tag{5.4}$$

This approach is not used for $\chi^2 \gg 1$, because the data points give contradictory results and should not be averaged.

5.2. Fast-timing lifetime measurements

The following Sections illustrate the mandatory steps of the data preparation and analysis of a FEST experiment at IFIN-HH. The focus will be on the fast-timing lifetime measurement of ^{174,176,178,180}Hf, but the same approach has been taken for the ^{152}Gd data. The results of the Hf and Gd experiments have already been reported and discussed by the author in Refs. [138, 139], respectively. The narrative of this work follows these publications.

The first Section expounds the process of the data analysis starting from the raw data.

5.2.1. Data preparation

Raw data are written to disk as *listmode* files, so called "runs", each containing $\sim 2\,\mathrm{h}$ of data. Every *listmode* entry contains the identification number (id) of the detector registering the event (analogue-to-digital converter (ADC) channel), the recorded signal height, and the time information relative to a trigger signal, e.g. a $\gamma\gamma$ coincidence, of all the detected events in a defined time window. The raw data have to be sorted using the sorting code `gsort` of the GASPWARE package [197] developed at the Instituto Nazionale di Fisica Nucleare (INFN) Legnaro and the IFIN-HH Bucharest. Resulting, in the case of the fast-timing experiments, energy and time spectra, matrices, cubes or hypercubes ($E_\gamma E_\gamma$ coincidence matrices, $E_\gamma E_\gamma \Delta t$ cubes, or $E_\gamma E_\gamma E_\gamma \Delta t$ hypercubes). The sorting code allows via an input file (an example input file can be found in the Appendix B.1) to implement energy and time calibration polynomials during the sorting procedure, as well as to set additional conditions on the detectors, e.g. selecting

specific decay transitions with energy gate conditions in additional detectors. Furthermore, the crucial time-walk calibration (see Section 5.2.4) can already be included in this input file.

These calibration procedures will be outlined in the following, beginning with the energy and time calibration of the LaBr$_3$(Ce) and HPGe detectors.

5.2.2. Energy calibration

The obtained pulse-height energy-spectra of the HPGe and LaBr$_3$(Ce) detectors have to be calibrated with γ-ray energies of a calibration source, e.g. ^{152}Eu with its well-known strong γ-decay transitions in the range of 121 to 1408 keV [51] (see Figure 5.1). A calibration curve can be obtained from the calibration points of the source (▼) by fitting a polynomial $E_i = \sum_n a_n C_i^n$ to the calibration data and obtaining the energy E_i corresponding to a channel number C_i [109]. In the case of the HPGe detectors polynomials of third order and for the LaBr$_3$(Ce) detectors polynomials of fourth and fifth order have been used. These polynomials for each detector were already included in the sorting procedure.

It is useful to also perform an energy-width calibration of the FWHM of the peaks to be able to discriminate single and double peaks of the experimental data. The total FWHM$_T$ of a peak can be written as [109]:

$$\text{FWHM}_T^2 = \text{FWHM}_D^2 + \text{FWHM}_X^2 + \text{FWHM}_E^2, \qquad (5.5)$$

$$\text{FWHM}_D^2 = (2.35)^2 F \epsilon E, \qquad (5.6)$$

where FWHM$_D^2$ denotes the peak width from statistical effects, FWHM$_X^2$ stands for the peak width due to charge carrier collection and FWHM$_E^2$ is the FWHM due to electronic noise. Furthermore, F is the Fano factor [109], ϵ the energy required to create an electron-hole pair and E the γ-ray energy. Figure 5.1 (*bottom*) shows the determined FWHM (✖) as a function of the γ-ray energy for the calibration run of detector HPGe 0. According to Eq. (5.6), a square root function was fitted to the data (red dashed line).

The energy calibration of the LaBr$_3$(Ce) detectors has to be performed in more steps, because of the greater degree of non-linearity in the energy response compared to the HPGe detectors. After a first energy calibration with a calibration source, a gain matching has to be performed with known γ-ray transitions from in-beam data, due to the count rate dependence of the detection efficiency of
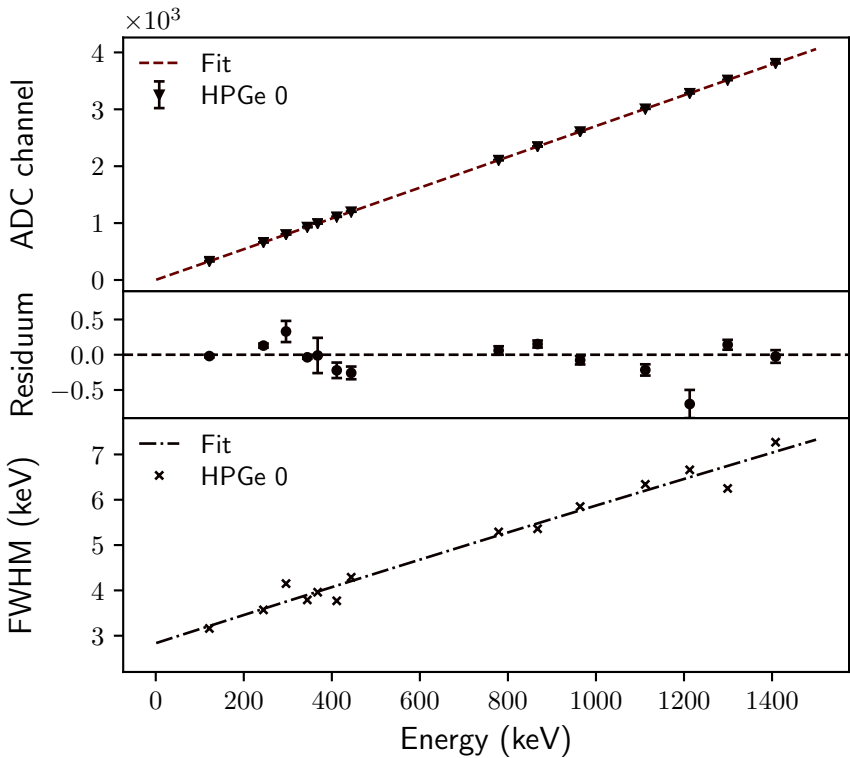
Figure 5.1.: (*top*) Channel over Energy from the ^{152}Eu source measurement for detector HPGe 0. (*middle*) Residuum of the fit of (*top*) to the data. (*bottom*) Width calibration of the detector, using Eq. (5.6).

the LaBr$_3$(Ce) detectors. Moreover, the detected energy of the LaBr$_3$(Ce) detectors shifts with time because of temperature and voltage fluctuations. For this reason, these effects have to be corrected on a run-by-run basis.

Figure 5.2 shows the calibrated HPGe and LaBr$_3$(Ce) energy sum spectra of all detectors. Transitions of the ^{152}Eu calibration source used for the calibration of the detectors are marked by ▼. For the HPGe detectors, additional transitions
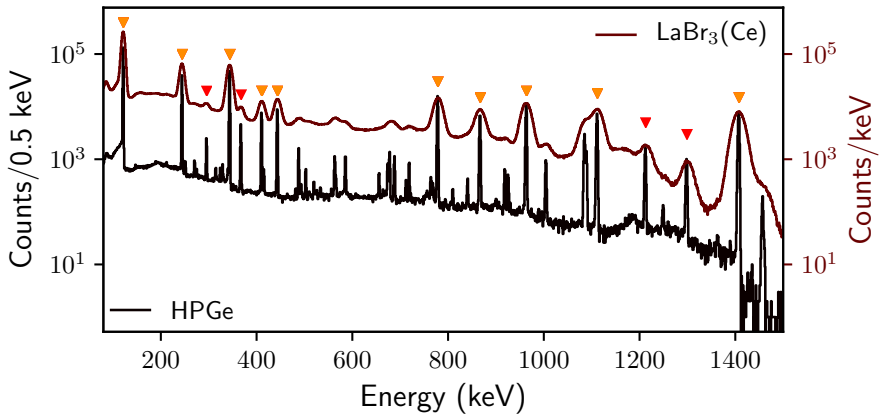
Figure 5.2.: Energy-calibrated γ-ray spectra of the first HPGe and the first LaBr$_3$(Ce) detectors of the ROSPHERE detector array. The utilized γ-ray energies of the ^{152}Eu calibration source are marked by ▼ for the LaBr$_3$(Ce) and HPGe detectors. Additional γ-ray energies were used for the HPGe detectors (▼).

of the decay of ^{152}Eu were used (▼), which have been omitted for the calibration of the LaBr$_3$(Ce) detectors, because they could not be resolved in every detector, due to the worse intrinsic energy resolution of LaBr$_3$(Ce) detectors in comparison to HPGe detectors.

5.2.3. Time alignment

The time difference between two signals is processed by the TAC into a logic signal with an amplitude proportional to the time difference. The TAC can be calibrated by using a generic prompt signal with different known delays, e.g. by using different cables with known lengths. The timing information of the HPGe detectors is processed by a time-to-digital converter (TDC) and can be calibrated in the same way.
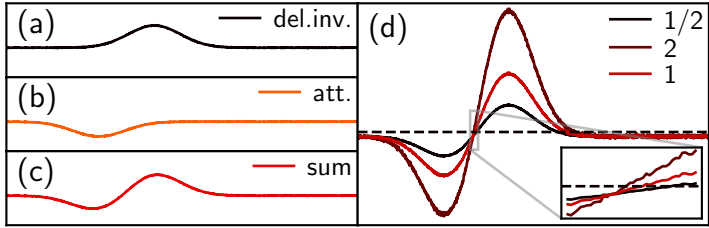
Figure 5.3.: (*left*) Working principle of a CFD: The incoming signal is split up. One signal is inverted and delayed (a) and the other one attenuated (b). Finally, both signals are summed up (c). (d) Due to signal noise, the threshold determining the zero crossing of the summed signal cannot be set to zero, but has to be placed slightly above zero. This leads to small differences in the determination of the signal time depending on the signal amplitude, i.e. time walk. Shown is the zero-crossing for three different input amplitudes, 0.5, 1 and 2.

5.2.4. Time-walk calibration

The time-walk calibration of the experimental setup is essential for the determination of lifetimes in the picosecond range (see Section 3.3.1). The time difference obtained from the TAC signals includes not only the time difference between the start and the stop signal, i.e. the effective lifetime τ_{eff} of all states between these two transitions, but also the time response of the setup $t_{\mathrm{tw,i}}$, i.e.

$$\Delta t_{\mathrm{exp}} = \tau_{\mathrm{eff}} + t_{\mathrm{tw,1}}(E_{\gamma,1}) + t_{\mathrm{tw,2}}(E_{\gamma,2}). \tag{5.7}$$

The time response of the setup usually depends on the energy of the detected photons, resulting in the energy-dependent time walk. The effect can be reduced with the usage of a CFD. Whose working principle is shown in Figure 5.3. An input signal is split into two signals. The first signal is delayed and inverted and the second one is attenuated. Subsequently, both signals are summed up and the zero crossing of the sum signal, which is independent of the input signal amplitude is determined. Nevertheless, even with a CFD, a time walk still remains. The threshold, determining the zero crossing, has to be placed above
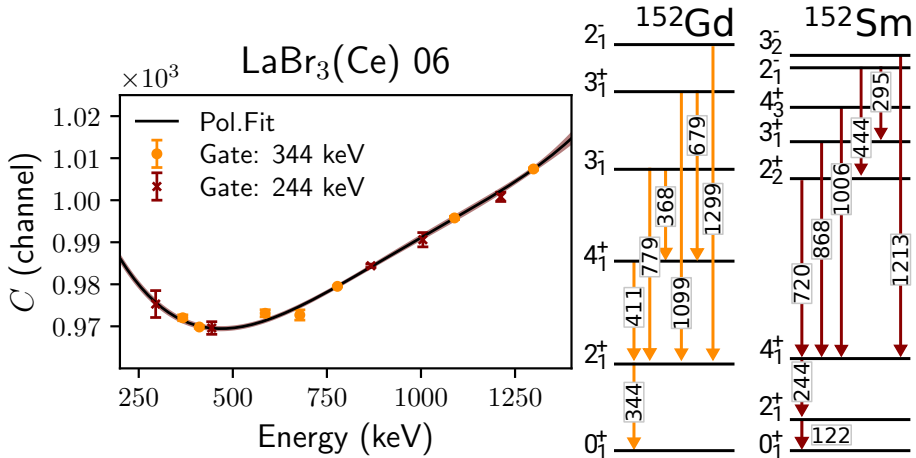
Figure 5.4.: (*left*) Centroid difference between a common stop transition, 244 keV (✖) and 344 keV (●) and coincident transitions. (*right*) Partial level scheme of ^{152}Gd and ^{152}Sm after the decay of ^{152}Eu. Transition energies are given in keV.

the noise of the baseline, creating a small offset in the determination of the zero crossing [as indicated by the inlay of Figure 5.3 (d)]. Therefore, it is necessary to determine the time walk of every detector of the setup.

One way to calibrate the system in the energy range of 244 keV up to 1.4 MeV is to use a ^{152}Eu source with its known γ-ray transitions and lifetimes. The characteristic γ-ray energy spectra can be used for the determination of the time walk. Figure 5.4 shows the partial level schemes of both decay paths of ^{152}Eu, to ^{152}Gd and ^{152}Sm, and the time difference between a common stop signal, i.e. the 344 keV ($2_1^+ \rightarrow 0_{GS}^+$) transition of ^{152}Gd or the 244 keV ($4_1^+ \rightarrow 2_1^+$) transition of ^{152}Sm, and the coincident decay transitions. The shown data (● and ✖), in Figure 5.4 (*left*), were already corrected for the vertical offset between both data sets, due to the difference in energy of the common stop signals and therefore the difference in the time response for 244 and 344 keV. The fit to the data with a polynomial function is depicted by the black line. The fit uncertainty is indicated by the shaded red area, only visible in the high energy region. The
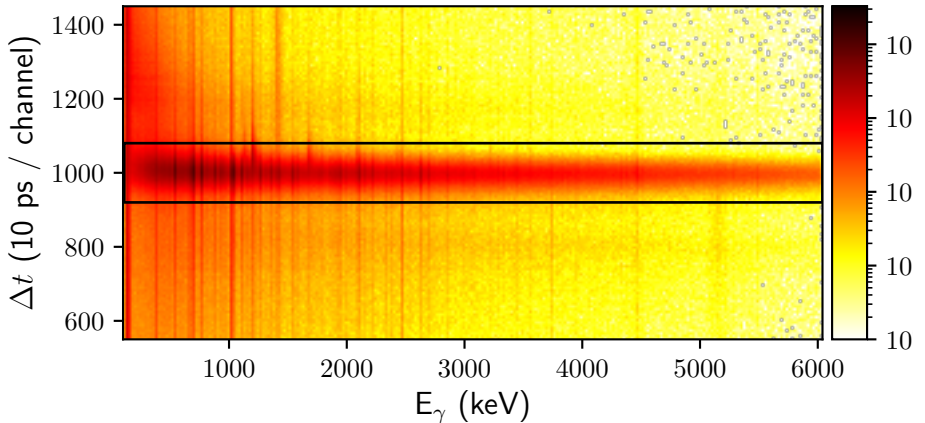
Figure 5.5.: $E_\gamma \Delta t$ matrix of the HPGe detectors. The area in the black box contains the prompt coincidence events. The zero point of the time differences was arbitrarily shifted to channel 1000.

time response of each detector was corrected by the fitted polynomials (see Appendix C.2 for the time walk determination of all detectors). For more details of the time response of $LaBr_3(Ce)$ detectors and other methods for the calibration of the setup the reader is referred to [134, 136].

5.2.5. Random background

Random background, can origin from the γ decay of nuclei, which are not investigated but produced in the reaction of the beam and the target, or the environment, i.e. uncorrelated random coincidences. Its contributions can distort the final result. A selection in the HPGe $E_\gamma \Delta t$ matrix, where Δt is the time-difference between two events registered in the HPGe detectors, can suppress these uncorrelated events. Figure 5.5 shows the $E_\gamma \Delta t$ matrix of the HPGe detectors of ROSPHERE. True coincidences are temporally correlated and create an area of prompt coincidences, resulting in a peak in the Δt projection of the matrix. The black box in Figure 5.5 marks the area of prompt coincidences. Random events on the contrary have no time correlation and create a plateau

---
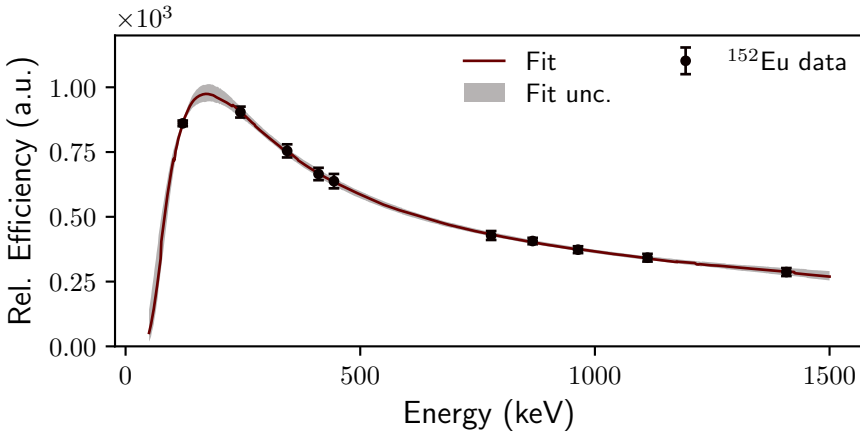
Figure 5.6.: Measured relative efficiency of HPGe detector HPGe 0 of RO-SPHERE using a ^{152}Eu source (●). A fit with Eq. (5.8) to the data is shown by the dark red line.

of random background in the Δt projection. A condition to exclude events that are outside of the selected area was set in the sorting code. Naturally, there are also random events in the selected area, but their influence has to be treated later during the determination of the lifetimes.

5.2.6. Efficiency calibration

Detector efficiency is limited by the finite size of the detector material and the geometry of the detectors. Moreover, the efficiency is dependent on the incident γ-ray energy. The detector efficiency has to be known, if γ-ray intensities are needed to extract observables from the γ-ray energy spectra, e.g. angular distributions or CoulEx cross-sections. For a FEST analysis information about the detector efficiencies are in general not necessary, but the procedure to determine the relative efficiency of ROSPHERE will be outlined here, since relative efficiencies are needed for the CoulEx analysis of ^{180}Hf.

The relative efficiency is determined from the measured peak areas A and the known transition intensities I via the relation $\epsilon = A/I$. Relative intensities

are sufficient for CoulEx experiments, since the transitions are normalized to a known transition, e.g. the $2_1^+ \rightarrow 0_{GS}^+$ transition. The energy dependence is found by fitting the calibration points from the calibration source via the following fit function [109]:

$$\epsilon = \exp\left[\sum_i^N p[i] \times \log(E)^i\right]. \tag{5.8}$$

Figure 5.6 shows the efficiency curve of the first HPGe detector, HPGe 0, of the ROSPHERE detector array from a ^{152}Eu calibration source (●). The dark red line shows the fit to the data using Eq. (5.8).

5.2.7. [174,176,178,180]Hf results

After completing all the necessary steps, i.e. energy, efficiency and time-walk calibrations, the time alignment of the detectors and the random background subtraction, energy spectra and matrices can be extracted from the data. Figure 5.7 presents the obtained partial energy spectra of the HPGe and LaBr$_3$(Ce) detectors for the four different reactions, populating excited states of (a) [174]Hf, (b) [176]Hf, (c) [178]Hf, and (d) [180]Hf. Transitions, that were used for the determination of lifetimes, are marked (▲).

As mentioned in Section 3.3.1, mean lifetimes in the range of nanoseconds have been determined with the slope method using $E_\gamma E_\gamma$ coincidences within the LaBr$_3$(Ce) detectors. Examples of such long-lived states are the 2^+_1 states of [174,176,178,180]Hf and the 2^-_1 state of [176]Hf. The time-difference spectra were extracted by setting an energy condition on a start and a stop transition in the $E_\gamma E_\gamma \Delta t$ cubes. The resulting time-difference spectra have to be corrected for random coincidences and Compton background below the full energy peaks. Thus, the method discussed in Refs. [36, 203] was applied. In each case, four different time-difference spectra were created, by gating on the energy (A) of the start and the stop transition, (B) of the start transition and a background region of the stop transition, (C) of the background of the start transition and the stop transition, and (D) of the two previously defined background regions. Applying coincidence logic the final time-difference spectra are given by the combination (A)-(B)-(C)+(D). The background energy gates were chosen on the right side of the start/stop transitions to exclude possible Compton events from the transitions themselves. In the case of the 2^+_1 state, energy gates were set on the $4^+_1 \rightarrow 2^+_1$ and $2^+_1 \rightarrow 0^+_{GS}$ transitions and in the case of the 2^-_1 state of [176]Hf, on the $2^-_2 \rightarrow 2^-_1$ and $2^-_1 \rightarrow 2^+_1$ transitions [see Figure 5.9 and 5.11 for the partial level schemes of the investigated isotopes]. The time-difference spectra of the delayed case, including the fits, are depicted in Figures 5.8 and 5.10(a). The decay cascades are shown on the left of each sub figure. The fit regions were chosen by moving a gate with a defined time width of a few hundred picoseconds across the time difference spectra. Only the regions where the slope stays constant were used for the fit. Thus, eliminating the influence from the prompt peak and background contributions.

The centroid shift method (see Section 3.3.1) has been employed for the determination of lifetimes of short-lived excited states in the range of a few ten
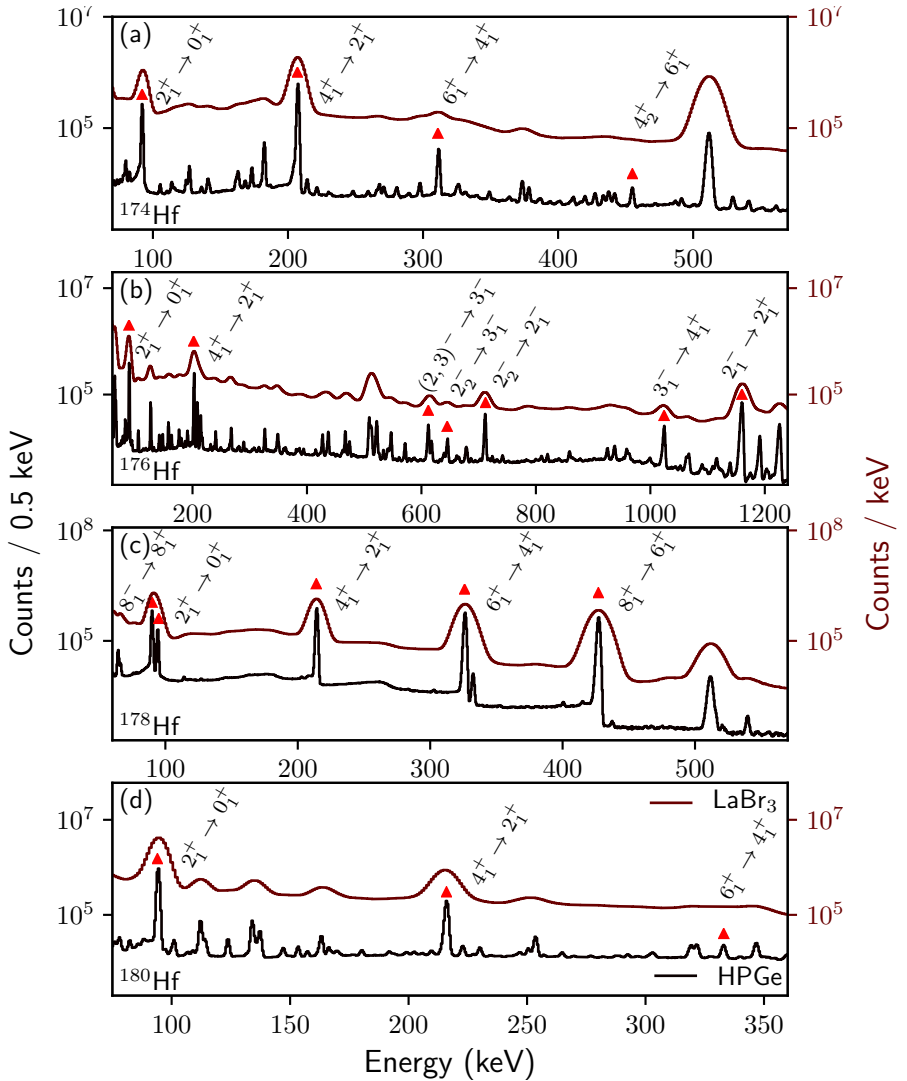
Figure 5.7.: Partial energy spectra for (a) ^{174}Hf, (b) ^{176}Hf, (c) ^{178}Hf, and (d) ^{180}Hf [LaBr$_3$(Ce) (red) and HPGe (black)]. See Section 5.2.7.
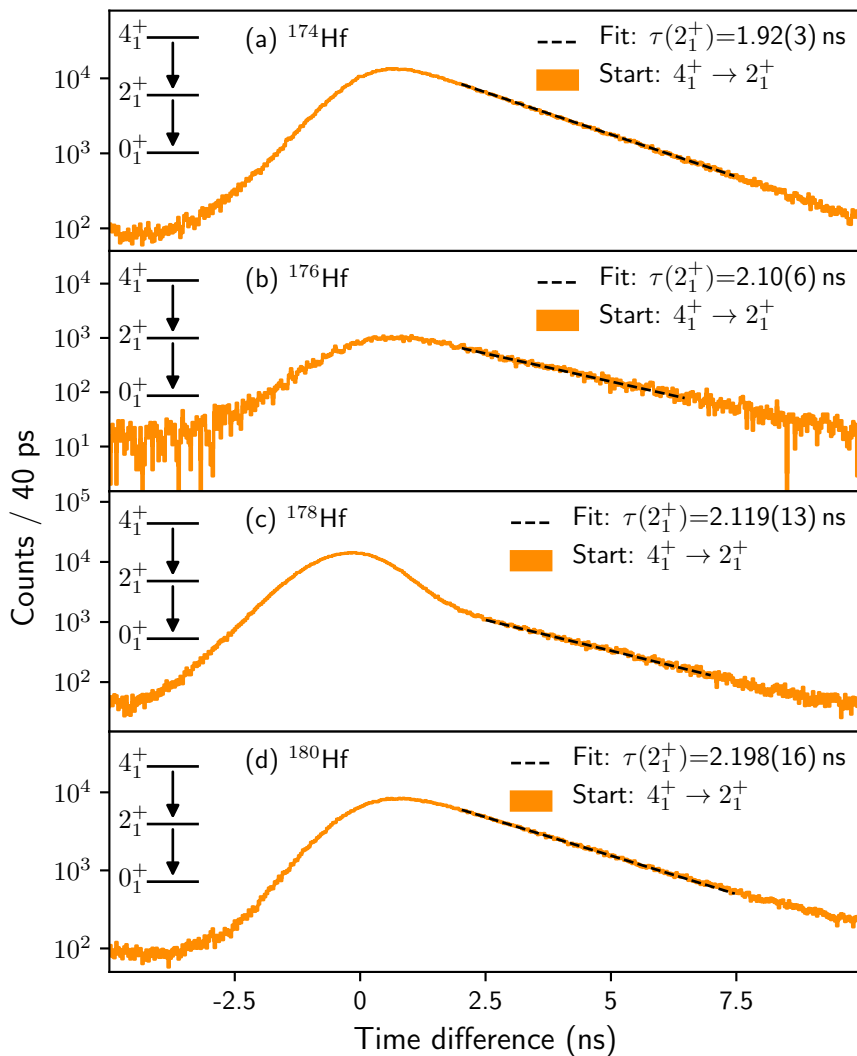
Figure 5.8.: Logarithmic plots of the time-difference spectra for the decays of 2_1^+ states of the isotopes ^{174,176,178,180}Hf from (a)-(d). Linear fits are indicated by the dashed black lines.
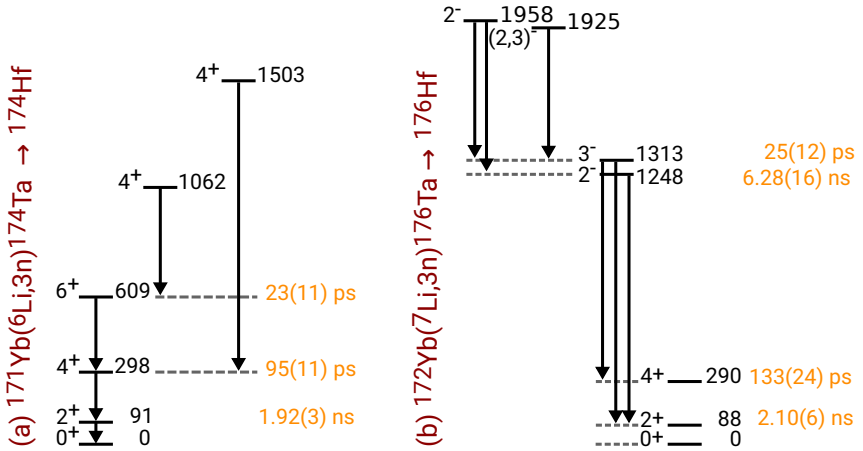
Figure 5.9.: Partial level schemes of ^{174}Hf (a), ^{176}Hf (b). Shown are the states used for the FEST lifetime determination. The determined mean lifetimes are given in yellow.

picoseconds, here the 4_1^+, 6_1^+ and 3_1^- states. Figures 5.12 and 5.10 (b) present the obtained delayed and anti-delayed time-difference spectra for the short-lived yrast states of ^{174,176,178,180}Hf and for the 3_1^- state of ^{176}Hf, respectively. The high transition density of the β decay to ^{176}Hf [see Figure 5.7 (b)] made it necessary to decrease the gate widths in this case, resulting in lower statistics of the time distributions and therefore larger uncertainties of the determined lifetimes.

Each individual case will be discussed in the following Sections.

^{174}**Hf**

A partial level scheme of states of ^{174}Hf populated by the electron capture decay of ^{174}Ta to ^{174}Hf is depicted in Figure 5.9 (a). Mainly positive-parity states are populated by this reaction [204] . States of the yrast band of ^{174}Hf are excited up to the 6_1^+ state. From the γ-ray energy spectrum transitions feeding and depopulating these states have been identified [see Figure 5.7 (a)]. The mean lifetimes of the three yrast states 2_1^+, 4_1^+ and 6_1^+ have been extracted. For the

determination of $\tau(4_1^+)$, the $4_3^+ \rightarrow 4_1^+$ and $4_1^+ \rightarrow 2_1^+$ transitions have been used, because the sum energy of the $6_1^+ \rightarrow 4_1^+$ and $4_1^+ \rightarrow 2_1^+$ γ-ray transitions $[E(6_1^+ \rightarrow 4_1^+) + E(4_1^+ \rightarrow 2_1^+) = 517\,\text{keV}]$ is close to 511 keV. Therefore, Compton scattered events from 511 keV e^-e^+ annihilation γ rays contaminate the coincidence area of the $6_1^+ \rightarrow 4_1^+$ and $4_1^+ \rightarrow 2_1^+$ transitions.

^{176}Hf

The electron capture decay of ^{176}Ta populates numerous excited states of ^{176}Hf. This results in a complex decay scheme [205, 206], as can be seen in the γ-ray energy spectrum depicted in Figure 5.7 (b). The relevant part of the level scheme for this work is shown in Figure 5.9 (b). Besides the yrast band a low-lying negative-parity $K = 2$ band of ^{176}Hf is strongly populated by this decay. As a result, it was possible to determine the mean lifetimes of the 2_1^- state, and for the first time of the 3_1^- state (see Figure 5.10). For the determination of $\tau(3_1^-)$ two populating transitions have been used, i.e. the two transitions populating the 3_1^- state at 611 keV $[(2,3)^- \rightarrow 3_1^-]$ and at 645 keV $(2_2^- \rightarrow 3_1^-)$ in combination with the decay to the 4_1^+ state. The quoted mean lifetime is the weighted mean of both values, $\tau(3_1^-) = 25(12)\,\text{ps}$ (see Appendix 5.1.2). The extracted mean lifetime of the 2_1^- state, $\tau(2_1^-) = 6.28(16)\,\text{ns}$, is lower than the adopted value of $\tau(2_1^-) = 6.72(25)\,\text{ns}$ given in Ref. [31], but in good agreement with a part of the quoted references of the data sheets, e.g. Ref. [207].
The gates for the determination of the mean lifetimes have to be carefully selected in the LaBr$_3$(Ce) detectors, especially for ^{176}Hf, due to the high transition density of the energy spectra. All selected energy gates were cross checked within the energy spectra of the HPGe detectors, due to their higher energy resolution compared to the LaBr$_3$(Ce) detectors.

^{178}Hf

The β decay of ^{178}Ta following FE primarily populates the 8^- isomeric state of ^{178}Hf at an energy of 1147 keV. It decays via the emission of γ rays through the yrast band to the GS. Consequently, mainly yrast transitions are visible in the obtained γ-ray spectrum [see Figure 5.7 (c)]. The decay transition depopulating the isomeric state, $8_1^- \rightarrow 8_1^+$ at 88.9 keV, and the transition $2_1^+ \rightarrow 0_{\text{GS}}^+$ at 93.2 keV are very close in energy. For this reason, these transitions can not be
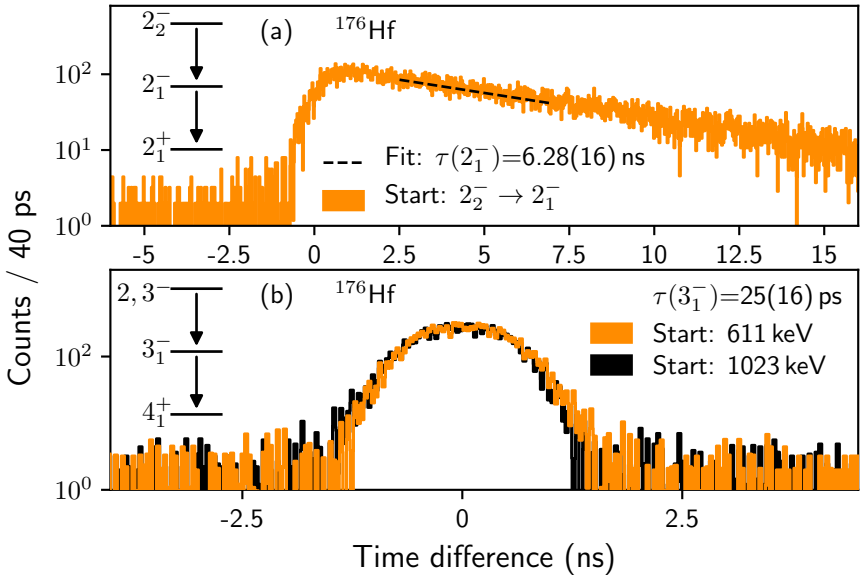
Figure 5.10.: (a) Logarithmic plots of the time-difference spectrum for the decay of 2_1^- state of the isotopes ^{176}Hf. The linear fit is indicated by the dashed black line. (b) Delayed (black) and anti-delayed (orange) time distributions of the cascade $(2/3)^- \to 3_1^- \to 4_1^+$.

separated with the LaBr$_3$(Ce) detectors. Additional energy gates in the HPGe detectors are not able to isolate one of them, since both transitions are from the same decay cascade. Selecting the coincidence region in the $E_\gamma E_\gamma$ plane, results in a time-difference spectrum which is a superposition of two time-difference distributions; on one hand a distribution of the pair of coincidence γ rays from the $2_1^+ \to 0_{GS}^+$ and $4_1^+ \to 2_1^+$ transitions and on the other hand a distribution of the pair of coincidence γ rays from the $8_1^- \to 8_1^+$ and $4_1^+ \to 2_1^+$ transitions. The ordering of the energy gates is reversed for the two cases. The 88 keV γ ray corresponds to a transition populating the cascade and the cascade is depopulated via the 214 keV γ-ray transition (anti-delayed case), whereas the 2_1^+ state is populated via the 214 keV transition and decays via the 93 keV γ-ray transi-
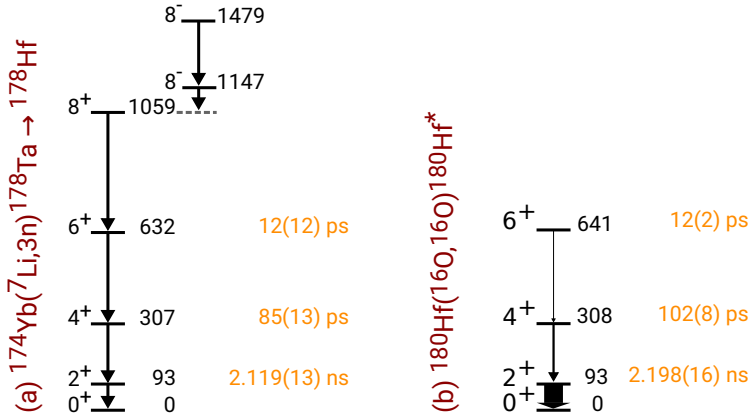
Figure 5.11.: Partial level schemes of ^{178}Hf (a), ^{180}Hf (b). Shown are the states used for the FEST lifetime determination. The determined mean lifetimes are given in yellow. In the case of ^{180}Hf, the transition widths correspond to the observed γ-ray intensities.

tion [delayed case, see Figure 5.11 (a)]. Thus, the time-difference distribution is a superposition of a delayed and an anti-delayed distribution, and the tails correspond to the effective mean lifetime of the 4_1^+, 6_1^+ and the 8_1^+ states on one side of the time distribution and to the mean lifetime of the 2_1^+ state on the other side. The tail of the long-lived 2_1^+ state can be identified in the time distribution [see Figure 5.8 (c)]. Additionally, the mean lifetime of the 4_1^+ state (for the first time) and of the 6_1^+ state have been determined using the centroid shift method.

^{180}Hf

Excited states of ^{180}Hf were populated by CoulEx. Hence, it was possible to determine the mean lifetimes using FEST and CoulEx. The CoulEx analysis was performed with the computer code CLX [116], which is based on the original code of Winther and De Boer [208].
The ^{180}Hf target was already in use in a FE experiment directly before the discussed CoulEx experiment. Therefore, the material was still activated and

transitions stemming from the decay of the FE reaction products, e.g. ^{181}Ta, ^{182}W and ^{184}W, can still be identified in the HPGe energy spectrum [see Figure 5.7 (d)]. Moreover, due to a ^{178}Hf contamination in the target material, its lifetimes have to be taken into account. The transition energies of the $2^+_1 \rightarrow 0^+_{GS}$ and the $4^+_1 \rightarrow 2^+_1$ transitions in both isotopes, ^{178}Hf and ^{180}Hf, are very close in energy (93.2 keV vs. 93.3 keV and 213.4 keV vs. 215.3 keV). Consequently, both transitions cannot be separated in the LaBr$_3$(Ce) detectors for the two isotopes. The partial level scheme of ^{180}Hf is depicted in Figure 5.11 (b). However, the $6^+_1 \rightarrow 4^+_1$ transitions of both isotopes are 9 keV apart and have been identified in the HPGe energy spectrum. Using the observed intensity of the $6^+_1 \rightarrow 4^+_1$ transition of ^{178}Hf at 332 keV and the measured mean lifetimes (2^+_1, 4^+_1) of ^{178}Hf of this work (see Table 5.1), the ^{178}Hf contribution can be subtracted.

The relative CoulEx cross sections are equal to the relative yields of excited states:

$$\frac{Y(J^\pi_i)}{Y(2^+_1)} = \frac{\sigma_{\text{CoulEx}}(J^\pi_i)}{\sigma_{\text{CoulEx}}(2^+_1)}. \tag{5.9}$$

The experimental yield of a state J^π_i can be calculated by subtracting the populating γ-ray intensities of the state from the depopulating γ-ray intensities. Figuratively, the yield quantifies how often a state was populated via CoulEx. The yields were obtained from the efficiency-corrected γ-ray intensities, after subtraction of the ^{178}Hf γ-ray intensities, and normalization to the $2^+_1 \rightarrow 0^+_{GS}$ transition. The CoulEx calculation with CLX has been performed by varying the matrix elements of the $4^+_1 \rightarrow 2^+_1$ and $6^+_1 \rightarrow 4^+_1$ transitions and comparing the resulting relative CoulEx cross sections with the experimental yields. Uncertainties were determined by a variation of the matrix elements within the range of the uncertainties of the calculated experimental yields. The energy loss of the beam of 18 MeV in the target has been taken into account. The obtained mean lifetimes from the CoulEx analysis and the FEST measurement are listed in Table 5.1. Both values $\tau(4^+_1) = 100(23)$ ps from FEST and $\tau(4^+_1) = 103(12)$ ps from CoulEx, are in good agreement within their uncertainties. Consequently, a weighted average of these independent evaluations can be calculated: $\tau(4^+_1) = 102(11)$ ps.

The obtained experimental results of all Hf isotopes are given in Table 5.1. Another similar FEST experiment of Hf isotopes was recently performed by Rudigier et al. [40]. Since their determined lifetimes are in good agreement
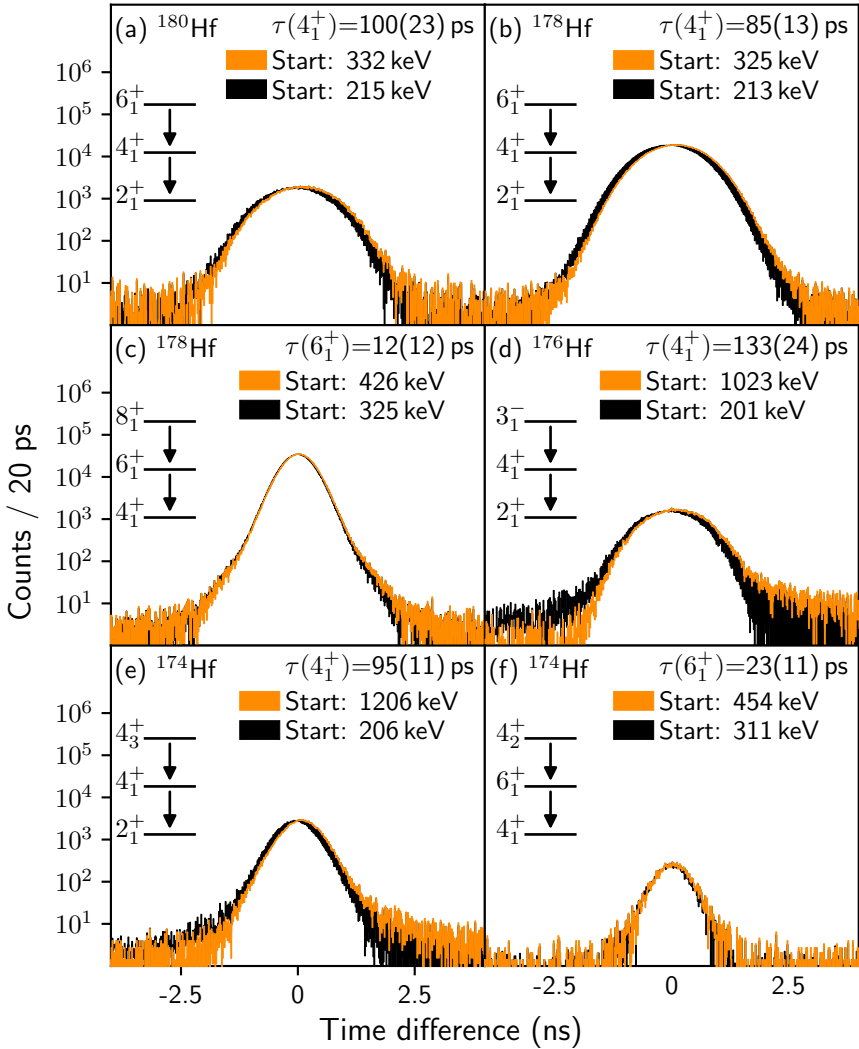
Figure 5.12.: Logarithmic plots of the time-difference spectra of short lived yrast states of ^{180,178,176,174}Hf.

with the values of this work, weighted average values of the lifetimes of these values are given in Table 5.1. The mean lifetimes are directly related to the transition strength in the case of pure radiation character [see Eq. (3.11)]. Since the decay between states of the yrast band of even-even nuclei is dominated by $E2$ radiation, the $B(E2)$ values can be directly calculated from the obtained mean lifetimes. For this purpose, Eq. (3.11) has to be multiplied by $(1 + \alpha)$ to include electron conversion, with the electron conversion coefficient α. The conversion coefficients for the determination of the $B(E2)$ values have been taken from Ref. [209].

Table 5.1.: Measured mean lifetimes of excited states of ^{174,176,178,180}Hf. Adopted literature values were taken from Refs. [30–33, 40]. CoulEx analysis values are indicated with CLX. Two cascades were used to determine $\tau(3_1^-)$ of ^{176}Hf, resulting in an adopted value of $\tau(3_1^-) = 25(12)$ps. Weighted average value of $\tau(2_1^+)$, $\tau(4_1^+)$ and $\tau(6_1^+)$ of ^{174,176}Hf were taken from [40] and this work. $\tau_{\text{weighted}}(4_1^+)$ of ^{180}Hf has been taken from the CoulEx calculation and FEST. $B(E2; \lambda \to \lambda - 2)$ were determined from τ_{weighted} with α taken from Ref. [209].

	J_n^P	Gate-1	Gate-2	$\tau_{\text{exp.}}$ (ps)	$\tau_{\text{lit.}}$ (ps)	τ_{weighted} (ps)	$\alpha^{\blacklozenge}$	$B(E2)$ (W.u.)
^{174}Hf	2_1^+	$4_1^+ \to 2_1^+$	$2_1^+ \to 0_1^+$	1920(30)	1847(58)$^{\blacktriangledown}$	1905(30)	5.12(8)	195$^{+4}_{-4}$
	4_1^+	$4_3^+ \to 4_1^+$	$4_1^+ \to 2_1^+$	95(11)	111(7)$^{\blacktriangledown}$	106(7)	0.258(4)	289$^{+16}_{-21}$
	6_1^+	$4_2^+ \to 6_1^+$	$6_1^+ \to 4_1^+$	23(11)	23(7)$^{\blacktriangledown}$	23(6)	0.071(1)	173$^{+59}_{-35}$
^{176}Hf	2_1^+	$4_1^+ \to 2_1^+$	$2_1^+ \to 0_1^+$	2100(60)	2121(87)$^{\blacktriangledown}$	2107(49)	5.77(9)	183$^{+4}_{-5}$
	4_1^+	$3_1^- \to 4_1^+$	$4_1^+ \to 2_1^+$	133(24)	130(9)$^{\blacktriangledown}$	130(8)	0.279(4)	255$^{+13}_{-18}$
	2_1^-	$2_2^- \to 2_1^-$	$2_1^- \to 2_1^+$	6280(160)	6720(250)$^{\blacklozenge}$	6407(200)	—	—
	3_1^-	$2_2^- \to 3_1^-$	$3_1^- \to 4_1^+$	26(18)$^{\blacklozenge}$	—	—	—	—
	3_1^-	$(2,3)^- \to 3_1^-$	$3_1^- \to 4_1^+$	25(16)$^{\blacklozenge}$	—	25(12)*	—	—
^{178}Hf	2_1^+	$4_1^+ \to 2_1^+$	$2_1^+ \to 0_1^+$	2119(13)	2155(33)$^{\blacklozenge}$	2124(12)	4.66(7)	162$^{+3}_{-2}$
	4_1^+	$6_1^+ \to 4_1^+$	$4_1^+ \to 2_1^+$	85(13)★	—	85(13)*	0.232(4)	280$^{+50}_{-40}$
	6_1^+	$8_1^+ \to 6_1^+$	$6_1^+ \to 4_1^+$	12(12)	16(1)$^{\blacklozenge}$	16(1)	0.062(1)	223$^{+12}_{-16}$
^{180}Hf	2_1^+	$4_1^+ \to 2_1^+$	$2_1^+ \to 0_1^+$	2198(16)	2191(14)$^{\approx}$	2194(11)	4.63(7)	155$^{+2}_{-2}$
	4_1^+	$6_1^+ \to 4_1^+$	$4_1^+ \to 2_1^+$	100(23)	102(14)$^{\approx}$	102(11)	0.225(4)	227$^{+26}_{-22}$
	4_1^+	CLX		103(12)				
	6_1^+			12(2)	14(1)$^{\approx}$	14(1)	0.059(1)	228$^{+14}_{-19}$

◆ Data taken from Ref. [209]   ▼ Data taken from Ref. [40]   ◆ Data taken from Ref. [31]   ◆ Data taken from Ref. [32]   ≋ Data taken from Ref. [33]   ★ Obtained for the first time from this work.

5.2.8. ^{152}Gd results

γ-ray spectroscopy

The γ-ray transitions of ^{152}Gd can be clearly identified in the HPGe-detector energy spectrum, due to their energy resolution of about 2.5 keV @ 300 keV and 3 keV @ 1.4 MeV. Figure 5.13 (a) shows the total projection of the $E_\gamma E_\gamma$ coincidence matrix of all HPGe detectors between 170 and 900 keV [137]. The γ-ray transitions of interest for the determination of $\tau(0_2^+)$, i.e. the $2_2^+ \rightarrow 0_2^+$ transition at 315 keV and the $0_2^+ \rightarrow 2_1^+$ transition at 271 keV, are marked by ◆ [see also the partial level scheme of ^{152}Gd in Figure 5.15 (c)]. The yrast band was populated up to the 10_1^+ state ($10_1^+ \rightarrow 8_1^+$ transition at 553 keV). Many additional transitions from other excitation bands can be identified, but will not be further discussed in this work. The inset of Figure 5.13 (a) shows the total projection zoomed in on the relevant energy region around 300 keV. The γ-ray transitions of ^{152}Gd are marked by ◆. Further transitions from other reaction channels, such as CoulEx of the α beam with the Au backing of the target or FE of the beam with the beam dump, are indicated by ▼. For the determination of the mean lifetime $\tau(0_2^+)$ additional energy conditions were set on the detected energy of the HPGe detectors, creating HPGe gated $E_\gamma E_\gamma \Delta t$ cubes. These additional conditions are necessary, since the peaks of the contaminants (CoulEx and FE) cannot be separated in the LaBr$_3$(Ce) energy spectra. Figure 5.13 (b) exemplary shows the result of a gate on the $4_2^+ \rightarrow 2_2^+$ transition at 351 keV in the HPGe detectors, on the energy projection of the LaBr$_3$(Ce)-detector-coincidence matrix. The LaBr$_3$(Ce) γ-ray energy spectrum with a second gate on the LaBr$_3$(Ce) energy is shown in Figure 5.13 (c). The peak at 315 keV (originating from the $2_2^+ \rightarrow 0_2^+$ transition) can clearly be distinguished from the $2_1^+ \rightarrow 0_{GS}^+$ transition at 344 keV. After checking the HPGe energy spectra with the same coincidence conditions interference from the known contaminants can be excluded and clean gates can be set on the relevant transitions in the LaBr$_3$(Ce) detectors to determine the lifetime of the first excited 0^+ state of ^{152}Gd.

Lifetime determination

After applying the corrections outlined in Sections 5.2.2 to 5.2.5, two HPGe energy-gated $E_\gamma E_\gamma \Delta t$ cubes were sorted for the LaBr$_3$(Ce) detectors. The region of the coincident start and stop transitions, e.g. 271 keV and 315 keV for the 0_2^+
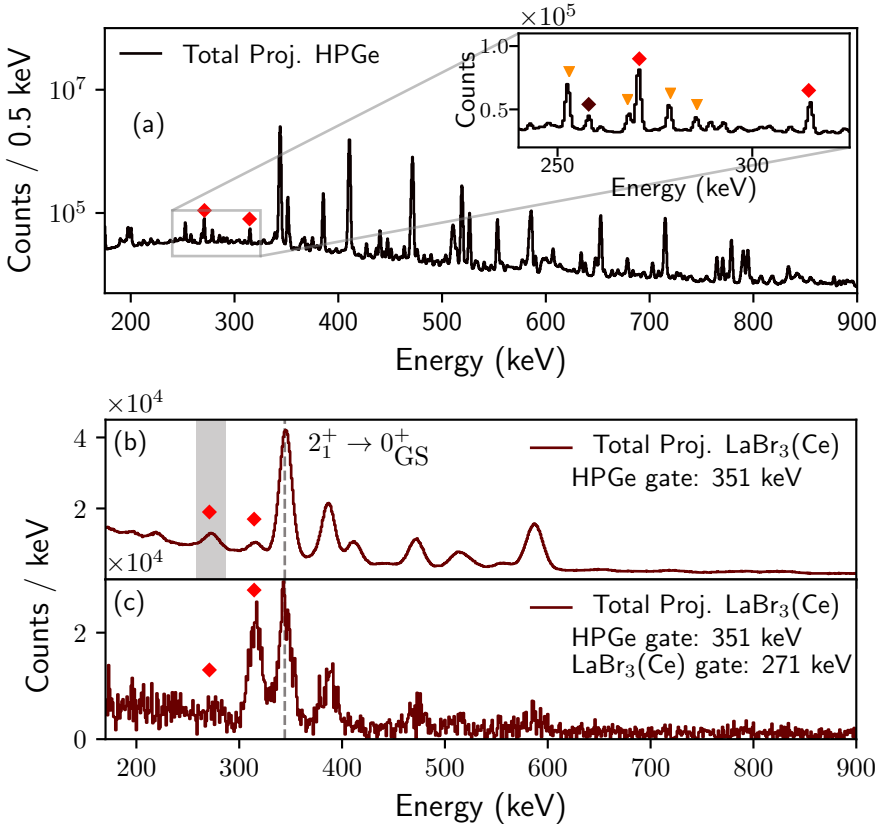
Figure 5.13.: (a) Total projection of the $E_\gamma E_\gamma$ matrix of the HPGe detectors between 170 and 900 keV. The important transitions for the determination of $\tau(0_2^+)$ of ^{152}Gd are marked by ◆. In the inset the transitions from the Au target backing and other FE reaction products are marked (▼). The $8_2^+ \to 7_1^-$ transition of ^{152}Gd is indicated by ◆. (b) HPGe gated total projection of the $E_\gamma E_\gamma$ matrix of the LaBr$_3$(Ce) detectors, (c) in coincidence with the 271 keV transition in the LaBr$_3$(Ce) detectors marked by the shaded area.

state, have been selected in the energy-energy plane of these cubes, resulting in the time-difference spectra for the combination of start and stop transitions. Depending on the effective mean lifetime of the nuclear states between the transitions either the centroid shift method or the slope method were applied. A correction for random coincidences and the Compton background was performed by applying the method described in Section 5.2.7. Some lifetimes of ^{152}Gd and ^{152}Sm, known from literature, in the picosecond and in the nanosecond range were determined to benchmark the applied calibrations and corrections. The results can be found in Table 5.2 alongside their respective literature value. For the 2_1^+ and 4_1^+ states of ^{152}Gd these are in good agreement. However, there is a disagreement between the value for the 2_1^+ state of ^{152}Sm and the adopted value found in the nuclear data sheets [51]. Nevertheless, several experiments in the data sheets are in agreement with the measured value of $\tau(2_1^+) = 2049(10)$ ps, e.g. the average value of $\tau(2_1^+)$ from CoulEx experiments is 2.049(17) ns.

As was already mentioned in the previous section, different energy conditions were imposed on the HPGe detectors, selecting the decay cascade of the second 0^+ state of ^{152}Gd. Hence, two different data sets were evaluated, one with a gate condition in the HPGe detectors on the ground-state transition of the first 2^+ state at 344 keV and a second one with a gate condition in the HPGe detectors above the start and stop signal, i.e. the $4_2^+ \rightarrow 2_2^+$ transition at 351 keV. Figure 5.14 depicts the $E_\gamma E_\gamma$ matrices from the LaBr$_3$(Ce) detectors for these two cases, where dark red circles mark the coincidence area of the $2_2^+ \rightarrow 0_2^+$ transition and the $0_2^+ \rightarrow 2_1^+$ transition. Figure 5.15 (a) and (b) show the resulting time-difference spectra, where yellow data points correspond to the delayed case and the black data points to the anti-delayed one. The centroid difference between the delayed and the anti-delayed time distribution is equivalent to twice the mean lifetime [see Eq. (3.19)]. Both obtained lifetime values agree well with each other and the weighted average of both values was determined to be 96(6) ps or $T_{1/2} = 67(4)$ ps.
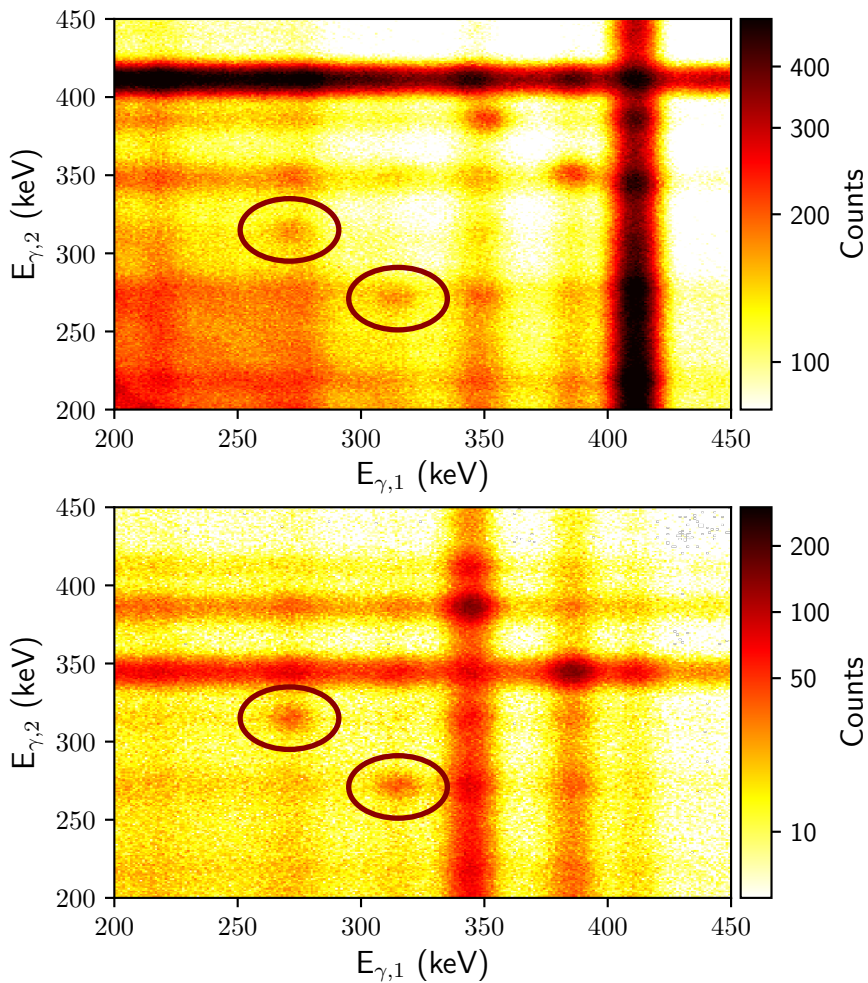
Figure 5.14.: (*top*) $E_\gamma E_\gamma$ matrix of the LaBr$_3$(Ce) detectors, gated on the 344 keV transition in the HPGe detectors. (*bottom*) The same with a gate on the 351 keV transition in the HPGe detectors.
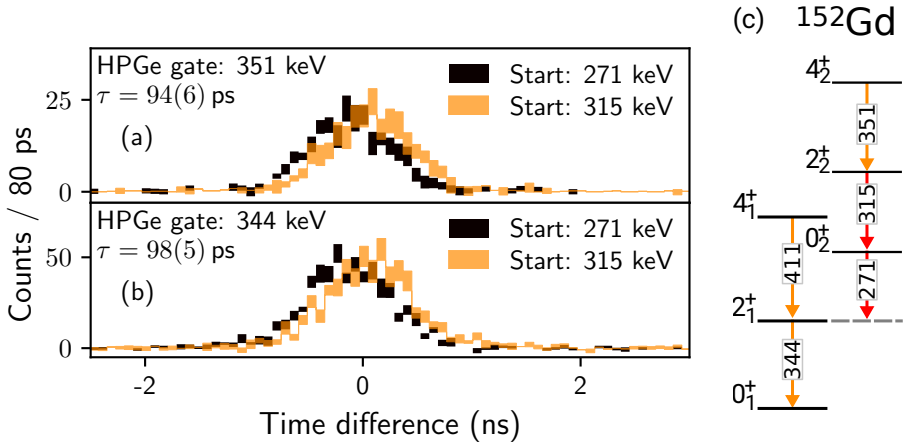
Figure 5.15.: Time-difference spectra with a gate condition in the HPGe detectors on the (a) 351 keV transition and the (b) 344 keV transition. The (anti-)delayed time-distribution is shown in yellow (black) with a start gate on the 315 keV (271 keV) transition. (c) Partial level scheme of ^{152}Gd.

Table 5.2.: List of obtained lifetimes of ^{152}Sm and ^{152}Gd. The reported mean lifetime of the 0_2^+ state is the average of two different data sets, see text. Literature values were taken from the nuclear data sheets [51].

	J_n^π	Gate-1	Gate-2	$\tau = \Delta C/2$ (ps)	$\tau_{\text{lit.}}$ (ps)
^{152}Sm	2_1^+	$4_1^+ \rightarrow 2_1^+$	$4_1^+ \rightarrow 0_{\text{GS}}^+$	2049(10)	2024(16)
^{152}Gd	2_1^+	$4_1^+ \rightarrow 2_1^+$	$2_1^+ \rightarrow 0_{\text{GS}}^+$	51(6)	46(4)
	2_1^+	$2_2^+ \rightarrow 2_1^+$	$2_1^+ \rightarrow 0_{\text{GS}}^+$	46(6)	46(4)
	4_1^+	$6_1^+ \rightarrow 4_1^+$	$4_1^+ \rightarrow 2_1^+$	9(6)	11(1)
	0_2^+	$2_2^+ \rightarrow 0_2^+$	$0_2^+ \rightarrow 2_1^+$	96(6)	53(12)

5.3. TDRIV g-factor measurement of ^{18}O

The following chapter describes the analysis of the ECR-TDRIV measurement of the g factor of the first excited state of ^{18}O. First the data preparation will be explained and then the calibration procedure for the HPGe detectors and in particular the DSSD will be presented.

5.3.1. Data preparation

The data of the Cologne experiment were written to disk in a listmode output format in subrun files, each containing ten minutes of data. The listmode data can be processed using the sorting code Cologne (SOCO) [210]. The sorting code allows, through the use of several configuration files (`*.conf`, see Appendix B.3), the calibration of the data and the extraction of spectra and matrices with different gating conditions, including background subtraction. More details can be found in the SOCO manual [211].

Particle-γ time difference and random background subtraction

In a first step the timestamp offsets of all the individual detectors (HPGe + DSSD) were corrected w.r.t. a reference detector, i.e. here, the first strip of the DSSD, using the `timestamp-shift` command of SOCO. In this way the coincidence window and the windows for the random time background subtraction were determined. These windows are crucial to group the data into events, by grouping coincident hits, within the determined coincidence window, together into events. Figure 5.16 depicts the time difference between one HPGe detector and the first strip of the DSSD. Temporally correlated particles and γ rays create a prompt peak of true coincidences on a plateau of random coincidences of uncorrelated particles and γ rays. Indicated by the shaded areas in Figure 5.16 are the prompt gate and the background gates to the left and right of the prompt peak used in this work. The combined width of both background gates is equal to the width of the prompt gate. Random background subtracted matrices can be created, by subtracting matrices, gated on the background region, from matrices gated on the prompt region.

After determining the width of the prompt and the background region, the event building was performed with the additional requirement, that only events were
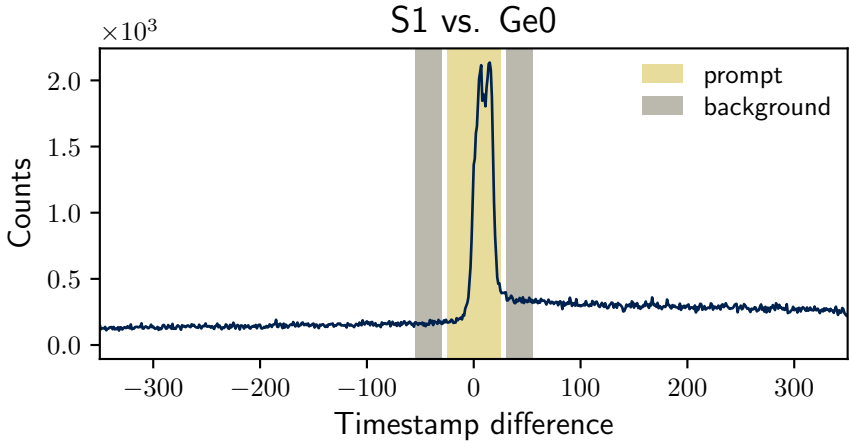
Figure 5.16.: Time difference between hits in the first strip of the DSSD (S1) and the HORUS detector Ge0. The shaded areas mark the gates set on the peak of prompt coincidences and the random background.

taken into account, where one DSSD detector and one HPGe detector registered an event.

The calibration of the utilized detectors with calibration sources is another mandatory step of the analysis. The procedure will be outlined in the following section.

5.3.2. Energy calibration

The HPGe detectors of the HORUS setup were calibrated before the experiment with a ^{226}Ra source and its known γ-ray positions and intensities [212].
Due to changes to the setup between this calibration run and the final setup, the detectors had to be recalibrated. For this purpose in-beam γ-ray transitions stemming from FE reaction products and commonly known background transitions, which could be identified in the energy spectrum, were used. These γ-ray transitions can be found in Table 5.3. The general calibration procedure was already explained in Section 5.2.2 of the FEST experiment and will be omitted here. Figure 5.17 shows the known energy of the calibration transitions over

Table 5.3.: List of γ rays used for energy calibration of the HPGe detectors of the HORUS setup.

In-beam		Background	
E_γ (keV)	Origin	E_γ (keV)	Origin
135.9	^{70}As	511.0	β^+ decay
1039.5	^{70}Ge	608.9	^{214}Bi
1454.3	^{58}Ni	1460.8	^{40}K
360.4	^{67}Ga	1763.0	^{214}Bi
		2614.5	^{208}Bi

their determined position and the final fits to the data using cubic polynomials. In principle, energy drifts can occur in all parts of the electronic setup [213], e.g. due to induced changes of the signal voltage by temperature changes of the experimental environment. Temperature changes result in a variation voltage of
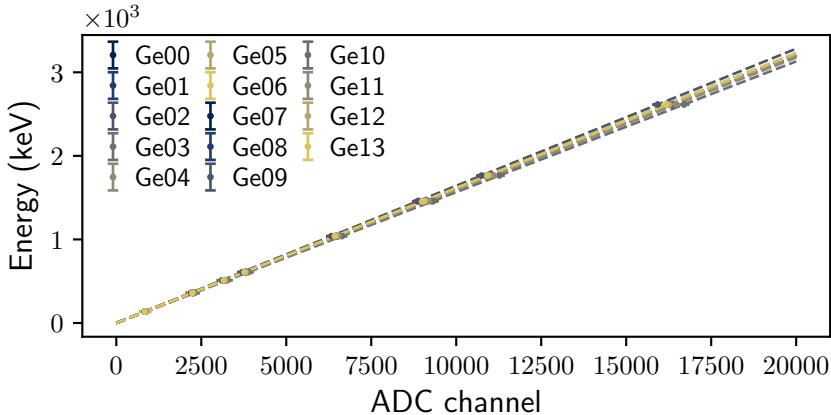
Figure 5.17.: Energy calibration of the HORUS HPGe detectors.

the high voltage supply or they shift the operational point of the pre-amplifiers. For that reason, each detector was corrected for eventual run shifts on a subrun basis.

The calibrated sum spectra of all HORUS detectors, without any particle conditions, for each target-to-degrader distance can be found in Appendix D.4.

DSSD

The next step in the analysis is the calibration of the segments of the DSSD. The reaction products were identified by identifying the corresponding γ-ray transitions in a particle energy-gated HPGe energy spectrum. Then the energy calibration has been performed by comparing the particle energy spectrum with calculated energies of the reaction partners from the reaction kinematics. Figure 5.18 illustrates the reaction kinematics of the employed CoulEx reaction. The kinetic energy (MeV) of the outgoing reaction products, i.e. ^{18}O and ^{28}Ni, over their scattering angle is shown on the left side and on the right side the scattering angle of target-like reaction products as a function of the scattering angle of beam-like reaction products is depicted. The beam attenuation, due to the energy loss in the target($\sim 6\,$MeV) was already considered, resulting in a beam energy of 50 MeV at the center of the target. The shaded area marks the angular coverage of the DSSD. The target-like reaction products, i.e. ^{58}Ni nuclei, are already nearly stopped in the 1.8 mg/cm^2 Ta degrader foil and can therefore be ignored for the further discussion. Moreover, such events would contaminate the data, since it is only possible for target-like particles to scatter in forward direction, when the impact parameter of the reaction is small. For the employed beam energy of 56 MeV (above the Coulomb barrier $V_C = 39.8\,$MeV), this regime is dominated by the nuclear interaction. It has to be ensured, that the investigated particle-γ coincidence events stem from a purely electromagnetic interaction of the beam with the target. Therefore, the maximum scattering angle for so-called "safe" CoulEx has been determined. The minimum distance in a heavy ion collision between the target and the projectile is

$$d(\theta_{\mathrm{CMS}}) = a_0 \left[1 + \frac{1}{\sin \theta_{\mathrm{CMS}}/2} \right], \tag{5.10}$$
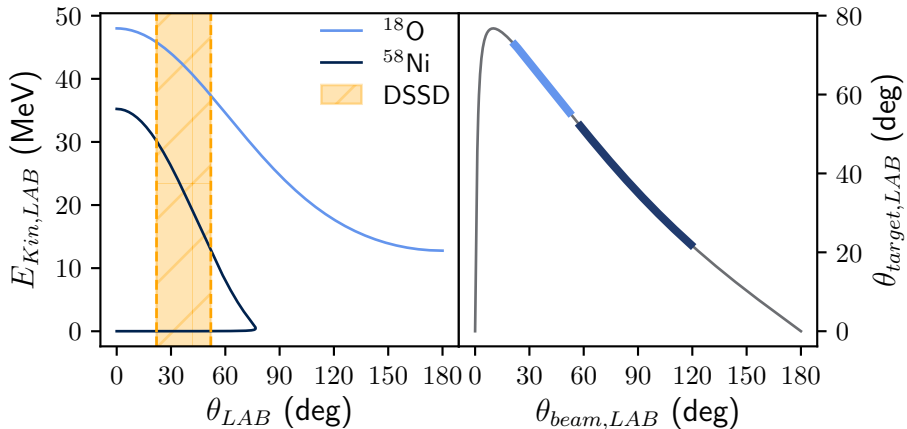
Figure 5.18.: (*left*) Kinetic energy of the reaction products plotted over their scattering angle in the laboratory frame. The shaded area indicates the angular coverage of the DSSD. (*right*) Laboratory scattering angle of ^{58}Ni nuclei shown as a function of beam-like reaction products (^{18}O). The thick lines indicate the angular coverage of the DSSD for beam-like (blue) and target-like (dark blue) reaction products.

where a_o is the distance of closest approach in a head-on collision, which leads together with the Cline criterion for safe CoulEx [178]

$$d(\theta) = 0.72 \frac{A_p + A_t}{A_t} \frac{Z_p Z_t}{E_{\text{LAB}}} \geq R_p + R_t + 5 \, \text{fm}, \tag{5.11}$$

to a condition for the scattering angle. The scattering angle of the oxygen ions in the LAB system has to be smaller than 44.3°. Figure 5.19 shows the minimum distance as a function of the scattering angle in the center-of-mass (CMS) system. The oxygen particles reach the DSSD after passing the degrader foil with an energy between 32 and 40 MeV. The energy loss in the target depends on the scattering angle of the particles, because particles scattered at the angle θ_b
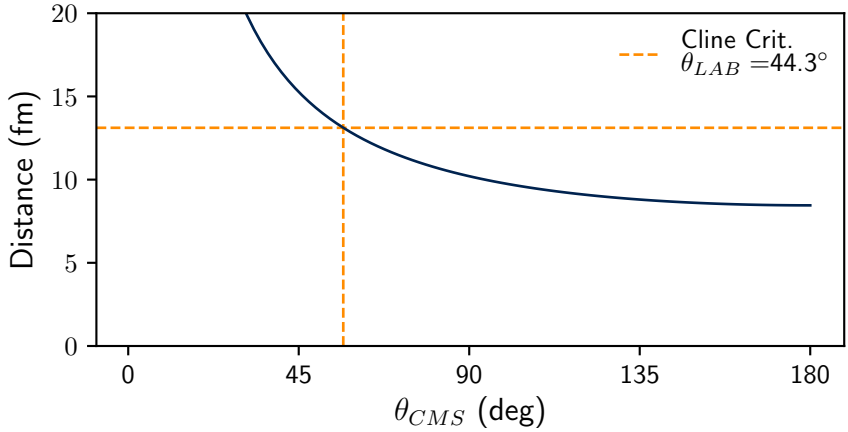
Figure 5.19.: Determination of Safe CoulEx scattering angle in the laboratory system.

have to cross a longer distance in the degrader material. That is

$$\Delta E(\theta_b) = \frac{\Delta E(\theta_b = 0)}{\cos \theta_b},$$ (5.12)

where ΔE is the energy loss in the material and θ_b is the scattering angle of the particle. The detected energy of the DSSD has been calibrated using the information of the reaction kinematics and the energy loss of the oxygen particles in the degrader foil. During the experiment a drastic change of the detected energy spectrum was observed (compare the particle energy spectra in Appendix D.2), due to radiation damage from impinging ionizing particles to the DSSD [214], which results in a decrease of the amount of collected charge and a downward shift of the measured particle energies (see also [215]). For this reason, for each segment of the DSSD the maximum of the energy spectrum between the channels 2000 and 32000 was determined for every subrun, excluding electronic noise in the lower channels, e.g. from the plunger signals. Finally calibration polynomials have been applied to the energy spectra on a subrun-to-subrun basis. Figure 5.20 shows the corrected energy spectra of all rings and strips for the first plunger-degrader distance of 50 µm. The fifth strip $S05$ was removed from
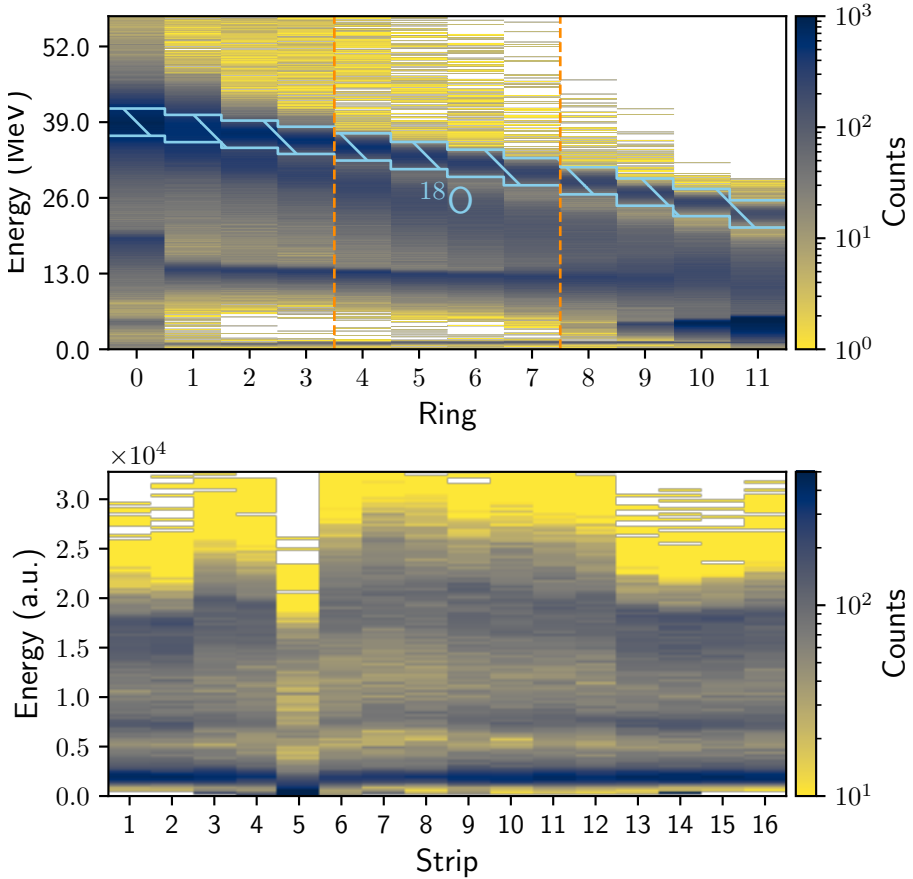
Figure 5.20.: Calibrated energy spectra of the DSSD rings (*top*) and strips (*bottom*) for the target-degrader distance of 50 μm. The oxygen-like particles are framed by the light blue line. The dashed orange line shows the three separated rings of the DSSD.

the further analysis. It was not working correctly during the experiment and detected mainly low energy noise (see Figure 5.20 (*bottom*)).

5.3.3. Relative efficiency of HORUS

After the energy calibration, the relative efficiency of each detector of HORUS was determined with a ^{226}Ra calibration source. The general procedure for the determination of the relative efficiency has already described in Section 5.2.6. The γ-ray transitions of the ^{226}Ra source and their relative intensities were taken from Ref. [216] and are tabulated in Table 5.4. The relative efficiency as a function of energy are depicted in the Appendix D.3.

Table 5.4.: List of γ rays of the ^{226}Ra source used for relative efficiency calibration of the HPGe detectors of the HORUS setup and their transition energy, relative (Rel.) and absolute (Abs.) intensity. Data taken from Ref. [216].

	Transition energy (keV)	Rel. intensity (%)	Abs. intensity (%)
^{222}Rn	186.211(13)	7.815(25)	3.555(11)
^{214}Bi	241.997(3)	15.997(48)	7.268(37)
	295.224(2)	40.48(8)	18.414(36)
	351.932(2)	78.26(16)	35.60(17)
^{214}Po	609.312(7)	100	45.49(19)
	768.356(10)	10.755(36)	4.892(16)
	934.061(12)	6.814(22)	3.10(1)
	1120.287(10)	32.77(7)	14.91(3)
	1238.111(12)	12.819(29)	5.831(13)
	1377.669(12)	8.722(25)	3.968(11)
	1764.494(14)	33.66(10)	15.31(5)
	2204.21(4)	10.80(6)	4.913(23)

5.3.4. Particle-γ coincidences

The reaction products were identified in the particle-gated HPGe energy spectra. Due to the fact, that the beam energy was set above the Coulomb barrier of the (^{18}O,^{58}Ni) reaction, the cross section for FE reactions is high. It is therefore necessary to separate the different reaction channels by setting conditions on the energy and the scattering angle of the outgoing particles in the particle detectors. Figure 5.22 shows the projections of a $E_\gamma E_p$ matrix of the sum energy of all HORUS detectors[1] against the energy of the four inner most rings of the DSSD for the first plunger distance of 50 μm, ensuring safe CoulEx (see previous Section). The three different projections (a-c) on E_γ were obtained by setting three different conditions on the particle energy, as indicated by the inlay energy spectra. FE reaction products (▼) have less energy in comparison to the reaction products of one- or two-nucleon transfer (◆) and CoulEx reaction products (■). Hence, the energy peak corresponding to outgoing oxygen-like particles can be easily identified. The γ-ray transitions from FE reactions are strongly suppressed by selecting the correct energy of the particles in the DSSD [see Figures 5.22 (c) and 5.23 (c)]. Unfortunately, the energy and mass of reaction products stemming from one- and two-nucleon transfer reactions are similar to ^{18}O CoulEx reaction products. Both cannot be disentangled, but the transition energies of the transfer reaction products are below the $2_1^+ \rightarrow 0_{GS}^+$ γ-ray transition of ^{18}O at 1982 keV (see Figure 5.21). Because of the degradation of the DSSD detector during the experiment, the energetically low-lying FE peak in the particle spectrum vanishes for later runs (compare Figure 5.22 and Figure 5.23). The downward shift of the FE energy shifts that peak below the threshold and cannot be seen anymore in the last data. But the particles from the CoulEx reaction and the transfer reactions can still be identified in the particle spectrum.

^{18}O

	E (keV)	τ (ps)
4$^+$	3555	24.8(12)
2$^+$	1982	2.8(7)
0$^+$	0	

1.19(6) W.u.

3.32(9) W.u.

Figure 5.21.: Partial level scheme of ^{18}O.

---

[1]Without Doppler correction.
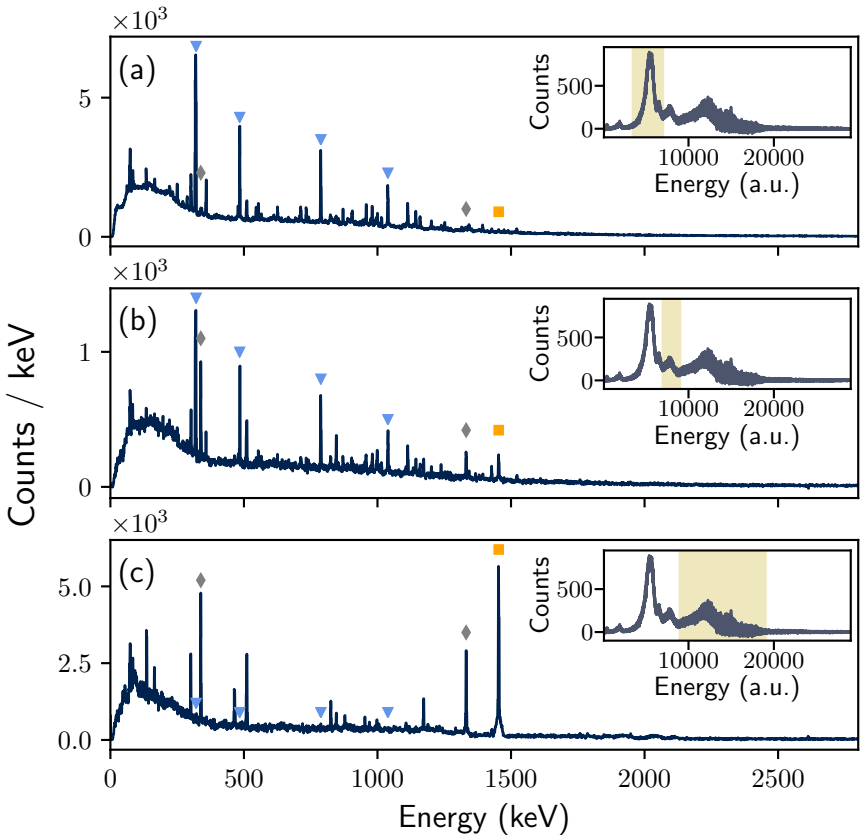
Figure 5.22.: Particle gated energy spectra of HORUS at a plunger distance of 50 μm. The inlay shows the energy spectrum of the four inner most rings of the CD. The shaded area marks the gate for the HPGe projections. Comparing (*top*) and (*middle*) with (*bottom*) the FE reaction channel (▼) can be cleanly disentangled from the CoulEx (■) + xn transfer reactions (◆). The $2^+_1 \rightarrow 0^+_{GS}$ transition of ^{18}O at 1982 keV is Doppler broadened.
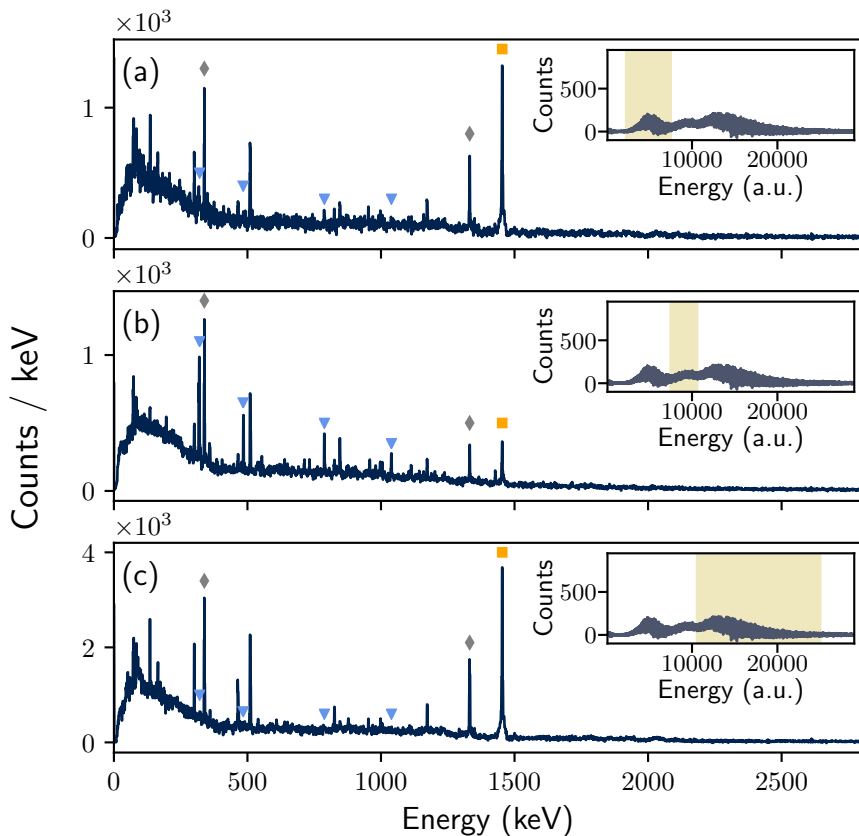
Figure 5.23.: Particle gated energy spectra of HORUS at a plunger distance of 10 μm. The inlay shows the energy spectrum of the four inner most rings of the CD. The shaded area marks the gate for the HPGe projections.

5.3.5. Doppler shift

Since the g factor is measured via the oscillation of the particle-γ angular correlation as a function of time, it is necessary to determine the velocity of the excited ions emerging from the target. Therefore, the energy of the $2_1^+ \rightarrow 0_{GS}^+$ transition of ^{18}O has been determined for different γ-ray scattering angles α. As mentioned before in Section 3.4.1, the detected energy E_γ depends on α^L

$$E_\gamma = E_0 \frac{\sqrt{1-\beta^2}}{1-\beta \cos \alpha^L}. \tag{5.13}$$

Figure 5.24 shows the energy of the $2_1^+ \rightarrow 0_{GS}^+$ transition of ^{18}O as a function of the γ-ray scattering angle α^L. The solid line illustrates the fit to the data via Eq. (5.13) and its uncertainty, resulting in $\beta = 0.072(1)$.
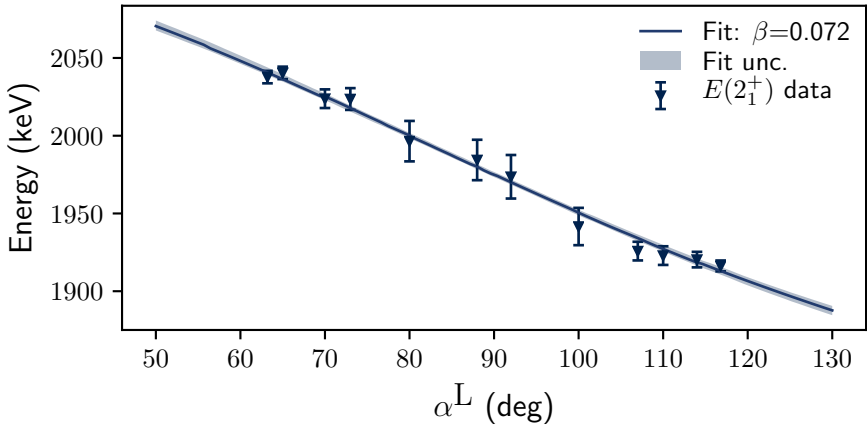
Figure 5.24.: Measured energy of the $2_1^+ \rightarrow 0_{GS}^+$ transition of ^{18}O as a function of scattering of the γ rays α^L, i.e. the angle between the DSSD segment and the HPGe detector, for the longest target-to-degrader distance at 165(1) μm.

5.3.6. Angular correlations and determination of the g factor

The DSSD segments and the HPGe detectors (see Table 4.4 and Table 4.3) can form 672 particle-γ combinations (14 HPGe× 16 DSSD strips× 3 DSSD rings). Ensuring safe CoulEx (see Section 5.3.2), only the 224 time-dependent angular correlations, with the inner ring of the DSSD, were taken into account. This number is further reduced by ignoring combinations that include the faulty DSSD strip $S05$ (see Section 5.3.2), resulting in 210 angular correlation groups. HPGe energy spectra, with a condition on the registered particle energy in the inner ring (see Section 5.3.4), were investigated for all 210 combinations. Thus, for each DSSD segment - HPGe detector combination the peak areas of the $2_1^+ \rightarrow 0_{GS}^+$ transition of ^{18}O were determined for every target-to-degrader distance. Here, the γ-ray from the decay in flight and the further shifted γ-ray after the degrader are not resolved and the peak area of the sum of both has been determined. The partial energy spectra for each detector combination and distance can be found in the Appendix D.4. The peak areas were determined by integrating the energy spectra and subtracting the background content, calculated by a fit to the data close to the peak (on both sides) with a polynomial of second order. Asymmetric uncertainties were assumed for the bin contents of the energy spectra, due to the low count rates, as suggested by the collider detector at Fermilab (CDF) group in Ref. [217] (Uncertainty: $\pm 0.5 + \sqrt{N + 0.25}$). The background subtracted peak areas were corrected for the Lorentz boost, by multiplying the peak areas with the corresponding correction factor [see Eq. (3.47)].

The observed number of counts $N_{p-\gamma}$ for a specific target-to-degrader distance and a HPGe-DSSD detector combination is

$$N_{p-\gamma} = N_0 \epsilon_p \epsilon_\gamma W(\theta_p, \theta_\gamma, \Delta\phi_{p-\gamma}), \qquad (5.14)$$

where N_0 is a normalization constant, dependent on the experimental details, ϵ_γ and ϵ_p are the efficiencies of the HPGe detector and the DSSD segment and $W(\theta_p, \theta_\gamma, \Delta\phi_{p-\gamma})$ is the angular correlation function, Eq. (3.27). As described in Ref. [218], by taking the ratio of the number of counts in one HPGe detector-DSSD segment combination to the sum over all HPGe detector-DSSD detector segments in one ring of the DSSD, the efficiencies of HPGe detectors and, under the assumption that the efficiency in one ring is constant as a function of ϕ, the efficiencies of the particle segments can be factored out, resulting

in

$$\frac{N_{\text{det}}N(\theta_p, \theta_\gamma, \Delta\phi_i)}{\sum_i N(\theta_p, \theta_\gamma, \Delta\phi_i)} = \frac{W(\theta_p, \theta_\gamma, \Delta\phi_i)}{W(\theta_p, \theta_\gamma)}, \tag{5.15}$$

where N_{det} is the number of particle strips in one ring of the DSSD and $W(\theta_p, \theta_\gamma)$ is given by Eq.(3.27) with $q \equiv 0$. Hence, only the attenuation coefficients G_2 and G_4 remain as free parameters of the perturbed angular correlation function. As introduced in Section 3.4.1, the attenuation coefficients G_k depend on the Larmor frequency, Eq. (3.26), and thereby on the g factor [see Eq. (3.37)].

The 210 angular correlation groups were evaluated based on Eq.(3.27), assuming $|g| = 0.28$, and ordered according to the amplitude of the oscillations. Three different groups can be established, 30 combinations should show a larger amplitude of the oscillation (strong), 28 combinations a medium amplitude (medium) and 152 combinations a negligible amplitude (weak). The angular correlation data of Ge00-DSSD combinations as a function of $\Delta\phi$ is shown for all eleven set target-to-degrader distances in Figure 5.25. As mentioned previously, combinations including the strip $S05$ of the DSSD, which registered a lot of noise at low energies (see Figure 5.20) were omitted for the analysis and are marked by □.

The angular correlation (orange region) corresponding to the final result (see below) is included in Figure 5.25. The remaining angular correlations are shown in Appendix D.5. Eq. (5.15) was fitted to the three above established groups for all target-to-degrader distances, using the Monte-Carlo methodology introduced in Section 5.1.1, with the following assumptions

- the velocity of the emerging ions: $\beta = \frac{v}{c} = 0.072(1)$.

- the offset of target-to-degrader distance: $\Delta d = 15(2)\,\mu m$.

- the magnetic field, assuming a hydrogen-like electron configuration: $B_{1s} = 8.574\,\text{kT}$.

- the mean lifetime of the 2_1^+ state, taken from Ref. [80]: $\tau(2_1^+) = 2.80(7)\,\text{ps}$.

- the statistical tensors were taken from the output of the CLX calculation, including the matrix elements for the $0_1^+ \rightarrow 2_1^+$ transition [80] and the quadrupole moment $Q = -0.035(9)\,\text{eb}$ (weighted average taken from values of Ref. [86]) (see the input file in Appendix B.3).
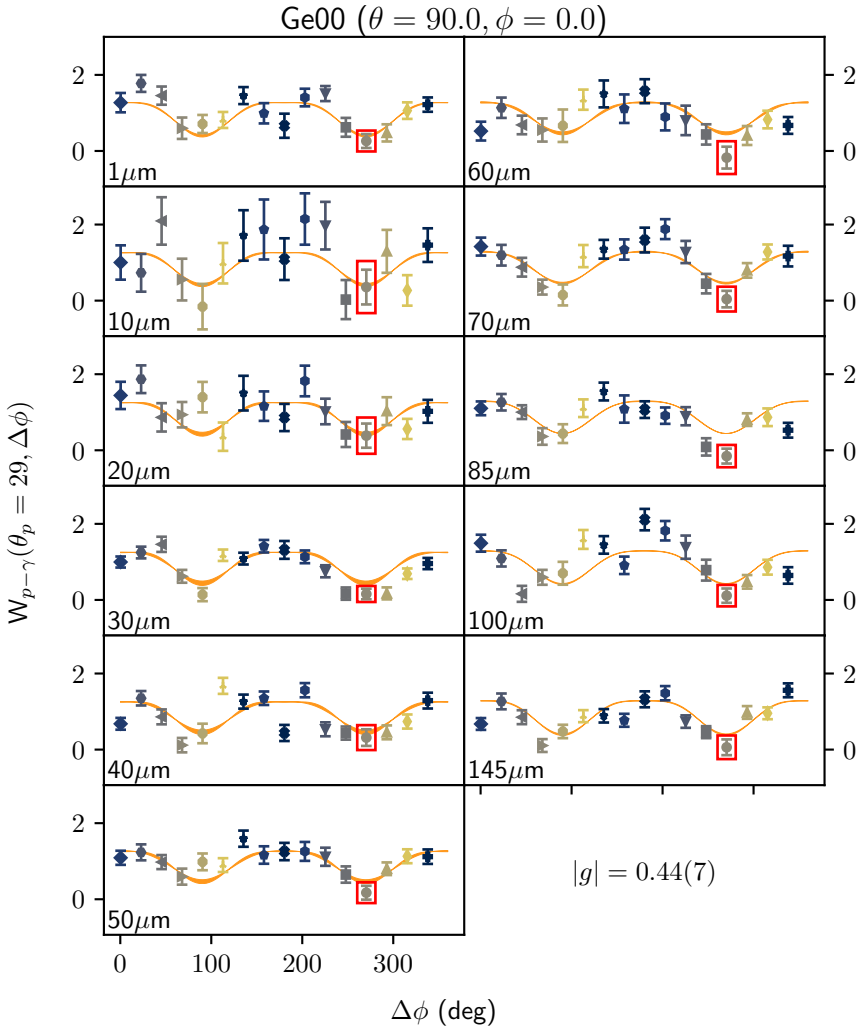
Figure 5.25.: Angular correlation as a function of $\Delta\phi$ of the HPGe detector Ge00 of HORUS in combination with all strips of the inner ring of the DSSD.

The obtained results for the g factor are $|g| = 0.31^{+0.11}_{-0.06}$ in the case of strong oscillations, and there are two possible solutions for the case of medium oscillations $|g| = 0.48^{+0.05}_{-0.03}$ or $|g| = 0.96^{+0.09}_{-0.10}$. The second solution was dismissed, due to the disagreement with the result for the case of strong oscillations. The uncertainties include at this point only the statistical uncertainties from the fit to the data sets. The fit to the group of weak oscillations did not converge, due to the large uncertainties of the data points and only weak expected oscillations. Further systematic uncertainties stem from the finite opening angle of the DSSD segments ($\theta_p = 22° - 35°$), the uncertainty in the target-to-degrader distance of $\pm 2\,\mu$m and the uncertainty in the lifetime of the 2^+_1 state, resulting in:

$$|g(2^+_1)| = \begin{cases} 0.31^{+0.16}_{-0.09}, & \text{(strong)}, \\ 0.48^{+0.08}_{-0.07}, & \text{(medium)}. \end{cases} \tag{5.16}$$

A simultaneous fit to both data sets (strong and medium) results in a value of

$$|g(2^+_1)| = 0.44^{+0.08}_{-0.07}. \tag{5.17}$$

The two groups of medium and strong oscillations were ordered according to whether the γ-ray intensities should initially increase ($W_\uparrow$) or decrease ($W_\downarrow$). The weighted average of both resulting groups was calculated and a ratio of the group initially increasing and the group initially decreasing was formed $R = \overline{W}_\uparrow / \overline{W}_\downarrow$. This ratio is depicted in Figure 5.26 as a function of the distance for the medium oscillation data set (a) and the final fit to both data sets (strong and medium) (b). Here, the ratios of each two distances (apart from the last distance, which stands alone) were combined and the weighted average is presented. Additionally, the ratio corresponding to the determined g factor is shown as a dashed line. The uncertainty bands correspond to the angular correlation with a g factor in the above stated limits, Eqs. (5.16) and (5.17).
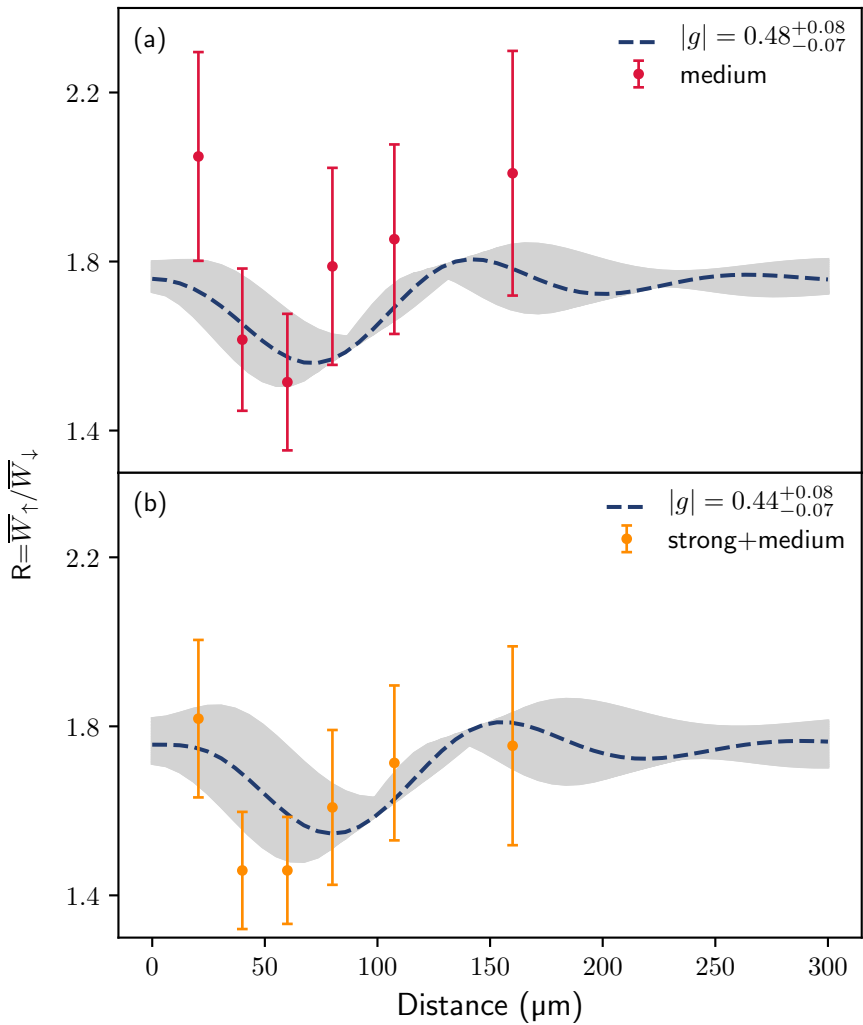
Figure 5.26.: Ratio $R = \overline{W}_\uparrow / \overline{W}_\downarrow$ as a function of the distance. The g factor is determined by the frequency of the oscillation.

6. Discussion

The first part of this chapter will discuss the implications of the determined mean lifetimes of the Hf isotopes. Next the case of ^{152}Gd will be examined and the last part addresses the results from the g factor measurement of the first excited state of ^{18}O.

6.1. Evolution of $E2$ strengths of ^{174,176,178,180}Hf.

6.1.1. Quadrupole collectivity around mid-shell

The recently remeasured lifetimes from Refs.[36, 40] and this work reveal a new picture. The determined $B(E2)$ values do not show the saturation around mid-shell anymore, but a maximum shifted towards a lower neutron number, as can be seen in Figure 6.1 (a). Here, the $B(E2)$ transition strength from the 2_1^+ state to the GS of the Er (◆), Yb (✖), Hf (■) and W (▼) isotopes is shown as a function of the P parameter[221]

$$P \equiv \frac{N_\pi N_\nu}{N_\pi + N_\nu}, \tag{6.1}$$

where $N_{\pi,\nu}$ are the number of valence protons(π) and valence neutrons (ν) or proton and neutron holes with respect to major shell closures, e.g. $N = 82$ and $N = 126$ or $Z = 50$ and $Z = 82$. P can be seen as the average number of proton-neutron interactions per valence nucleon [20]. Nuclei with $P < 4$ show spherical characteristics, whereas nuclei with $P > 5$ are deformed. The turning point of each isotopic chain in Figure 6.1 marks mid-shell, since the number of valence particles (holes) maximizes at mid-shell. As can be seen, the maximum of the $E2$ strengths does not lie at the turning point, but on the upper branch (lower neutron number) of the depicted isotopic chains. The pre-mid-shell data, coming from lower P, of the different isotopic chains follow the same trend and
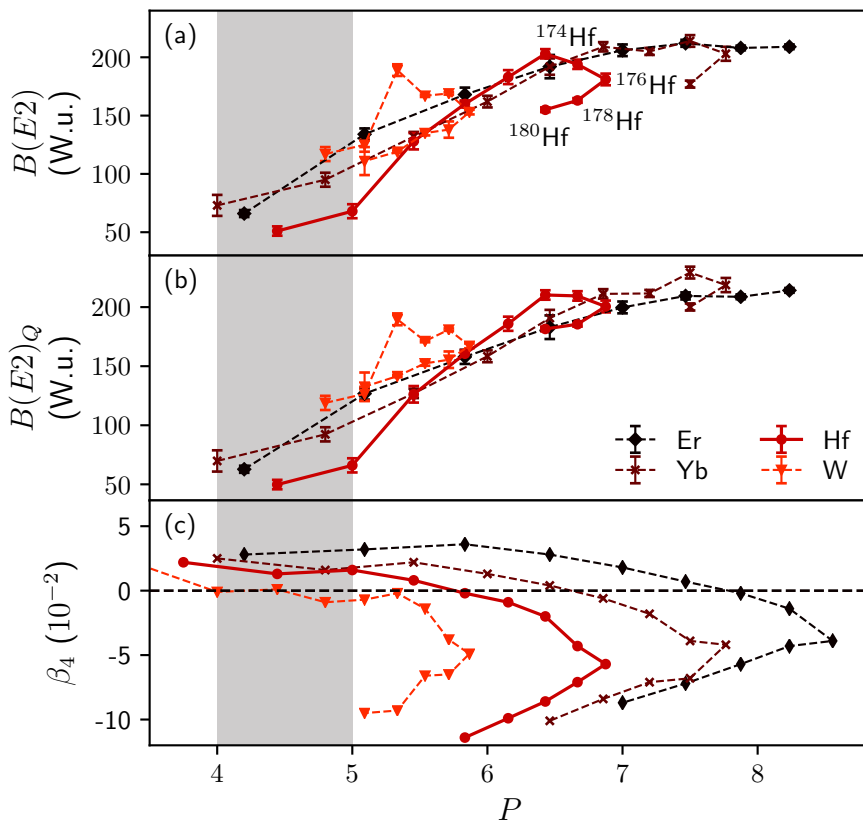
Figure 6.1.: (a) $B(E2; 2_1^+ \rightarrow 0_{\text{GS}}^+)$ transitions strengths as a function of $P = N_\pi N_\nu/(N_\pi + N_\nu)$ of the Er, Yb, Hf and W isotopic chains. Data taken from [21–34, 40] and this work. (b) "Quadrupole" $B(E2)$ values, $B(E2)_Q$, vs. P obtained by removing the β_4 hexadecapole deformations as described in [219]. β_2 values are taken from [41] and the β_4 values from [220]. (c) β_4 hexadecapole deformations as a function of P. Data taken from [220].

the collectivity, i.e. the $B(E2)$ strength, increases with P. But the $E2$ strengths drop unexpectedly before mid-shell for the W, Hf and Y isotopes. In the case of Er the available data does not extend beyond mid-shell. Furthermore, after the infliction point, the $E2$ strengths are significantly lower and the pre-mid-shell maximum of the $B(E2)$ strengths gets more pronounced for higher proton numbers. Zamfir et al. [219] attributed the different trends of the $B(E2)$ values before and after mid-shell to the influence of the hexadecapole deformation parameter β_4 on the quadrupole moment Q. The quadrupole moment can be expanded $Q \propto \beta_2(1 + 0.36\beta_2 + 0.97\beta_4 + ...)$. The $B(E2)$ strength is proportional to Q^2. A "pure quadrupole" $B(E2)$ value [219] can be defined by removing the influence of β_4

$$B(E2; 2_1^+ \rightarrow 0_{\text{GS}}^+)_Q = B(E2; 2_1^+ \rightarrow 0_{\text{GS}}^+)\left(\frac{Q(\beta_4 = 0)}{Q(\beta_4 \neq 0)}\right)^2. \qquad (6.2)$$

These values are depicted in Figure 6.1 (b). Due to the applied correction the $B(E2)$ strengths of nuclei with negative values of β_4 is increased in comparison to nuclei with positive values of β_4. The deformation parameters for the calculation of $B(E2)_Q$ have been taken from [41] or if not experimentally available from [220]. Figure 6.1 (c) shows the trend of β_4 as a function of P. The values are near-constant until they turn negative around $N = 98$. Consequently, the early drop of the $E2$ strength is reduced. Even though experimental data on hexadecapole deformation is scarce, there are numerous indications in the high-N, high-Z region of this major shell (e.g. Ref. [222]). But to date no microscopic explanation for the resulting drop in $B(E2)$ strength has been provided.

Another observable discussed in conjunction with the evolution of collectivity is the double difference of binding energies, introduced in Ref. [225], i.e. the average proton-neutron interaction of the last proton pair with the last neutron pair [226]

$$\delta V_{pn}(Z, N) = \frac{1}{4}\{[BE(Z, N) - BE(Z, N - 2)] \\ - [BE(Z - 2, N) - BE(Z - 2, N - 2)]\}, \qquad (6.3)$$

where $BE(Z, N)$ is the binding energy of a nucleus with Z protons and N neutrons. The double difference δV_{pn} depends, in general [227], on the occupied neutron and proton orbitals. It is large where the overlap of the proton and neutron orbitals is large. The δV_{pn} values of the rare earth isotopes are depicted in
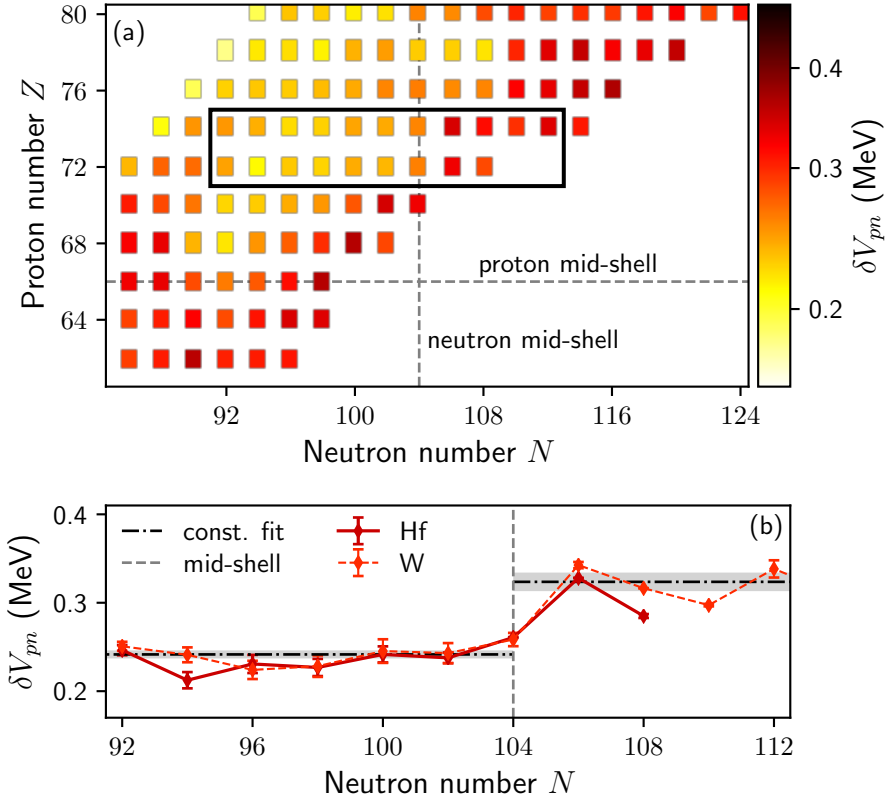
Figure 6.2.: (a) Depicted is the double difference δV_{pn} [42] in a N-Z chart. $N=104$ is marked by the dotted-dashed line. The area marked in black is shown in (b). The dotted-dashed lines are fits with a constant to the Hf data before and after mid-shell, illustrating the sudden increase of δV_{pn} at $N=104$ and the constant behavior before and after $N=104$. The vertical grey dashed line marks the neutron mid-shell at $N=104$. Binding energies taken from Refs. [223, 224].

a N-Z chart in Figure 6.2 (a), with the binding energies taken from Refs. [223, 224]. High values of δV_{pn} are obtained in the area below the neutron and proton mid-shell and in the area above the neutron and proton mid-shell. The values in the upper left quadrant, i.e. below neutron mid-shell and above proton mid-shell, are in comparison smaller. Figure 6.2 (b) shows the projection, marked by the black square in (a). δV_{pn} is nearly constant for the W and Hf isotopes, but jumps by $\sim 100\,\text{keV}$ at $N = 104$. If neutrons already scatter early into the corresponding orbitals, the abrupt increase of δV_{pn} may already be reflected at $N < 104$.

The measured $B(E2)$ values of the yrast bands of the Hf isotopes can be further investigated by looking at the ratio $B_{4/2} = B(E2; 4_1^+ \rightarrow 2_1^+)/B(E2; 2_1^+ \rightarrow 0_{GS}^+)$. The resulting values from this work and the adopted values from neighbouring isotopes are shown in Figure 6.3 (b). The determined values agree overall with the predictions of a rigid rotor $B_{4/2,\text{rot}} = 1.44$, even though the uncertainty for $B_{4/2}$ of ^{178}Hf is large and prevents a definite assignment. However, as shown in Figure 6.3 (a), the $B(E2)$ values of higher lying states deviate from the rotational limit. The $B(E2; 6_1^+ \rightarrow 4_1^+)$ transition strength of ^{174}Hf is unexpectedly lower than the corresponding $B(E2; 4_1^+ \rightarrow 2_1^+)$ value and the same trend cannot be excluded for ^{176}Hf within the experimental uncertainty. Unfortunately, data on higher lying transitions of the yrast band are not available. But similar results were obtained in Ref. [40] for the Hf isotopes and in Ref. [228] for ^{162}Yb. These $B(E2)$ values also indicate a change in rotational structure past $N = 100$, in agreement with the previous arguments on the hexadecapole deformation and the δV_{pn}.

6.1.2. $K^\pi = 2^-$ band of ^{176}Hf

Apart from the evolution of the $E2$ transition strength, the observation of the low-lying negative parity states 2_1^- and 3_1^- allowed the investigation of the $K = 2^-$ rotational band of ^{176}Hf (see Refs. [205, 206]). The transition connecting these two states has not been observed yet and it was unfortunately also not observed in this work. The expected energy of 65 keV may be obscured by x-ray transitions and is in competition with the decay via internal conversion[1]. The $E1$ decay transitions to the yrast band are, according to the Alaga rules [229],

---

[1] The internal conversion coefficient is 19.8(16) for a $E2$ transition at 65 keV and increases rapidly with the multipolarity.
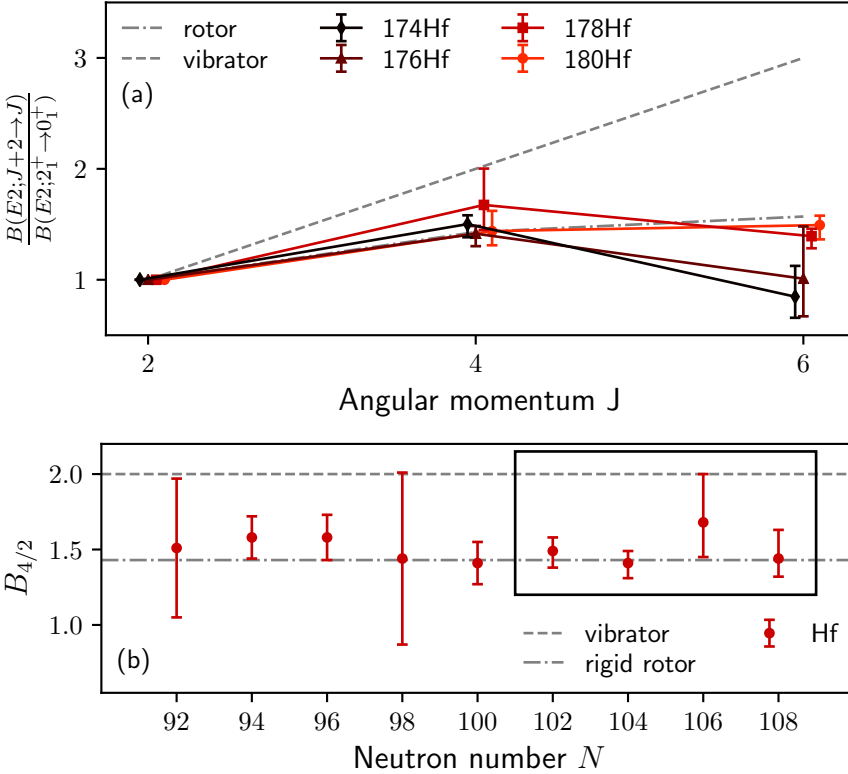
Figure 6.3.: (a) $B(E2; J \rightarrow J - 2)$ transition strengths normalized to the $B(E2; 2_1^+ \rightarrow 0_{GS}^+)$ transition strength as a function of the nuclear spin J of ^{174,176,178,180}Hf. The isotopes are slightly shifted for a better visibility. (b) Ratio $B_{4/2}$ of the $B(E2)$ transition strengths $B(E2; 4_1^+ \rightarrow 2_1^+)$ and $B(E2; 2_1^+ \rightarrow 0_{GS}^+)$. Shown in the black box are the averaged values from this work and [32, 33, 40]. Literature data taken from [25–29]. The dotted-dashed line represents the value obtained in the rigid rotor limit and the dashed line in the vibrator limit.

first forbidden transitions with $\Delta K = 2$. In Ref. [205] a large admixture of $M2$ and $E3$ strength has been determined for the decay transitions of the 2_1^- state by measuring conversion electrons. The decay transitions of the 3_1^- state have been confirmed to be of $E1$ character.

Under the assumption that the transition width of the $3_1^- \to 2_1^-$ transition is negligible, upper limits for the $E1$ transition strengths of the decay transitions $3_1^- \to 4_1^+$ and $3_1^- \to 2_1^+$ have been determined, using the extracted mean life-time of $\tau(3_1^-) = 25(12)\,\text{ps}$ (see Section 5.2.7). These transitions are suppressed by three orders of magnitude in comparison to other $E1$ strength of ^{176}Hf. An overview of the $E1$ strength distribution of ^{176}Hf is given in Ref. [230].

The extracted mean lifetime of the 2_1^- state is slightly below the adopted literature value [31], but in good agreement with other measurements, e.g. Ref. [207]. From the new weighted average value of $\tau(2_1^-)$ (see Table 5.1) the transition strengths of its decay $2_1^- \to 2_1^+$ can be determined with the known multipole mixing ratios from [207] and the branching ratios from [31]. The transition strengths are given in Table 6.1.

Table 6.1.: The $B(E\lambda)$ strengths of ^{176}Hf were determined with the known branching ratios taken from Ref. [31], the conversion coefficients taken from Ref. [209] and the multipole mixing ratios of the $2_1^- \to 2_1^+$ transition $\delta(M2/E1) = 0.129(35)$ and $\delta(E3/E1) = 0.28(7)$ taken from Ref. [207].

Transition	I_γ (%)	$\sigma\lambda$	$B(\sigma\lambda)$ in $\mu_N^2 \text{b}^{2\lambda-2}/e^2\text{b}^\lambda$	$B(\sigma\lambda)$ in W.u.
$2_1^- \to 2_1^+$	100(8)	$E1$	$4(2) \times 10^{-10}$	$2(1) \times 10^{-8}$
		$M2$	$10(3) \times 10^{-3}$	$2(1) \times 10^{-2}$
		$E3$	$6(2) \times 10^{-2}$	30(12)
$3_1^- \to 4_1^+$	47(4)	$E1$	$8^{+6}_{-3} \times 10^{-8}$	$4^{+3}_{-2} \times 10^{-6}$
$3_1^- \to 2_1^+$	100(8)	$E1$	$9^{+9}_{-3} \times 10^{-8}$	$4^{+5}_{-1} \times 10^{-6}$

6.2. $\tau(0_2^+)$ of ^{152}Gd - possible new signatures for a QPT

The determined mean lifetime $\tau(0_2^+) = 96(6)$ ps of ^{152}Gd is nearly twice the previous stated lifetime from Ref. [68] of 53(12) ps. The quoted uncertainty is a combination of the statistical uncertainty in determining the centroids of the time distributions and the uncertainty of the energy-dependent time-walk calibration. As was shown in Section 3.2, the mean lifetime of an excited state τ is proportional to the inverse of the reduced transition strength $B(\sigma\lambda)$ [see Eq. (3.11)]. Thus, after determining the new value for the lifetime $\tau(0_2^+)$ it is possible to calculate the $E2$ transition strength (with the conversion coefficient $\alpha = 0.0826(12)$ taken from Ref. [209])

$$B(E2; 0_2^+ \to 2_1^+) = 0.528^{+0.036}_{-0.029}\, e^2\, \mathrm{b}^2,$$
$$= 115^{+6}_{-8}\, \mathrm{W.u.} \tag{6.4}$$

In addition, a new value for the $\rho^2(E0)$ transition strength can be determined using the dimensionless ratio of the $E0$ and $E2$ transition strengths defined by Rasmussen [231]

$$X(E0/E2) \equiv \frac{B(E0)}{B(E2)} = \frac{\rho^2(E0)e^2R^4}{B(E2)}, \tag{6.5}$$

where R is the nuclear radius ($\sim 1.2 \times A^{1/3}$). With the measured value of the ratio $X(E0/E2) = 0.0122(5)$ given in Ref. [232] and the newly determined $B(E2; 0_2^+ \to 2_1^+)$ value one obtains

$$\rho^2(E0) = 37.9^{+3.2}_{-2.5} \times 10^{-3}. \tag{6.6}$$

It has been shown in the framework of the IBM in Ref. [65], that the $E0$ transition strength $\rho^2(E0)$ sharply increases and maximizes at the critical point of the spherical to quadrupole deformed shape transition. Bonnet et al. showed in Ref. [66], using the CBS model, that $\rho^2(E0)$ decreases from the critical point toward the rigid rotor limit. Figure 6.4 (b) presents the experimental data of $\rho^2(E0)$ of the even-even Nd (▼), Sm (■) and Gd (●) isotopic chains around $N = 90$ as a function of the P parameter. The data included in Figure 6.4 is tabulated in Table 6.2. The abbreviations $B(E2)_i = B(E2; 0_i^+ \to 2_1^+)$, $\rho^2(E0) =$
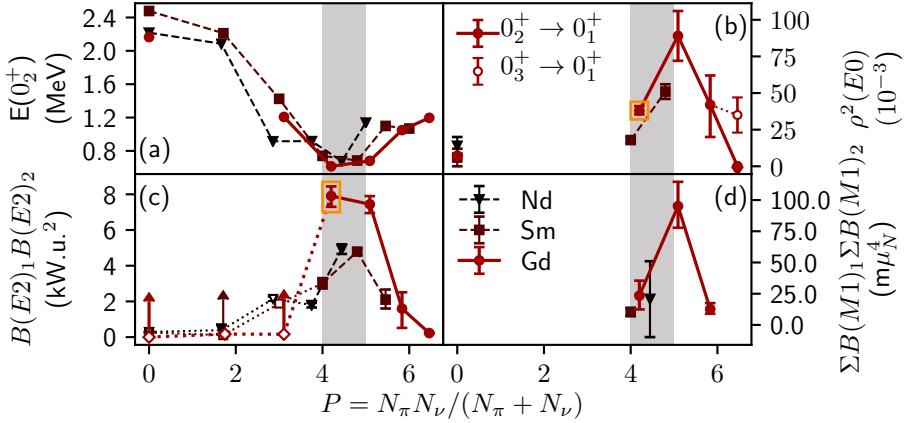
Figure 6.4.: Evolution of (a) the energy of the first excited 0^+ state, (b) the $E0$ transition strength $\rho^2(E0; 0_2^+ \to 0_{GS}^+)$, (c) the product of $B(E2)_1 \times B(E2)_2$, and (d) the product of summed $M1$ strength $\Sigma B(M1)_1 \times \Sigma B(M1)_2$ of the Nd ($\blacktriangledown$), Sm ($\blacksquare$) and Gd ($\bullet$) isotopes around $N = 90$ as a function of P. Marked by orange boxes are the obtained values from this work. The shaded grey area marks the area of transitional nuclei between spherical nuclei ($P < 4$) and deformed nuclei ($P > 5$). Data taken from Refs. [21–25, 41, 46–52, 232–235].

$\rho^2(E0; 0_2^+ \to 0_{GS}^+)$ and $B(M1)_i = \Sigma B(M1; 0_i^+ \to 1_{sc}^+)$ have been used. Even though experimental data are sparse, they reveal the expected trend of $\rho^2(E0)$. The experimental values of $\rho^2(E0)$ are small at the magic shell closure $N = 82$ ($P = 0$) and increase in the transitional region, maximize near $N = 90$ (^{152}Sm and ^{154}Gd), before they decrease towards deformed nuclei (Gd). In addition to $\rho^2(E0; 0_2^+ \to 0_{GS}^+)$, the $E0$ strength connecting the 0_3^+ state to the 0_{GS}^+ is depicted for ^{158}Gd, supporting the statement of a sizeable $E0$ strength in deformed nuclei. The obtained value from this work supports the hypothesis of $\rho^2(E0)$ as a signature for a QPT. Including the new value, the maximum of the $\rho^2(E0)$ strength is more pronounced and the uncertainty has been considerably reduced in comparison to the old value of $\rho^2(E0) = 6.6(14) \times 10^{-3}$. Furthermore, the

$E0$ strength of ^{152}Gd remains sizeable, supporting the argument that ^{152}Gd is located at the QPT. As mentioned in the CBS section (Section 2.1.2), the $E0$ strength can be related to a product of $B(E2)$ strengths

$$\rho^2(E0) = C \times B(E2; 0_1^+ \rightarrow 2_1^+) \times B(E2; 0_2^+ \rightarrow 2_1^+), \qquad (6.7)$$

$$\text{with } C = \left(\frac{3Z}{4\pi}\right)^2 \frac{1}{(eR^2)^4}, \qquad (6.8)$$

where Z is the proton number, and R the nuclear radius. Figure 6.4 (c) shows the product $B(E2)_1 \times B(E2)_2$ as a function of P. The position of the maximum for the product of $B(E2)$ values is shifted to a lower P value, as can be seen from the known Nd and Sm values. The position does not exactly coincide with the location of the maximum of the $E0$ strength for the Gd isotopes. The reason may be related to the application of the Q-phonon scheme in the derivation of Eq.(6.7).

The peak of the $B(E2)$ product at the QPT critical point can be qualitatively understood in the context of the geometrical Davydov-Chaban model [238] and the vibrational model. Taking the intrinsic frame expression for the $E2$-transition operator

$$Q_{2\mu} = Q_0 D_{\mu 0}^2 \beta, \qquad (6.9)$$

results in

$$B(E2; 0_1^+ \rightarrow 2_1^+) \times B(E2; 0_2^+ \rightarrow 2_1^+) = Q_0^4 |\langle 0_1^+ | \beta^2 | 0_2^+ \rangle|^2. \qquad (6.10)$$

By using wave functions obtained from the Davydov-Chaban and vibrator models and typical values for the deformation β and the fluctuation of the deformation, numerical estimates can be calculated for the three cases of spherical, transitional and deformed nuclei (see Appendix A.3 for more details) and are presented in Table 6.3.

An estimation of the $B(E2)$ product for vibrational nuclei, such as ^{150}Gd and ^{148}Sm, can be calculated, by taking the relation $B(E2; 0_2^+ \rightarrow 2_1^+) = 2 \cdot B(E2; 2_1^+ \rightarrow 0_1^+)$ from vibrator models. Hence, a reasonable upper limit is (the approximated values are marked by ♠ in Table 6.2)

$$B(E2)_1 B(E2)_2 = 2(B(E2)_1)^2. \qquad (6.11)$$

Table 6.2.: $B(E2)$, $\rho^2(E0)$ and $B(M1)$ observables of the Nd, Sm and Gd isotopes around $N = 90$.

	P	$E(0_2^+)$ (keV) $^◐$	$B(E2)_1$ (W.u.) $^▰$	$B(E2)_2$ (W.u.) $^◐$	$B(E2)_1 B(E2)_2$ (kW.u.^{2}) $^◆$	$\rho_i^2(E0)$ (10^{-3}) $^◆$	$B(M1)_1 B(M1)_2$ mμ_n^4 $^♥$
^{146}Gd	0.00	2164.7	≥ 0.6	—	$\geq 0.001^▲$	7.2(9)	—
^{148}Gd	1.75	—	$9.8^{+4.5}_{-2.4}$	—	$0.17^{+0.14}_{-0.11}{}^▲$	—	—
^{150}Gd	3.11	1207.1	$\geq 9^▲$	—	$\geq 0.162^▲$	—	—
^{152}Gd	4.20	615.4	68.7(27)	$115^{+6}_{-8}{}^★$	$7.9^{+0.6}_{-0.6}{}^★$	$37.9^{+3.2}_{-2.5}{}^★$	25^{+11}_{-12}
^{154}Gd	5.09	680.7	158.0(7)	47(3)	$7.5^{+0.4}_{-0.5}$	89(17)	91^{+23}_{-12}
^{156}Gd	5.83	1049.5	188.3(4)	8^{+4}_{-7}	$1.53^{+0.99}_{-1.00}$	42(21)	13^{+4}_{-5}
^{158}Gd	6.46	1196.2	200.8(43)	$1.17^{+0.18}_{-0.13}$	$0.23^{+0.4}_{-0.2}$	≤ 0.08	—
^{144}Sm	0.00	2477.7	11.6(9)	—	$0.26(4)^▲$	6(6)	—
^{146}Sm	1.71	2211	$10.5^{+0}_{-3.1}$	—	$\geq 0.11^▲$	—	—
^{148}Sm	3.00	1424.5	30.7(15)	—	$1.88(18)^▲$	—	—
^{150}Sm	4.00	740.5	56.9(11)	53(5)	3.01(29)	18(2)	$10(3)^{▰▰}$
^{152}Sm	4.80	684.8	143.67(8)	33.3(12)	$4.80^{+0.16}_{-0.18}$	51(5)	—
^{154}Sm	5.45	1099.3	177.2(18)	12(3)	$2.1^{+0.6}_{-0.5}$	—	—
^{156}Sm	6.00	1068	≤ 289	—	—	—	—
^{142}Nd	0.00	2217.5	12.05(58)	—	$0.29(3)^▲$	14(6)	—
^{144}Nd	1.67	2084.7	22.48(67)	19(12)	$0.39^{+0.30}_{-0.24}$	—	—
^{146}Nd	2.86	915.4	32.76(96)	—	$1.88(18)^▲$	—	—
^{148}Nd	3.75	916.9	57.5(13)	31.2(22)	$1.80^{+0.12}_{-0.14}$	—	—
^{150}Nd	4.44	675.9	114.4(13)	43.1(23)	$4.94^{+0.26}_{-0.28}$	—	$21^{+30}_{-31}{}^{▰▰}$
^{152}Nd	5.00	1139	170.2(91)	—	—	—	—

$^◐$ Data taken from Refs. [21–24, 48–52]. $^{▰▰}$ Data taken from Ref. [41]. $^◆$ Data taken from Refs. [232, 236]. $^♥$ Data taken from Ref. [233]. $^▲$ Upper limit from Ref. [53]. $^◐$ Approximation using Eq. (6.11). $^★$ From this work. $^{▰▰}$ $B(M1)_1$ taken from Ref. [237], $B(M1)_2$ taken from Refs. [234, 235].

Table 6.3.: Numerical estimates for $B(E2)_1 \times B(E2)_2$.

	$B(E2)_1 \times B(E2)_2$
spherical nuclei:	$1.0 \times 10^{-3} Q_0^4$
transitional nuclei:	$12.8 \times 10^{-3} Q_0^4$
deformed nuclei:	$0.2 \times 10^{-3} Q_0^4$

Thereby, it can be shown that for vibrational nuclei, where to date only the $B(E2; 0_1^+ \rightarrow 2_1^+)$ transition strength is known, the product of $B(E2)$ strengths is small. Furthermore, there is indeed a maximum at or between $N = 88$ and $N = 90$.

In addition, Figure 6.4 (d) presents another observable, which can be related to the product of $B(E2)$ strengths in the IBM, the product

$$B(M1; 0_1^+ \rightarrow 1_{sc}^+)B(M1; 0_2^+ \rightarrow 1_{sc}^+) =$$

$$\left(\frac{10.6}{Z^2 \left(1 - \frac{E(0_2^+)}{2E(1_{sc}^+)} \right)} \right) B(E2; 0_1^+ \rightarrow 2_1^+)B(E2; 0_2^+ \rightarrow 2_1^+), \qquad (6.12)$$

where 1_{sc}^+ is the scissors mode (see Ref. [239] for more information on the scissors mode). The full derivation of Eq. (6.12) is shown in Appendix A.1. J. Beller has shown in his work [233][2], that the product of $M1$ strength also maximizes at the critical point of a QPT in the case of the gadolinium isotopes ^{152,154,156}Gd. For the neighbouring elements, there are to date only two further values known on the decay of the scissors mode to the 0_2^+ state available from Ref. [234, 235] and thereby the product of summed $M1$ strength. These two values for ^{150}Sm and ^{150}Nd agree within their uncertainties with the above statements. The value of ^{150}Sm (below the QPT at $N = 88$) is small and the value of ^{150}Nd at the critical point is larger, even though its uncertainty does not allow a final conclusion, but data on their isotopic neighbours could clarify the picture.

---

[2]Therein, for the first time $\Sigma B(M1; 1_{sc.}^+ \rightarrow 0_2^+)$ has been determined for nuclei across the QPT.

6.3. g-factor measurement of ^{18}O

In the nuclear chart the nucleus ^{18}O is located just two neutrons away from the doubly magic nucleus ^{16}O. Therefore, its excited states are expected to be dominated by neutron excitations. The g factor of the 2_1^+ state of ^{18}O has previously been determined by Goldring et al., $0.20 \leq |g| \leq 0.36$ [240] (time-integral RIV), Speidel et al. $|g| = 0.35(4)$ [241] and more precisely by Asher et al. [242]. The latter obtained $|g| = 0.287(15)$, with the traditional TDRIV method, i.e. the current adopted value in the nuclear data sheets. In agreement with a neutron excitation, the sign of the g factor has been determined to be negative by Forterre et al. [243] with TF. The measurement of Goldring et al. suffered from a low ion velocity. The kinetic energy was only $E(^{18}\text{O}) = 33\,\text{MeV}$. Therefore, the charge-state distribution contained a sizeable amount of 6^+ ions and assumptions about the electron configuration had to be made, leading to only an upper and lower limit of the g factor. Only for the case of hydrogen-like ions can the hyperfine field at the location of the nucleus be calculated, because the electron configuration is known. Similarly, Speidel et al. had to make assumptions about the charge-state populations and the electronic configurations. They measured the decoupling of the angular momentum J and the nuclear spin I as a function of an externally applied magnetic field in order to determine the g factor. As mentioned in the introduction (see Chapter 1.2), the adopted value of the g factor of Asher deviates from the theoretical SM prediction with the USDB interaction by more than five standard deviations. Recent studies using the ECR-TDRIV and TF techniques have shown that the magnetic moments of other isotopes in the sd-shell, i.e. ^{22}Ne [159], ^{24}Mg [78], and of ^{26}Mg [82], are reproduced well by these SM calculations. Hence, it needs to be clarified if the deviations of ^{18}O data are due to the experimental data or a short coming of the used USDB interaction, since deviations between theory and experiment only occur at the edges of the sd shell. The value obtained from this work with the ECR-TDRIV technique,

$$g(2_1^+) = -0.44^{+0.07}_{-0.08}, \tag{6.13}$$

is slightly below the adopted value from Asher et al., but within its uncertainty it agrees well with the SM prediction and the values of Goldring and Speidel. The different experimental values are compared in Figure 6.5, including the prediction of the SM using the USDB interaction. Based on the new value of the
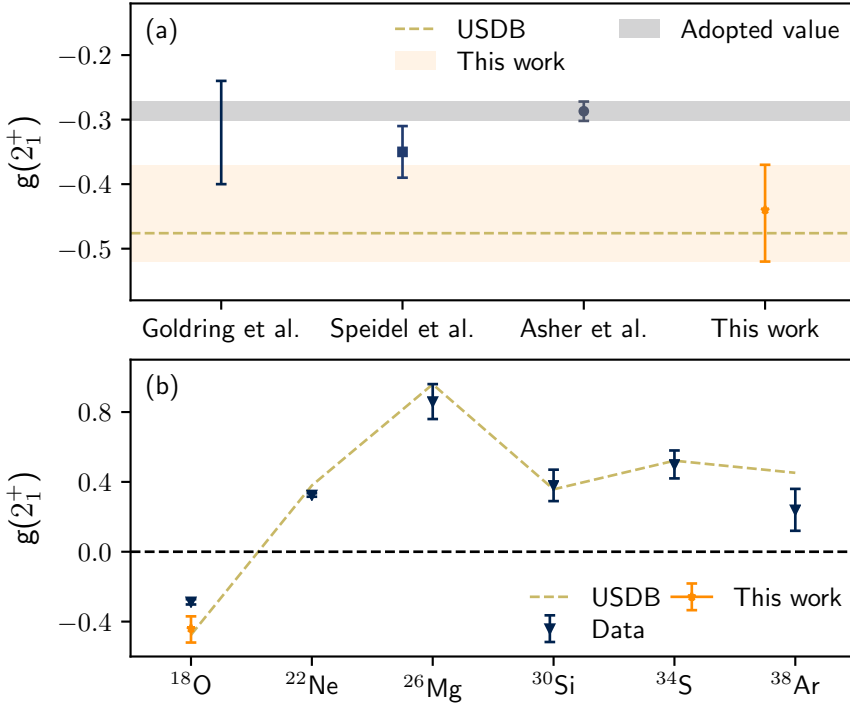
Figure 6.5.: (a) Comparison of different experimental values of $g(2_1^+)$ of ^{18}O. (b) Comparison between experimental data of the $N = Z + 2$ isotopes in the sd-shell.

g factor no final conclusion can be drawn. The uncertainty of the value from this work stems mainly from the low statistics of the measured particle-γ coincidences (see Figures D.7 ff. in the Appendix). Most evaluated groups sensitive to the oscillation of the angular correlation are located at or close to the minimum of the angular correlation, resulting in small γ-ray intensities. Minor roles play the uncertainties arising from the determination of the target-to-degrader dis-

tance and the uncertainty due to the angular coverage of the combined DSSD segments.

Different approaches can be taken to improve the presented measurement. The limiting factor of the performed experiment has been the count rates of the DSSD segments. As can be seen in the DSSD energy spectra (see Appendix D.2), the DSSD segments visibly degraded over the experiment due to radiation damage. It would be possible to increase the detection efficiency of γ rays by a factor of ~ 2, by shortening the distance of the HPGe detectors to the target. Thereby, the covered solid angle is increased. However, the employed target chamber has to be replaced with a target chamber with a smaller diameter. Another approach would be to place the DSSD farther away from the beam dump or to shield it against possible back scattered particles from the beam dump. Thus, allowing to significantly increase the beam current on the target. Moreover, improvements could be made, by placing more HPGe detectors close to the sensitive region around $\theta = 90°$. Thereby, the sensitivity of the setup to the oscillation of the angular correlation is increased. This step would require a different detector setup, since the HORUS detector array does not have additional detector holding structures at $\theta = 90°$.

7. Conclusion & outlook

In this work, two different techniques of γ-ray spectroscopy, also foreseen for RIB, have been successfully applied to stable nuclei. Mean lifetimes of low-lying excited states have been determined for the rare-earth isotopes ^{174,176,178,180}Hf and ^{152}Gd. The presented FEST experiments have been performed at IFIN-HH with the ROSPHERE detector array in a mixed configuration with LaBr$_3$(Ce) and HPGe detectors. For the population of excited nuclear states FE and CoulEx reactions have been employed.

The evolution of collectivity in the $N = 82$ to $N = 126$ shell has been investigated with the help of the extracted $E2$ transition strengths. The extracted mean lifetime of the 0_2^+ state of ^{152}Gd, $\tau(0_2^+) = 96(6)$ ps, is in disagreement with the previous measured value. The new value and the connected $\rho^2(E0; 0_2^+ \rightarrow 0_{GS}^+) = 38(3) \times 10^{-3}$ strength and $B(E2; 0_2^+ \rightarrow 2_1^+) = 115_{-8}^{+6}$ W.u. strength revealed a correlation between the $E0$ strength, an established signature of a QPT [65, 66], and the product of $B(E2; 0_1^+ \rightarrow 2_1^+) \times B(E2; 0_2^+ \rightarrow 2_1^+)$ for the gadolinium isotopic chain. Additionally, this product of $B(E2)$ strengths can be related to another possible new signature, i.e. the product $\Sigma B(M1; 1_{sc}^+ \rightarrow 0_{GS}^+) \times \Sigma B(M1; 1_{sc}^+ \rightarrow 0_2^+)$ connecting the mixed-symmetry scissors mode to the GS and the 0_2^+ state, which has been investigated in Ref. [233]. Further investigations of the $E0$ strength in neighbouring isotopic chains of gadolinium could give new insight into the correlation between the $E0$, $E2$ and $M1$ observables. The investigation of the $M1$ strength of the scissors mode of the neodymium, samarium and dysprosium chains are ongoing [234, 235, 244, 245].

Towards mid-shell, the early peak of collectivity at $N = 100$ has been identified for the Hf isotopes from the determined lifetimes of the 2_1^+ states of ^{174,176,178,180}Hf in agreement with other recent measurements [40]. In total 13 mean lifetimes of excited states of ^{174,176,178,180}Hf have been determined, two ($\tau(4_1^+) = 85(13)$ ps of ^{178}Hf and $\tau(3_1^-)$ of ^{176}Hf) for the first time. Several observables, such as δV_{pn} and the determined $B(E2; 6_1^+ \rightarrow 4_1^+)$ strengths, hint at a change in rotational structure of these isotopes past $N = 100$.

Apart from the evolution of the $E2$ strength, the low-lying negative parity band of ^{176}Hf has been investigated. Here, the determined mean lifetime of the 2_1^- state is in good agreement with older measurements and $\tau(3_1^-) = 25(12)\,\text{ps}$ has been determined for the first time. For a comparison of the hafnium data to the evolution of the $E2$ transition strength of the tungsten isotopes, recently a RDDS measurement of ^{170}W has been performed at INFN, Legnaro, which is analyzed by K. Ide in her master thesis [246]. For the investigation of the exotic nuclei around $A \sim 190$ and at at $N = 126$ the FEST experiments S452 and S450, respectively, are scheduled and will be performed at the Gesellschaft für Schwerionenforschung (GSI) in the close future.

The second part of this thesis covered the measurement of magnetic moments of excited nuclear states with the ECR-TDRIV technique [77], developed for the application to RIB. To further refine the technique, it has been employed for the determination of the g factor of the 2_1^+ state of ^{18}O. A CoulEx experiment has been performed at the Tandem accelerator of the IKP der Universität zu Köln. The experimental setup consisted of the HORUS detector array in combination with the DARCY plunger device and a DSSD for particle identification. The g factor has been determined through the oscillation of the angular correlation of de-excitation γ rays to $g(2_1^+) = -0.44^{+0.07}_{-0.08}$, proving the feasibility of such experiments with stable beams. The obtained value is two σ away from the adopted value from the nuclear data sheets [80], but in agreement with previous measurements. Within its uncertainty, it is also in agreement with SM calculations using the USDB interaction, which deviate from all previous measurements. However, the value is not precise enough to draw a final conclusion. Further investigations with a follow-up experiment and the comparison to other theoretical predictions on the basis of ab-initio calculations [247, 248] are foreseen to clarify the situation. Possible obstacles and improvements for future ECR-TDRIV experiments have been discussed in this work. As a next step, the technique should be applied to RIBs. A first RIB experiment has been performed at the isotope separator on-line device (ISOLDE) facility at conseil européen pour la recherche nucléaire (CERN), investigating ^{28}Mg, but no final results have been obtained so far [159].

A. Derivations

A.1. Relation between $E2$ and $M1$ strength in even-even nuclei

The following derivation is based on Ref. [249]. Within the Q-phonon scheme it can be demonstrated [233] that the $M1$-branching ratio of the 1^+ scissors mode (sc) to the first and second 0^+ states is related to the ratio of $B(E2)$ values from these two 0^+ states to the 2_1^+ state

$$\left(1 - \frac{E(0_2^+)}{2E(1_{sc}^+)}\right)^2 \frac{B(M1; 0_2^+ \to 1_{sc}^+)}{B(M1; 0_1^+ \to 1_{sc}^+)} = \frac{B(E2; 0_2^+ \to 2_1^+)}{B(E2; 0_1^+ \to 2_1^+)}. \tag{A.1}$$

Eq. (A.1) can be derived, starting with the IBM-2 Hamiltonian

$$H = H_\pi + H_\nu - \kappa \sum_\mu (-)^\mu Q_{\pi,\mu} Q_{\nu,-\mu}, \tag{A.2}$$

where π denotes the proton part and ν the neutron part. Calculating the double commutator of the Hamiltonian and the $M1$-transition operator results in

$$\sum_\eta (-)^\eta [[H, \mathfrak{M}_\eta(M1)], \mathfrak{M}_{-\eta}(M1)]$$
$$= -6\kappa (g_\pi + g_\nu)^2 \sum_\mu (-)^\mu Q_{\pi,\mu} Q_{\nu,-\mu}, \tag{A.3}$$

with the $M1$-transition operator

$$\mathfrak{M}(M1) = g_\pi L_\pi - g_\nu L_\nu. \tag{A.4}$$

Taking the matrix elements $\langle 0_1^+ | \ldots | 0_1^+ \rangle$ (see Ref. [250]) and $\langle 0_1^+ | \ldots | 0_2^+ \rangle$ of Eq. (A.3) we obtain

$$2E(1_{sc}^+) \left| \langle 0_1^+ \| \mathfrak{M}(M1) \| 1_{sc}^+ \rangle \right|^2 = \frac{3}{2} \kappa (g_\pi + g_\nu)^2 \frac{N}{Z} \left| \langle 0_1^+ \| \mathfrak{M}(E2) \| 1_{sc}^+ \rangle \right|^2$$
(A.5a)

$$(2E(1_{sc}^+) - E(0_2^+)) \langle 0_1^+ \| \mathfrak{M}(M1) \| 1_{sc}^+ \rangle \langle 1_{sc}^+ \| \mathfrak{M}(M1) \| 0_2^+ \rangle =$$
$$\frac{3}{2} \kappa (g_\pi + g_\nu)^2 \frac{N}{Z} \langle 0_1^+ \| \mathfrak{M}(E2) \| 2_1^+ \rangle \langle 2_1^+ \| \mathfrak{M}(E2) \| 0_2^+ \rangle . \quad \text{(A.5b)}$$

Dividing Eq. (A.5b) by Eq. (A.5a) and taking the result in square results in Eq. (A.1). Furthermore, it was shown empirically in Ref. [105] that

$$B(M1; 0_1^+ \rightarrow 1_{sc}^+) = \frac{10.6}{Z^2} B(E2; 0_1^+ \rightarrow 2_1^+). \quad \text{(A.6)}$$

Multiplying Eq. (A.6) squared with Eq. (A.1) results in

$$B(M1; 0_1^+ \rightarrow 1_{sc}^+) B(M1; 0_2^+ \rightarrow 1_{sc}^+) =$$
$$\left(\frac{10.6}{Z^2 \left(1 - \frac{E(0_2^+)}{2E(1_{sc}^+)} \right)} \right) B(E2; 0_1^+ \rightarrow 2_1^+) B(E2; 0_2^+ \rightarrow 2_1^+), \quad \text{(A.7)}$$

$$\Rightarrow B(M1)_1 \cdot B(M1)_2 \propto B(E2)_1 \cdot B(E2)_2. \quad \text{(A.8)}$$

$B(E2)_i$ replaces $B(E2; 0_i^+ \rightarrow 2_1^+)$ and $B(M1)_i = \sum B(M1; 0_i^+ \rightarrow 1_{sc}^+)$. The left-hand-side (lhs) of Eq. (A.8) was shown to be a possible new signature for a QPT in Ref. [233]. A peak is expected around the QPT because one of the factors $(B(M1)_i)$ is either forbidden or suppressed for the ideal vibrational or rotational limits. This is indeed the case for the Gd-$M1$-data around $N = 90$ (^{154}Gd), Figure. 6.4,(c). Unfortunately, there is no data for the neighbouring isotopic chains. Hitherto, the right-hand-side (rhs) of Eq. (A.8) should also be unknown signature for a QPT.

A.2. Relation between $\rho(E0)$ and $B(E2)_1 \times B(E2)_2$

Starting from the definition of the $E0$ strength from Ref. [236]

$$\rho_{if}^2 = \frac{|\langle \Psi_f | T(E0) | \Psi_i \rangle|^2}{(eR^2)^2},\tag{A.9}$$

and the $E0$ and $E2$ transition operators for axially symmetric quadrupole deformation from Ref. [66]

$$T(E0) = \frac{3Z}{4\pi} eR^2 \beta^2,\tag{A.10a}$$

$$T(E2) = \frac{3Z}{4\pi} eR^2 \beta,\tag{A.10b}$$

with the nuclear radius $R = 1.2A^{1/3}$ and the deformation parameter operator β.

$$\begin{aligned}
\rho^2(E0) &= \left(\frac{3Z}{4\pi}\right)^2 |\langle \Psi_f | \beta^2 | \Psi_i \rangle|^2 \\
&= \left(\frac{3Z}{4\pi}\right)^2 |\Sigma_i \langle \Psi_f | \beta | 2_i^+ \rangle \langle 2_i^+ | \beta | \Psi_i \rangle|^2 \\
&\approx \left(\frac{3Z}{4\pi}\right)^2 |\langle \Psi_f | \beta | 2_1^+ \rangle \langle 2_1^+ | \beta | \Psi_i \rangle|^2.
\end{aligned}\tag{A.11}$$

In the last step the assumption of the Q-phonon scheme, that the first 2_1^+ state exhausts nearly all the $E2$ transition strength from the ground state (empirically proven in Ref. [104]), was used. Together with the above definition of the $E2$ transition operator one obtains

$$\rho^2(E0) = C \cdot B(E2; 0_1^+ \to 2_1^+) B(E2; 0_2^+ \to 2_1^+).\tag{A.12}$$

$$\text{with } C = \left(\frac{3Z}{4\pi}\right)^2 \frac{1}{(eR^2)^4}.\tag{A.13}$$

A.3. $B(E2)_1 \times B(E2)_2$ maximum at QPT

The following arguments are taken from [249]. It can be qualitatively shown, that the product $B(E2)_1 \times B(E2)_2$ maximizes at the critical point of a QPT. Using the intrinsic frame expression for the $E2$-transition operator

$$Q_{2\mu} = Q_0 D_{\mu 0}^2 \beta, \qquad (A.14)$$

we obtain the following expression for the product of $B(E2)$-transition strengths

$$B(E2; 0_1^+ \to 2_1^+) B(E2; 0_2^+ \to 2_1^+) = Q_0^4 |\langle 0_1^+ | \beta^2 | 0_2^+ \rangle|^2. \qquad (A.15)$$

First, for the case of transitional and deformed nuclei the Davydov-Chaban model [251] can be used to determine the wave functions of the 0_1^+- and 0_2^+-states

$$\Psi(0_1^+) = \mathcal{N}_0^{-\frac{1}{2}} \beta^{-\frac{3}{2}} \exp\left(-\frac{1}{2} \frac{(\beta - \beta_0)^2}{2\beta_{00}^2} \right), \qquad (A.16a)$$

$$\Psi(0_2^+) = \mathcal{N}_1^{-\frac{1}{2}} \beta^{-\frac{3}{2}} \exp\left(-\frac{1}{2} \frac{(\beta - \beta_0)^2}{2\beta_{00}^2} \right) \frac{(\beta - \beta_0)}{\sqrt{2}\beta_{00}}, \qquad (A.16b)$$

with the normalization constants $\mathcal{N}_i$. $\beta_{00} = \frac{\hbar}{2\sqrt{BC}}$ where C is the stiffness coefficient of β vibrations at the minimum of the potential and B is the mass coefficient. β_0 gives the position of the maximum of the wave function.
Inserting these wave functions into Eq. (A.15) results in

$$B(E2; 0_1^+ \to 2_1^+) B(E2; 0_2^+ \to 2_1^+)$$

$$= 8 Q_0^4 \beta_{00}^4 \frac{\left| a(1 + \mathrm{Erf}(a) + \frac{2}{\sqrt{\pi}} \left(1 + a^2 - a \right) e^{-a^2} \right|^2}{(1 + \mathrm{Erf}(a)) \left(1 + \mathrm{Erf}(a) - \frac{2}{\sqrt{\pi}} e^{-a^2} \right)}, \qquad (A.17)$$

where $a = \frac{\beta_0}{\sqrt{2}\beta_{00}}$.
In the second case for the spherical limit $\beta_0 = 0$ and using the harmonic oscillator potential $V(\beta) = 1/2 C \beta^2$ the wave functions are

$$\Psi(0_1^+) = \mathcal{N}_0^{-\frac{1}{2}} \beta^{-2} \exp\left(-\frac{1}{2} \frac{\beta^2}{2\beta_{00}^2} \right), \qquad (A.18a)$$

$$\Psi(0_2^+) = \mathcal{N}_1^{-\frac{1}{2}} \beta^{-2} \exp\left(-\frac{1}{2} \frac{\beta^2}{2\beta_{00}^2} \right) (\beta^2 - \beta_{00}^2), \qquad (A.18b)$$

and therefore

$$B(E2;0_1^+ \to 2_1^+)B(E2;0_2^+ \to 2_1^+) = 2Q_0^4\beta_{00}^4. \qquad (A.19)$$

With the two expressions Eq. (A.19) and (A.17), it is possible to get numerical estimates for the product $B(E2)_1 \cdot B(E2)_2$ for the three cases of 1) the spherical limit, 2) transitional nuclei and 3) deformed nuclei.

- Spherical limit: $\beta_{00} = 0.15$:

$$B(E2;0_1^+ \to 2_1^+)B(E2;0_2^+ \to 2_1^+) = 1.0 \cdot 10^{-3}Q_0^4.$$

- Transitional nuclei: $\beta_{00} = 0.2$ and $\frac{\beta_0}{\sqrt{2}\beta_{00}} = 1$:

$$B(E2;0_1^+ \to 2_1^+)B(E2;0_2^+ \to 2_1^+) = 12.8 \cdot 10^{-3}Q_0^4.$$

- Deformed nuclei: $\beta_{00} = 0.03$ and $\beta_0 = 0.3$:

$$B(E2;0_1^+ \to 2_1^+)B(E2;0_2^+ \to 2_1^+) = 0.2 \cdot 10^{-3}Q_0^4.$$

B. Input files

B.1. gsort input file

The setup-file is seperated into three sections:

- Format: data format, detectors or fixed parameters (detector)
- Declaration: selection of events, general rules (hgatedef)
- Analysis: calibration of parameters, creation of spectra etc. (recal)

Listing B.1: gsort input file

```
1  ***************************************
2  ** Definition of the file format
3  format GASP
4
5  ** Definition of the detectors and their parameter and resolution
6  ** Definition of additional placeholder parameters need for e.g. the
7  ** time-walk calibration
8  header     F   1     8192
9  detector   G   14    2   8192 4096
10 detector   L   11    2   8192 8192 PLUS 2  8192 8192
11 detector   A   11                    PLUS 2  8192 8192
12
13 ** Definition of gates on the parametesr
14 ** ?0 corresponds to the energy and ?1 to the time information
15 *Gate 0 on 351 + 385 keV - HPGe
16 hgatedef G0 2
17         769 774
18         701 705
19 ** Gate 1 on 519 keV - HPGe
20 hgatedef G0 1
21         1037 1040
22
23 ** Gate 2 on 344keV - LaBr
```

```
24   hgatedef L0 1
25           338       351
26
27   ** Calibrations of the different parameters
28   ** Syntax: recal parameter file offset gain gate detectors
29   **               for gate and detectors: lower and upper limit
30   recal G0  Cal/GeE-2nd.cal        0.00 2.00 10 8192 0 14
31   recal G1  Cal/Ge-TDC-Feb2014.cal 1000.00 0.50 10 4000 0 14
32   recal G1  Cal/GeTSHIFTS.cal       0.00 1.00 10 4000 0 14
33
34   ** copy uncalibrated energy information of the LaBr to L3
35   copy L0 L3
36   recal       L0 Cal/le-gmatch        NORUN 0.00  1.00  10 8000 0 11
37   recal_mult L0 Cal/pint_LE.mcal      NORUN 0.00  1.00  10 8000 0 11
38   recal       L0 Cal/LE-gcor-87.cal   RUN   0.00  1.00  10 8000 0 11
39   recal       L1 Cal/TAC-10ps-Feb2014 NORUN 0.00  1.00  10 8000 0 11
40   recal       L1 Cal/LT-Shifts        NORUN 0.00  1.00  10 8000 0 11
41
42   ** Time-walk calibration
43   ** copy L0 to L2, calibrate L2 via calibration polynoms from file
44   ** subtract L2 from L1 with a offset
45   copy L0 L2
46   recal       L2   Cal/La-walkcorr-1          0.00  1.00  10 2000 0 11
47   add  L1 L2 L1 Fact 1.00 -1.00 Off 1000
48   gate L1 10 8000 IN 0 11
49
50   ************
51   ** Create Projections of all the detector parameters for each detector
52   proje
53   ** Create E(g1)-E(g2) matrix of HPGe detectors
54   sort2d_symm  G0 Ge-symm-TW-2      Res 8192
55
56   ** Create E(g1)-E(g2)-dT cube of the LaBr detectors with a gate on
57   ** HPGe detectors H1
58   sort3d_diff  L0 L0 L1 1000 La-La-dT-g351-385  Res 2048 2048 2048 H1 1
59
60   ****************************************
```

B.2. CLX input file

A CLX input file can be separated into three sections:

- The first part includes the title, input/output control flags, the number of levels/highest multipolarity/maximum energy, proton number and mass number of the projectile, and the target, projectile or target excitation (not in all versions of CLX included), the beam energy (MeV) and the angular coverage

- In the second part the levels are defined with number, spin, energy (MeV), parity(1=+,-1=-) and K quantum number

- Matrix elements connecting the declared states are defined in the last part with initial state, final state, matrix element and the multipolarity (negative values for magnetic transitions)

Listing B.2: CLX input file of the ^{180}Hf(^{16}O,^{16}O)^{180}Hf* experiment

```
1  160 -> 180Hf @NIPNE
2  11101111
3  5         2         0
4  0         0         0
5  8         16
6  72        180
7  2
8  55
9  0         180       1
10
11 1         0         0.0000   1 0
12 2         2         0.0933   1 0
13 3         4         0.3086   1 0
14 4         6         0.6408   1 0
15
16 1         2         0.967    2
17 2         3         0.211    2
18 3         4         0.18     2
```

Listing B.3: CLX input file of the ^{58}Ni(^{18}O,^{18}O*)^{58}Ni experiment

```
1  180 -> 58Ni
```

```
 2 | 11101111
 3 | 3          2          0
 4 | 0          0          0
 5 | 8          18
 6 | 28         58
 7 | 1
 8 | 55
 9 | 1          180        1
10 |
11 | 1          0          0.000      1 0
12 | 2          2          1.982      1 0
13 | 3          4          3.555      1 0
14 |
15 | 1          2          0.069      2
16 | 2          2          -0.046     2
17 | 2          3          0.030      2
18 | 3          3          0          2
```

B.3. SOCO2 channel configuration files

The sorting code SOCO uses several configuration files. They contain

- source.conf: definition of the detectors and their origin

- channel.conf: definition of the channel id, corresponding to the defined detectors and their time relation

- calibration.conf: calibration polynomials for the defined channel ids

- matrix_def.conf and matrix_correl.conf: definition of matrices

- requirements.conf: possible conditions on the created events

- gate.conf: conditions on single channels or defined types

More details can be found in the SOCO manual [211].

Listing B.4: source.conf

```
1 | # Type   Name    DGF      Crate    Slot     SubS
2 | SINGLE   R1R2    1419     0        12       0
3 | SINGLE   S1S2    1423     0        15       0
```

```
4  SINGLE  Ge0     1429    0       20      0
5  ...
```

Listing B.5: channel.conf

```
1  # ID    DetID   SId     Type            Name    Offset  IsTr    On/Off
2  28      0       0       Ge              Ge00    15      1       1
3  0       100     0       GASP            R1R2    -3      1       1
4  4       104     0       LABR            R9R10   -4      1       1
5  8       108     0       Silicon         R17R18  -2      1       1
6  12      201     0       Solar           S1S2    0       1       1
7  ...
```

Listing B.6: calibration.conf

```
1  # ID    p0      p1      p2      ...
2  28      -0.3405 0.1615  -8.5e-09
3  ...
```

Listing B.7: matrix_def.conf

```
1  #MatrixId       Name            DimX    DimY    IsSym.
2  0               Ge_Ge           4096    4096    1
```

Listing B.8: matrix_correl.conf

```
1  # MatrixID      Channel ID X    Channel ID Y    window  background
2  # GG matrix
3  0       28      29      20      30
4  ...
```

Listing B.9: requirement.conf

```
1  # Type  Min     Max
2  GASP    1       20
```

Listing B.10: gate.conf

```
1  # Type  Min     Max
2  GASP    5000    16000
```

C. Supplementary data for the FEST experiments.

C.1. CASCADE calculation: α beam, ^{149}Sm target

Table C.1.: CASCADE calculation of a α beam on ^{149}Sm target [117].
Compound Nucleus: ^{153}Gd, $V_{Coulomb}$=17.18 MeV, $L_{crit.}$=17$\hbar$

E	(MeV)	17.0	18.0	19.0	20.0	21.0	22.0	23.0
Cl0	$\hbar$	1.5	4.2	5.9	7.2	8.2	29.2	10.0
Nuc.	chan.				σ (mb)			
^{153}Gd	γ	0.0	0.1	0.1	0.1	0.1	0.0	0.0
^{152}Gd	n	132.3	251.7	381.7	310.2	182.5	118.7	74.9
^{151}Gd	2n		6.8	15.1	215.1	457.6	625.4	763.0
σ_{fusion}		132.3	258.6	396.0	525.5	640.4	744.4	838.3

C.2. Time-walk calibration of ROSPHERE
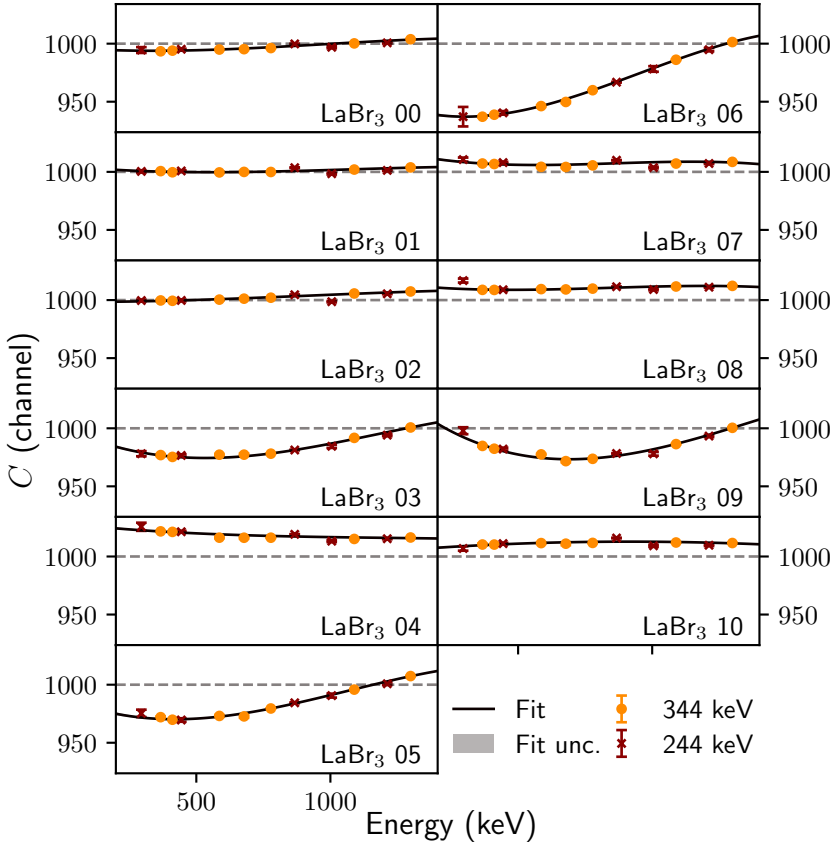
Figure C.1.: Time-walk calibration of the LaBr$_3$(Ce) detectors of ROSPHERE. The same range was used to indicate the stronger energy dependence of the detectors 5 and 6 in comparison to the other detectors.

D. Supplementary data for the TDRIV experiment.

D.1. CASCADE calculation: ^{18}O beam, ^{58}Ni target

Table D.1.: CASCADE calculation of a ^{18}O beam on a ^{58}Ni target [117].
Compound Nucleus: ^{76}Kr, $V_{Coulomb}$=41.66 MeV, $L_{crit.}$=38$\hbar$

E	(MeV)	46.0	48.0	50.0	52.0	54.0	56.0	58.0
Cl0	$\hbar$	14.1	16.8	19.0	21.0	22.8	24.5	26.0
Nuc.	chan.				σ (mb)			
^{74}Br	np	21.4	17.8	21.5	17.9	21.5	18.6	19.1
^{73}Br	2np	38.7	52.5	64.4	67.1	70.5	64.1	64.4
^{74}Se	2p	22.0	21.3	23.6	20.7	21.5	18.8	17.7
^{73}Se	n2p	125.5	180.6	206.4	238.4	246.8	255.7	256.9
^{72}Se	2n2p	3.1	7.3	15.9	31.2	48.8	80.4	102.5
^{73}As	3p	13.3	15.3	18.7	19.6	22.3	21.8	23.4
^{72}As	n3p		1.0	2.9	8.8	12.5	21.7	25.0
^{71}As	pα	10.7	11.1	12.8	12.1	12.9	12.6	13.2
^{70}As	npα	24.4	33.5	51.0	60.8	74.7	79.0	88.9
^{70}Ge	2pα	19.2	31.3	37.4	47.3	54.4	60.3	65.8
^{69}Ge	n2pα		0.3	0.5	2.4	4.7	10.5	16.1
^{67}Ga	p2α	2.5	4.1	7.0	10.9	14.2	20.2	23.1
σ_{fusion}		291.7	389.9	478.4	558.6	631.3	697.8	758.4

D.2. Particle spectra - ^{18}O TDRIV
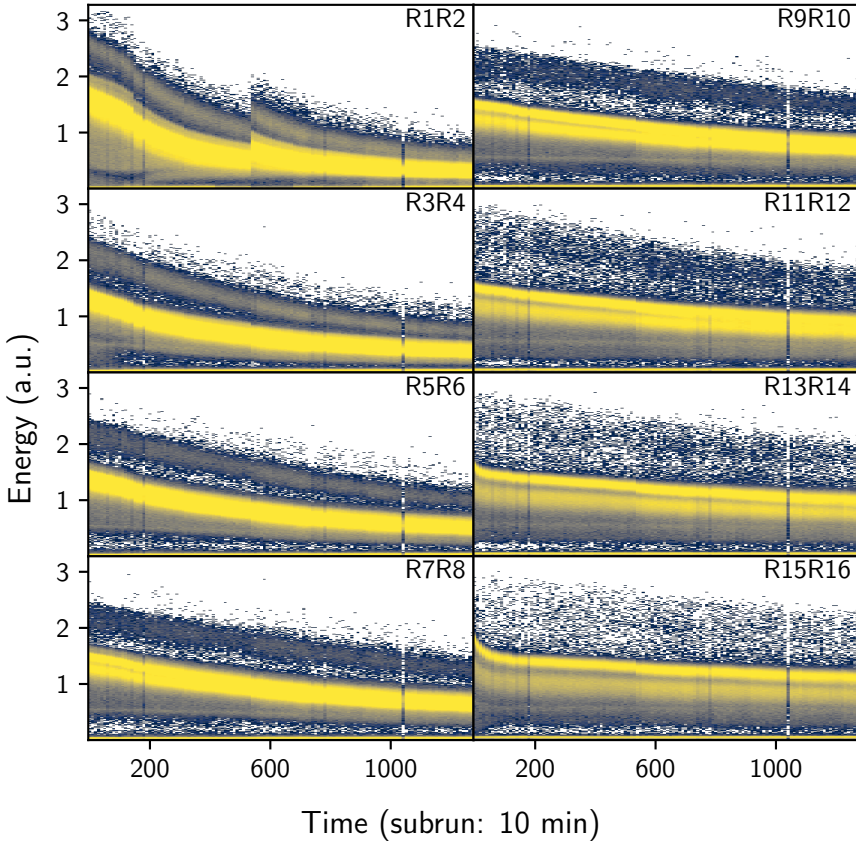
Figure D.1.: Uncalibrated particle energy spectra (rings) over time.

D. Supplementary data for the TDRIV experiment.
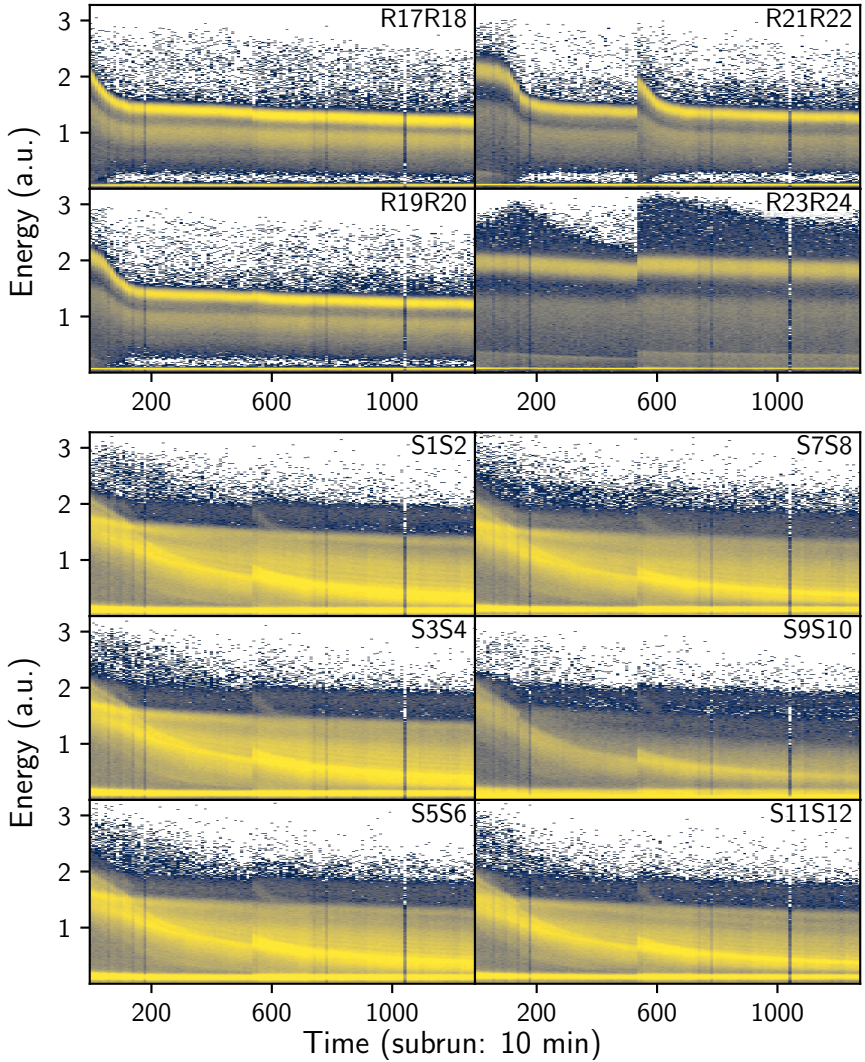
Figure D.2.: Uncalibrated particle energy spectra (rings and strips) over time.
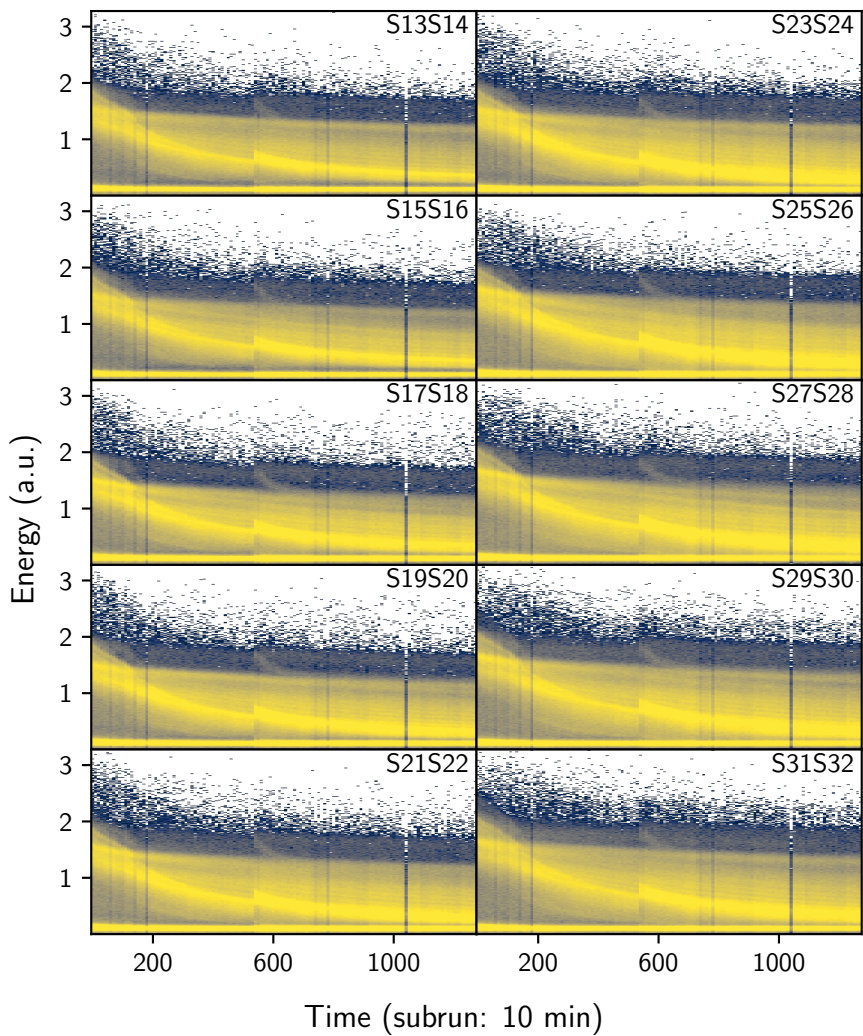
Figure D.3.: Uncalibrated particle energy spectra (strips) over time.

D. Supplementary data for the TDRIV experiment.

D.3. Relative efficiency of HORUS
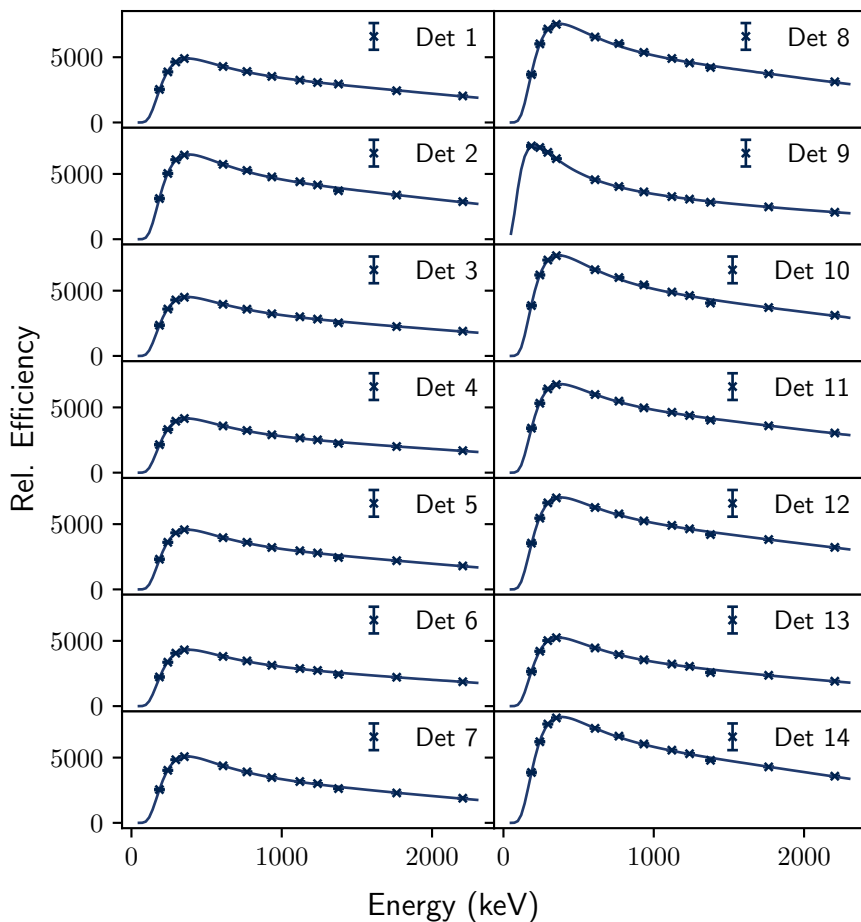
Figure D.4.: Relative efficiency of HORUS from a ^{226}Ra calibration source.

D.4. HPGe energy spectra - ^{18}O TDRIV
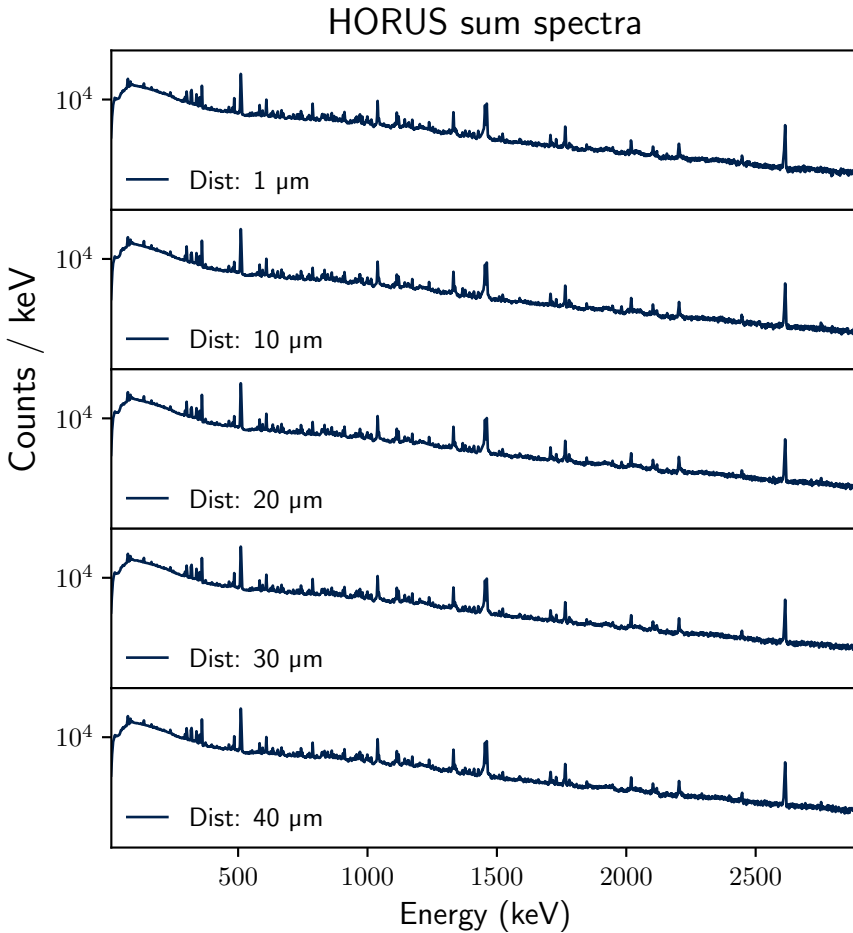
Figure D.5.: Calibrated energyspectra of HORUS without particle gates at a distance of 1, 10, 20, 30, and 40 µm.

D. Supplementary data for the TDRIV experiment.
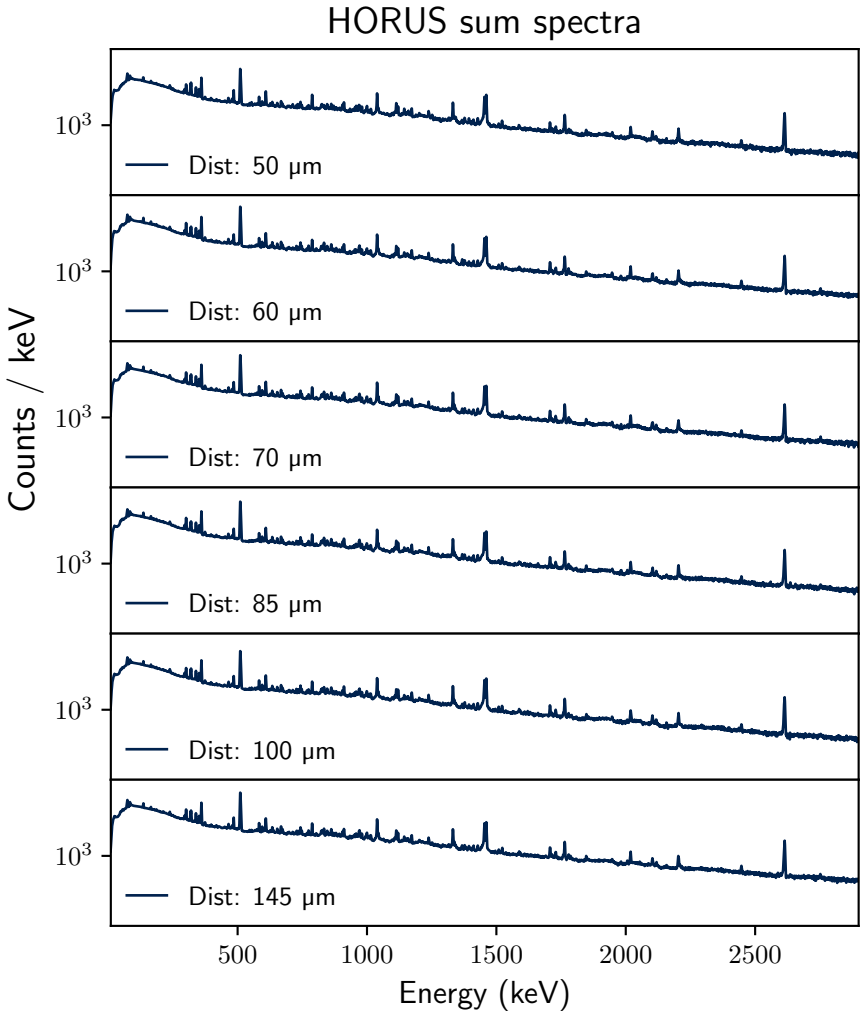
Figure D.6.: Calibrated energyspectra of HORUS without particle gates at a distance of 50, 60, 70, 85, 100 and 145 µm.
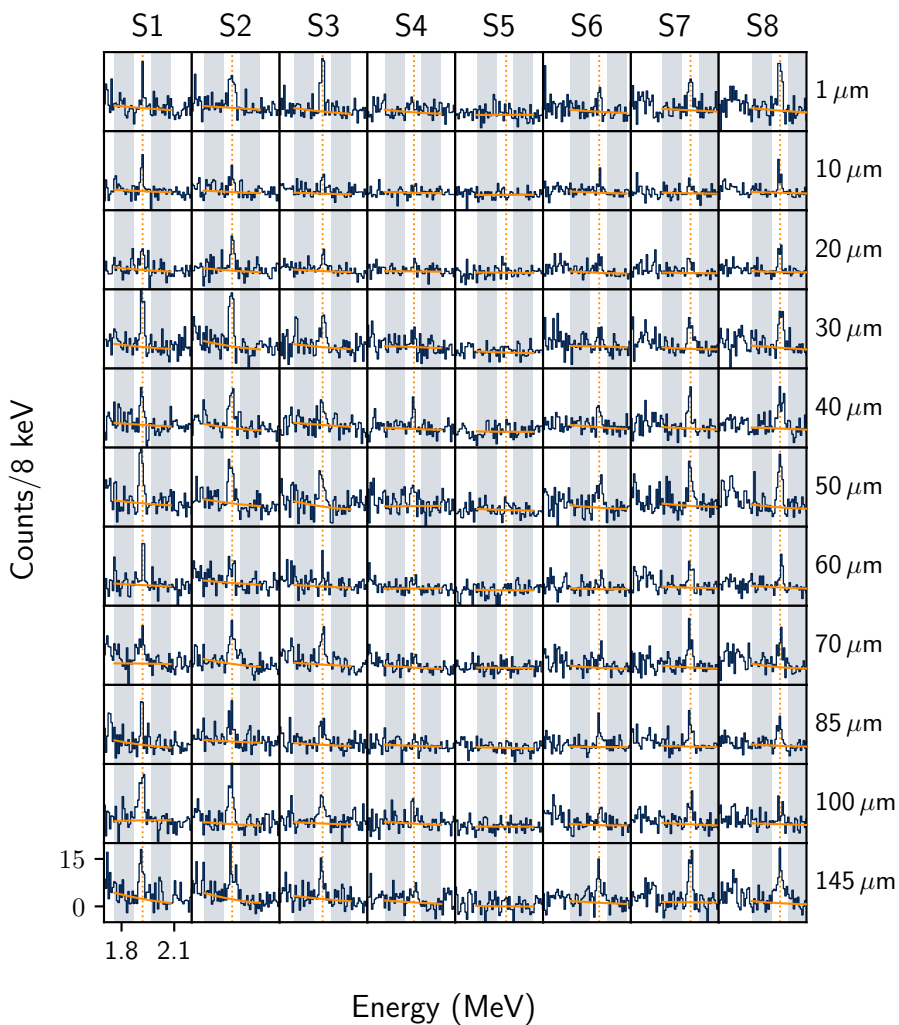
Figure D.7.: Particle gated energyspectra of Ge 0 of HORUS.
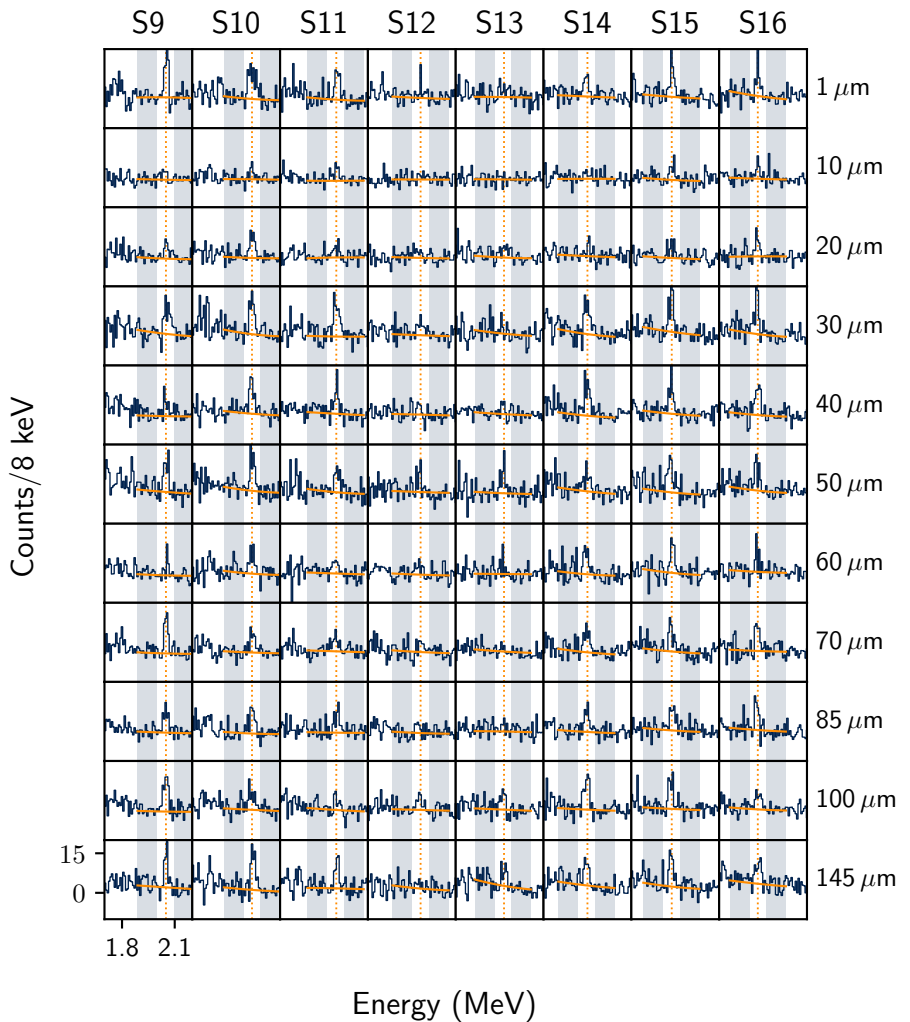
Figure D.8.: Particle gated energyspectra of Ge 0 of HORUS.
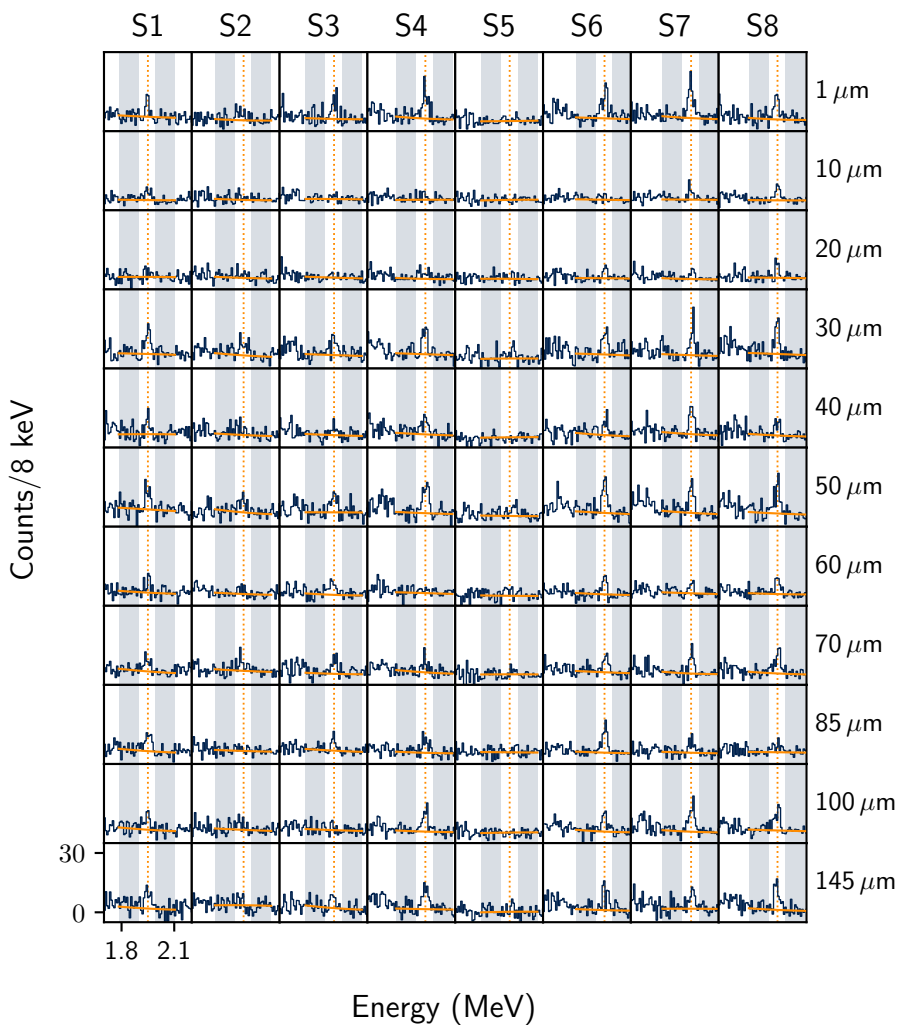
Figure D.9.: Particle gated energyspectra of Ge 1 of HORUS.
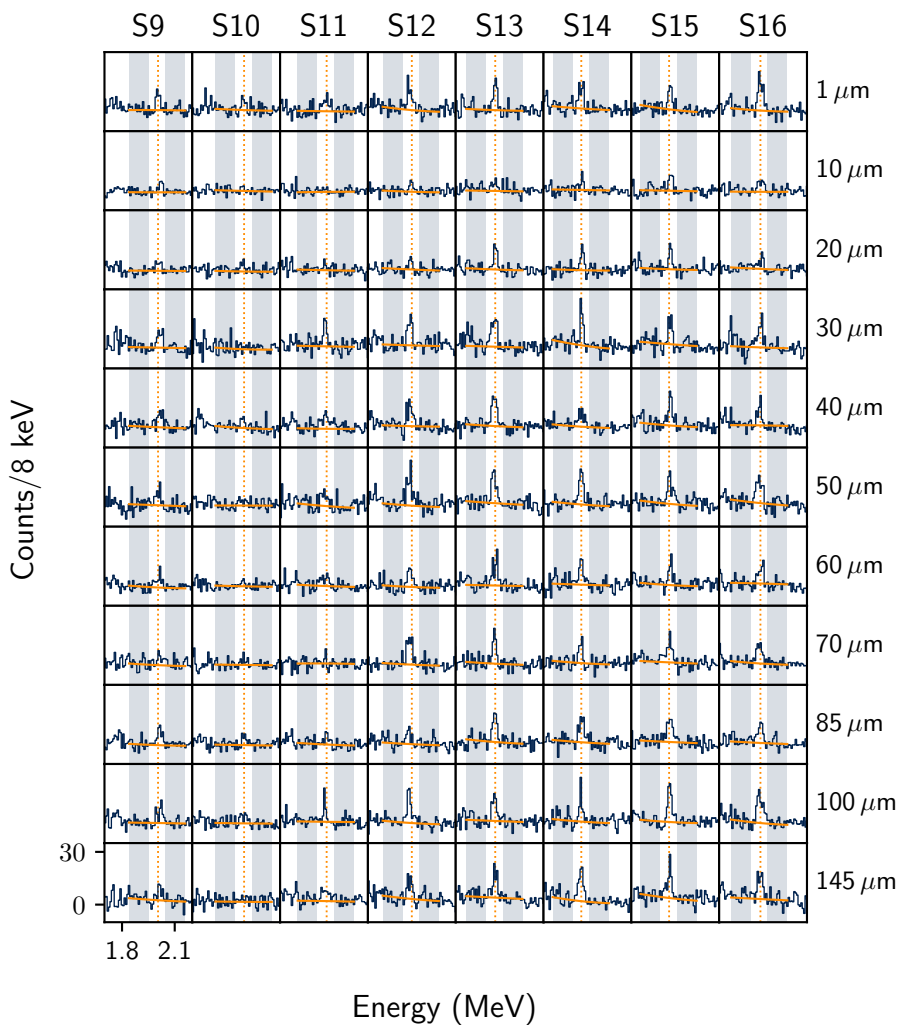
Figure D.10.: Particle gated energyspectra of Ge 1 of HORUS.
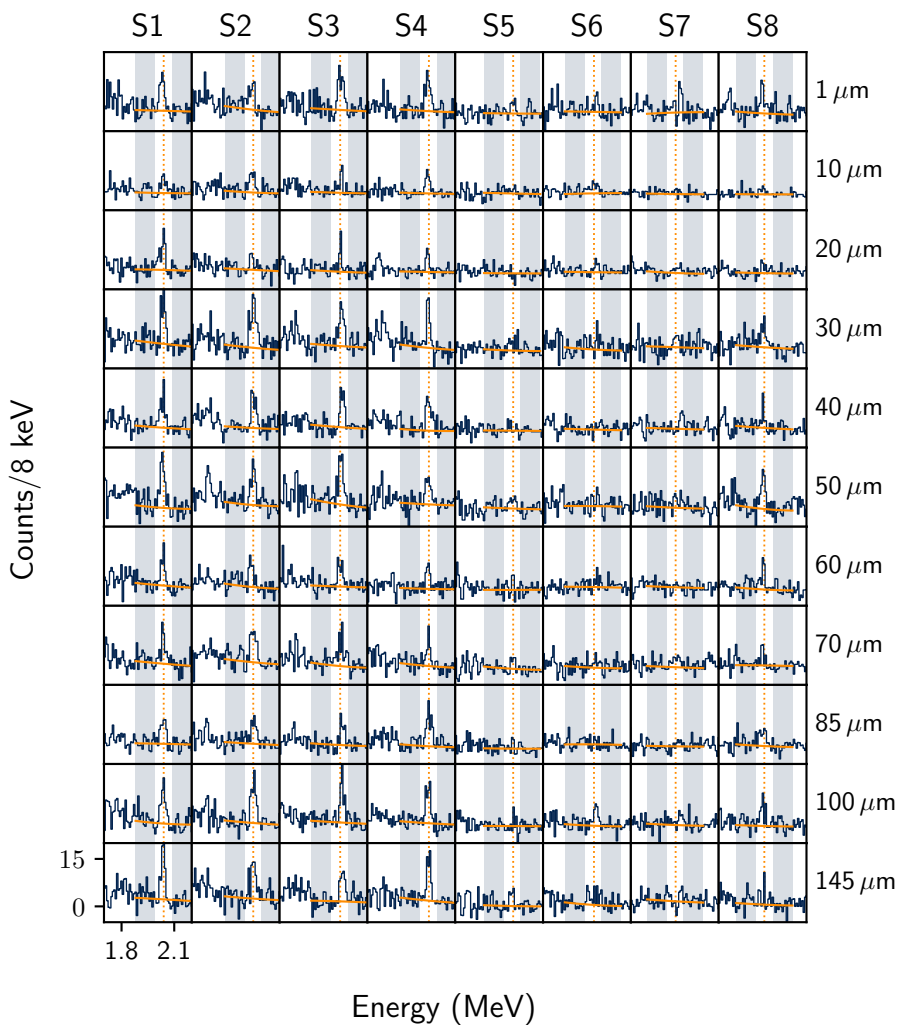
Figure D.11.: Particle gated energyspectra of Ge 2 of HORUS.
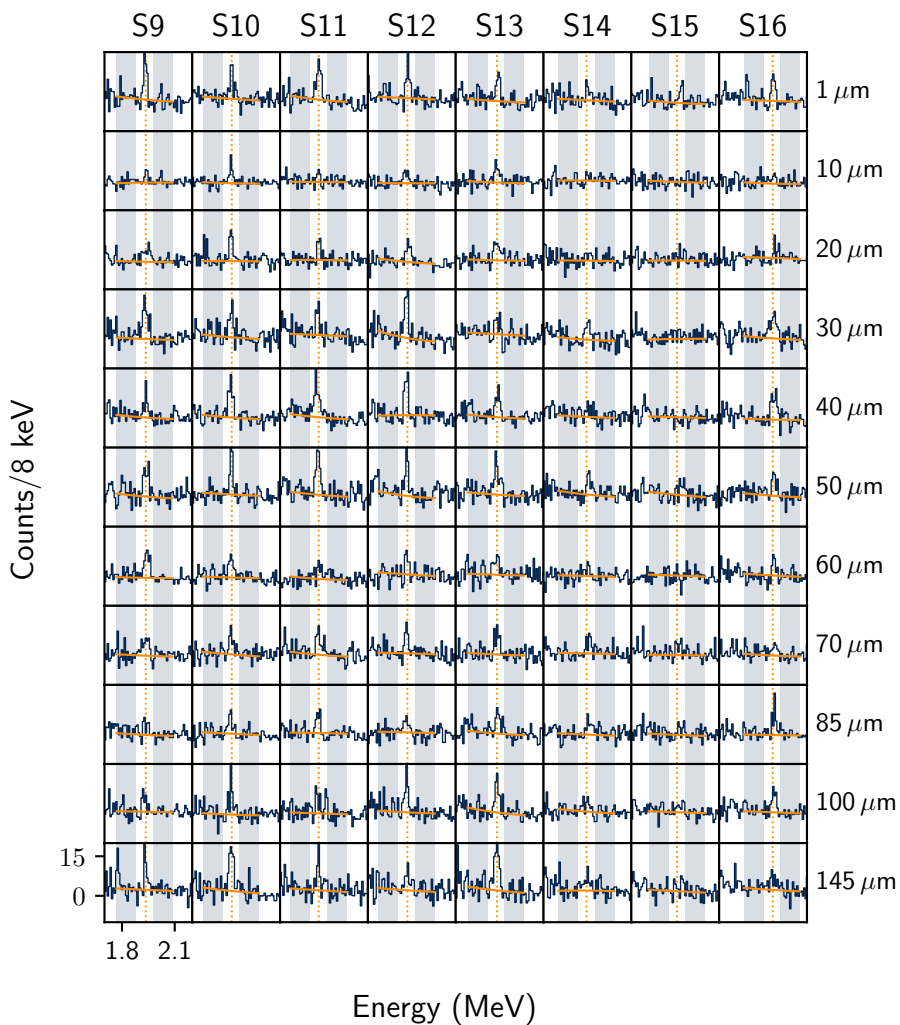
Figure D.12.: Particle gated energyspectra of Ge 2 of HORUS.
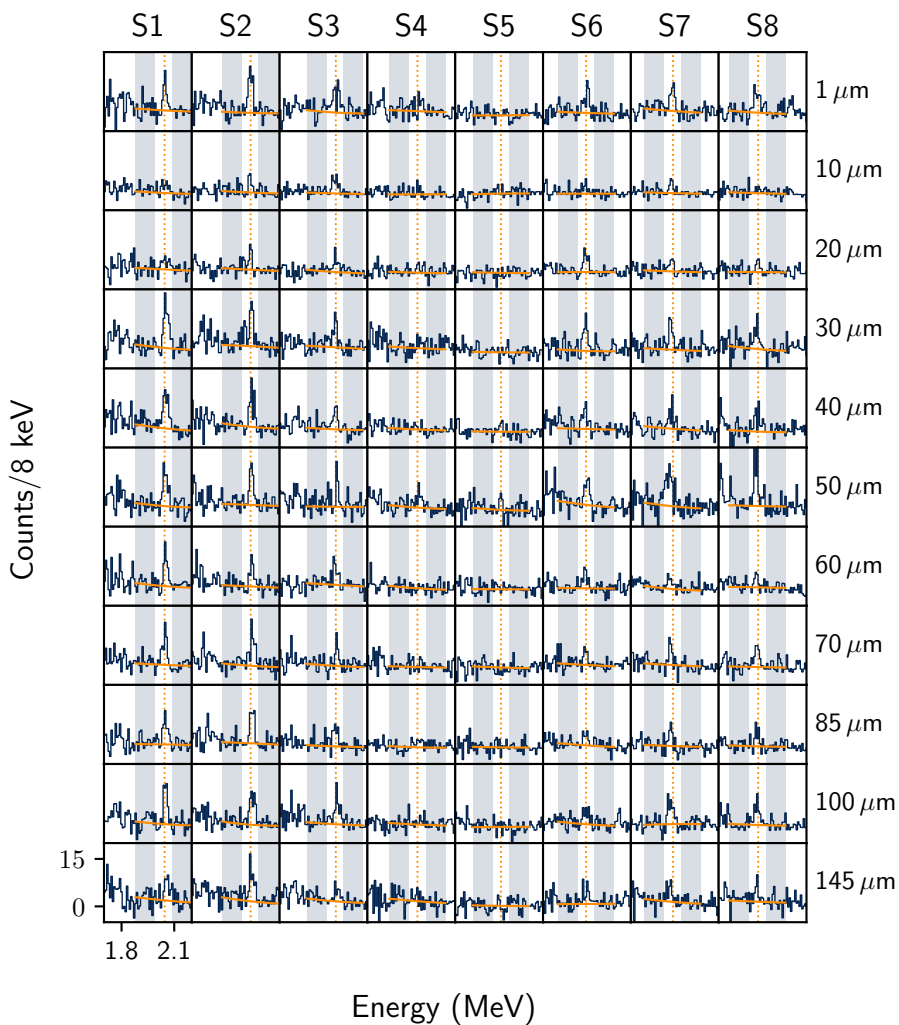
Figure D.13.: Particle gated energyspectra of Ge 3 of HORUS.
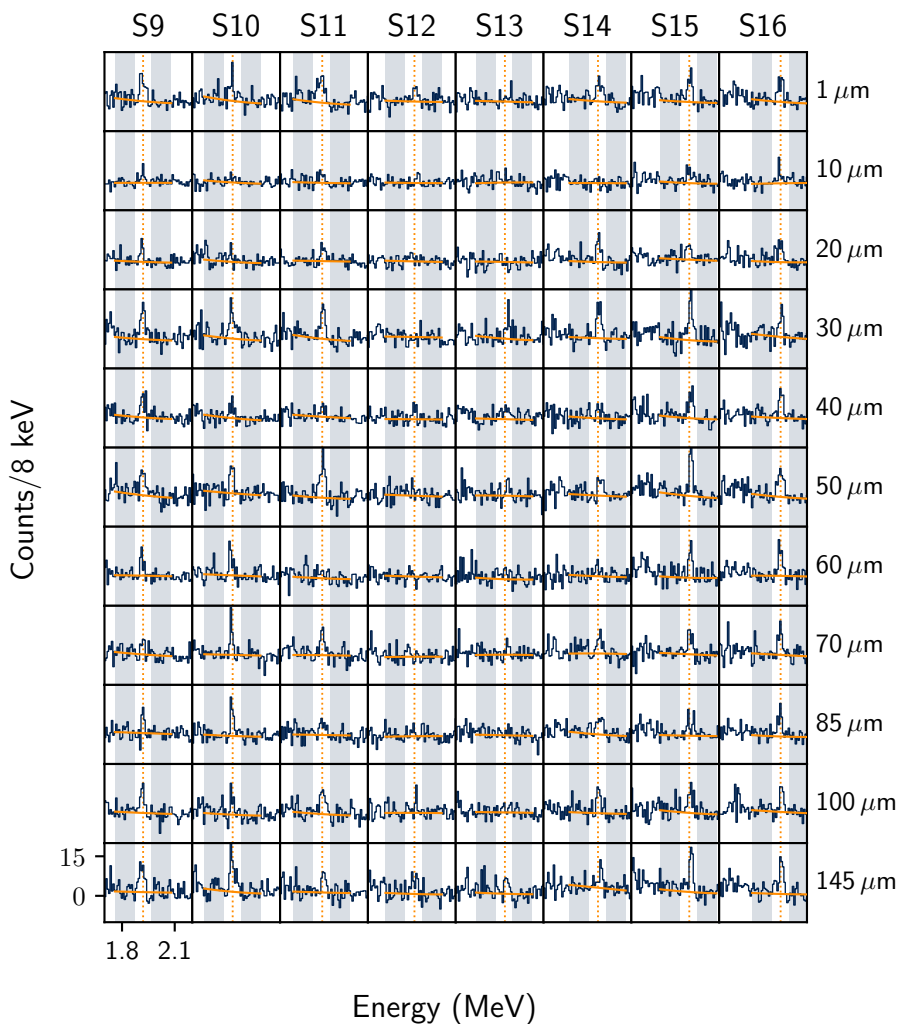
Figure D.14.: Particle gated energyspectra of Ge 3 of HORUS.
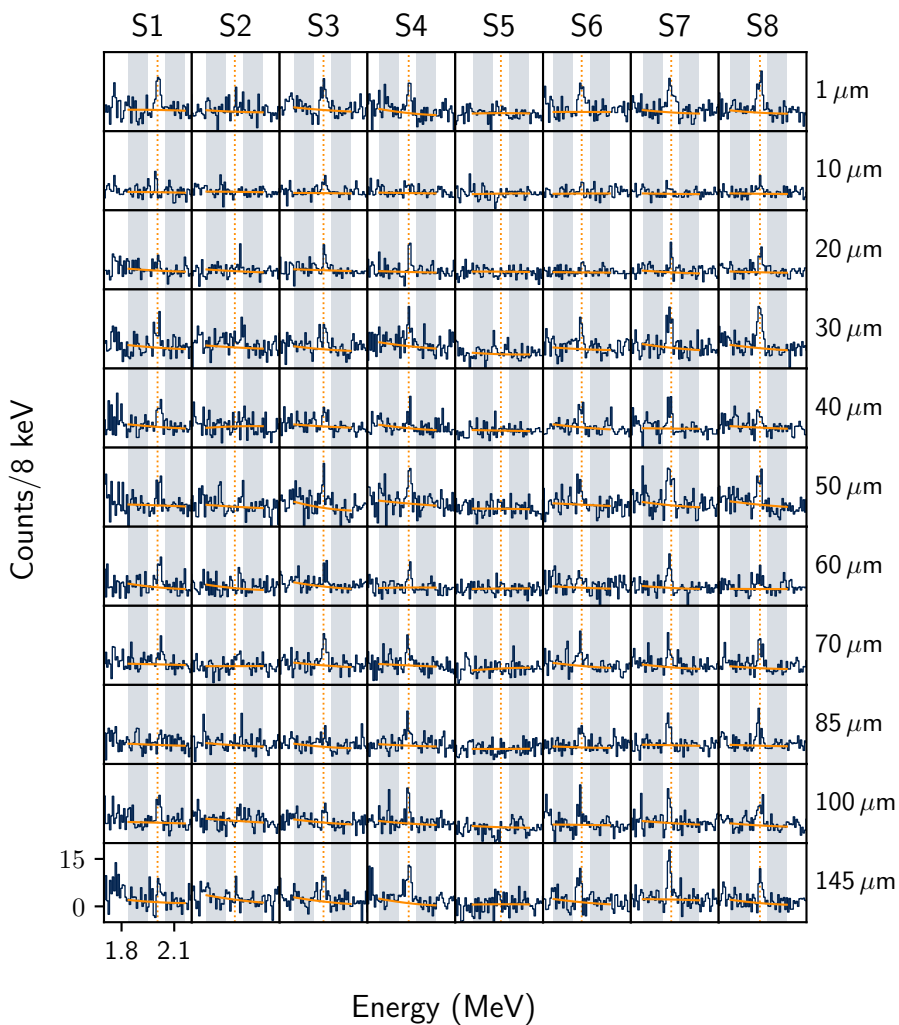
Figure D.15.: Particle gated energyspectra of Ge 4 of HORUS.

D. Supplementary data for the TDRIV experiment.
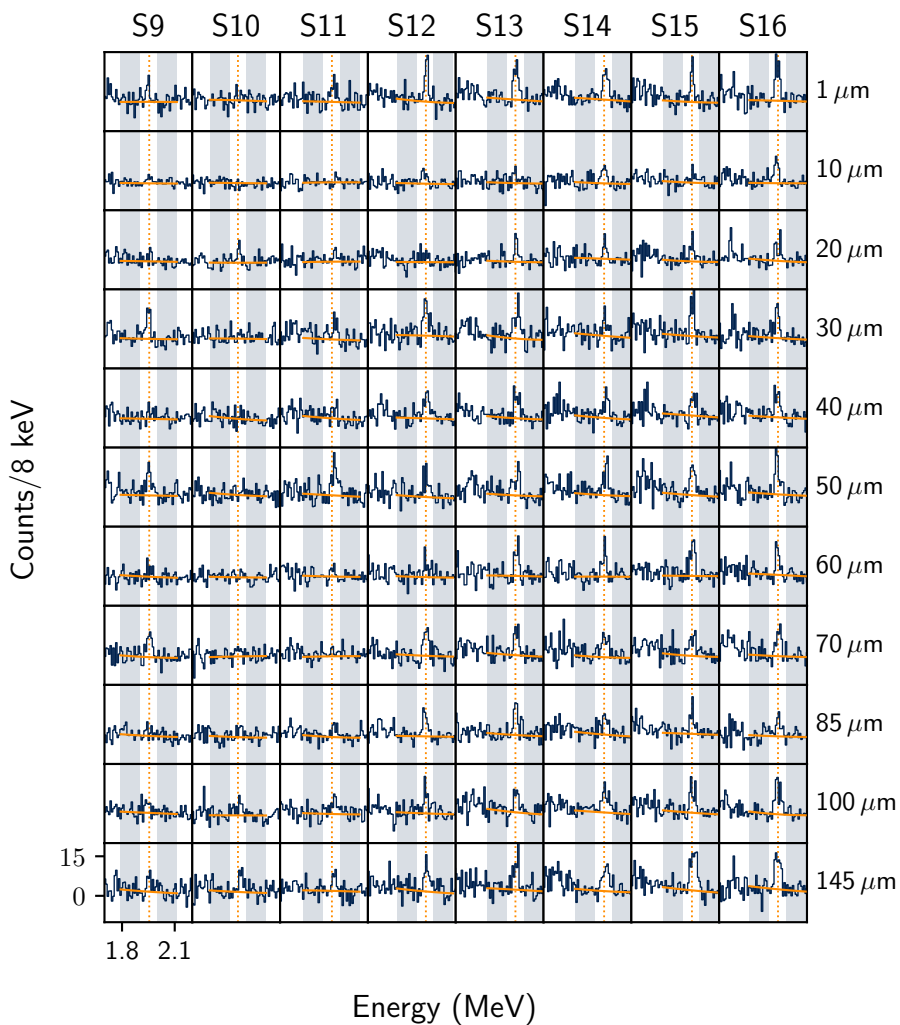
Figure D.16.: Particle gated energyspectra of Ge 4 of HORUS.
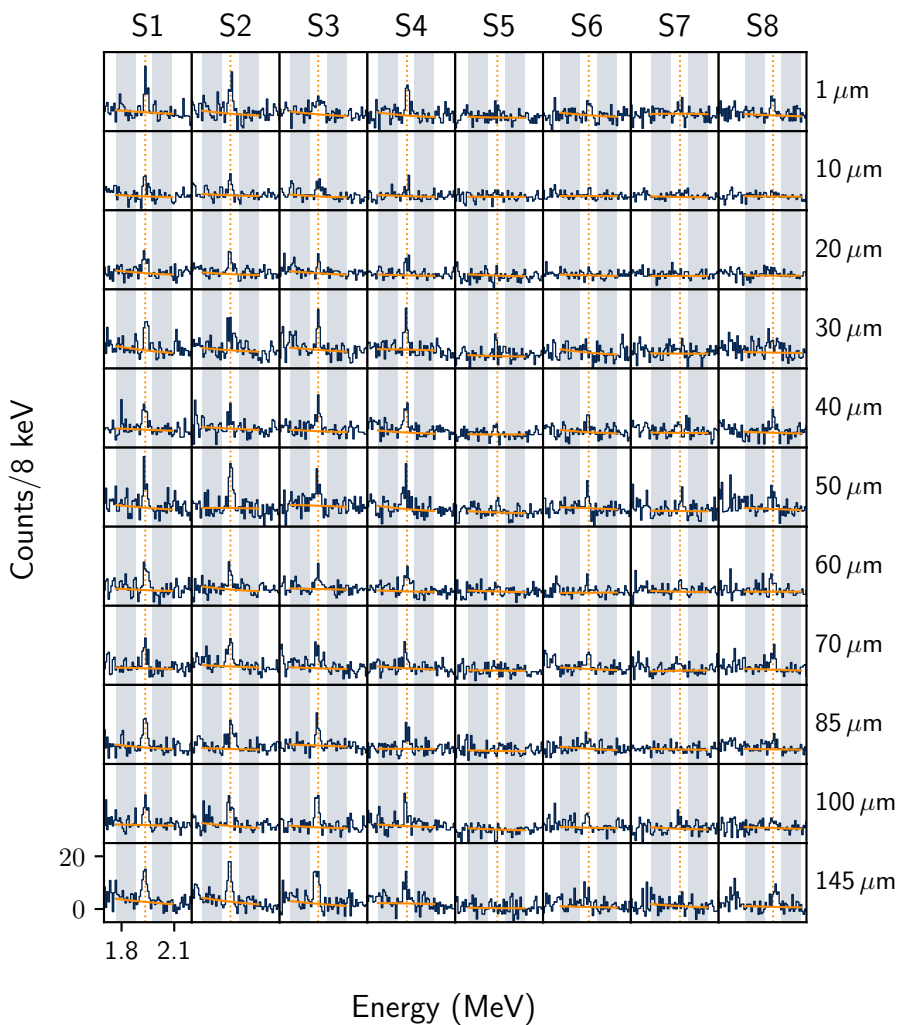
Figure D.17.: Particle gated energyspectra of Ge 5 of HORUS.
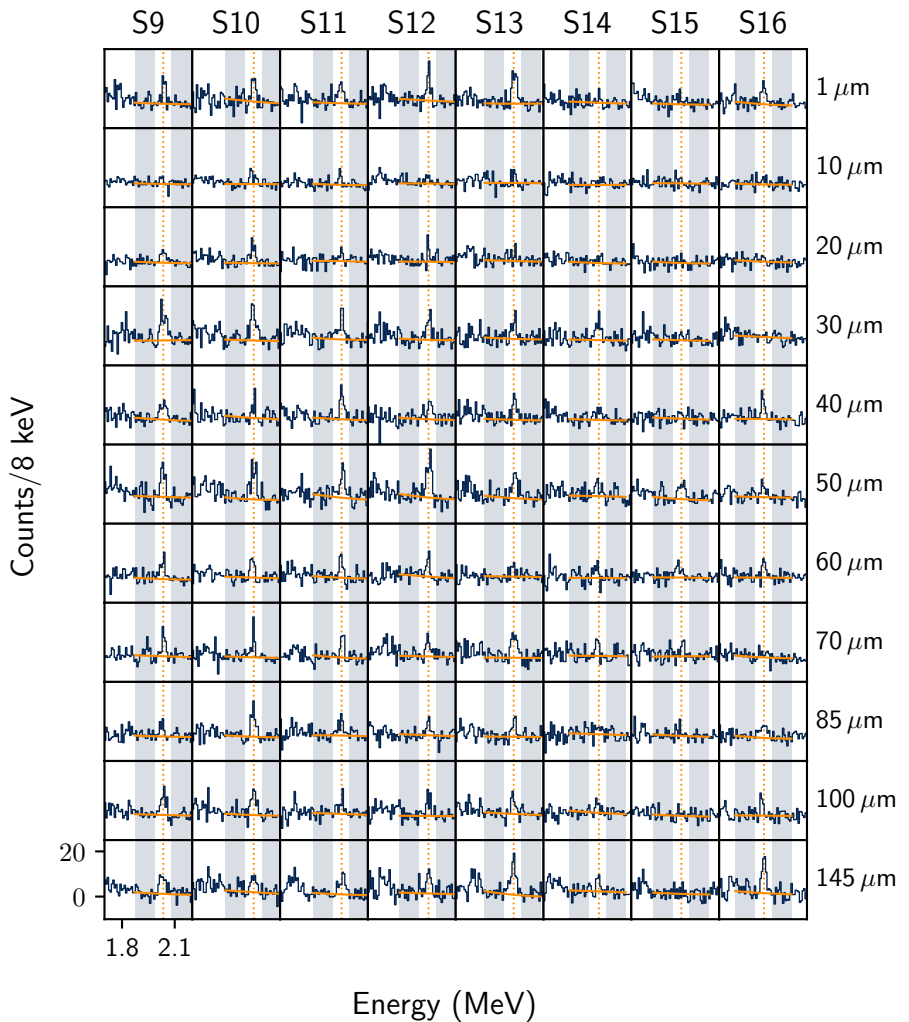
Figure D.18.: Particle gated energyspectra of Ge 5 of HORUS.
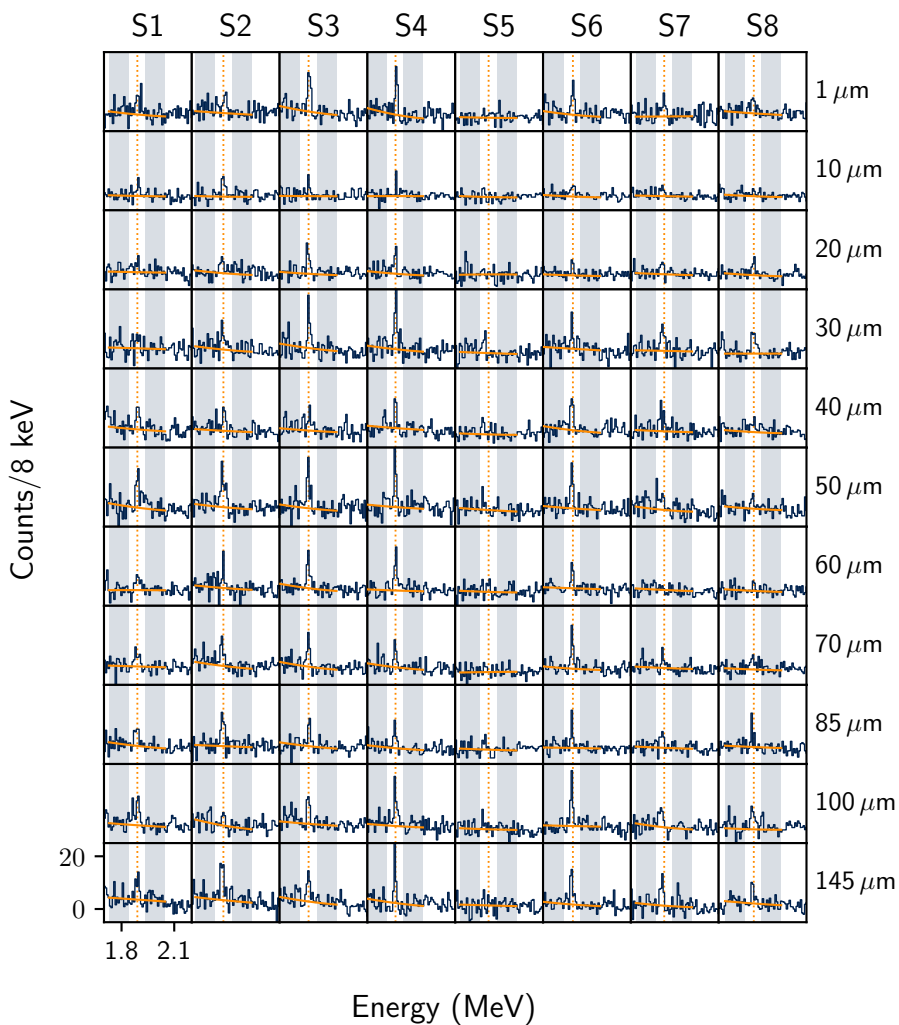
Figure D.19.: Particle gated energyspectra of Ge 6 of HORUS.
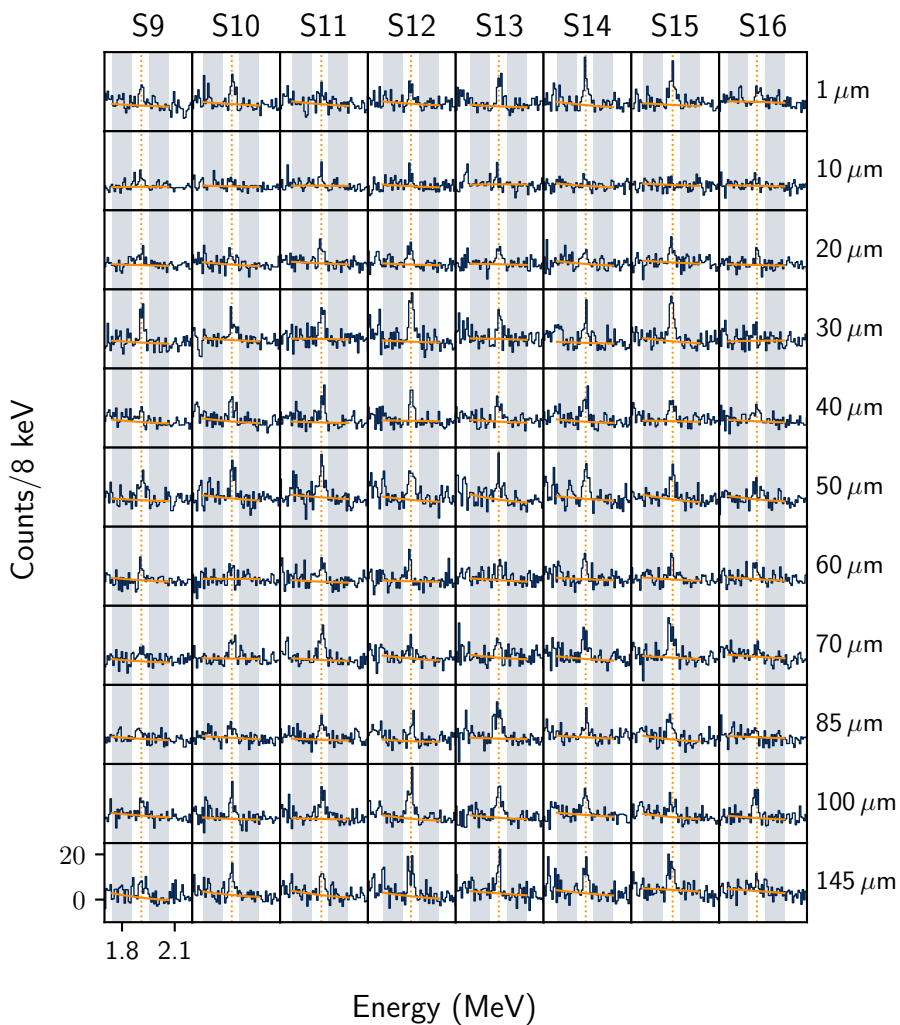
Figure D.20.: Particle gated energyspectra of Ge 6 of HORUS.
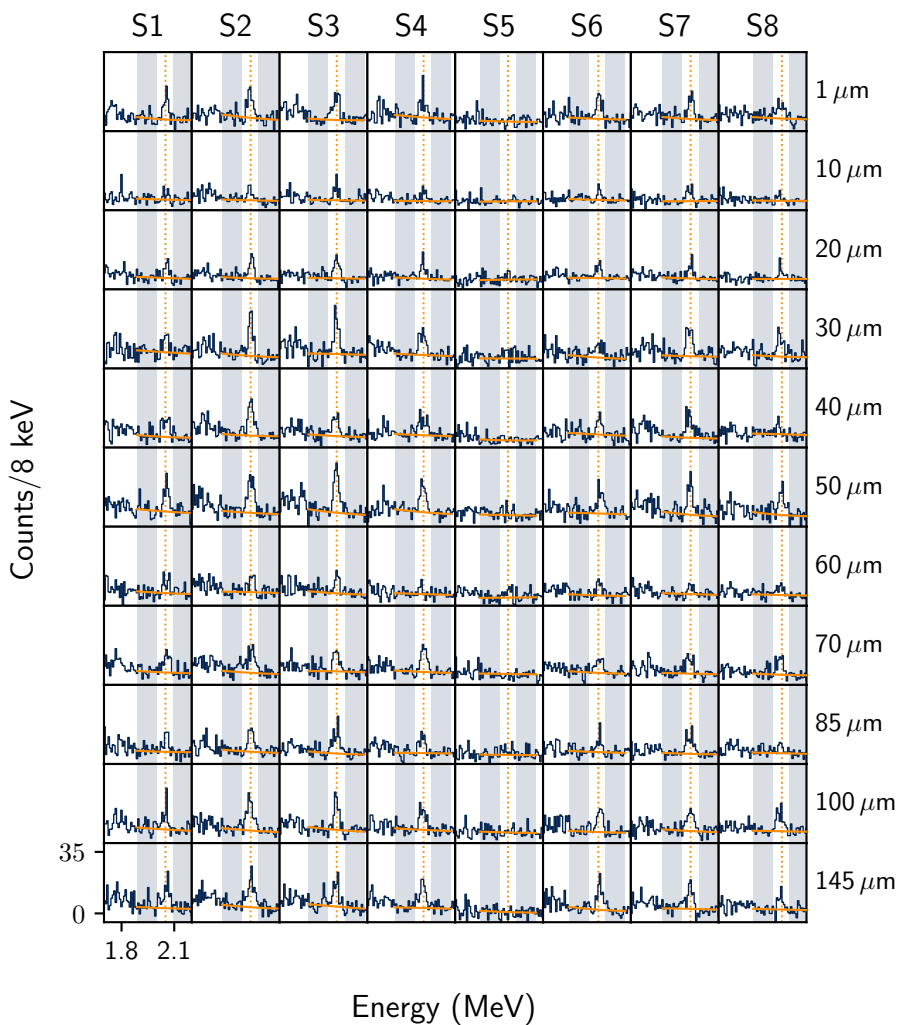
Figure D.21.: Particle gated energyspectra of Ge 7 of HORUS.

D. Supplementary data for the TDRIV experiment.
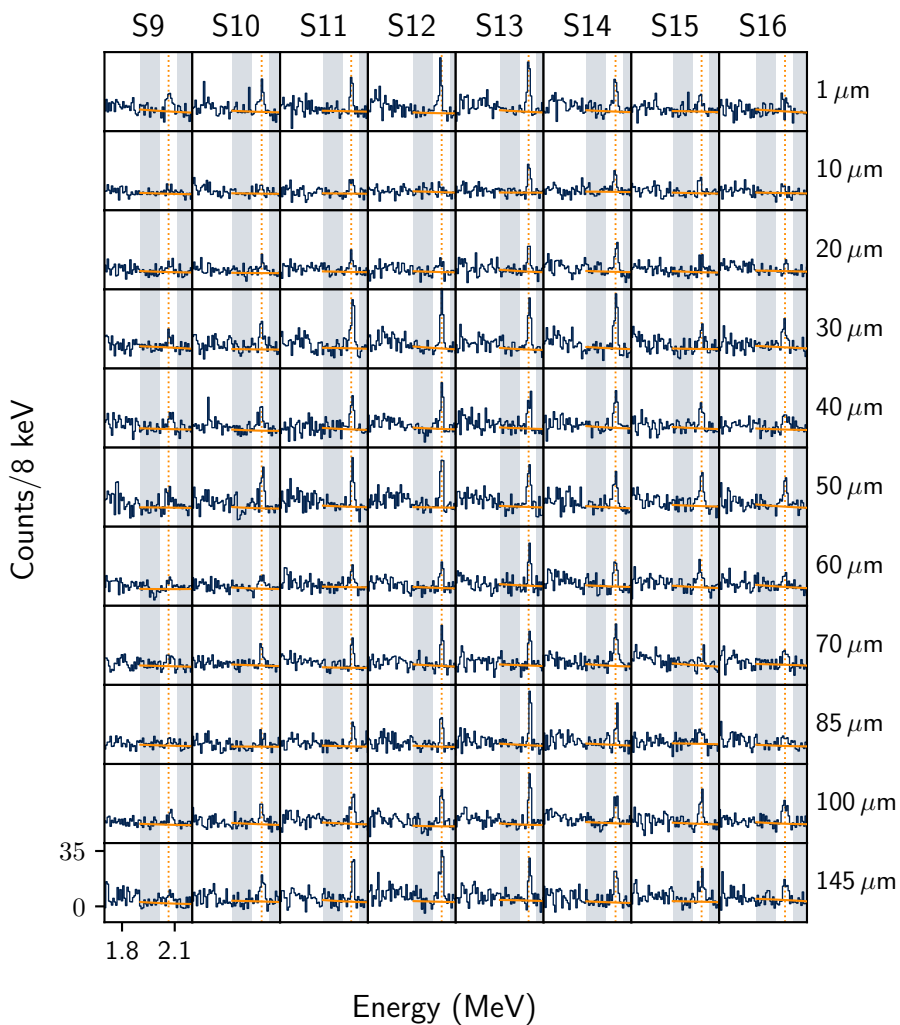
Figure D.22.: Particle gated energyspectra of Ge 7 of HORUS.
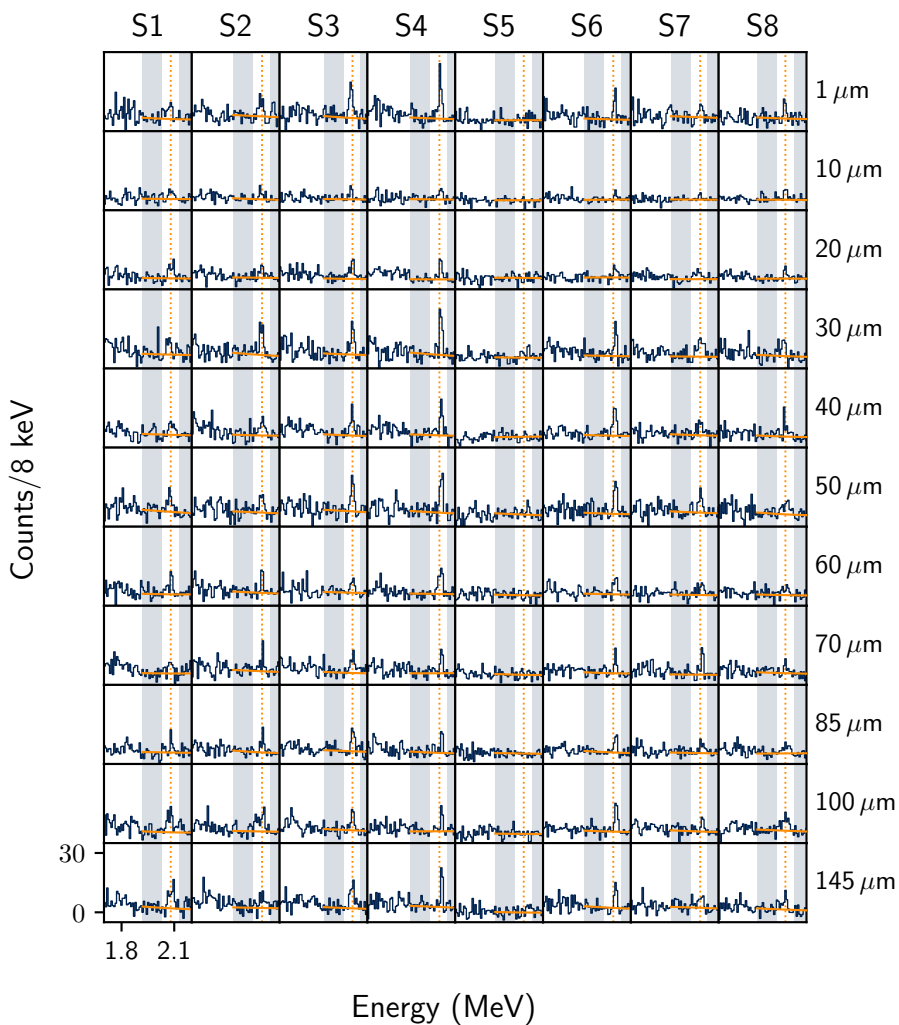
Figure D.23.: Particle gated energyspectra of Ge 8 of HORUS.
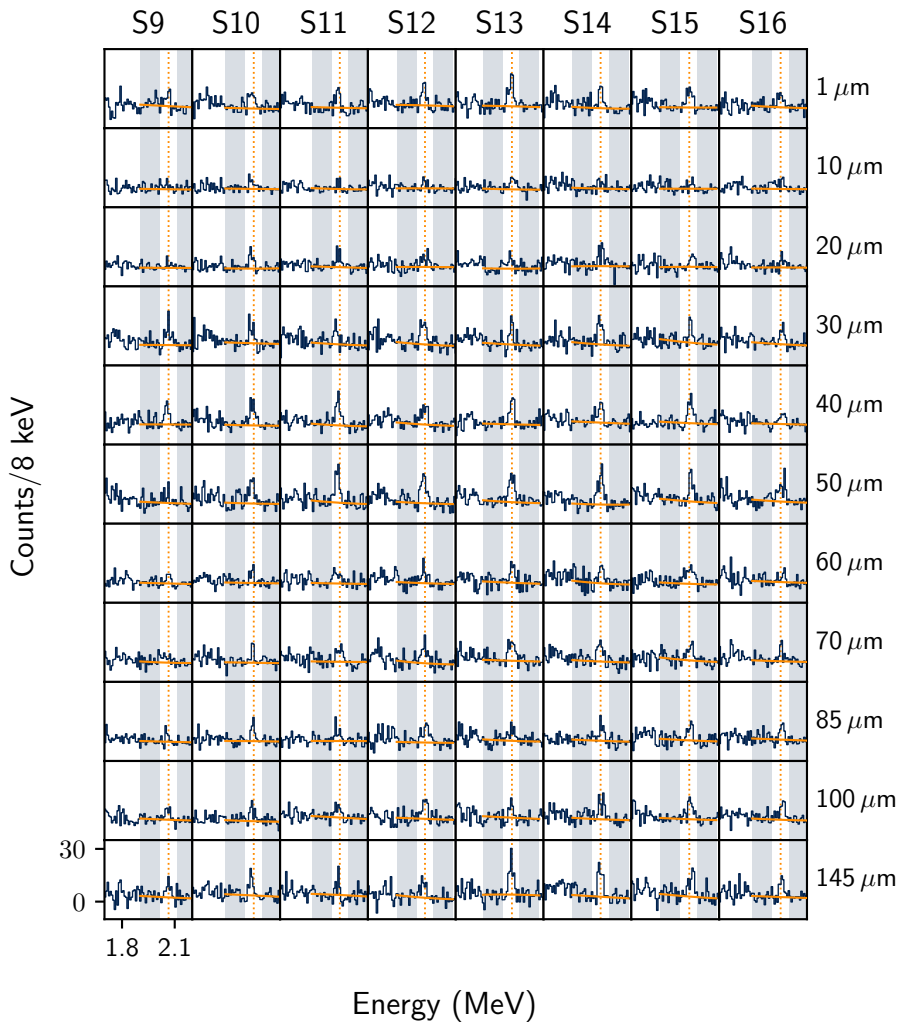
Figure D.24.: Particle gated energyspectra of Ge 8 of HORUS.
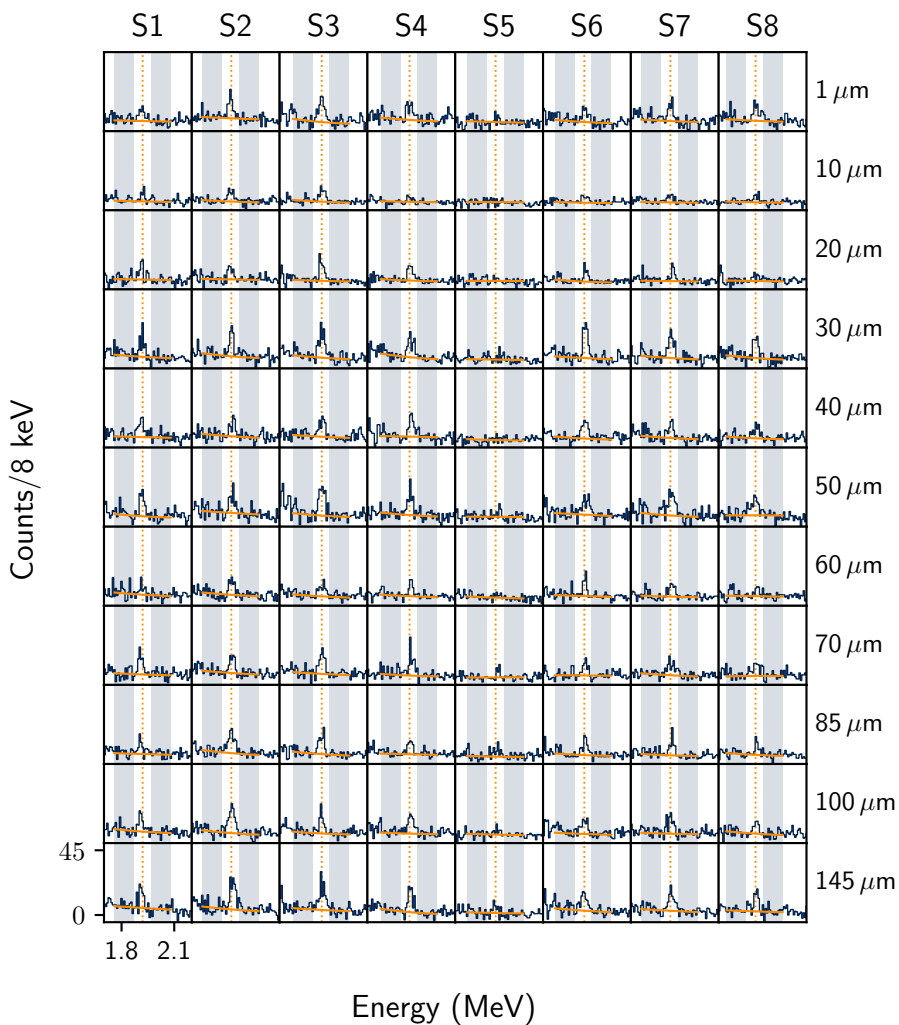
Figure D.25.: Particle gated energyspectra of Ge 9 of HORUS.
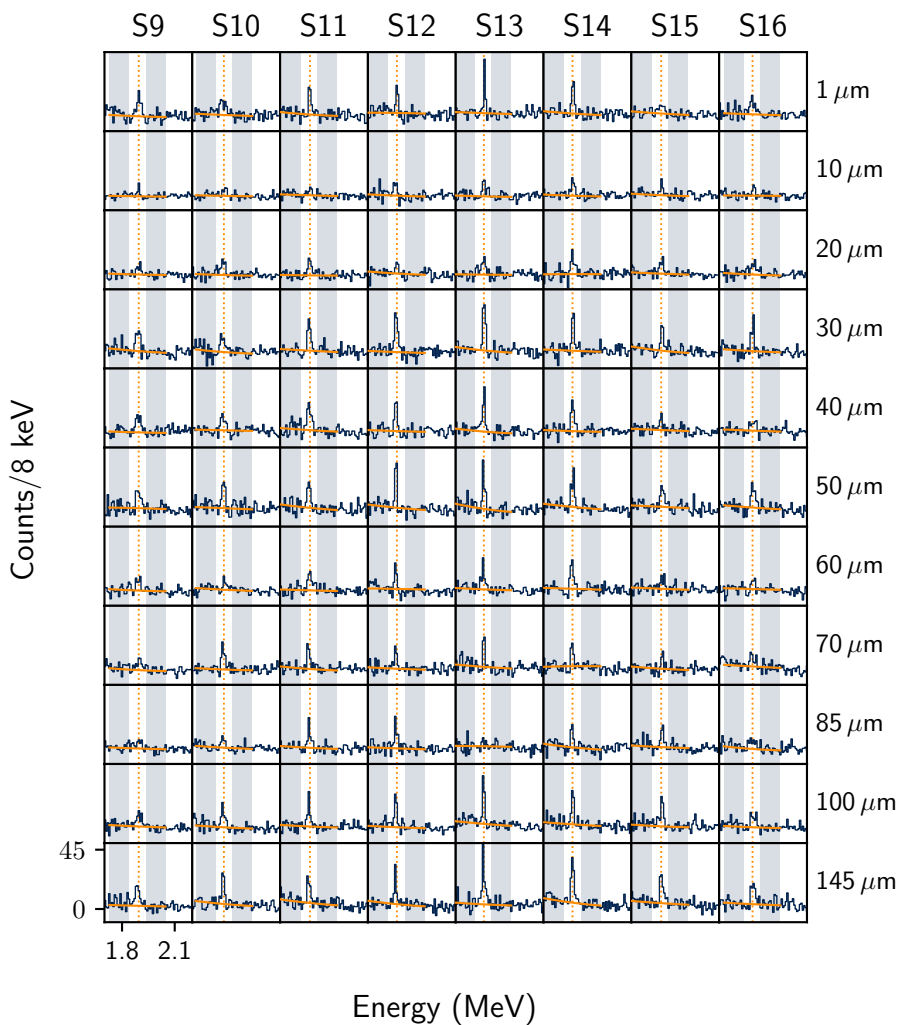
Figure D.26.: Particle gated energyspectra of Ge 9 of HORUS.
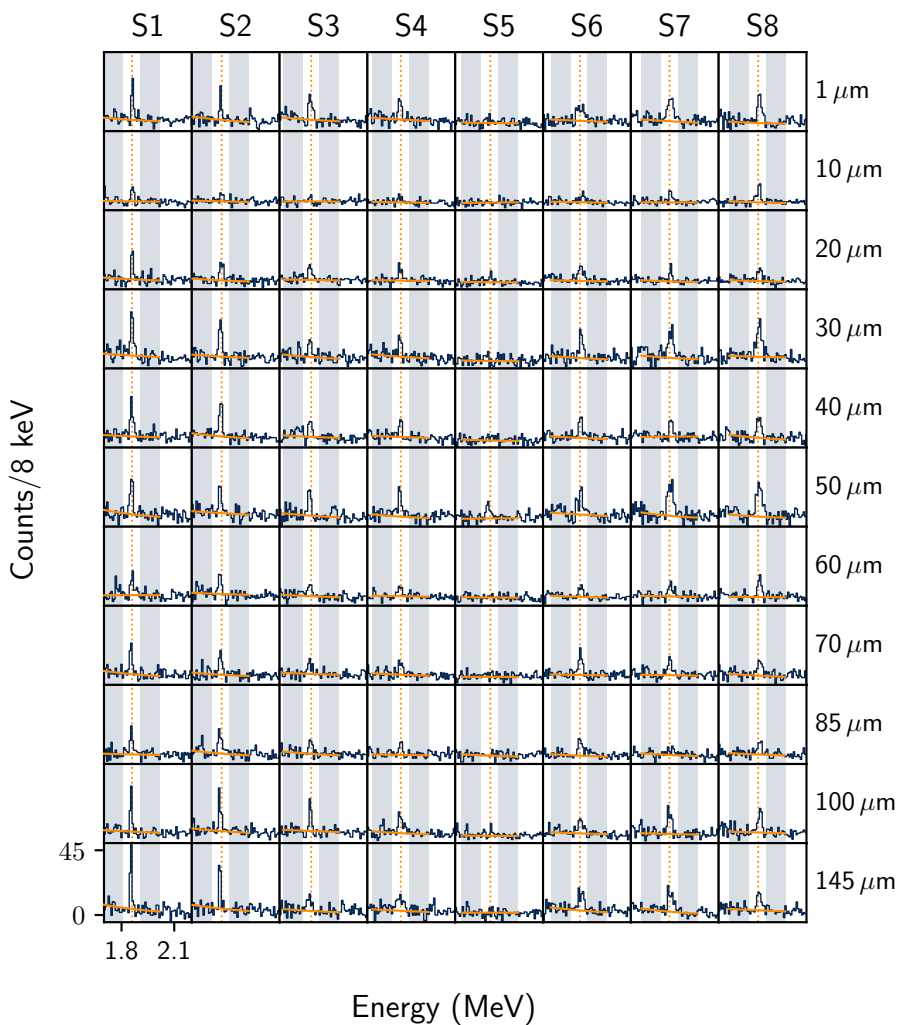
Figure D.27.: Particle gated energyspectra of Ge 10 of HORUS.

D. Supplementary data for the TDRIV experiment.
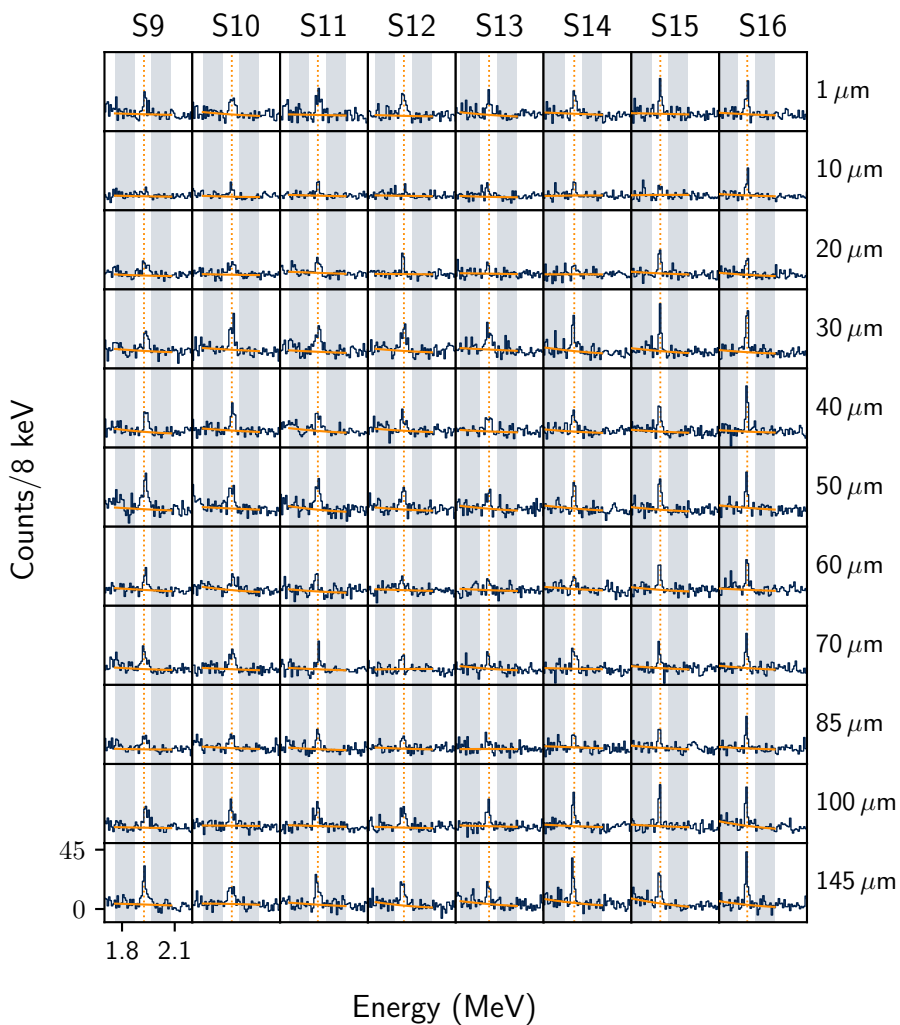
Figure D.28.: Particle gated energyspectra of Ge 10 of HORUS.
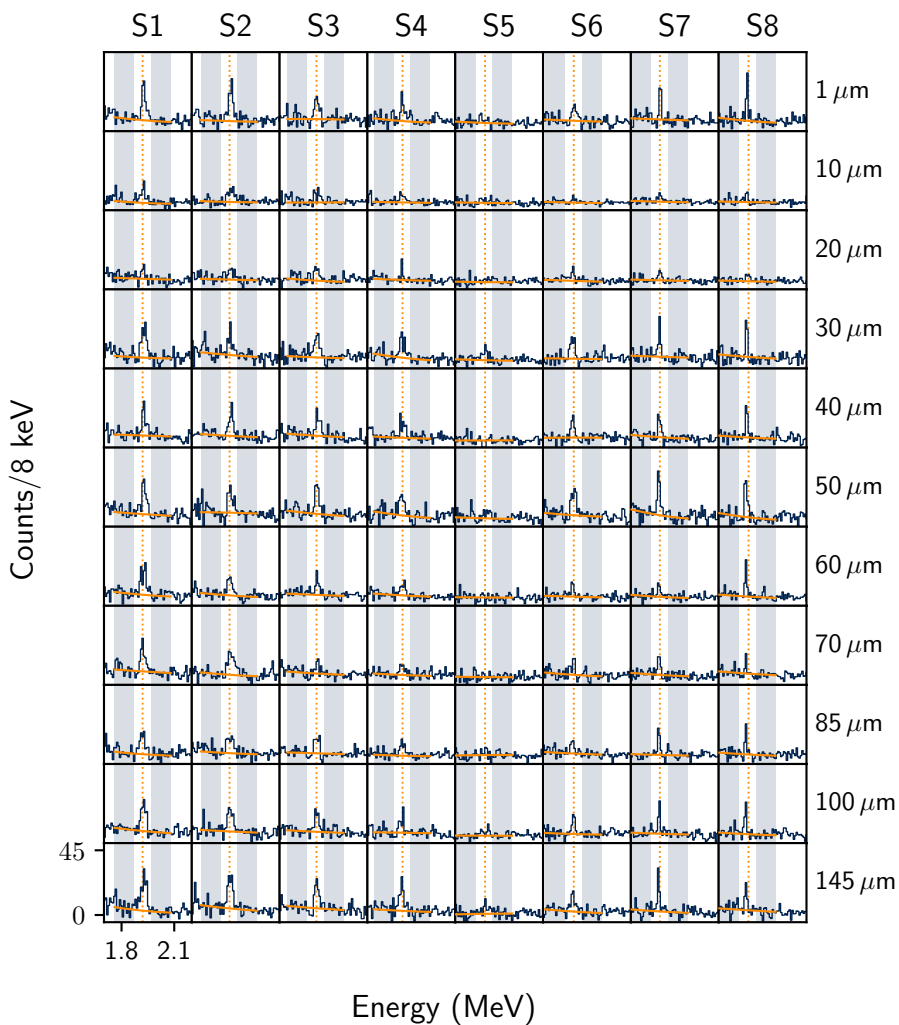
Figure D.29.: Particle gated energyspectra of Ge 11 of HORUS.

D. Supplementary data for the TDRIV experiment.
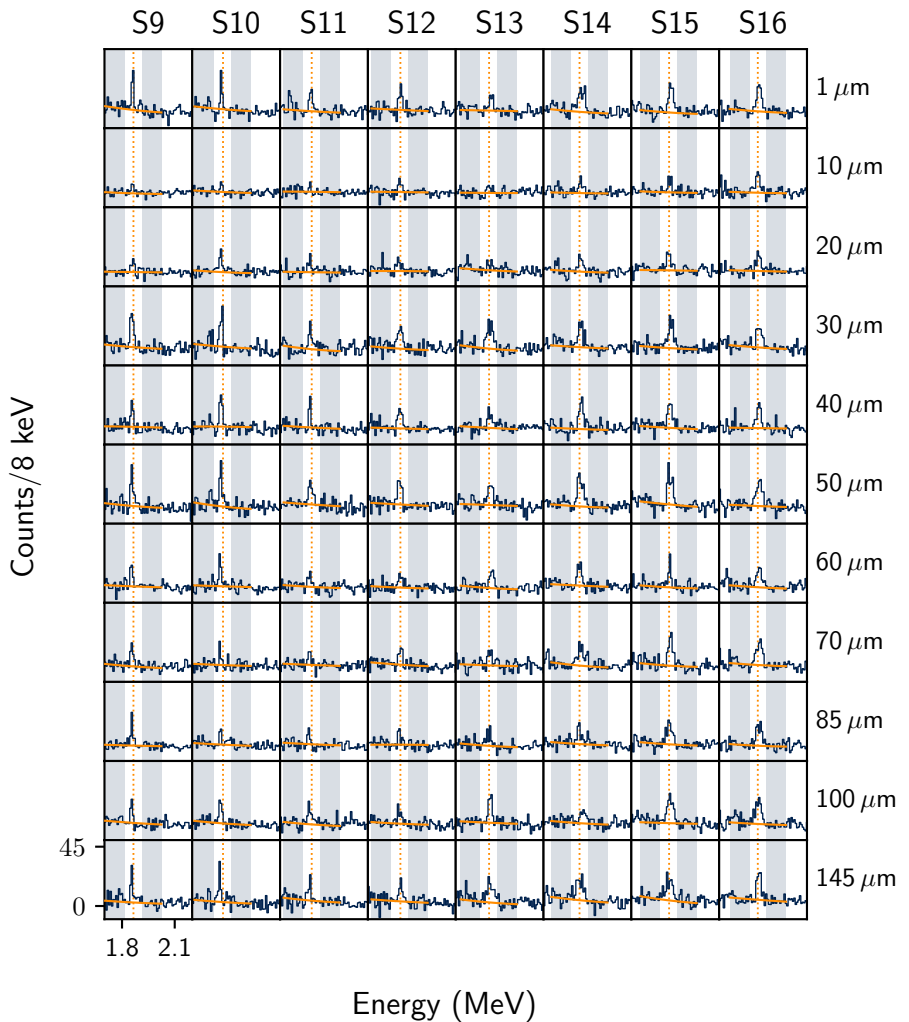
Figure D.30.: Particle gated energyspectra of Ge 11 of HORUS.
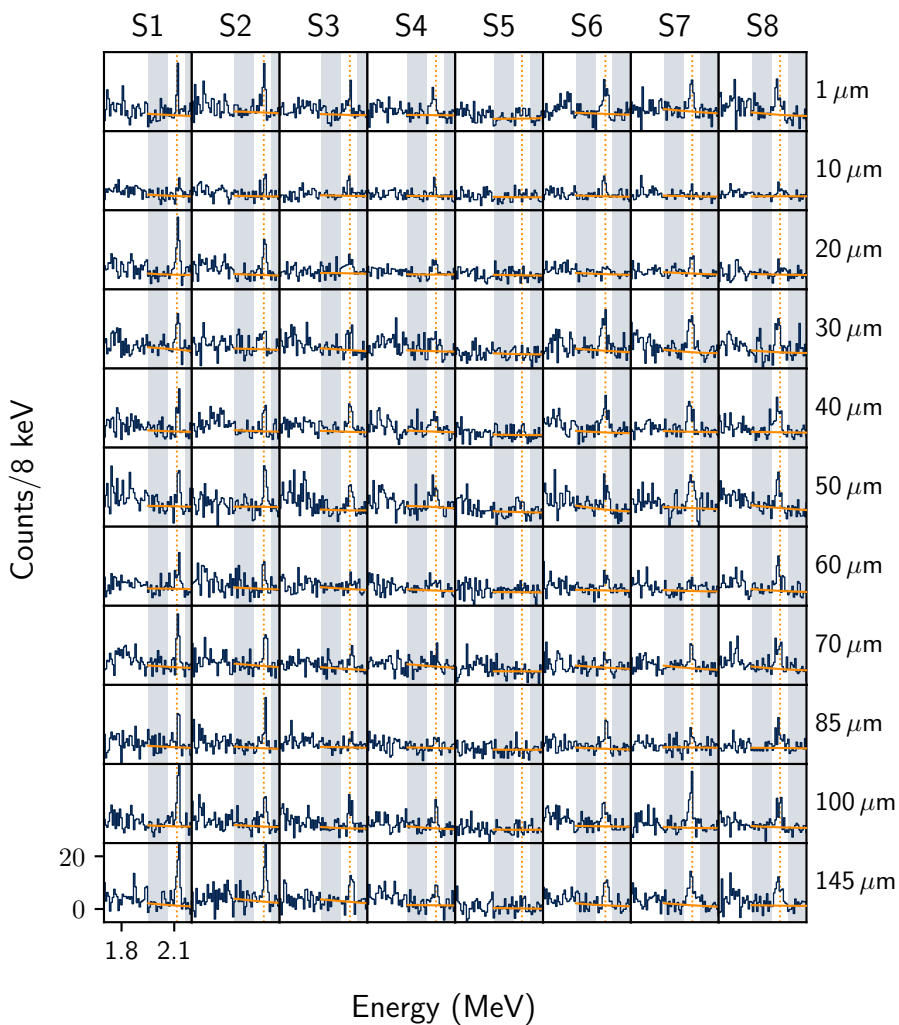
Figure D.31.: Particle gated energyspectra of Ge 12 of HORUS.
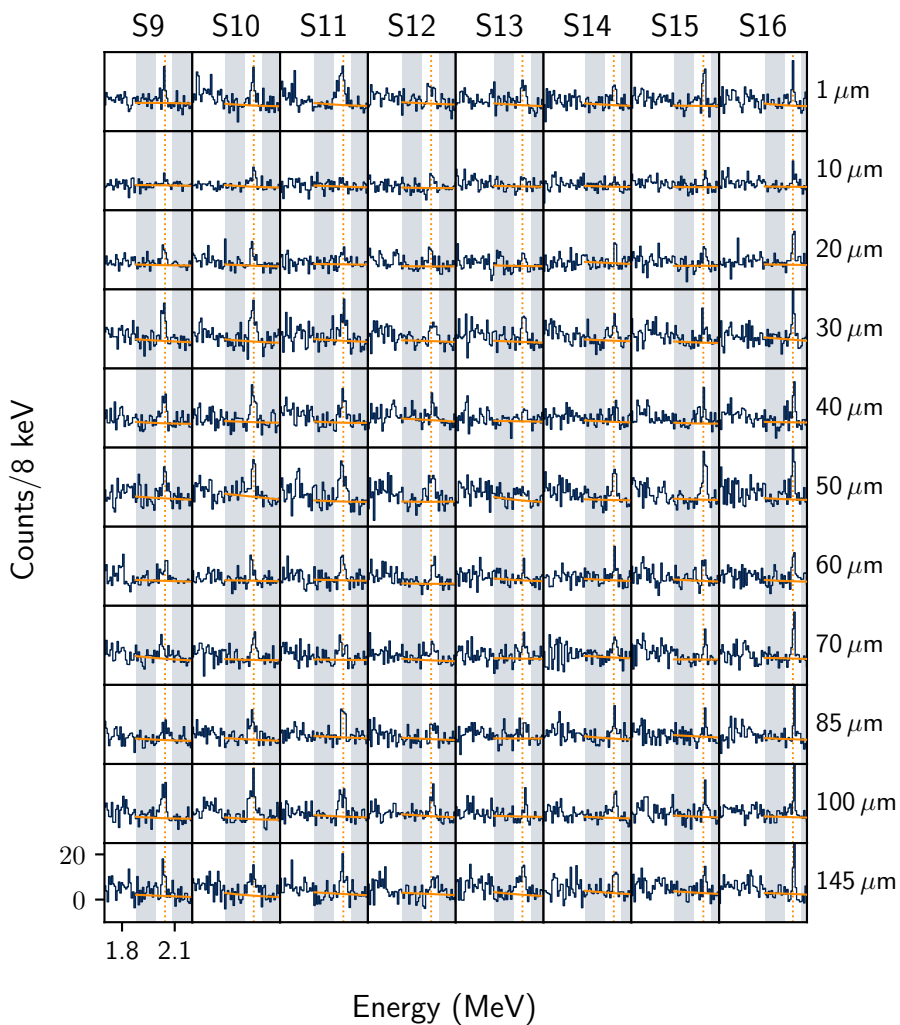
Figure D.32.: Particle gated energyspectra of Ge 12 of HORUS.
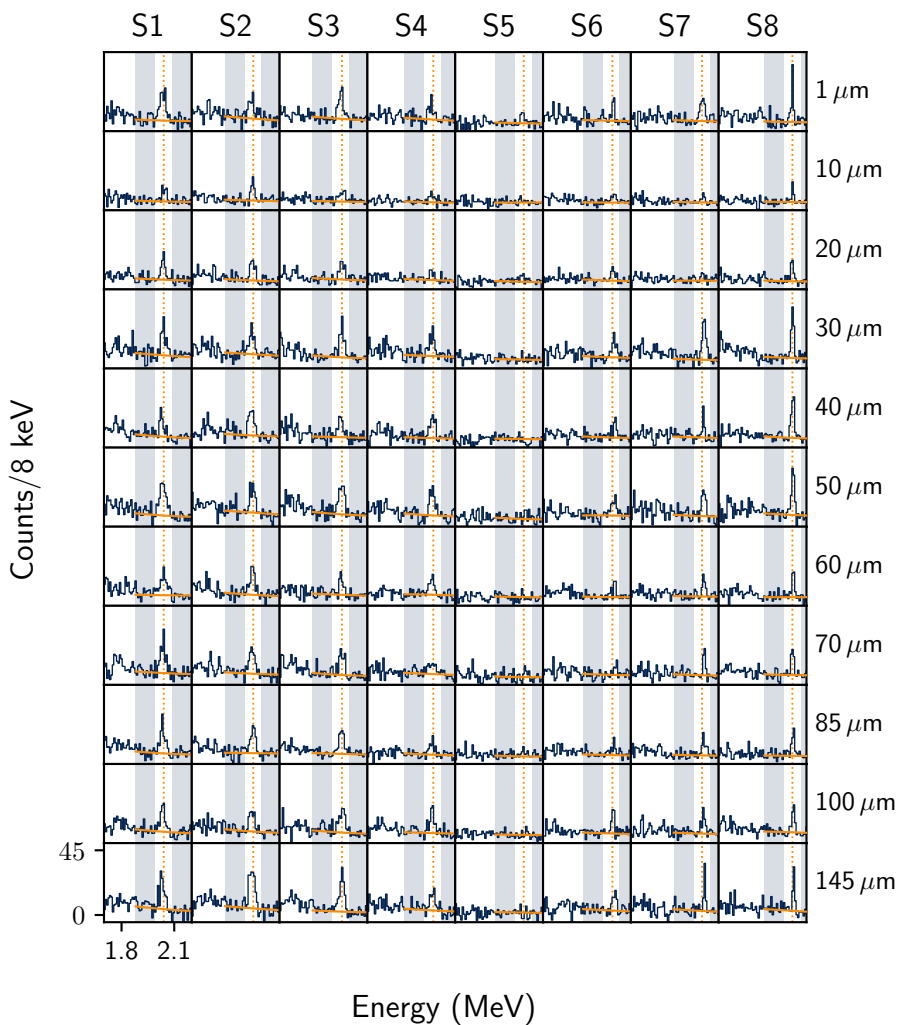
Figure D.33.: Particle gated energyspectra of Ge 13 of HORUS.
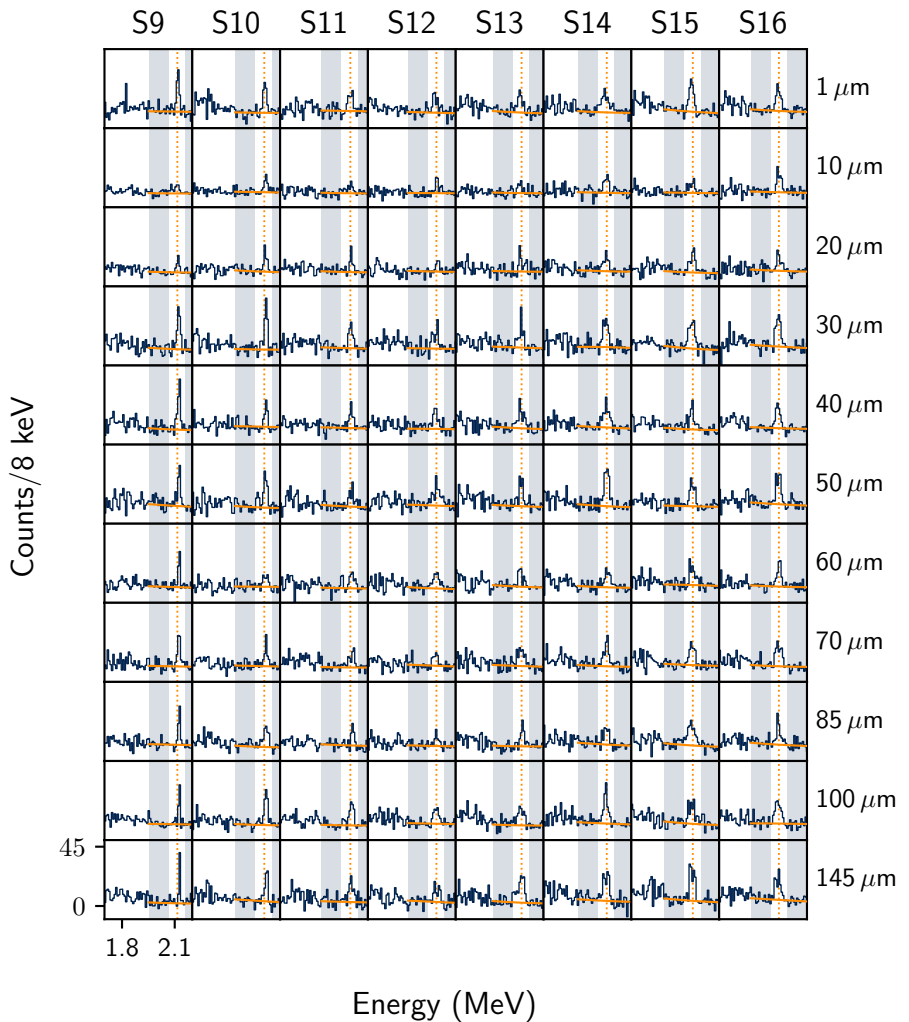
Figure D.34.: Particle gated energyspectra of Ge 13 of HORUS.

D.5. Angular correlations as a function of $\triangle \phi$

D. Supplementary data for the TDRIV experiment.
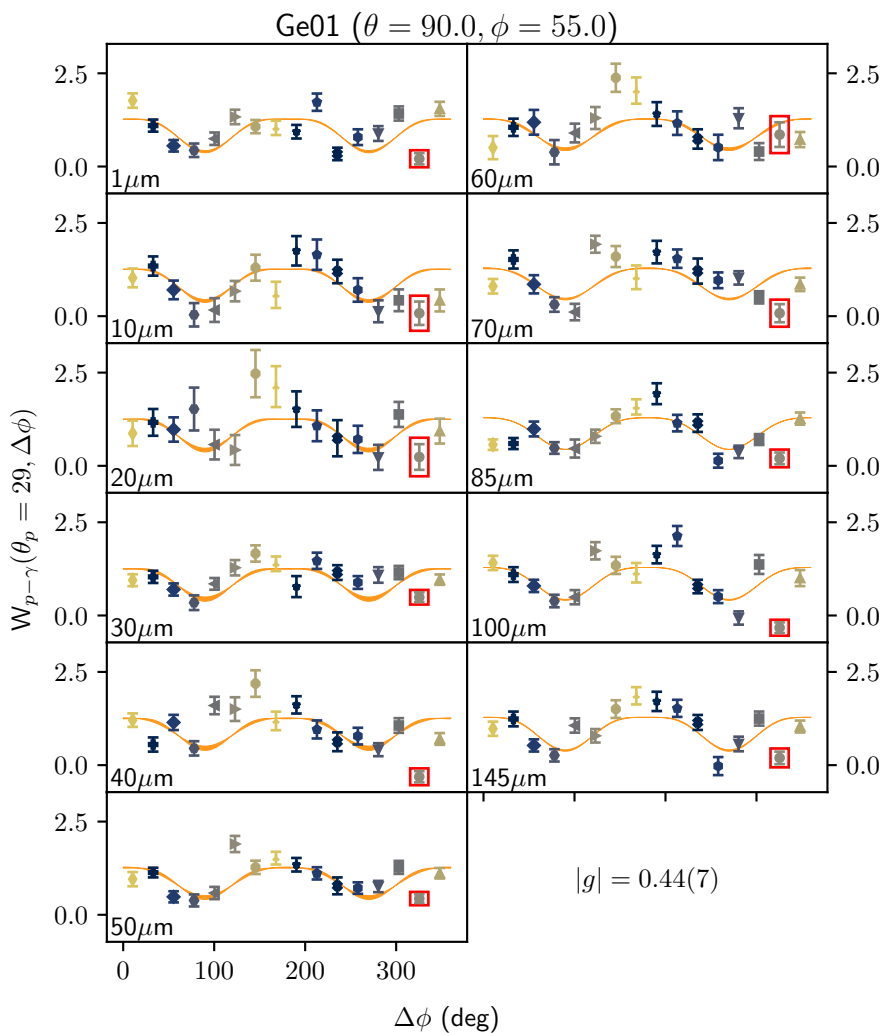
Figure D.35.: Angular correlation Ge01.
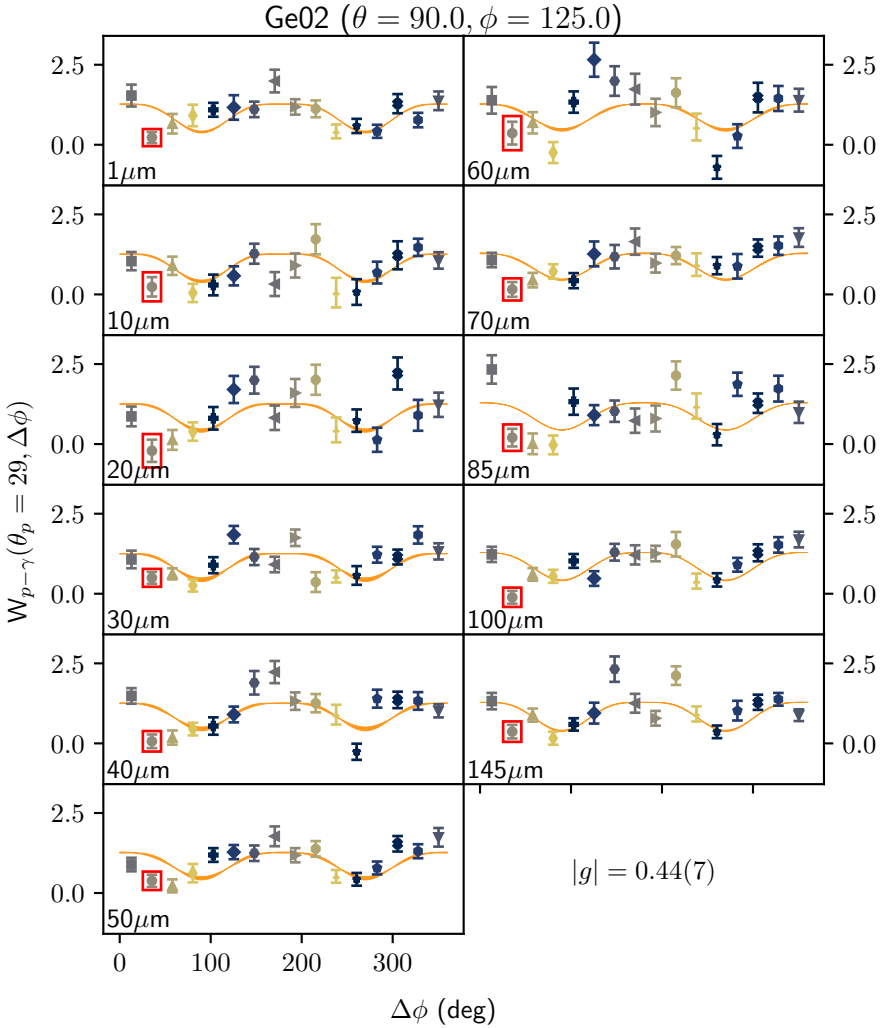
Figure D.36.: Angular correlation Ge02.

D. Supplementary data for the TDRIV experiment.
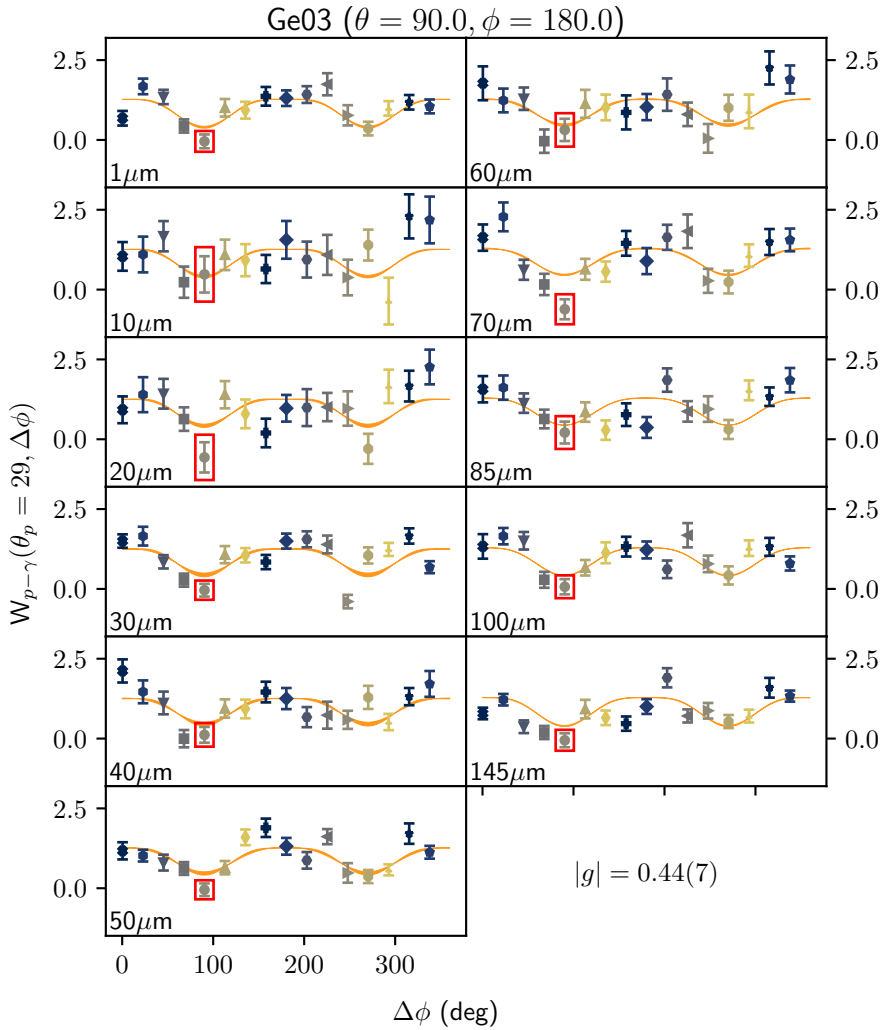
Figure D.37.: Angular correlation Ge03.
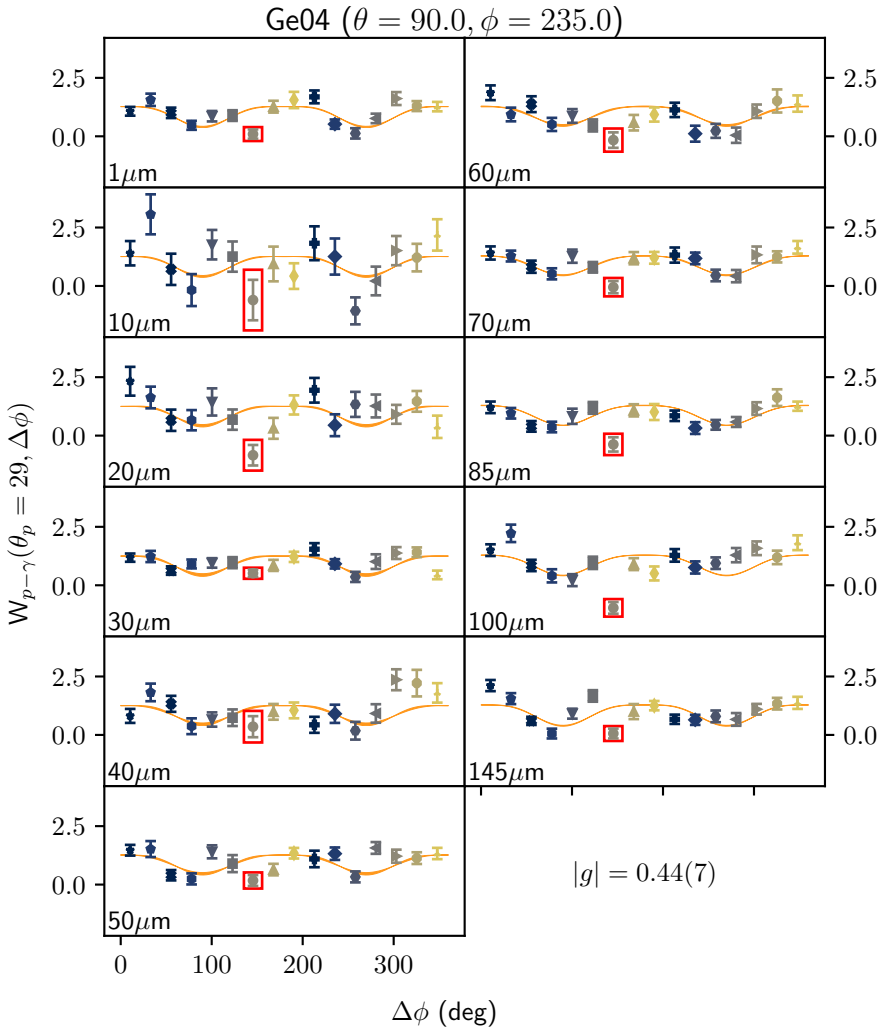
Figure D.38.: Angular correlation Ge04.

D. Supplementary data for the TDRIV experiment.
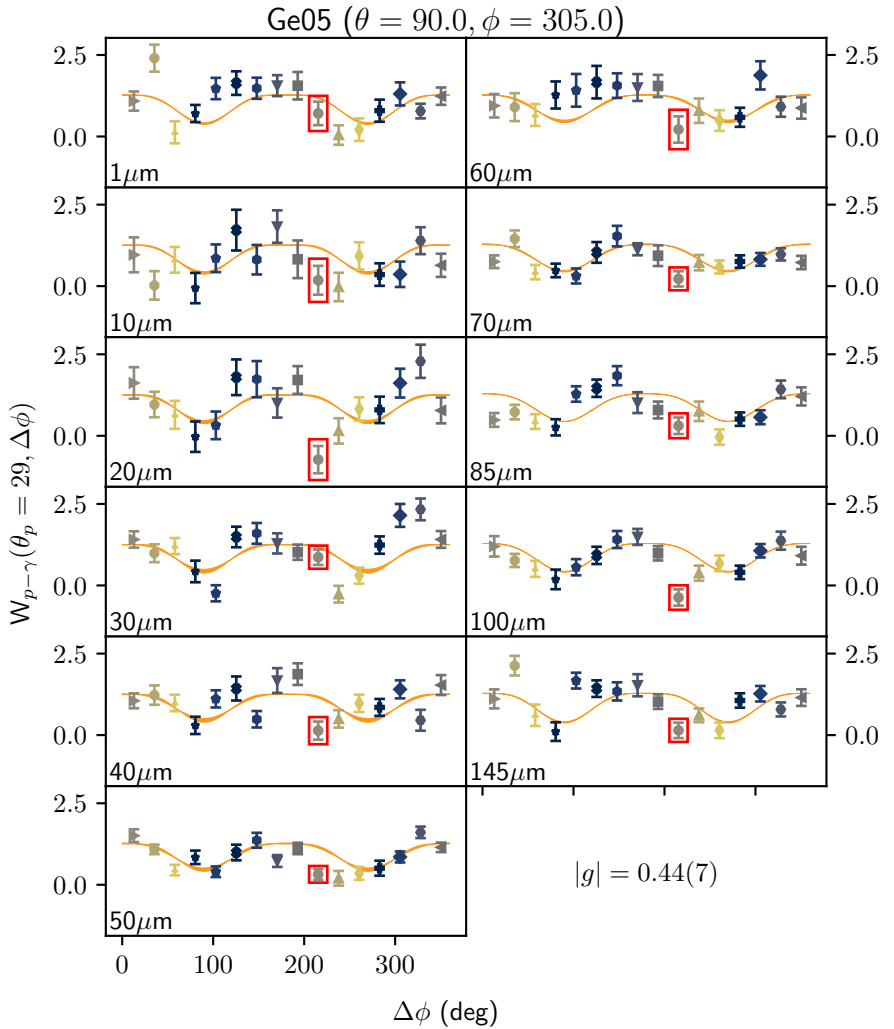
Figure D.39.: Angular correlation Ge05.
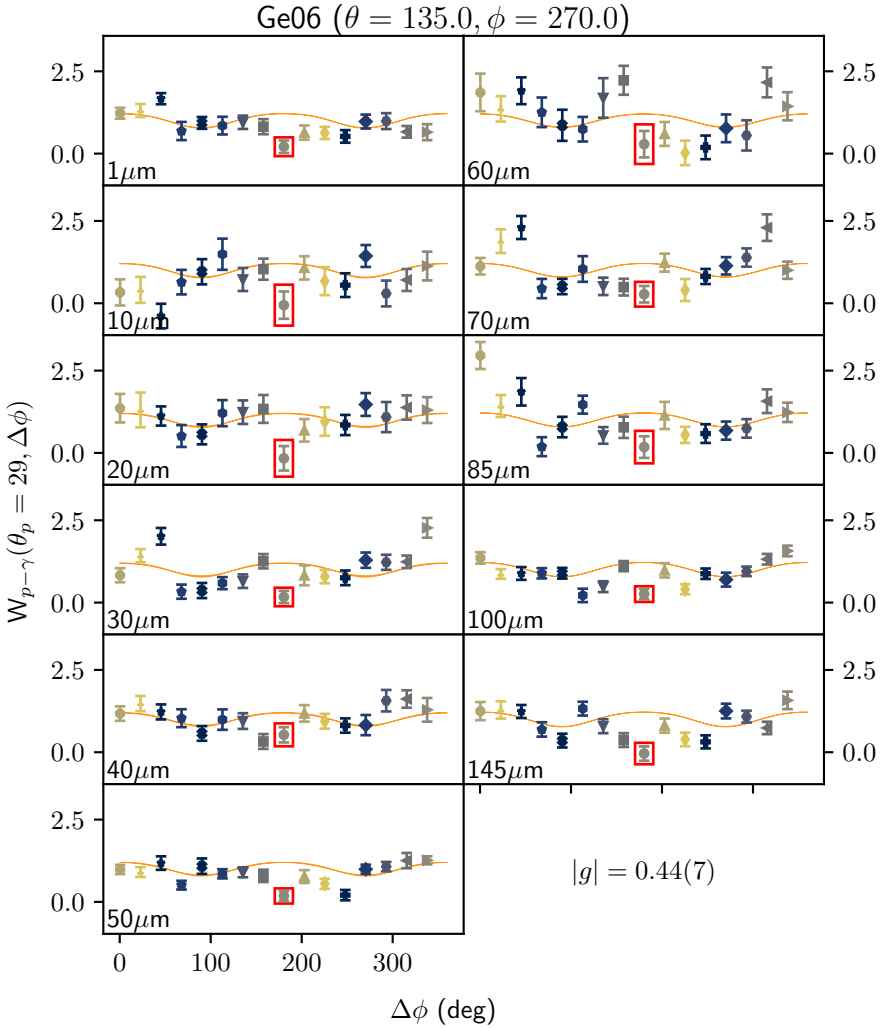
Figure D.40.: Angular correlation Ge06.
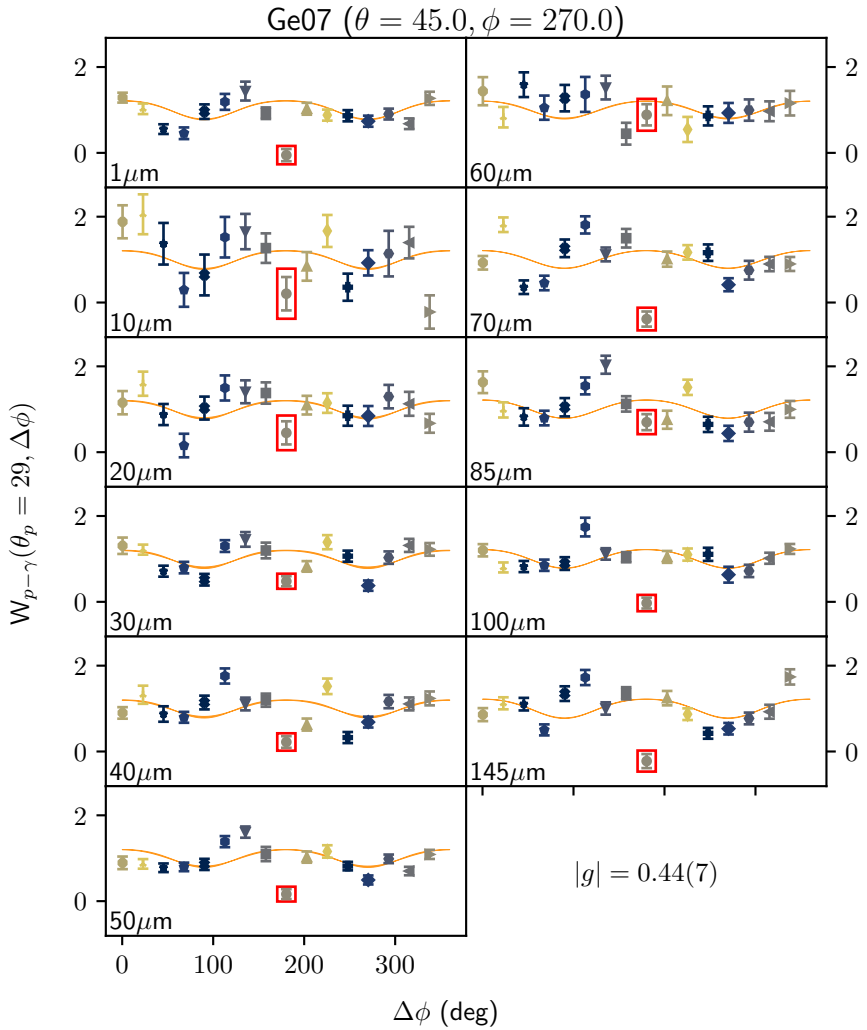
Figure D.41.: Angular correlation Ge07.
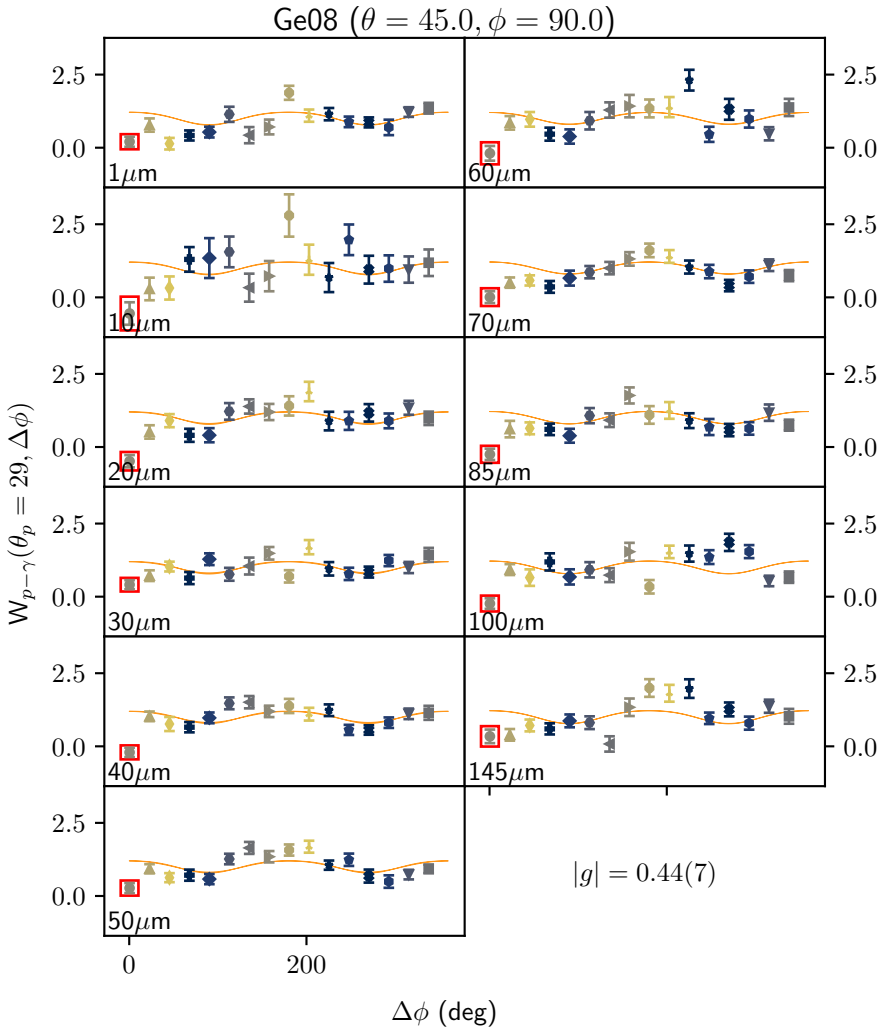
Figure D.42.: Angular correlation Ge08.
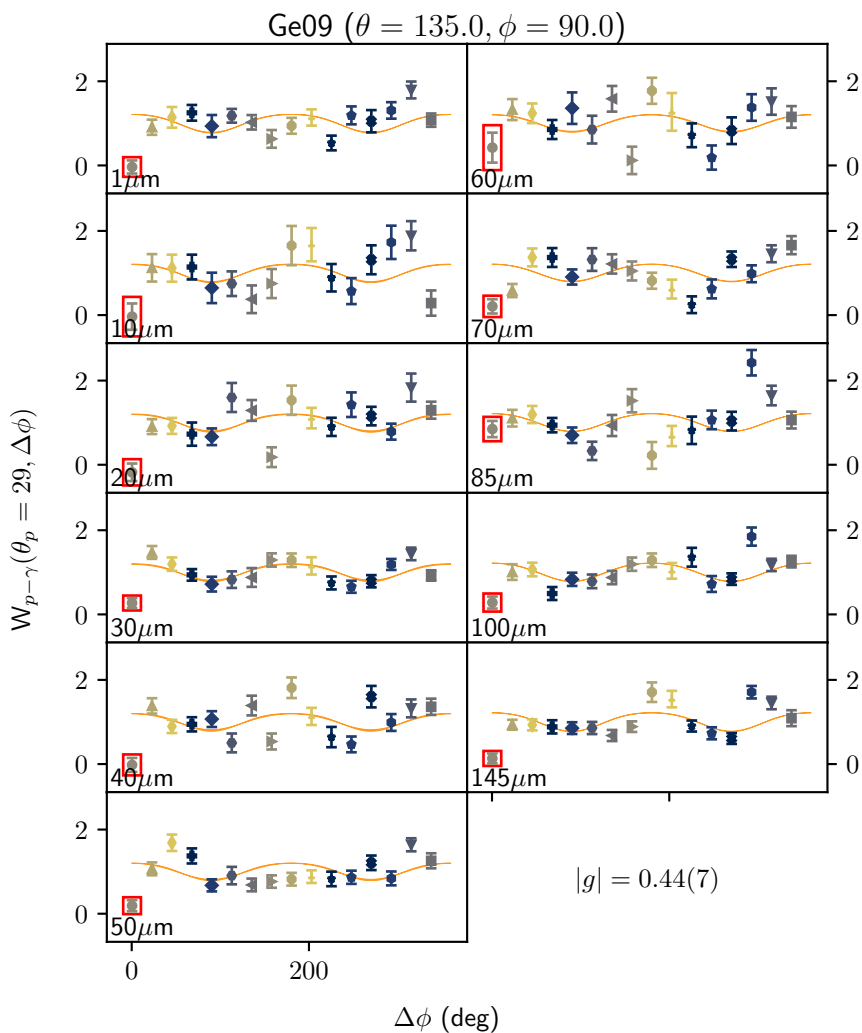
Figure D.43.: Angular correlation Ge09.
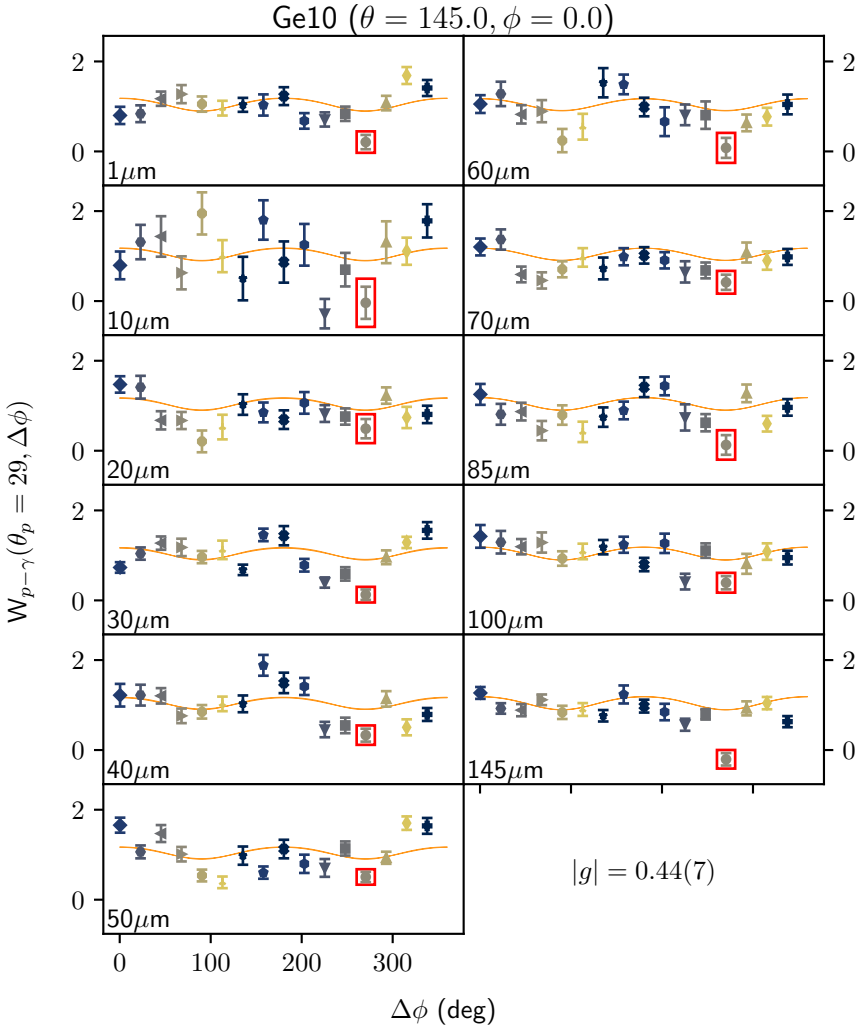
Figure D.44.: Angular correlation Ge10.
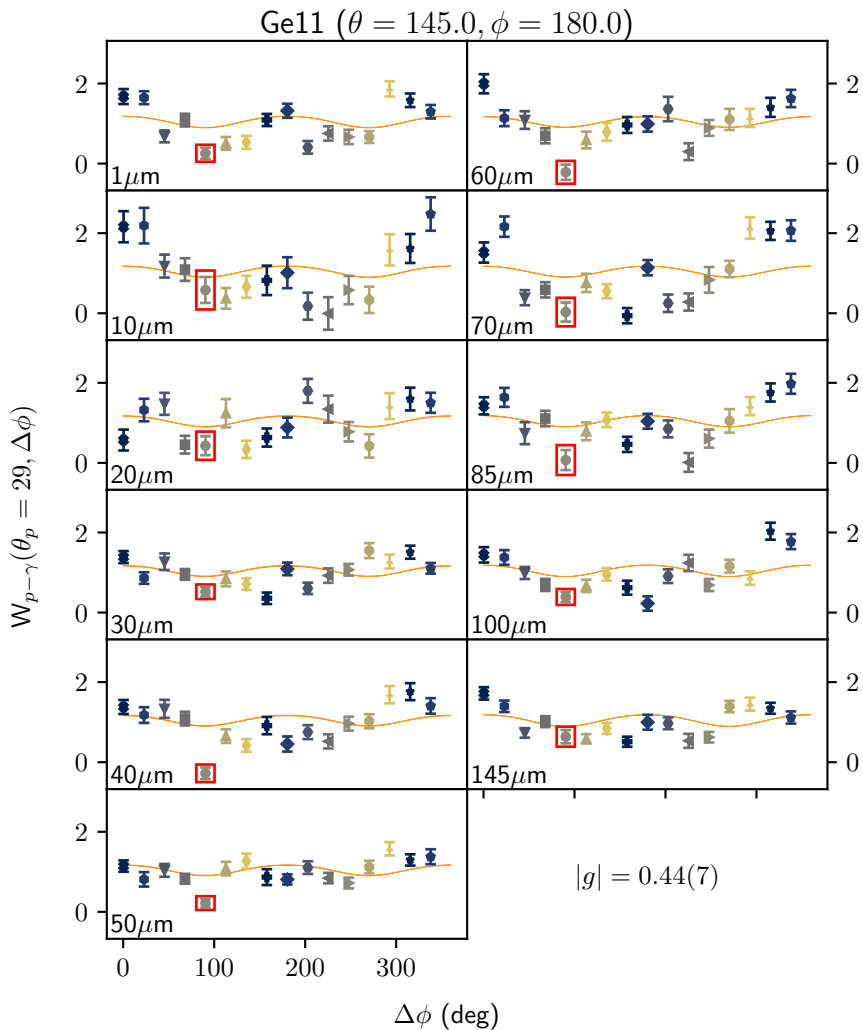
Figure D.45.: Angular correlation Ge11.
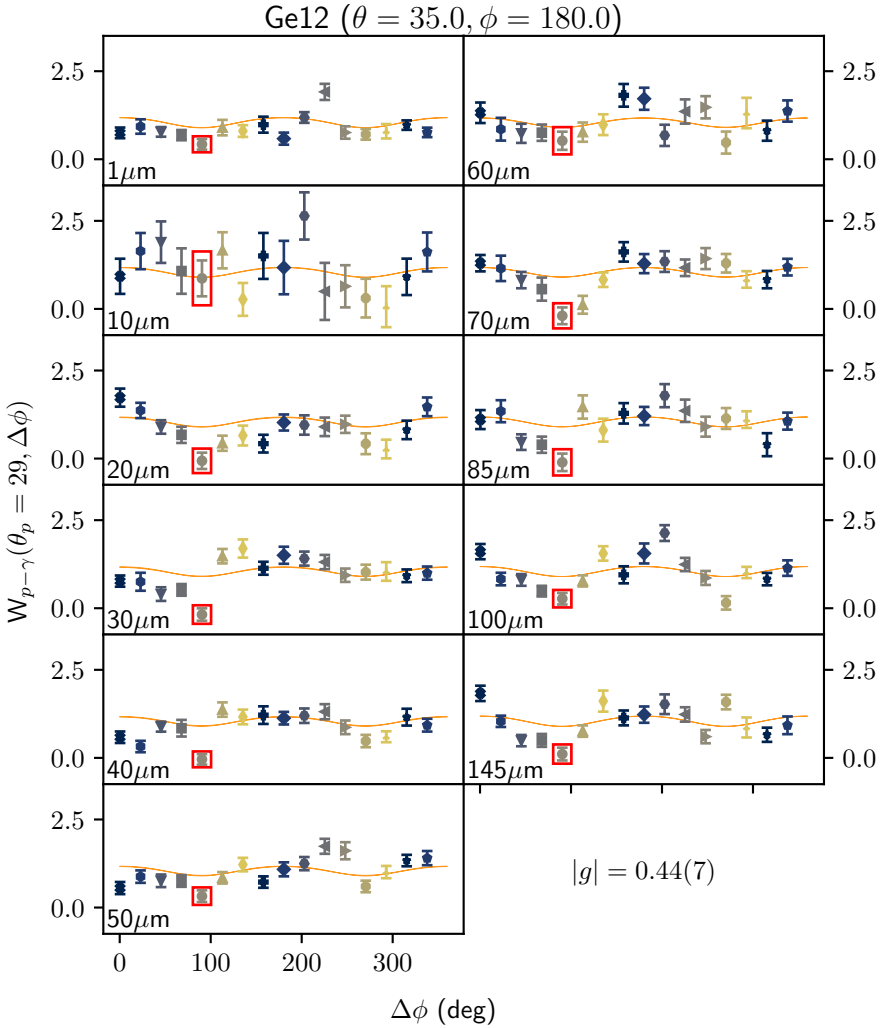
Figure D.46.: Angular correlation Ge12.

D. Supplementary data for the TDRIV experiment.
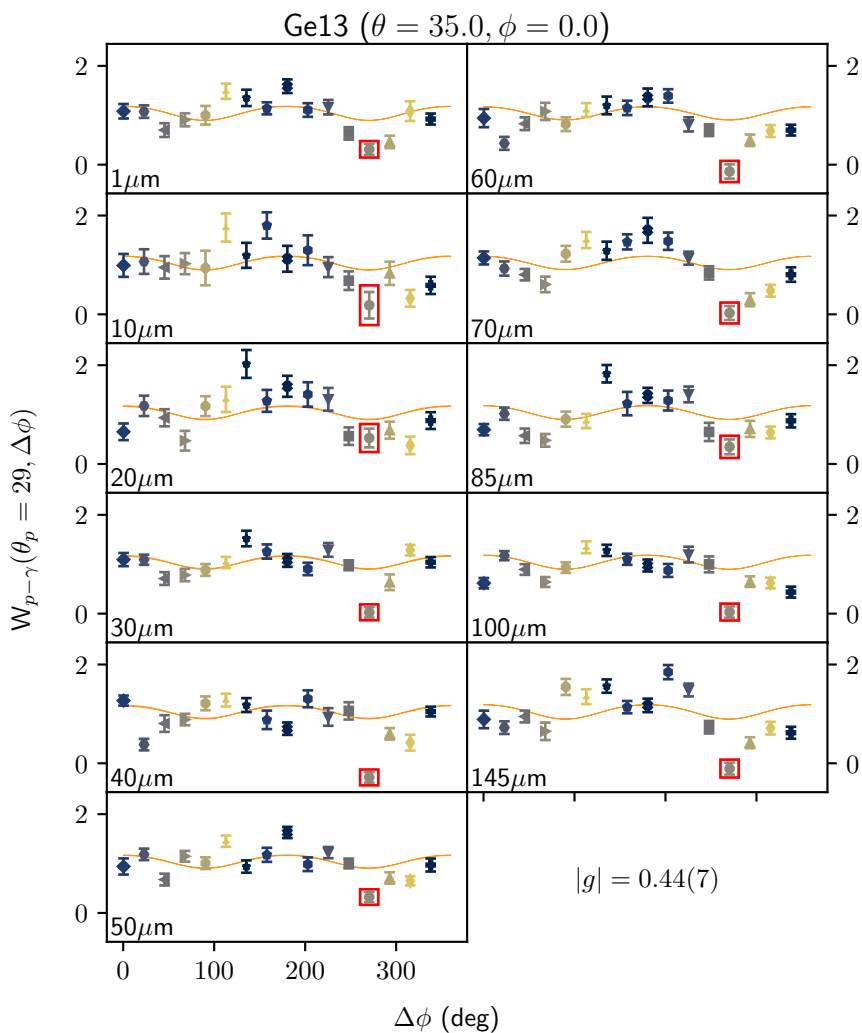
Figure D.47.: Angular correlation Ge13.

Bibliography

[1]   H. Becquerel, *Sur les radiations émises par phosphorescence*, C. R. Acad. Sci. **122**, 420 (1896).

[2]   E. Rutherford, *LXXIX. The scattering of and particles by matter and the structure of the atom*, Philos. Mag. J. Sci. **21**, 669 (1911).

[3]   E. Epelbaum, H.-W. Hammer, and U. Meißner, *Modern theory of nuclear forces*, Rev. Mod. Phys. **81**, 1773 (2009).

[4]   W. Marciano and H. Pagels, *Quantum chromodynamics*, Nature, 479 (1979).

[5]   F. Geissel, G. Münzenberg, and K. Riisager, *Secondary exotic nuclear beams*, Annu. Rev. Nucl. Part. Sci. **45**, 163 (1995).

[6]   T. Nakamura, H. Sakurai, and H. Watanabe, *Exotic nuclei explored at in-flight separators*, Prog. Part. Nucl. Phys. **97**, 53 (2017).

[7]   E. Simpson, *The Colourtul Nuclide Chart*, (2019) `http://people.physics.anu.edu.au/~ecs103/chart` (visited on 09/12/2019).

[8]   B. Singh, *From ENSDF database*, (2019) `https://www.nndc.bnl.gov/ensdf/` (visited on 08/19/2019).

[9]   E. V. D. van Loef and et al., *Scintillation properties of LaCl3:Ce3+ crystals: fast, efficient, and high-energy resolution scintillators*, IEEE Trans. Nucl. Sci. **48**, 341 (2001).

[10] S. Akkoyun et al., (AGATA collaboration), *AGATA—Advanced GAmma Tracking Array*, Nucl. Instrum. Methods. Phys. Res., Sec. A **668**, 26 (2012).

[11] I. Y. Lee et al., *GRETINA: A gamma ray energy tracking array*, Nucl. Phys. A **746**, 255 (2004).

[12] S. Paschalis et al., *The performance of the Gamma-Ray Energy Tracking In-beam Nuclear Array GRETINA*, Nucl. Instrum. Methods. Phys. Res., Sec. A **709**, 44 (2013).

[13] T. Otsuka et al., *Evolution of Nuclear Shells due to the Tensor Force*, Phys. Rev. Lett. **95**, 232502 (2005).

[14] T. Otsuka et al., *Novel Features of Nuclear Forces and Shell Evolution in Exotic Nuclei*, Phys. Rev. Lett. **104**, 012501 (2010).

[15] J. Dobaczewski et al., *Shell structure of exotic nuclei*, Prog. Part. Nucl. Phys. **59**, 432 (2007).

[16] O. Sorlin and M.-G. Porquet, *Nuclear magic numbers: New features far from stability*, Prog. Part. Nucl. Phys. **61**, 602 (2008).

[17] B. Bastin et al., *Collapse of the $N = 28$ Shell Closure in ^{42}Si*, Phys. Rev. Lett. **99**, 022503 (2007).

[18] K. Tshoo et al., *$N = 16$ Spherical Shell Closure in ^{24}O*, Phys. Rev. Lett. **109**, 022501 (2012).

[19] H. N. Liu et al., *How Robust is the $N = 34$ Subshell Closure? First Spectroscopy of ^{52}Ar*, Phys. Rev. Lett. **122**, 072502 (2019).

[20] R. F. Casten, *Nuclear Structure from a Simple Perspective* (Oxford University Press, 2005).

[21] C. W. Reich, *Nuclear Data Sheets for A = 156*, Nucl. Data Sheets **113**, 2537 (2012).

[22] N. Nica, *Nuclear Data Sheets for A = 158*, Nucl. Data Sheets **141**, 1 (2017).

[23] C. W. Reich, *Nuclear Data Sheets for A=160*, Nucl. Data Sheets **105**, 557 (2005).

[24] C. W. Reich, *Nuclear Data Sheets for A = 162*, Nucl. Data Sheets **108**, 1807 (2007).

[25] B. Singh and J. Chen, *Nuclear Data Sheets for A=164*, Nucl. Data Sheets **147**, 1 (2018).

[26] C. M. Baglin, *Nuclear Data Sheets for A = 166*, Nucl. Data Sheets **109**, 1103 (2008).

[27] C. M. Baglin, *Nuclear Data Sheets for A = 168*, Nucl. Data Sheets **111**, 1807 (2010).

[28] C. M. Baglin, *Nuclear Data Sheets for A = 170*, Nucl. Data Sheets **96**, 611 (2002).

[29] B. Singh, *Nuclear Data Sheets for A = 172*, Nucl. Data Sheets **75**, 199 (1995).

[30] E. Browne and H. Junde, *Nuclear Data Sheets for A = 174*, Nucl. Data Sheets **87**, 15 (1999).

[31] M. S. Basunia, *Nuclear Data Sheets for A = 176*, Nucl. Data Sheets **107**, 791 (2006).

[32] E. Achterberg, O. A. Capurro, and G. V. Marti, *Nuclear Data Sheets for A = 178*, Nucl. Data Sheets **110**, 1473 (2009).

[33] E. A. McCutchan, *Nuclear Data Sheets for A = 180*, Nucl. Data Sheets **126**, 151 (2015).

[34] B. Singh, *Nuclear Data Sheets for A = 182*, Nucl. Data Sheets **130**, 21 (2015).

[35] F. Iachello and A. Arima, *The interacting boson model* (Cambridge University Press, 2006).

[36] V. Werner et al., *Evolution of collectivity near mid-shell from excited-state lifetime measurements in rare- earth nuclei*, Phys. Rev. C **93**, 034323 (2016).

[37] J. Y. Zhang et al., *Consistent interpretation of B(E2) values and g factors in deformed nuclei*, Phys. Rev. C **73**, 037301 (2006).

[38] Z. Berant et al., *g factor of the 2_1^+ state of ^{164}Yb*, Phys. Rev. C **69**, 034320 (2004).

[39] B. A. Bian et al., *Systematics of g factors of 2_1^+ states in even-even nuclei from Gd to Pt: A microscopic description by the projected shell model*, Phys. Rev. C **75**, 014312 (2007).

[40] M. Rudigier et al., *Evolution of E2 transition strength in deformed hafnium isotopes from new measurements on ^{172}Hf, ^{174}Hf, and ^{176}Hf*, Phys. Rev. C **91**, 044301 (2015).

[41] B. Pritychenko et al., *Tables of E2 transition probabilities from the first 2+ states in even-even nuclei*, Atom. Data Nucl. Data Tables **107**, 1 (2016).

[42] R. B. Cakirli, K. Blaum, and R. F. Casten, *Indication of a mini-valence Wigner-like energy in heavy nuclei*, Phys. Rev. C **82**, 061304 (2010).

[43] A. Costin et al., *Lifetime measurement for the 2_1^+ state of ^{170}Hf*, Phys. Rev. C **74**, 067301 (2006).

[44] J.-M. Régis et al., *Sub-nanosecond lifetime measurements using the Double Orange Spectrometer at the cologne 10MV Tandem accelerator*, Nucl. Instrum. Methods. Phys. Res., Sec. A **606**, 466 (2009).

[45] M. Rudigier et al., *Lifetime of the first excited 2^+ state in ^{172}W and ^{178}W*, Nucl. Phys. A **847**, 89 (2010).

[46] T. D. Johnson et al., *Nuclear Data Sheets for A = 142*, Nucl. Data Sheets **112**, 1949 (2011).

[47] A. A. Sonzogni, *Nuclear Data Sheets for A = 144*, Nucl. Data Sheets **93**, 599 (2001).

[48] Y. Khazov, A. Rodionov, and G. Shulyak, *Nuclear Data Sheets for A = 146*, Nucl. Data Sheets **136**, 163 (2016).

[49] N. Nica, *Nuclear Data Sheets for A = 148*, Nucl. Data Sheets **117**, 1 (2014).

[50] S. K. Basu and A. A. Sonzogni, *Nuclear Data Sheets for A = 150*, Nucl. Data Sheets **114**, 435 (2013).

[51] M. J. Martin, *Nuclear Data Sheets for A = 152*, Nucl. Data Sheets **114**, 1497 (2013).

[52] C. W. Reich, *Nuclear Data Sheets for A = 154*, Nucl. Data Sheets **110**, 2257 (2009).

[53] **J. Wiederhold**, *Fast-timing lifetime measurement of ^{150}Gd. - in preparation*, 2020.

[54] R. F. Casten and N. V. Zamfir, *Empirical Realization of a Critical Point Description in Atomic Nuclei*, Phys. Rev. Lett. **87**, 052503 (2001).

[55] R. Krücken et al., *B(E2) Values in ^{150}Nd and the Critical Point Symmetry X(5)*, Phys. Rev. Lett. **88**, 232501 (2002).

[56] D. Tonev et al., *Transition probabilities in* ^{154}Gd*: Evidence for X(5) critical point symmetry*, Phys. Rev. C **69**, 034334 (2004).

[57] O. Möller et al., *Electromagnetic transition strengths in* ^{156}Dy, Phys. Rev. C **74**, 024313 (2006).

[58] R. F. Casten, *Quantum phase transitions and structural evolution in nuclei*, Prog. Part. Nucl. Phys. **62**, 183 (2009).

[59] E. Cheifetz et al., *Experimental Information Concerning Deformation of Neutron Rich Nuclei in the A* ~ 100 *Region*, Phys. Rev. Lett. **25**, 38 (1970).

[60] P. Federman and S. Pittel, *Towards a unified microscopic description of nuclear deformation*, Phys. Lett. B **69**, 385 (1977).

[61] C. Kremer et al., *First Measurement of Collectivity of Coexisting Shapes Based on Type II Shell Evolution: The Case of* ^{96}Zr, Phys. Rev. Lett. **117**, 172503 (2016).

[62] W. Witt et al., *Sub-shell closure and shape coexistence in the transitional nucleus* ^{98}Zr, Phys. Rev. C **98**, 041302 (2018).

[63] E. A. McCutchan, N. V. Zamfir, and R. F. Casten, *Mapping the interacting boson approximation symmetry triangle: New trajectories of structural evolution of rare-earth nuclei*, Phys. Rev. C **69**, 064306 (2004).

[64] P. Cejnar and J. Jolie, *Quantum phase transitions in the interacting boson model*, Prog. Part. Nucl. Phys. **62**, 210 (2009).

[65] P. von Brentano et al., *Alternative Interpretation of Sharply Rising E*0 *Strengths in Transitional Regions*, Phys. Rev. Lett. **93**, 152502 (2004).

[66] J. Bonnet et al., *E*0 *transition strengths from X(5) to the rigid rotor*, Phys. Rev. C **79**, 034307 (2009).

[67] S. Zerguine, P. Van Isacker, and A. Bouldjedri, *Consistent description of nuclear charge radii and electric monopole transitions*, Phys. Rev. C **85**, 034331 (2012).

[68] N. R. Johnson et al., *Lifetimes of states in the transitional nucleus* ^{152}Gd, Phys. Rev. C **26**, 1004 (1982).

[69] G. Neyens, *Nuclear magnetic and quadrupole moments for nuclear structure research on exotic nuclei*, Rep. Prog. Phys. **66**, 633 (2003).

[70] G. Neyens, *Nuclear magnetic and quadrupole moments for nuclear structure research on exotic nuclei*, Rep. Prog. Phys. **66**, 1251 (2003).

[71] C. Hoffman et al., *Evidence for a doubly magic ^{24}O*, Phys. Lett. B **672**, 17 (2009).

[72] E. K. Warburton, J. A. Becker, and B. A. Brown, *Mass systematics for $A = 29 - -44$ nuclei: The deformed A~32 region*, Phys. Rev. C **41**, 1147 (1990).

[73] B. A. Brown and W. D. M. Rae, *The Shell-Model Code NuShellX@MSU*, Nucl. Data Sheets **120**, 115 (2014).

[74] B. A. Brown and W. A. Richter, *New "USD" Hamiltonians for the sd shell*, Phys. Rev. C **74**, 034315 (2006).

[75] W. A. Richter, S. Mkhize, and B. A. Brown, *sd-shell observables for the USDA and USDB Hamiltonians*, Phys. Rev. C **78**, 064302 (2008).

[76] G. Goldring, *Hyperfine interactions in isolated ions*, edited by R. Bock, Vol. 3, Heavy Ion Collisions (North Holland Publishing, 1982), p. 483.

[77] A. E. Stuchbery, P. F. Mantica, and A. N. Wilson, *Electron-configuration-reset time-differential recoil-in-vaccum technique for excited-state g-factor measurements on fast exotic beams*, Phys. Rev. C **71**, 047302 (2005).

[78] A. Kusoglu et al., *Magnetism of an Excited Self-Conjugate Nucleus: Precise Measurement of the g Factor of the 2_1^+ State in ^{24}Mg*, Phys. Rev. Lett. **114**, 062501 (2015).

[79] A. Kusoglu, *Nuclear Moments and Lifetimes of Excited States in Exotic Nuclei*, PhD thesis (Istanbul University, 2016).

[80] D. R. Tilley et al., *Energy levels of light nuclei A = 18–19*, Nucl. Phys. A **595**, 1 (1995).

[81] M. S. Basunia, *Nuclear Data Sheets for A = 22*, Nucl. Data Sheets **127**, 69 (2015).

[82] B. P. McCormick et al., *Probing the N = 14 subshell closure: g factor of the $^{26}Mg(2_1^+)$ state*, Phys. Lett. B **779**, 445 (2018).

[83] M. S. Basunia, *Nuclear Data Sheets for A = 30*, Nucl. Data Sheets **111**, 2331 (2010).

[84] N. Nica and B. Singh, *Nuclear Data Sheets for A = 34*, Nucl. Data Sheets **113**, 1563 (2012).

[85] J. Chen, *Nuclear Data Sheets for A=38*, Nucl. Data Sheets **152**, 1 (2018).

[86] N. J. Stone, *Table of nuclear magnetic dipole and electric quadrupole moments*, Atom. Data Nucl. Data Tables **90**, 75 (2005).

[87] K. S. Krane, *Introductory Nuclear Physics* (John Wiley & Sons, 1988).

[88] A. Bohr and B. R. Mottelson, *Nuclear Structure - Volume II: Nuclear Deformations* (World Scintific Publishing, 1999).

[89] I. Talmi, *Simple models of Complex Nuclei* (Harwood Academic Publishers, 1993).

[90] G. Scharff-Goldhaber and J. Weneser, *System of Even-Even Nuclei*, Phys. Rev. **98**, 212 (1955).

[91] A. Bohr and B. R. Mottelson, *Collective and individual-particle aspects of nuclear structure*, Mat. Fys. Medd. Dan. Vid. Selk. **27** (1953).

[92] F. Iachello, *Dynamic Symmetries at the Critical Point*, Phys. Rev. Lett. **85**, 3580 (2000).

[93] F. Iachello, *Analytic Description of Critical Point Nuclei in a Spherical-Axially Deformed Shape Phase Transition*, Phys. Rev. Lett. **87**, 052502 (2001).

[94] N. Pietralla and O. M. Gorbachenko, *Evolution of the "β excitation" in axially symmetric transitional nuclei*, Phys. Rev. C **70**, 011304 (2004).

[95] G. Gneuss and W. Greiner, *Collective potential energy surfaces and nuclear structure*, Nucl. Phys. A **171**, 449 (1971).

[96] K. Dusling and N. Pietralla, *Description of ground-state band energies in well-deformed even-even nuclei with the confined β-soft rotor model*, Phys. Rev. C **72**, 011303 (2005).

[97] L. N. Cooper, *Bound Electron Pairs in a Degenerate Fermi Gas*, Phys. Rev. **104**, 1189 (1956).

[98] D. D. Warner and R. F. Casten, *Revised Formulation of the Phenomenological Interacting Boson Approximation*, Phys. Rev. Lett. **48**, 1385 (1982).

[99] P. O. Lipas, P. Toivonen, and D. D. Warner, *IBA consistent-Q formalism extended to the vibrational region*, **155**, 295 (1985).

[100] R. F. Casten, *Shape phase transitions and critical-point phenomena in atomic nuclei*, Nature Phys. **2**, 811 (2006).

[101] R. F. Casten et al., *Algebraic Approaches to Nuclear Structure*, edited by R. F. Casten (Harwood Academic Publishers, 1993).

[102] G. Siems et al., *Multiple quadrupole "phonon" excitations in ^{130}Ba*, Phys. Lett. B **320**, 1 (1994).

[103] T. Otsuka and K.-H. Kim, *Multiphonon structure of γ-unstable or O(6) nuclei*, Phys. Rev. C **50**, R1768–R1770 (1994).

[104] N. Pietralla et al., *Distribution of Low-Lying Quadrupole Phonon Strength in Nuclei*, Phys. Rev. Lett. **73**, 2962 (1994).

[105] N. Pietralla et al., *Odd-spin yrast states as multiple quadrupole-phonon excitations*, Phys. Lett. B **349**, 1 (1995).

[106] N. Pietralla et al., *2_1^+ and 2_2^+ states in collective nuclei as multiple Q-phonon excitations*, Phys. Rev. C **57**, 150 (1998).

[107] Y. V. Palchikov, P. von Brentano, and R. V. Jolos, *Universal description of the 0_2^+ state in collective even-A nuclei*, Phys. Rev. C **57**, 3026 (1998).

[108] J. Suhonen, *From Nucleons to Nucleus - Concepts of Microscopic Nuclear Theory* (Springer Verlag, 2007).

[109] G. F. Knoll, *Radiation Detection and Measurement* (John Wiley & Sons, 2000).

[110] H. Morinaga and T. Yamazaki, *In-beam Gamma-ray Spectroscopy* (North Holland Publishing, 1976).

[111] Sóti, Z., Magill, J., and Dreher, R., *Karlsruhe Nuclide Chart 10th edition 2018*, Euro. Phys. J. N **5**, 6 (2019).

[112] K. Alder et al., *Study of Nuclear Structure by Electromagnetic Excitation with Accelerated Ions*, Rev. Mod. Phys. **28**, 432 (1956).

[113] K. Alder and A. Winther, *Coulomb Excitation* (Academic Press, 1966).

[114] K. Alder and A. Winther, *Electromagnetic Excitation* (North Holland Publishing, 1975).

[115] R. Shankar, *Principles of Quantum Mechanics* (Springer Verlag, 1994).

[116] H. Ower, *Coulombanregung von Hochspinzuständen in ^{232}Th, ^{234}U und ^{236}U*, PhD thesis (Johann Wolfgang Goethe-Universität, 1980).

[117] F. Pühlhofer, *On the interpretation of evaporation residue mass distributions in heavy-ion induced fusion reactions*, Nucl. Phys. A **280**, 267 (1977).

[118] O. B. Tarasov and D. Bazin, *LISE++: Radioactive beam production with in-flight separators*, Nucl. Instrum. Methods. Phys. Res., Sec. B **266**, 4657 (2008).

[119] A. Gavron, *Statistical model calculations in heavy ion reactions*, Phys. Rev. C **21**, 230 (1980).

[120] A. Bohr and B. R. Mottelson, *Nuclear Structure - Volume I: Single-Particle Motion* (World Scintific Publishing, 1999).

[121] V. F. Weisskopf, *Radiative Transition Probabilities in Nuclei*, Phys. Rev. C **3**, 1073 (1951).

[122] F. Metzger, *Resonance Fluorescence in Nuclei*, edited by O. R. Frisch, Vol. 7, Progress in Nuclear Physics (Pergamon Press, 1959), p. 53.

[123] U. Kneissl, H. H. Pitz, and A. Zilges, *Investigaion of nuclear structure by resonance fluorescence scattering*, Prog. Part. Nucl. Phys. **37**, 349 (1996).

[124] U. Kneissl, N. Pietralla, and A. Zilges, *Low-lying dipole modes in vibrational nuclei studied by photon scattering*, J. Phys. G **32**, R217 (2006).

[125] P. J. Nolan and J. F. Sharpey-Schafer, *The measurement of the lifetimes of excited nuclear states*, Rep. Prog. Phys. **42**, 1 (1979).

[126] A. Z. Schwarzschild and E. K. Warburton, *The measurement of short nuclear lifetimes*, Annu. Rev. Nucl. Part. Sci. **18**, 265 (1968).

[127] A. Dewald, O. Möller, and P. Petkov, *Developing the Recoil Distance Doppler-Shift technique towards a versatile tool for lifetime measurements of excited nuclear states*, Prog. Part. Nucl. Phys. **67**, 786–839 (2012).

[128] K. S. Shah et al., *LaBr$_3$:Ce Scintillators for Gamma Ray Spectroscopy*, IEEE Trans. Nucl. Sci. **50**, 2410 (2003).

[129] E. V. D. van Loef et al., *High-energy-resolution scintillator: Ce3+ activated LaBr3*, Appl. Phys. Lett. **79**, 1573 (2001).

[130] M. Moszynski et al., *Intrinsic energy resolution and light yield nonproportionality of BGO*, IEEE Trans. Nucl. Sci. **51**, 1074 (2004).

[131] K. Wisshak and F. Käppeler, *Large barium fluoride detectors*, Nucl. Instrum. Methods. Phys. Res., Sec. A **227**, 91 (1984).

[132] H. Mach, R. L. Gill, and M. Moszyński, *A method for picosecond lifetime measurements for neutron-rich nuclei: (1) Outline of the method*, Nucl. Instrum. Methods. Phys. Res., Sec. A **280**, 49 (1989).

[133] M. Moszyński and H. Mach, *A method for picosecond lifetime measurements for neutron-rich nuclei*, Nucl. Instrum. Methods. Phys. Res., Sec. A **277**, 407 (1989).

[134] J.-M. Régis et al., *The mirror symmetric centroid difference method for picosecond lifetime measurements via – coincidences using very fast LaBr3(Ce) scintillator detectors*, Nucl. Instrum. Methods. Phys. Res., Sec. A **622**, 83 (2010).

[135] J.-M. Régis et al., *The generalized centroid difference method for picosecond sensitive determination of lifetimes of nuclear excited states using large fast-timing arrays*, Nucl. Instrum. Methods. Phys. Res., Sec. A **726**, 191 (2013).

[136] N. Mărginean et al., *In-beam measurements of sub-nanosecond nuclear lifetimes with a mixed array of HPGe and LaBr3:Ce detectors*, Euro. Phys. J. A **46**, 329 (2010).

[137] D. Bucurescu et al., *The ROSPHERE γ-ray spectroscopy array*, Nucl. Instrum. Methods. Phys. Res., Sec. A **837**, 1 (2016).

[138] **J. Wiederhold** et al., *Fast-timing lifetime measurement of ^{152}Gd*, Phys. Rev. C **94**, 044302 (2016).

[139] **J. Wiederhold** et al., *Evolution of E2 strength in the rare-earth isotopes ^{174,176,178,180}Hf*, Phys. Rev. C **99**, 024316 (2019).

[140] L. M. Fraile et al., *Technical Report for the Design, Construction and Commisioning of FATIMA, the FAst TIMing Array*, tech. rep. (FAIR HISPEC-DESPEC Collaboration, 2015).

[141] Facility for Antiproton and Ion Research in Europe GmbH (FAIR GmbH), *Facility for Antiproton and Ion Research*, (2019) `https://fair-center.de/` (visited on 06/27/2019).

[142] J.-M. Régis et al., *Germanium-gated γ–γ fast timing of excited states in fission fragments using the EXILL&FATIMA spectrometer*, Nucl. Instrum. Methods. Phys. Res., Sec. A **763**, 210 (2014).

[143] M. Jentschel et al., *EXILL— a high-efficiency, high-resolution setup for γ-spectroscopy at an intense cold neutron beam facility*, J. Inst. **12**, P11003 (2017).

[144] P. Koseoglou, *Lifetime measurements in the neutron-rich ^{148}Ce nuclide at the low-Z boundary of the N = 90 shape-phase transition*, PhD thesis (Technische Universität Darmstadt, 2019).

[145] I. Y. Lee, *The GAMMASPHERE*, Nucl. Phys. A **520**, c641 (1990).

[146] N. Jovančević et al., *Spectroscopy of Neutron Induced Reactions with the -ball Spectrometer*, Acta. Phys. Pol. B **50**, 297 (2019).

[147] L. Boström et al., *Numerical analysis of the time spectrum of delayed co-incidences, I*, Nucl. Instrum. Methods **44**, 61 (1966).

[148] Z. Bay, *Calculation of Decay Times from Coincidence Experiments*, Phys. Rev. **77**, 419 (1950).

[149] A. E. Stuchbery, *γ-ray angular distributions and correlations after projectile-fragmentation reactions*, Nucl. Phys. A **723**, 69 (2003).

[150] T. Mayer-Kuckuk, *Kernphysik* (Vieweg+Teubner Verlag, 2002).

[151] A. Landé, *Termstruktur und Zeemaneffekt der Multipletts*, Z. Phys. **15**, 189 (1923).

[152] NIST, *CODATA values of the fundamental constants.*, (2019) `https://physics.nist.gov/cuu/Constants/index.html` (visited on 09/17/2019).

[153] T. Aoyama et al., *Tenth-Order QED Contribution to the Electron g−2 and an Improved Value of the Fine Structure Constant*, Phys. Rev. Lett. **109**, 111807 (2012).

[154] N. Benczer-Koller, M. Hass, and J. Sak, *Transient magnetic fields at swift ions traversing ferromagnetic media and application to measurements of nuclear moments*, Annu. Rev. Nucl. Part. Sci. **30**, 53 (1980).

[155] K.-H. Speidel, O. Kenn, and F. Nowacki, *Magnetic moments and nuclear structure*, Prog. Part. Nucl. Phys. **49**, 91 (2002).

[156]   A. E. Stuchbery et al., *Pushing the limits of excited-state g-factor measurements*, Euro. Phys. J. Web Conf. **178**, 02005 (2018).

[157]   A. E. Stuchbery, *Transient-field strengths for high-velocity light ions and applications to g-factor measurements on fast exotic beams*, Phys. Rev. C **69**, 064311 (2004).

[158]   G. Kumbartzki et al., *First g factor measurement using a radioactive ^{76}Kr beam*, Phys. Lett. B **591**, 213 (2004).

[159]   A. Boukhari, *Study of the nuclear spin-orientation in incomplete fusion reactions. Measurement of the magnetic moment of the 2^+ states in ^{22}Ne and ^{28}Mg*, PhD thesis (Université Paris-Saclay, 2019).

[160]   R. E. Horstman et al., *Recoil-distance measurements of g-factors for ^{24}Mg (2_1^+) and ^{20}Ne (2_1^+)*, Nucl. Phys. A **248**, 291 (1975).

[161]   M. E. Rose, *The Analysis of Angular Correlation and Angular Distribution Data*, Phys. Rev. **91**, 610 (1953).

[162]   K. Krane, *Solid-angle correction factors for coaxial Ge(Li) detectors*, Nucl. Instrum. Methods **98**, 205 (1972).

[163]   K. Krane, *Solid-angle correction factors for "five-sided" coaxial Ge(Li) detectors*, Nucl. Instrum. Methods **109**, 401 (1973).

[164]   E. P. Wigner, *On the matrices which reduce the Kronecker products of representations of S. R. groups*, 1940; Reprinted in J. C. Biedenharn and H. van Dam, eds., *Quantum Theory of Angular Momentum* (Academic Press, 1965), p. 87.

[165]   C. Stahl, *New methods for the γ-ray spectroscopy with position-sensitive detector systems*, PhD thesis (Technische Universität Darmstadt, 2015).

[166]   D. Pelte and D. Schwalm, *In-beam gamma-ray spectroscopy with heavy ions*, edited by R. Bock, Vol. 3, Heavy Ion Collisions (North Holland Publishing, 1982), p. 1.

[167]   Bracco, Angela, *The NuPECC long range plan 2017: perspectives in nuclear physics*, Europhysics News **48**, 21 (2017).

[168]   Y. Blumenfeld, T. Nilsson, and P. Van Duppen, *Facilities and methods for radioactive ion beam production*, Phys. Scr. T **152**, 014023 (2013).

[169] D. Dobrescu, D. V. Mosu, and S. Papureanu, *The Bucharest FN Tandem Accelerator: Modernization and Development*, AIP Conference Proceedings **1099**, 51 (2009).

[170] A. Linnemann, *Das HORUS-Würfelspektrometer und Multiphononanregungen in* ^{106}Cd, PhD thesis (Universität zu Köln, 2006).

[171] L. Netterdon et al., *The γ-ray spectrometer HORUS and its applications for nuclear astrophysics*, Nucl. Instrum. Methods. Phys. Res., Sec. A **754**, 94 (2014).

[172] B. Wolf, *Handbook of Ion Sources* (CRC Press, 1995).

[173] R. V. D. Graaff, *Tandem Electrostatic Accelerators*, Nucl. Instrum. Methods **8**, 195 (1960).

[174] W. Witt, *Type-II Shell Evolution in 98Zr*, PhD thesis (Technische Universität Darmstadt, 2019).

[175] V. Werner et al., *Shape transitions between and within Zr isotopes*, Euro. Phys. J. Web Conf. **223**, 01070 (2019).

[176] T. Beck et al., *SORCERER: A novel particle-detection system for transfer-reaction experiments at ROSPHERE*, Nucl. Instrum. Methods. Phys. Res., Sec. A **951**, 163090 (2019).

[177] **J. Wiederhold**, *Fast-timing Lebensdauermessung von* ^{152}Gd, M.Sc. Thesis (Technische Universität Darmstadt, 2015).

[178] D. Cline, Bull. Am. Phys. Soc. **14**, 726 (1969).

[179] M. Schiffer et al., *A dedicated AMS setup for medium mass isotopes at the Cologne FN tandem accelerator*, Nucl. Instrum. Methods. Phys. Res., Sec. B **406**, 287 (2017).

[180] M. G. Klein et al., *A new HVE 6 MV AMS system at the University of Cologne*, Nucl. Instrum. Methods. Phys. Res., Sec. B **269**, 3167 (2011).

[181] E. Fairstein, S. Wagner, et al., *IEEE standard test procedures for germanium gamma-ray detectors*, IEEE Std. (1996).

[182] E. Ricard, *Critical phase/shape transitions in heavy nuclei*, PhD thesis (Yale University, 2006).

[183] Micron Semiconductors Ltd, *Double-sided silicon strip detector S3*, (2019) http://www.micronsemiconductor.co.uk/product/s3/.

[184] F. Perez and B. E. Granger, *IPython: A System for Interactive Scientific Computing*, Comp. Sci. Engin. **9**, 21 (2007).

[185] S. van der Walt, S. C. Colbert, and G. Varoquaux, *The NumPy Array: A Structure for Efficient Numerical Computation*, Comp. Sci. Engin. **13**, 22 (2011).

[186] T. E. Oliphant, *A guide to NumPy* (Trelgol Publishing, 2006).

[187] W. McKinney, *Data Structures for Statistical Computing in Python*, in Proc. Python Sci. Conf. Edited by S. van der Walt and J. Millman (2010), p. 51.

[188] T. E. Oliphant, *Python for Scientific Computing*, Comp. Sci. Engin. **9**, 10 (2007).

[189] K. J. Millman and M. Aivazis, *Python for Scientists and Engineers*, Comp. Sci. Engin. **13**, 9 (2011).

[190] A. Meurer et al., *SymPy: symbolic computing in Python*, PeerJ Comp. Sci. **3**, e103 (2017).

[191] J. D. Hunter, *Matplotlib: A 2D Graphics Environment*, Comp. Sci. Engin. **9**, 90 (2007).

[192] Met Office, *Cartopy: a cartographic python library with a Matplotlib interface*, version 0.17.0 (Exeter, Devon, 2010-2018).

[193] Inkscape Project, *Inkscape*, version 0.92.4, Jan. 14, 2019.

[194] J. Mayer et al., *HDTV - Nuclear Spectrum Analysis Tool*, version 18.04, `https://gitlab.ikp.uni-koeln.de/staging/hdtv` (visited on 09/02/2019).

[195] O. Papst and U. Friman-Gayer, *Development version of: HDTV - Nuclear Spectrum Analysis Tool*, `https://github.com/op3/hdtv` (visited on 09/02/2019).

[196] J. Theuerkauf et al., *Program Tv*, Institut für Kernphysik, Universität zu Köln (1993), version 1.1.

[197] D. Bazzaco, C. A. Ur, and N. Marginean, *GASP Data Analysis Program Package GASPware*, version 6.11, 2001.

[198] BIPM, IEC, IFCC, ILAC, ISO, IUPAP and OIML 2008, *Evaluation of measurement data - Guide to the expression of uncertainty in measurement* (Joint Committee for Guide in Metrology, JCGM 100:2008, 2008).

[199]   U. Gayer et al., *Experimental M*1 *response of* ^{40}Ar *as a benchmark for neutrino-nucleus scattering calculations*, Phys. Rev. C **100**, 034305 (2019).

[200]   U. Friman-Gayer, *Probing Nuclear Structure Relevant for Neutrinoless Double-Beta Decay with Nuclear Resonance Flusorescence*, PhD thesis (Technische Universität Darmstadt, 2020).

[201]   D. Scott, *Multivariate Density Estimation: Theory, Practice, and Visualization* (John Wiley & Sons, 1992).

[202]   M. Tanabashi et al., (Particle Data Group), *Review of Particle Physics*, Phys. Rev. D **98**, 030001 (2018).

[203]   E. R. Gamba, A. M. Bruce, and M. Rudigier, *Treatment of background in* $\gamma-\gamma$ *fast-timing measurements*, Nucl. Instrum. Methods. Phys. Res., Sec. A **928**, 93 (2019).

[204]   M. T. Gillin and N. F. Peek, *Excited States of* ^{174}Hf *from the Decay of* ^{174}Ta, Phys. Rev. C **4**, 1334 (1971).

[205]   F. M. Bernthal, J. O. Rasmussen, and J. M. Hollander, *Decays of* ^{176}Ta, ^{176}Lu, *and* ^{176m}Lu *to Levels in* ^{176}Hf, Phys. Rev. C **3**, 1294 (1971).

[206]   T. L. Khoo et al., *Low-K bands in* ^{176}Hf *populated in the* $(\alpha, 2n)$ *reaction*, Nucl. Phys. A **202**, 289 (1973).

[207]   K. E. G. Löbner, H. A. Smith, and M. E. Bunker, *E1-M2-E3 mixing of the 1159.3 keV transition in 176Hf*, Nucl. Phys. A **179**, 276 (1972).

[208]   A. Winther and J. De Boer, *A computer program for multiple Coulomb excitation, reprinted in K. Alder and A. Winther, Coulomb excitation* (Academic Press, 1966).

[209]   T. Kibédi et al., *Evaluation of theoretical conversion coefficients using BrIcc*, Nucl. Instrum. Methods. Phys. Res., Sec. A **589**, 202 (2008).

[210]   N. Saed-Samii, J. Mayer, and N. Warr, *SOCOv2*, version 2, (2019) `https://gitlab.ikp.uni-koeln.de/nima/soco-v2` (visited on 09/12/2019).

[211]   N. Saed-Samii, *SOCOv2 Manual*, version 2 (2017).

[212]   J. Morel et al., *Precise determination of photon emission probabilities for the main X- and -rays of 226Ra in equilibrium with daughters*, Appl. Radiat. Isotopes **60**, 341 (2004).

[213] G. Gilmore and J. D. Hemingway, *Practical gamma-ray spectrometry* (John Wiley & Sons, 1995).

[214] L. Kaya et al., *Characterization and calibration of radiation-damaged double-sided silicon strip detectors*, Nucl. Instrum. Methods. Phys. Res., Sec. A **855**, 109 (2017).

[215] K. Livingston et al., *Heavy ion radiation damage in double-sided silicon strip detectors*, Nucl. Instrum. Methods. Phys. Res., Sec. A **370**, 445 (1996).

[216] V. Christé, M. M. Bé, and C. Dulieu, *Evaluation of decay data of radium-226 and its daughters*, International Conference on Nuclear Data for Science and Technology (ND2007) (2007).

[217] Collider Detector at Fermilab (CDF) collaboration, *Error bars for poisson data*, (2019) https://www-cdf.fnal.gov/physics/statistics/notes/pois_eb.txt (visited on 08/19/2019).

[218] J. M. Allmond et al., *Magnetic moments of 2_1^+ states in $^{124,126,128}Sn$*, Phys. Rev. C **87**, 054325 (2013).

[219] N. V. Zamfir et al., *Hexadecapole deformations in actinide and trans-actinide nuclei*, Phys. Lett. B **357**, 515 (1995).

[220] P. Möller et al., *Nuclear ground-state masses and deformations: FRDM(2012)*, Atom. Data Nucl. Data Tables **109-110**, 1 (2016).

[221] R. F. Casten, D. S. Brenner, and P. E. Haustein, *Valence p-n interactions and the development of collectivity in heavy nuclei*, Phys. Rev. Lett. **58**, 658 (1987).

[222] W. G. Nettles et al., *Coulomb-nuclear interference measurements of hexadecapole deformations in ^{168}Yb and $^{178,180}Hf$*, J. Phys. G **14**, L223 (1988).

[223] W. J. Huang et al., *The AME2016 atomic mass evaluation: (I). Evaluation of input data; and adjustment procedures*, Chin. Phys. C **41**, 030002 (2017).

[224] M. Wang et al., *The AME2016 atomic mass evaluation (II). Tables, graphs and references*, Chin. Phys. C **41**, 030003 (2017).

[225] J.-Y. Zhang, R. F. Casten, and D. S. Brenner, *Empirical proton-neutron interaction energies linearity and saturation phenomena*, Phys. Lett. B **227**, 1 (1989).

[226] R. F. Casten and N. V. Zamfir, *The evolution of nuclear structure: the N_pN_n scheme and related correlations*, J. Phys. G **22**, 1521 (1996).

[227] R. B. Cakirli et al., *Proton-Neutron Interactions and the New Atomic Masses*, Phys. Rev. Lett. **94**, 092501 (2005).

[228] E. A. McCutchan et al., *Lifetime measurements of yrast states in* ^{162}Yb *and* ^{166}Hf, Phys. Rev. C **73**, 034303 (2006).

[229] G. Alaga et al., *Intensity rules for beta and gamma transitions to nuclear rotational states*, Dan. Mat. Fys. Medd. **29** (1955).

[230] M. Scheck et al., *Photon scattering experiments off* ^{176}Hf *and the systematics of low-lying dipole modes in the stable even-even Hf isotopes* ^{176,178,180}Hf, Phys. Rev. C **67**, 064313 (2003).

[231] J. O. Rasmussen, *Theory of E0 transitions of spheroidal nuclei*, Nucl. Phys. **19**, 85 (1960).

[232] T. Kibédi and R. H. Spear, *Electric monopole transitions between 0^+ states for nuclei throughout the periodic table*, Atom. Data Nucl. Data Tables **89**, 77 (2005).

[233] J. Beller, *Systematic investigation of novel decay branches of the scissors mode in gadolinium isotopes,* PhD thesis (Technische Universität Darmstadt, 2013).

[234] J. Kleemann, *Zerfallsverhalten der Scherenmode in der* $0\nu\beta\beta$-*Tochter* ^{150}Sm, B.Sc. Thesis (Technische Universität Darmstadt, 2016).

[235] J. Kleemann, *Decay Characteristics of the Scissors Mode of the* $0\nu\beta\beta$-*Decay Mother* ^{150}Nd, M.Sc. Thesis (Technische Universität Darmstadt, 2018).

[236] J. L. Wood et al., *Electric monopole transitions from low energy excitations in nuclei*, Nucl. Phys. A **651**, 323 (1999).

[237] J. Enders et al., *Parameter-free description of orbital magnetic dipole strength*, Phys. Rev. C **71**, 014306 (2005).

[238] A. Davydov and A. Chaban, *Rotation-vibration interaction in non-axial even nuclei*, Nucl. Phys. **20**, 499–508 (1960).

[239] K. Heyde, P. von Neumann-Cosel, and A. Richter, *Magnetic dipole excitations in nuclei: Elementary modes of nucleonic motion*, Rev. Mod. Phys. **82**, 2365 (2010).

[240] G. Goldring et al., *Hyperfine Interactions of the First Excited 2^+ State of ^{18}O in 7^+ and 6^+ Ions*, Phys. Rev. Lett. **28**, 763 (1972).

[241] K.-H. Speidel et al., *The magnetic moment of the first-excited 2^+ state in ^{18}O*, Phys. Lett. B **57**, 143 (1975).

[242] J. Asher et al., *A high-velocity recoil-in-vacuum determination of the g-factor and lifetime of the 1.97 MeV 2^+ level in ^{18}O*, J. Phys. G **2**, 477 (1976).

[243] M. Forterre et al., *The sign of the magnetic moment of the first 2^+ state in ^{18}O*, Phys. Lett. B **55**, 56 (1975).

[244] T. Beck, *private communication*, 2019.

[245] K. E. Ide et al., *E2 decay characteristics of the M1 Scissors Mode of ^{152}Sm - in preparation*, 2020.

[246] K. E. Ide, *RDDS measurement of ^{170}W - in preparation*, M.Sc. Thesis (Technische Universität Darmstadt, 2020).

[247] R. Roth, *private communication*, 2019.

[248] K. Vobig, *Electromagnetic Observables and Open-Shell Nuclei from the In-Medium No-Core Shell Model*, PhD thesis (Technische Universität Darmstadt, 2020).

[249] R. V. Jolos, *private communication*, 2016.

[250] K. Heyde and C. De Coster, *Correlation between E2 and M1 transition strengh in even-even vibrational, transitional, and deformed nuclei*, Phys. Rev. C **44**, R2262 (1991).

[251] A. S. Davydov and A. A. Chaban, *Rotation-vibration interaction in non-axial even nuclei*, Nucl. Phys. **20**, 499 (1960).

List of Figures

List of Tables

List of Acronyms

ADC	analogue-to-digital converter
AGATA	advanced gamma-tracking array
AMS	atomic mass spectroscopy
ANL	Argonne national laboratory
BGO	bismuth germanium oxide
CAD	computer-aided design
CASCADE	program to calculate fusion-evaporation cross sections
CBS	confined-β-soft rotor
CD	compact disc
CDF	collider detector at Fermilab
CERN	conseil européen pour la recherche nucléaire
CFD	constant fraction discriminator
CLX	multiple Coulomb excitation program
CMS	center-of-mass
CoulEx	Coulomb excitation
DAQ	data aquisition system
DARCY	Darmstadt Cologne Yale
DSAM	Doppler-shift attenuation method
DSSD	double-sided silicon strip detector
ECR-TDRIV	electron-configuration-reset time-differential recoil-in-vacuum
EM	electromagnetic
EXILL	EXOGAM at ILL
FAIR	facility for anti-proton and ion research
FATIMA	fast timing array

FE	fusion evaporation
FEST	fast electronic scintillation timing
FWHM	full width at half maximum
GASPWARE	gamma-ray spectrometer software
GRETINA	gamma-ray energy tracking in-beam nuclear array
GS	ground state
GSI	Gesellschaft für Schwerionenforschung
GUM	Guide to the Expression of Uncertainty in Measurement
hdtv	nuclear spectrum analysis tool
HO	harmonic oscillator
HORUS	high efficiency observatory for γ-ray unique spectroscopy
HPGe	high-purity germanium
IBM	interacting boson model
IFIN-HH	Institutul National de Cercetare-Dezvoltare pentru Fizica si Inginerie Nucleara (Horia Hulubei)
IKP	Institut für Kernphysik
INFN	Instituto Nazionale di Fisica Nucleare
IPN	l'institut de physique nucléaire
ISOLDE	isotope separator on-line device
LAB	laboratory
LaBr$_3$(Ce)	cerium doped lanthanum bromide
NRF	nuclear resonance fluorescence
NUC	nucleus
NUSHELLX	large scale shell model calculation code
PACE	projection angular-momentum coupled evaporation code
PDF	probability-distribution function
PDG	particle data group
PMT	photo-multiplier tube
PSA	pulse shape analysis
QCD	quantum chromodynamics
QPT	quantum phase transition

RDDS	recoil distance Doppler-shift
RIB	radioactive ion beam
RIV	recoil-in-vacuum
ROSPHERE	romanian array for spectroscopy in heavy ion reactions
SM	shell model
SNICS	source of negative ions by caesium sputtering
SOCO	sorting code Cologne
SORCERER	solar cells for reaction experiments at ROSPHERE
TAC	time-to-amplitude converter
TDC	time-to-digital converter
TDRIV	time-differential recoil-in-vacuum
TF	transient field
USDB	universal sd interaction B

List of Symbols

α	α decay, ^{4}He nucleus, angle or internal conversion coefficient
β	β decay, quadrupole deformation or velocity v/c or angle
β_4	hexadecapole deformation
χ	chiral (χEFT) or IBM parameter
δ	multipole mixing ratio
$\Delta\phi$	$\Delta\phi = \phi_\gamma - \phi_p$
ϵ	efficiency $\epsilon = A/I$
η	Sommerfeld parameter
γ	γ decay, degree of triaxiality or angle
λ	multipolarity, angular momentum or de Broglie wavelength
μ	magnetic moment (operator) or magnetic substate
ν	frequency or neutron
Ω	solid angle
ω	Larmor frequency
ϕ	azimuthal angle
π	parity or proton
ρ	statistical tensor
ρ^2	$E0$ transition strength
σ	cross section or transition character
τ	mean lifetime
θ	polar angle or scattering angle
ξ	dimensionless adiabaticity
ζ	IBM parameter

A	mass number of the nucleus or peak area
a	half-distance of closest approach in a head-on collision, collective coordinates, anti-delayed time distribution or the parameters $a_{kq} = B_{kq}Q_kF_k$ of the angular correlation function
B	magnetic field or orientation parameter
b	CoulEx excitation amplitudes
$B_{4/2}$	$B(E2; 4_1^+ \rightarrow 2_1^+)/B(E2; 2_1^+ \rightarrow 0_{\mathrm{GS}}^+)$
BE	binding energy
$B(E2; 2_1^+ \rightarrow 0_{\mathrm{GS}}^+)$	$E2$ transition strength
$B(\sigma\lambda)$	reduced transition probability
C	centroid or capacity
D	time distribution or Wigner-D matrix
d	distance, delayed time distribution or $L = 2$ boson
$\delta B(E2)$	$B(E2)_N - B(E2)_{N-2}$
E	energy
F	angular distribution coefficient
G	attenuation coefficient
g	g factor or dimensionless magnetic moment
H	Hamiltonian
I	nuclear spin operator or intensity
J	total angular momentum
l	angular momentum (operator)
$\mathfrak{M}$	multipole transition operator
m	mass or magnetic substate
N	neutron number, number of valence protons (neutrons), number of bosons bosons or number of counts
n	boson number operator or neutron
P	probability that a nucleus is excited from state i to state f, prompt response of the detection system, legendre polynom or $P = N_\pi N_\nu/(N_\pi + N_\nu)$ factor

Q	quadrupole moment, solid angle correction factor, quadrupole (structure) operator or charge state
r	radius or stiffness parameter of CBS
$R_{4/2}$	$E(4_1^+)/E(2_1^+)$
s	intrinsic spin (operator) or $L = 0$ boson
S_{2n}	two-neutron separation energy
T	kinetic energy or transition probability per unit time
t	time
$T_{1/2}$	half live
V	potential energy
v	velocity
W	angular distribution or angular correlation
Y	spherical harmonics or yield
Z	proton number

List of Publications

Publications

- **J. Wiederhold** et al., *Evolution of E2 strength in the rare-earth isotopes* ^{174,176,178,180}Hf, Phys. Rev. C **99**, 024316 (2019).

- M. Stoyanova et al., *Lifetimes of the 4_1^+ states of* ^{206}Po *and* ^{204}Po*: A study of the transition from noncollective seniority-like mode to collectivity*, Phys. Rev. C **100**, 064304 (2019).

- T. Beck et al., *SORCERER: A novel particle-detection system for transfer-reaction experiments at ROSPHERE*, Nucl. Instrum. Methods. Phys. Res., Sec. A **951**, 163090 (2019).

- **J. Wiederhold** et al., *Fast-timing lifetime measurement of* ^{152}Gd, Phys. Rev. C **94**, 044302 (2016).

- K. E. Ide et al., *E2 decay characteristics of the M1 Scissors Mode of* ^{152}Sm - *in preparation*, 2020.

- **J. Wiederhold**, *Fast-timing lifetime measurement of* ^{150}Gd. - in preparation, 2020.

Conference proceedings

- R. Kern et al., *Coulomb Excitation of Proton-rich N = 80 Isotones at HIE-ISOLDE - submitted*, J. Phys. Conf. Ser. (2020).

- E. Adamska et al., *γ-ray spectroscopy of* ^{85}Se *produced in* ^{232}Th *fission - submitted*, Acta. Phys. Pol. B (2020).

- **J. Wiederhold** et al., *Fast-Timing Lifetime Measurement of* ^{174,176,178,180}*Hf*, in Basic Concepts in Nuclear Physics: Theory, Experiments and Applications, edited by J.-E. Garcia-Ramos et al. (2019), p. 259.

- V. Werner et al., *Shape transitions between and within Zr isotopes*, Euro. Phys. J. Web Conf. **223**, 01070 (2019).

- N. Jovančević et al., *Spectroscopy of Neutron Induced Reactions with the -ball Spectrometer*, Acta. Phys. Pol. B **50**, 297 (2019).

- **J. Wiederhold** et al., *Signatures for a nuclear quantum phase transition from E0 and E2 observables in Gd isotopes*, J. Phys. Conf. Ser. **1023**, 012024 (2018).

- M. Stoyanova et al., *A study on the transition between seniority-type and collective excitations in 204Po and 206Po*, Euro. Phys. J. Web Conf. **194**, 03002 (2018).

- A. Khaliel et al., (IS 628 collaboration), *Shape transitions between and within Zr isotopes*, HNPS proceedings **0**, 1795 (2019).

- R. Kern et al., *Search for Isovector Valence-Shell Excitations in 140Nd and 142Sm via Coulomb excitation reactions of radioactive ion beams*, Euro. Phys. J. Web Conf. **194**, 03003 (2018).

- C. Bauer et al., *Level lifetimes and quadrupole moments from Coulomb excitation in the Ba chain and the N = 80 isotones*, Euro. Phys. J. Web Conf. **38**, 10003 (2012).

Laboratory reports

- I. Zanon et al., *Shape Coexistence in the Neutron-Deficient 188 Hg Isotope*, LNL report 2017 (2018).

- I. Zanon et al., *Shape Coexistence in the Neutron-Deficient 190 Hg Isotope*, LNL report 2018 (2019).

- **J. Wiederhold** et al., *Fast-timing lifetime measurement of 152Gd with FATIMA-type LaBr$_3$ detectors*, GSI report 2017 (2018).

Erklärungen laut Promotionsordnung

§8 Abs. 1 lit. c PromO

Ich versichere hiermit, dass die elektronische Version meiner Dissertation mit der schriftlichen Version übereinstimmt.

§8 Abs. 1 lit. d PromO

Ich versichere hiermit, dass zu einem vorherigen Zeitpunkt noch keine Promotion versucht wurde. In diesem Fall sind nähere Angaben über Zeitpunkt, Hochschule, Dissertationsthema und Ergebnis dieses Versuchs mitzuteilen.

§9 Abs. 1 PromO

Ich versichere hiermit, dass die vorliegende Dissertation selbstständig und nur unter Verwendung der angegebenen Quellen verfasst wurde.

§9 Abs. 2 PromO

Die Arbeit hat bisher noch nicht zu Prüfungszwecken gedient.

Darmstadt, 17. Dezember 2019

Johannes Christoph Wiederhold